DISSERTATION

APPLICATION OF PASSIVE FLOW CONTROL TO MITIGATE THE THROMBOEMBOLIC POTENTIAL OF BILEAFLET MECHANICAL HEART VALVES: AN *IN-VITRO* STUDY

Submitted by

Márcio Henrique Forléo

Graduate Degree Program in Bioengineering

In partial fulfillment of the requirements

For the Degree of Doctor of Philosophy

Colorado State University

Fort Collins, Colorado

Summer 2014

Doctoral Committee:

Advisor: Lakshmi Prasad Dasi

Susan James
Christopher Orton
Frank Dinenno

ABSTRACT

APPLICATION OF PASSIVE FLOW CONTROL TO MITIGATE THE THROMBOEMBOLIC POTENTIAL OF BILEAFLET MECHANICAL HEART VALVES: AN *IN-VITRO* STUDY

Implantation of a bileaflet mechanical heart valve (BMHV) continues to be associated with risk of thromboembolic complications despite anti-coagulation therapy. Mechanical heart valves have been the gold standard in valve heart replacement since the 1950s with BMHVs currently still being the valve of choice for younger patients. Given that a large body of literature points to thromboembolic complications due to poor hemodynamics, improvements to the hemodynamic performance of BMHVs are needed. In this study, we explore the concept of passive flow controls that have been widely used in aerospace industry as a novel approach towards improving BMHV design. Passive flow control elements are small features on solid surfaces, such as vortex generators (VGs), that alter flow to achieve desired performance. The specific aims of this study are (1) develop a methodology to evaluate thromboembolic potential (TEP) of BMHVs using *in-vitro* particle image velocimetry technique, (2) quantify the efficacy of rectangular VGs distributed on BMHV leaflets to reduce TEP, and (3) quantify the hemodynamic performance impact of rectangular VGs.

An *in-vitro* pulsatile flow loop along with Particle Image Velocimetry (PIV) flow visualization technique was developed, validated, and utilized to acquire time-resolved

velocity fields and shear stress loading: Lagrangian particle tracking analysis of the upstream and downstream flow during diastole and systole enabled the calculation of predicted shear stress history and exposure times corresponding to platelets. This information was then used in numerical models of blood damage to predict the TEP of test heart valves using established platelet activation and platelet lysis parameters.

BMHV leaflets were constructed using 3D printing technology with VGs based on micro-CT scans of a model BMHV leaflet. Two configurations were constructed: co-rotating VGs and counter-rotating VGs. Co-rotating VGs consist of single features 1mm tall and 2.8mm long spaced equally apart (5mm) at an angle of attack of 23 degrees. Counter-rotating VGs consist of mirrored feature pairs 1mm from each other with the same dimensions as the co-rotating VGs. The leaflets were tested using the methodology described above to elucidate their effect on the TEP of the BMHV compared to the control leaflets. For systolic flow downstream of the valve, we report a decrease in the average platelet activation and average platelet lysis TEP (both normalized by the average exposure time) largely in the central jet, with the vortex generator equipped leaflets compared to the control leaflets at a p-value of 0.05. However, for diastolic flow upstream of the valve, we report an increase in the average platelet lysis TEP and average platelet activation TEP (both normalized by the average exposure time) largely in the regurgitant jet zone with the vortex generator equipped leaflets compared to the control leaflets at a p-value of 0.05.

Also, steady and pulsatile flow experiments were conducted to calculate the transvalvular pressure drop across the model BMHV with control leaflets (no VGs) and

leaflets containing VGs to calculate effective orifice area (EOA), which is an index of valve performance and is related to the degree to which the valve obstructs blood flow. We report a significant increase in EOA values for valves with leaflets containing passive flow control elements in both steady and pulsatile flow experiments compared to the control leaflets. Under steady flow, the co-rotating VGs configuration had the best EOA value compared to the control leaflet and counter-rotating vortex generator configuration. However, under pulsatile conditions, the counter-rotating VGs configuration had the best EOA value compared to the control leaflet and co-rotating vortex generator configuration. PIV measurements highlight the delay in flow separation caused by the VGs and corroborate the increased pulsatile flow EOA values.

This study shows that the TEP of BMHVs can be accurately evaluated using *in-vitro* PIV techniques and that there is room for improvement in BMHV design using passive flow control elements. With optimization of passive flow control configuration and design, it is possible to further decrease the TEP of BMHVs while increasing their hemodynamic performance; thus creating a safer, more efficient BMHV.

ACKNOWLEDGEMENTS

I would like to thank my advisor, Dr. Lakshmi Prasad Dasi, for his instruction and wealth of knowledge. His insight has been extremely valuable in shaping my research and career. I am also grateful to Dr. Susan James, Dr. Chris Orton, and Dr. Frank Dinenno for serving on my dissertation committee and providing their vast knowledge on my work.

I would also like to thank all of my labmates in the Cardiovascular and Biofluid Mechanics Laboratory for providing their input and ideas to my work; Brennan Johnson, Niaz Morshed, Evan Koenig, Brandon Moore, Michael Gogarty, Rachael Walker, Dr. David Bark.

This dissertation would never have been possible without many more people:

Thank you to my extended Salisbury family, the Briddells, for their thoughts, prayers, and lunch money that they sent my way.

Thank you to the best friends someone could have, Casey and Linnéa Geiger, for keeping me sane and for being my lifeline.

Thank you to Clint Jeane and Rachael Carlberg for always being there for me whenever I need help or someone to have a drink with.

Thank you to Jon McKeon for giving me a haven in his gym to blow off steam, have fun, and stay healthy.

Thank you to Dr. Michael Daine for his invaluable advice and guidance through my time as a doctoral student.

Last, but not least, I would like to thank my mom, Laura, and my grandmother, Vovó Lydia, for their endless support, encouraging words, and patience with the roller coaster of emotions I put them through day in and day out.

I dedicate this work to my late father, Cid Forleo, who instilled in me the value of an education, a love of science and engineering, and who – along with my mother – sacrificed a comfortable life in Brazil to provide me with the best education possible in the United States.

TABLE OF CONTENTS

LIST OF TABLES

LIST OF FIGURES

CHAPTER 1: INTRODUCTION

Heart valve disease is the second major component of cardiovascular disease after coronary disease and affects more than a million people every year worldwide. Over 280,000 heart valve replacements are performed per year worldwide; with 90,000 of these in the United States alone (Pibarot & Dumesnil, 2007). Nearly 65% of valve replacement procedures utilized mechanical heart valves due to their superior durability and acceptable bulk flow hemodynamics. Unfortunately, implantation of mechanical heart valves continues to be associated with a high risk of thromboembolic complications despite required lifelong *anti-coagulation* therapy (Black & Drury, 1994; Cannegieter, Rosendaal, & Briet, 1994; Jamieson et al., 2002; Mecozzi, Milano, De Carlo, & Sorrentino, 2002; Turitto & Hall, 1998). Given that a large body of literature points to thromboembolic complications due to poor hemodynamics, improvements to the hemodynamic performance of BMHVs are needed (A Bellofiore, 2011; Black & Drury, 1994; Bluestein, Li, & Krukenkamp, 2002; Bluestein, Niu, Schoephoerster, & Dewanjee, 1996; BR et al., 2001; Cannegieter et al., 1994). The gold standard in valve mechanical heart valve replacements has been the bileaflet mechanical valve with more than 130,000 of them implanted every year worldwide. The leaflet opening and closure mechanics in BMHVs are associated with strong non-physiological flows that create intense regions of high shear stress and recirculation (Bluestein, Rambod, & Gharib, 2000). These regions have been shown to cause platelet activation, aggregation, and hemolysis, leading to thromboemboli.

From an engineering perspective, it is indeed possible to mitigate shear stress using the concept of passive flow controls that are widely used in the aerospace industry. Passive flow control elements can be small features on solid surfaces that alter flow to achieve desired performance. Low aspect ratio plates and airfoils that are mounted normal to the surface along their long chords are called vortex generators. Because vortex generators are mounted at an angle relative to the oncoming flow, they form either clockwise or counterclockwise “wing tip” streamwise vortices depending on their orientation. The vortex generators are typically arranged in spanwise arrays that can be formed with single or symmetric pairs to produce either single-sign or counter-rotating streamwise vortex pairs. These vortices scale with the characteristic dimensions of the generating elements and lead to enhancement of entrainment (e.g., transfer of high momentum fluid towards the surface) and small-scale mixing of fluid with the embedding flow field. Applications have included the suppression or mitigation of flow separation in external and internal flows (Lin, 2002) and mixing enhancement with free shear flows that are typically dominated by large coherent vertical structures.

The objective of this study was two fold. The first goal was to investigate the propensity of BMHVs to cause damage to blood as it passed through the valve. Investigations looked at both the forward flow during ventricular systole and regurgitant flow during ventricular diastole. The second goal was to build and study BMHVs with passive flow control elements designed to mitigate shear stress and blood damage while improving hemodynamic performance. The overarching hypothesis of this study is that BMHV design may be improved to mitigate TEP through vortex generators.

The broader objective of this study was to provide a quantitative and qualitative description of the thromboembolic potential of BMHVs along with possible methods for improving overall valve performance.

CHAPTER 2: BACKGROUND

The sections in this chapter will provide background information on the anatomy, function, and disease of heart valves, the various types of replacement heart valve as treatment options, and possible complications associated with each valve. Thromboembolic complications caused by red blood cell and platelet damage due to shear stress will be described along with previous investigations that attempted to quantify the relationship between shear stress levels and thrombosis. Finally, this chapter will describe a possible approach to decrease the thromboembolic potential of BMHVs using passive flow control elements.

2.1 The Heart

The heart is a four chamber pump responsible for pumping blood through the circulatory systems; the pulmonary circuit and systemic circuit. The upper two chambers, the right and left atria, receive blood from veins and pump it to their respective ventricles. The lower two chambers, the right and left ventricles, receive blood from the atria and pump it to the lungs and the body. The right side of the heart (right atrium and right ventricle) is responsible for pumping deoxygenated blood from the heart (right ventricle) to the lungs – where it is re-oxygenated – and back to heart (into the left atrium). The left side of the heart (left atrium and left ventricle) is responsible for pumping oxygenated blood from the heart (left ventricle) to the rest of the body – where it delivers oxygen and becomes deoxygenated – and back to the heart (right atrium).

2.2 Heart Valves

The four heart valves within the heart control the flow direction of blood and open/close based upon the differential pressure on each side. The two antriventricular valves are located between the atria and ventricles of the heart; the tricuspid valve between the right atrium and right ventricle, and the mitral valve between the left atrium and left ventricle. The two semilunar valves are located between the ventricles and arteries; the pulmonary valve between the right ventricle and pulmonary artery, and the aortic valve between the left ventricle and aorta. Except for the mitral valve, the valves consist of three tissue flaps (known as leaflets).

2.2.1 Heart Valve Diseases and Replacement

Heart valve disease can be caused by rheumatic fever, ischemic heart disease, bacterial and fungal infection, connective tissue disorders, trauma, and malignant carcinoid (Black & Drury, 1994; Cebi & Bozkurt, 2004; Korossis, Fisher, & Ingham, 2000) which can be categorized into two types; regurgitation and stenosis. Regurgitation occurs when a valve does not close completely or properly, thus causing blood to leak backwards (Figure 1). This condition causes the heart to pump harder and over time, become enlarged and less efficient.

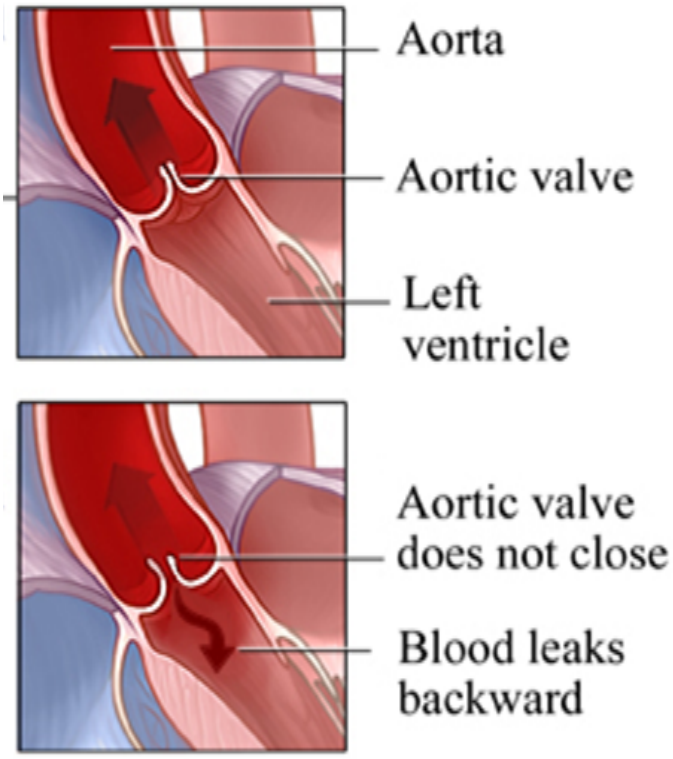

Figure 1: Aortic regurgitation: aortic valve does not close completely and blood leaks backward.

In stenosis, the valve does not open completely or properly, thus only allowing a fraction of blood to flow through (Black & Drury, 1994; Korossis et al., 2000) (Figure 2). The mitral and aortic valve usually have a higher failure rate than the tricuspid and pulmonary valve because they encounter flow conditions with higher pressure differences and flow rates.

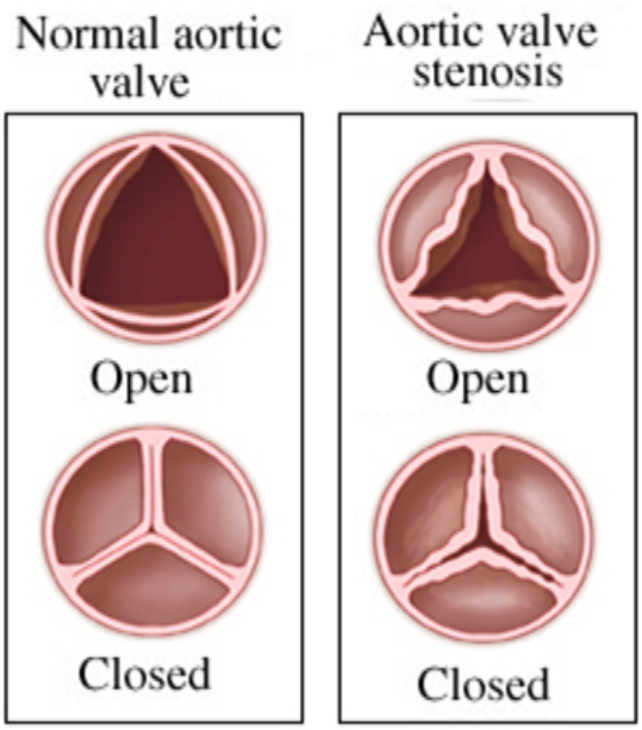

Figure 2: Aortic valve stenosis: leaflets do not open properly; only a portion of blood flows through.

2.3 Prosthetic Heart Valves

Prosthetic heart valves can be divided into three groups: mechanical heart valves, bioprosthetic heart valves (tissue valves), and polymeric heart valves. Bioprosthetic heart valves are made from a combination of synthetic and natural tissue such as chemically treated porcine or bovine pericardium to mimic the design and function of native heart valves. Polymeric heart valves are similar to bioprosthetic heart valves, however, they utilize flexible synthetic materials such as polyurethane to mimic the design and function of the native heart valve. Mechanical heart valves are manufactured

from synthetic materials such as pyrolytic carbon, ultra-high molecular weight polyethylene, etc.

2.3.1 Bioprosthetic Heart Valves

Bioprosthetic heart valves mimic the native heart valve in design and mechanics which in turn produces a lower potential in blood element damage than mechanical heart valves. However, the tissue that composes the leaflets degrades rapidly and is prone to calcification (Black & Drury, 1994). Bioprosthetic valves usually last ten years and often require replacement/reoperation.

Figure 3: Example of bioprosthetic heart valve: stented porcine tissue valve.

2.3.2 Polymeric Heart Valves

Polymeric heart valves attempt to combine the advantages of mechanical heart valves (durability) and bioprosthetic heart valves (hemodynamics) while eliminating the disadvantages of said mechanical heart valves (blood element damage potential requiring anti-coagulation therapy) and bioprosthetic heart valves (calcification). However, clinical outcomes have shown that polymeric valves are susceptible to

thromboembolic events, material failure, and in some cases calcification (Hyde, Chinn, & Phillips, 1999).

Figure 4: Example of polymeric heart valve: silicone and polyurethane copolymers.

2.3.3 Mechanical Heart Valves

Mechanical heart valves were the first type of prosthetic heart valves to be successfully implanted, specifically, the caged-ball heart valve in 1961. Improvements to mechanical heart design improved their hemodynamic performance (lower pressure drops and reduced turbulent fluid stresses) by replacing the caged-ball heart valve with the tilting-disk heart valve in the late 1960s. In the 1970s, bileaflet mechanical heart valves were introduced and became the gold standard in mechanical heart valve implantations. The bileaflet mechanical heart valve replaced the single tilting disk with two semi-circular leaflets and further improved the hemodynamic performance of mechanical heart valves.

Figure 5: Examples of mechanical heart valves. Left: Caged-ball. Middle: Tilting disk. Right: bi-leaflet.

Complications from mechanical heart valve implantation can include valve structural failure, non-structural valve malfunction, thrombosis, embolism, bleeding, and endocarditis (Grunkemeier & Anderson, 1998). Mechanical heart valve design evolution has reduced the complications associated with mechanical design and material, however, complications in the form of hemodynamic performance such as hemolysis, platelet activation, platelet lysis, and thromboembolic which require life-long anti-coagulation therapy (which itself can cause complications such as increased risk of infection, hemorrhaging, autoimmune response, and accelerated calcification (Danziger, 2008; Walker & Yoganathan, 1992)) after implantation can still occur (Black & Drury, 1994; Cannegieter et al., 1994; Ellis, Wick, & Yoganathan, 1998; Mecozzi et al., 2002; Vongpatanasin, Hillis, & Lange, 1996). This has been attributed to the structurally rigid design of the leaflets, the valve mechanics, and the intricate hinge mechanism for the rigid leaflets (Black & Drury, 1994; Bluestein et al., 2002, 2000). The lack of an integral compliance within the valve mechanics presumable leads to sharp stress gradients (Govindarajan et al., 2010; Herbertson, Deutsch, & Manning, 2011) within the flow and a

violent closure of the valve; which is often associated with the audible impact of the leaflets to the housing and the potential for momentary cavitation of blood in the wake of leaflet impact (Keefe B Manning, Herbertson, Fontaine, & Deutsch, 2008). The leaflet closure is a dynamic fluid-structure interaction event which begins with the reversal of pressure gradient across the BMHV initiated by the relaxation of the ventricular muscles (CHANDRAN & Aluri, 1997). Thus, the closure is largely dictated by the magnitude of the mean back pressure generated by the compliant arterial walls that provide the force for the closure (GILLJEONG & CHANDRAN, 1995). The mean aortic pressure (MAP) represents the backpressure that drives the leaflet closure and the transvalvular pressure dictates the velocity and strength of the regurgitant jet flow structures. In the case of BMHVs, the closure mechanics of the leaflets is associated with non-physiological flow; the formation of the closing vortex as a precursor to the eventual regurgitation jet that emanates from the b-datum line (which is defined as the gap between the two leaflets along the center of the valve orifice) of BMHVs (L P Dasi, Murphy, & Glezer, 2008; Lakshmi P Dasi, Simon, Sucosky, & Yoganathan, 2009; K B Manning, Kini, Fontaine, Deutsch, & Tarbell, 2003). The closing phase and the regurgitant phase have long been recognized as being critical in the context of blood damage (Fallon et al., 2006). Similarly to leaflet closure, leaflet opening is also a dynamic fluid-structure interaction event which begins with the reversal of pressure gradient across the BMHV initiated by the contraction of the ventricular muscles and is dictated by the magnitude of the mean pressure generated by the left ventricle that provides the force to eject blood from the ventricle. The opening mechanics of the leaflets is again associated with non-physiological flow; the formation of two opening

vortices which initiate vortex shedding from the two leaflets throughout ventricular systole diving the flow into two lateral and one central jet.

2.4 Blood and Blood Damage

Blood is composed of blood cell elements suspended in blood plasma. Plasma is mostly water and makes up 55-60% percent of the blood volume. Blood elements included red blood cells (RBCs), platelets, and white blood cells (WBCs). Red blood cells, platelets, and white blood cells account for 95%, 4.9%, 0.1% of the blood elements by volume, respectively. The volume fraction of blood elements in the blood is referred to as the hematocrit and is approximately 40-45% in normal blood. Red blood cells contain hemoglobin and deliver oxygen throughout the body. Platelets form clots (thrombosis) to repair vascular injuries to stop bleeding. White blood cells engulf and ingest foreign particles in the blood. Plasma itself is a Newtonian fluid, however, the presence of blood elements changes the flow characteristics and rheology of the fluid to a non-Newtonian fluid.

2.4.1 Red Blood Cell Damage

Red blood cells are flexible and biconcave discoid shaped with a thickness of around 2.8 microns, diameters in the range of 6-8 microns, and a life span of around 120 days. The cell membrane, composed of flexible phospholipids, is permeable, allowing for gas diffusion of oxygen and carbon dioxide between hemoglobin molecules in the cytoplasm. Given the shape and the flexibility of the RBC membrane, it can experience large amounts of deformation without tearing. Red blood cell membranes under shear are initially viscoelastic, but under high enough loads, can become viscoplastic (Chien, 1977). RBCs can undergo damage in the form of hemolysis, the rupturing of the cell

membrane, which releases hemoglobin to the surrounding plasma. Red blood cells can also be stretched to the point where the membrane can tear or for holes to form in the membrane that allow for hemoglobin to diffuse into the plasma. Hemolysis can be caused by either instantaneous damage at high stress or cumulative damage to the membrane over time.

2.4.2 Platelet Damage

Platelets have a diameter of around 3 microns and an average life span of 10 days. Non-activated platelets have a flat discoid shape. When activated by external stimuli, such as vascular injury, platelets activate and change their shape; the cytoskeleton changes and extends long pseudopods to adhere to the collagen that becomes exposed due to damaged endothelium. Platelet activation occurs in three stages (also known as the coagulation cascade): initiation, aggregation, and propagation. In initiation, the platelets ruptured release tissue factor into the blood which bind to other factors and activate prothrombin. Prothrombin produces thrombin and other factors that have a role in platelet aggregation, adhesion, and propagation. Platelets can be activated due to long exposure to shear stresses leading to the formation of free-floating emboli that can occlude smaller vessels and leading to stroke and death.

2.4.3 Blood Damage and Shear Stress

Blood damage due to prosthetic heart valves can be related to the flow physics, mechanical stresses, and forces imposed on the blood elements by the non-physiological flow environment created by the prosthetic heart valve.

2.4.3.1 Red Blood Cell and Shear Stress

The primary mechanism of hemolysis is the mechanical shear stress imposed on blood elements. Under a uniform stress field imposed by a Couette viscometer, the threshold shear stress for hemolysis after two minutes was 1,500 dynes/cm^2 with significant hemolysis occurring when shear stresses exceeded 3000 dynes/cm^2 (Nevaril, Lynch, & Alfrey, 1968). However, studies have shown that red blood cells are vulnerable to sublethal damage at shear stresses of 500 dynes/cm^2 and by as little as 10-100 dynes/cm^2 in the presence of foreign surfaces. Subsequent studies found the importance of exposure time to mechanical stresses and the resulting hemolysis (Leverett, Hellums, Alfrey, & Lynch, 1972). Blackshear separated hemolysis due to shear stress into three categories: hemolysis induced by surface interaction, by medium stresses occurring in flow (1000-2000 dynes/cm^2 for several seconds), and by high stresses occurring in flow (40000 dynes/cm^2 for milliseconds) (Blackshear, 1972). In medium shear stresses, RBCs would become damaged gradually and hemolysis was dependent on exposure time. In high shear stresses, hemolysis occurred immediately and exposure time was not a significant factor. Hellums expanded on this study and determined that there were two regimes for shear stresses and exposure time that led to hemolysis (J. D. Hellums, 1994). The first regime, low shear stress and short exposure time caused little hemolysis and the surface interaction caused most of the blood damage. In the second regime, high shear stresses and long exposure time causes very high hemolysis to occur with shear stress being the dominant factor. Lu examined the new concept of a threshold shear stress that must be surpassed to cause hemolysis by using a known jet flow field to relate shear stress values with red blood

cell damage. A threshold shear stress of 800 N/m^2 was determined with a 1ms exposure time. Beyond this stress, hemolysis increased with increasing shear stress and below this level, no hemolysis occurred (Lu, Lai, & Liu, 2001).

2.4.3.2 Platelets and Shear Stress

Recent studies have shown that thrombus formation due to shear activation occurs in a two-step mechanism (Fallon, 2006; Fallon et al., 2006). Platelets are activated by shear stress that results in mechanotransduction of the force to the GP1b receptor. This mechanotransduction enables binding of the GP1b receptor to vWF and a subsequent influx of the calcium ions, resulting in platelet activation. Upon activation, the GpIIb/IIIa receptor is activated and can then bind to other ligands such as fibrinogen, vWF, fibronectin, and vitronectin. At this time, Platelet Factor Four (PF4) is released as an indication of platelet activation. The coagulation cascade is propagated and can lead to the formation of thrombin-antithrombin III (TAT), which is a relative measure of thrombin formation. Cone and plate viscometers have been used to show that platelet activation can occur at shear stresses as low as 60-80 $dynes/cm^2$ (Fallon et al., 2006). Regions of flow stasis and recirculation have been shown to correlate to platelet deposition, particularly if these regions follow directly after a region of high shear stress (Bluestein et al., 1996). The regions of flow stagnation that occur at the blood-material interface on prosthetic heart valves immediately adjacent to these high shear stress flow environments could promote the deposition of damaged blood elements, leading to thrombus formation on the valve (A. Yoganathan, 1997).

2.4.3.3 Shear Stress on Red Blood Cells vs. Platelets

Shear stress and exposure time is a key factor in both hemolysis and platelet activation. For long exposure times, platelets are more sensitive to shear stress and incur more damage than red blood cells. The threshold shear stress for hemolysis has been found to be ten times higher (1500 dynes/cm^2) than the threshold shear stress for platelets lysis under an exposure time of two minutes (Bernstein, Marzec, & Johnston, 1977; J David Hellums & Brown, 1977). For very short exposure times, platelets were more resistant to damage at high shear stress than RBCs (Grunkemeier & Anderson, 1998). However, platelet activation has been shown to occur at shear stresses around 60-80 dynes/cm^2. Therefore, the research in this paper will focus on shear stress as related to platelet activation and platelet lysis since the threshold levels are significantly lower than hemolysis. Although blood damage resulting from heart valves, ventricle assist devices, and bypass pumps has been examined clinically (Kawahito, Adachi, & Ino, 2000; Spanier, Oz, Levin, & Weinberg, 1996), the shear-inducing flow conditions necessary to damage blood have best been elucidated in bileaflet mechanical heart valves.

2.5 Previous Investigations

Many *in-vitro* blood loop studies have addressed the platelet activation, platelet aggregation, and hemolysis caused by mechanical heart valves and stenoses. In one such study using porcine blood, hemolysis was shown to increase for both the forward and reverse flow conditions, corresponding to mitral and aortic positions (LAMSON et al., 1993). In this study, the aortic position was shown to be more damaging during leakage flow. Using human blood, Travis et al (BR et al., 2001; Travis et al., 2001) studied platelet activation with the Medtronic parallel valve, the St. Jude Medical

(SJM) Standard valve, and prototype valves with varying hinge gap widths. I was shown that platelet activation increases with time and that gap widths larger and smaller than the clinical quality SJM Standard valve induced more platelet activation and blood damage than the regular clinical quality SJM Standard valve (Travis et al., 2001). Clinical studies have shown higher incidences of platelet aggregates in patients with a stenotic native valve and also correlated areas of high shear stress, stagnation, and separation to thrombus formation in the SJM and the Carbomedics BMHVs (H L Leo, 2005; Maugeri, Santarelli, & Lazzari, 2000). The Medtronic Parallel valve demonstrated thrombus formation near the hinge inflow region in human clinical trials while successfully performing in pre-clinical animal studies (Lakshmi P Dasi et al., 2009). These preliminary studies show that blood damage and platelet activation occurs due to the non-physiological stresses experienced by blood elements, such as in the hinge region, b-datum line, and forward flow through 3 orifices. As an attempt to model the flow phenomena through BMHVs, recent studies have successfully developed an *in-vitro* blood loop to study the procoagulant nature of mechanical heart valves through the use of idealized geometries such as orifices and slits (Bakker, Kouwenhoven, Hartkamp, Hoogeveen, & Mali, 1995)(Bakker et al., 1995). The slits model the flow through the b-datum line with the orifices model the flow through the hinge gaps (Fallon et al., 2006)(Fallon et al., 2006). This system quantifies the amount of TAT and PF4 in the blood as positive indicators of coagulation and platelet activation, where a linear increase in the cumulative TAT over a period of one hour indicates a constant TAT production rate for blood flowing through a 400 micron round orifice. Studies have also used mathematical models to predict blood trauma such as the power-law mathematical

formulation to relate shear stress and exposure time to classify hemolytical potential in terms of free released hemoglobin (Giersiepen, Wurzinger, Opitz, & Reul, 1990; Grigioni et al., 2004). However, this formulation only quantifies the percent of free hemoglobin with respect to the total hemoglobin in blood when red blood cells are loaded with a constant shear stress (Grigioni, Morbiducci, D'Avenio, Benedetto, & Gaudio, 2005). More recently, models have been improved to account for damage cumulability and loading history to satisfy theories of multiple passage phenomena and sublethal damage. Grigioni et al set three conditions to check the physical consistency of power-law formulations to predict blood damage caused by time-varying shear: it must not clash with the principle of causality (preventing the reduction of damage in the presence of decreasing shear stress), it must be able to reproduce predictions when a uniform load is acting on blood cells, and it must be able to account for the loading history sustained by blood cells (Grigioni et al., 2005). Lagrangian measures to estimate the thromboembolic potential of prosthetic heart valves by using blood damage index models have been used in CFD studies and experimental models (Alessandro Bellofiore, Donohue, & Quinlan, 2011; Yun et al., 2012).

2.6 Flow Control

In the context of thromboembolic potential in BMHVs, the approach of passive flow control elements may be used in BMHVs to decrease the thromboembolic potential by altering the flow characteristics through the valve.

2.6.1 Vortex Generators

Passive devices for manipulating and controlling the evolution of both free and wall-bounded turbulent shear flows have been used in a broad range of internal and external

flows of aerodynamic, hydrodynamic and biological systems by implementing structural changes in the flow boundary using distributed arrays of elements that either protrude above the surface or indentations and grooves that penetrated into the surface. Figure 6 illustrates the effect of vortex generators on the airflow over an airplane wing.

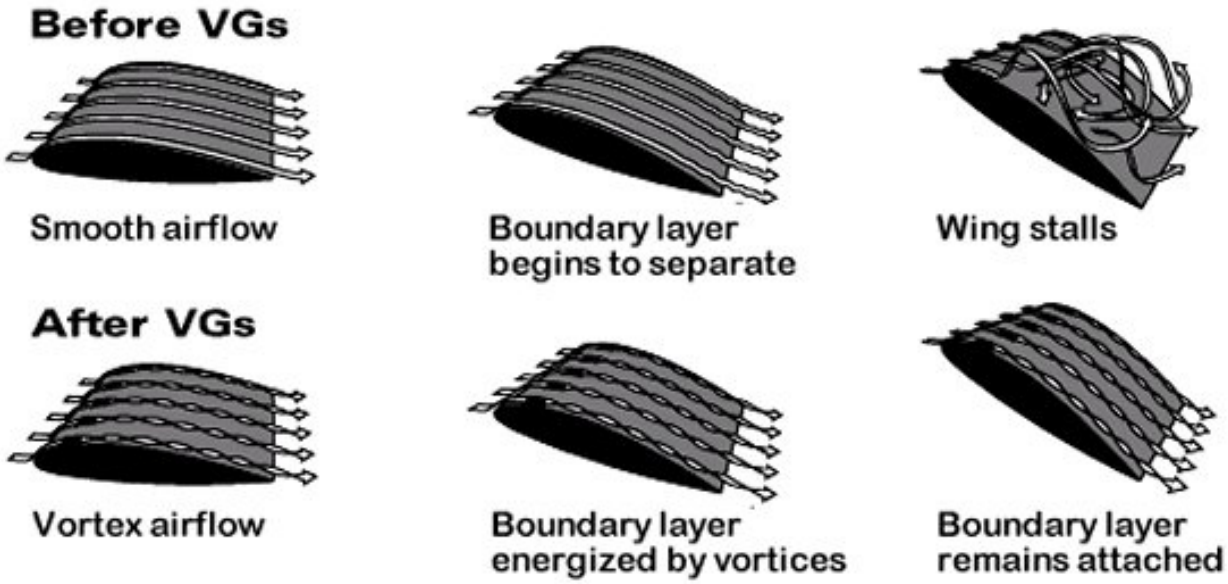

Figure 6: The effect of vortex generators in delaying flow separation on an airplane wing.

Typical implementations of devices that protrude from the surface have included transverse cylinders and plates and airfoils that are oriented parallel or normal to the flow (Bushnell & McGinley, 1989). In the parallel configuration these plates or airfoils typically shed spanwise vortices along the surface and can lead to premature transition to turbulence of the wall boundary layer, modification of the turbulent flow structure (Goodman, 1985), or to break up larger vertical eddies that are present in the flow (Guezennec & Nagib, 1990). Low aspect ratio plates and airfoils that are mounted normal to the surface along their long chords are called vortex generators. Because vortex generators are mounted at an angle relative to the oncoming flow, they form

either clockwise or counterclockwise “wing tip” streamwise vortices depending on their orientation. The vortex generators are typically arranged in spanwise arrays that can be formed with single or symmetric pairs to produce either single-sign or counter-rotating streamwise vortex pairs. These vortices scale with the characteristic dimensions of the generating elements and lead to enhancement of entrainment (e.g., transfer of high momentum fluid towards the surface) and small-scale mixing of fluid with the embedding flow field. Applications have included the suppression or mitigation of flow separation in external and internal flows (Lin, 2002) and mixing enhancement with free shear flows that are typically dominated by large coherent vertical structures. Earlier work in free turbulent jets has demonstrated that the interaction between the jet's predominantly azimuthal vorticity and the streamwise vortices induced by passive vortex generators can lead to mixing enhancement and therefore a reduction in shear. Moreover, the increase in small-scale motion within the flow leads to enhancement and consequently to dissipation of turbulent fluctuations. In early studies by Bradbury and Khadem (Bradbury & Khadem, 2006), axial vorticity was introduced by placing tabs at the jet exit such that they protruded into the flow (typically with an area blockage of 1-2% per tab). It was shown that even two tabs could significantly increase mixing and increase jet to reduce the potential core length and increase the decay of the centerline velocity thereby increasing jet spreading and reducing the flow shear. In later investigation, streamwise vorticity generation at the jet exit was promoted by enforcing azimuthal excitation through vortex generators or tabs at the edge of the nozzle (Ahuja & Brown, 1989; K. B. M. Q. Zaman & Foss, 1997; K. Zaman, Reeder, & Samimy, 1994) or by using corrugated, lobed, or indented nozzle edges.

2.7 Aortic Valve Area

2.7.1 Effective Orifice Area (EOA)

Effective orifice area is a measure of aortic valve area for prosthetic heart valves which is used as an index of hemodynamic performance and valve quality. EOA is related and dependent on the opening area of the valve. However, EOA is the minimal cross-sectional area of the downstream jet during systole (Garcia & Kadem, 2006) as seen in Figure 7.

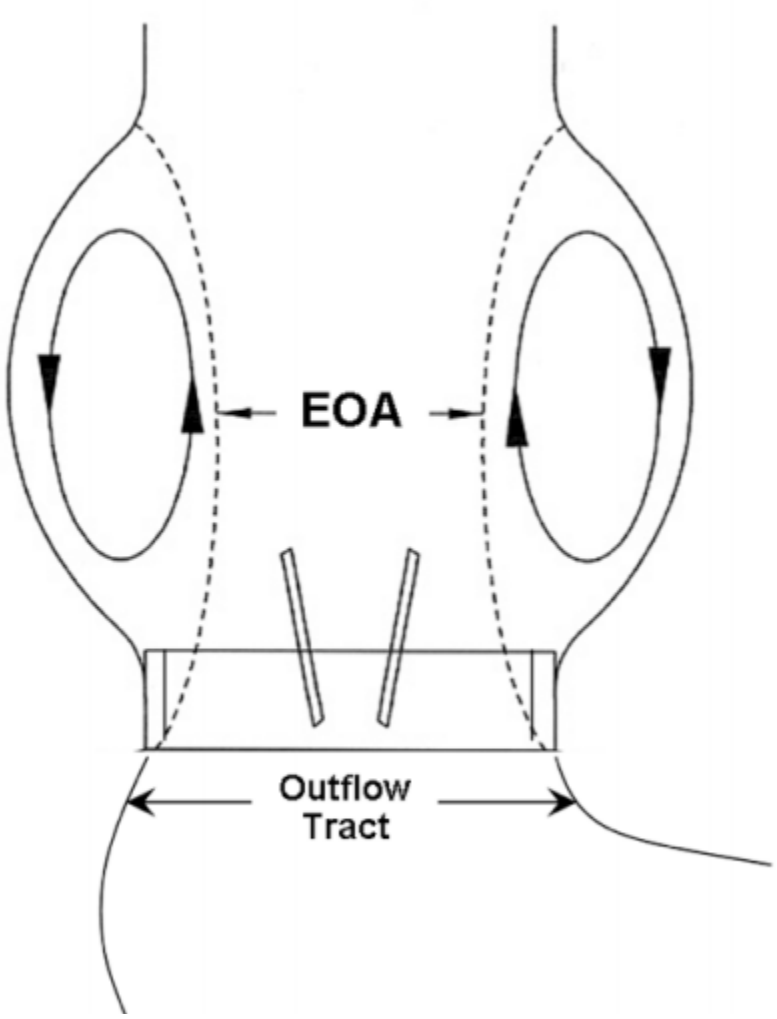

Figure 7: EOA is the minimal cross-sectional area of the downstream jet during systole.

During left ventricle ejection as the blood flows through the aortic valve, a downstream jet is formed. As the flow accelerates, static pressure in the vena contracta (location of the EOA) decreases. Downstream of the vena contracta, the blood decelerates and the jet vanishes in a region of turbulent mixing. In this area, the static pressure increases until it reaches a maximum beyond the location of reattachment of the flow. The mean downstream pressure is smaller than the mean upstream pressure due to energy losses during flow expansion.

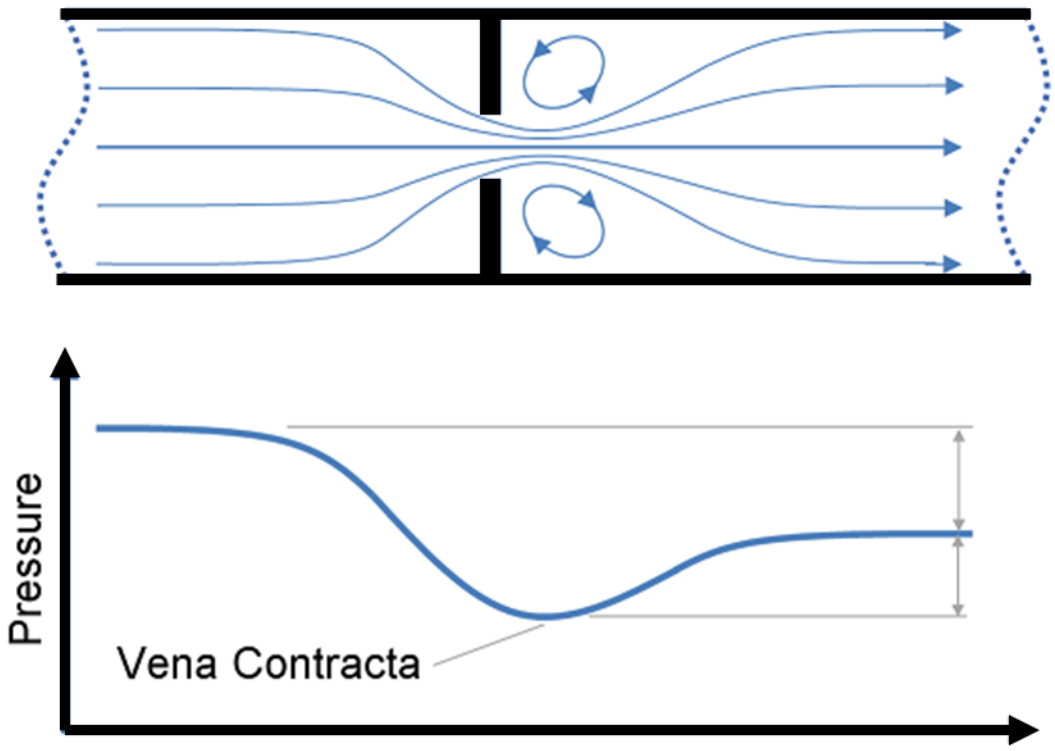

Figure 8: Pressure drop due to orifice in pipe flow.

EOA can be calculated using the Gorlin equation:

$$EOA\ (cm^2) = \frac{Q_{rms}}{51.6\sqrt{\Delta P}} \quad (1)$$

where

EOA is the effective orifice area

Q_{rms} is the root mean square flow rate in mL/s

ΔP is the mean pressure drop in mmHg

2.7.2 Geometric Orifice Area (GOA)

Geometric Orifice Area is the physical “open” area of the aortic valve orifice and can be measured using planimetry measurements (Garcia & Kadem, 2006).

The ratio of EOA to GOA is termed the contraction coefficient and has been shown to be highly dependent upon the valve inflow shape (de la Fuente Galán et al., 1996; Gilon et al., 2002). The performance index (PI) normalizes the EOA by valve orifice area (without occluders). Higher values of EOA, the contraction coefficient, and performance index corresponds to a smaller energy loss and better hemodynamic performance.

CHAPTER 3: SPECIFIC AIMS

The main objectives of this study are to relate the propensity of blood element damage to the flow structures of the bileaflet mechanical heart valves and to better understand the fluid mechanics of VGs in BMHVs as a possible improvement to decrease thromboembolic potential by employing vortex generators to mitigate shear stress. The following set of specific aims specify the studies which were performed to quantify the thromboembolic potential of bileaflet mechanical heart valves under physiological conditions and the effect of passive flow control elements to mitigate thrombus formation and/or improve hemodynamic performance. The overarching hypothesis of this study is that BMHV design may be improved to mitigate TEP through vortex generators.

3.1 Specific Aim 1: Establish methodology and quantify the TEP of the BMHV under physiological conditions.

Rationale: Given bileaflet mechanical heart valve's design features, the hemodynamics of blood as it passes through the valve is fundamentally altered compared to the native valve's hemodynamics. The b-datum regurgitation jet is one of the major areas of high shear stress that has been previously linked to thrombosis of the whole valve (Lakshmi P Dasi et al., 2009; Murphy, Dasi, Vukasinovic, Glezer, & Yoganathan, 2010). Recently, numerical models that relate shear stress to TEP have been applied to experimentally measured turbulent velocity field downstream of BMHVs under non-pulsatile flow conditions (A Bellofiore, 2011). A reliable, repeatable, and controllable methodology is needed to accurately quantify the TEP of BMHV under physiological conditions.

Approach: A pulsatile *in-vitro* flow loop was built and validated to consistently produce physiological cardiac conditions and allow for flow visualization of prosthetic valves in the aortic position. Instantaneous velocity data of a BMHV's b-datum regurgitant jet during ventricular diastole and three orifice jets during ventricular systole were measured *in-vitro* using state of the art time-resolved particle image velocimetry (TR-PIV). A numerical scheme using coupled lagrangian particle tracking with existing TEP models (A Bellofiore, 2011), using experimentally derived parameters for platelet activation and platelet lysis, was developed to quantify TEP of blood elements transitioning through the b-datum jet during ventricular diastole and the three orifice jets during ventricular systole.

3.2 Specific Aim 2: Evaluate the effect of vortex generators on TEP under physiological conditions.

Rationale: Previous studies have shown that vortex generators can reduce turbulent shear stress and thrombus formation due b-datum jet (L P Dasi et al., 2008; Rodriguez-Aumente, Ruiz-Rivas, & Lecuona, 2001). However, the reduction in TEP due to vortex generators has not been studied from a shear stress history of blood elements standpoint and the effect of vortex generators on TEP during systole has not been studied. Also, the detailed fluid mechanics of the influence of VGs on flow is needed to discern the interaction between VG design and configuration to flow characteristics.

Approach: For this Aim, I designed and manufactured BMHVs with vortex generators on the surface of the leaflets using 3D rapid prototyping technology. Two configurations of VGs will be utilized: co-rotating VGs and counter-rotating VGs. Co-rotating VGs consist

of single features 1mm tall and 2.8mm long spaced equally apart (5mm) at an angle of attack of 23 degrees. Counter-rotating VGs consist of mirrored feature pairs 1mm from each other with the same dimensions as the co-rotating VGs. TEP of these BMHVs will be quantified with the methodology described in Aim 1. This study is designed to provide new insights into how vortex generators can mitigate TEP of the b-datum jet and their effect on TEP during systole.

3.3 Specific Aim 3: Evaluate the effect of vortex generators on the hemodynamic performance of the bileaflet mechanical heart valve model.

Rationale: Given that each vortex generator feature added to the leaflets decreases the geometric orifice area (GOA) of the valve, which may impeded the flow of blood through the valve, there is the possibility that any mitigation of TEP in the b-datum jet will be offset by the decreased hemodynamic performance of the valve. Thus, it is important to quantify the effect of vortex generators on the hemodynamic performance of the BMHV.

Approach: In this Aim, I calculated the GOA of the BMHV model with each vortex generator configuration, performed high fidelity steady flow and pulsatile flow pressure drop measurements as dictated by ISO 5840 for Cardiac valve prostheses, consequently calculated EOA, and compared the findings with the BMHV model with the control leaflets. PIV measurements were also performed under pulsatile flow conditions to investigate the influence VGs on flow separation near the medial leaflet surfaces. This study provides insight on the effect of the vortex generators on the hemodynamic performance of the BMHV model as defined by EOA.

CHAPTER 4: EQUIPMENT AND MATERIALS

The sections in this chapter will describe the various equipment and materials, from model BMHVs to experimental apparatuses used to measure flow field velocity, pressure, flow rate, etc.

4.1 Bi-leaflet Mechanical Heart Valve Prosthesis

Bi-leaflet mechanical heart valves share similar design features across all the various manufacturers. They consist of two mobile semicircular disks known as the “leaflets” which are retained within the valve annular housing by four hinges. The hinges on BMHVs are designed to allow a small amount of blood to flow through the hinge gap when the valve is either open or closed. The straight medical edge and semicircular edge of the leaflets are chamfered to allow the leaflets to properly sit when closed. The two leaflets move independently of each other and open and close passively in response to the pressure differentials across the valve. When the valve is open, the leaflets' angle with respect to the plane of the valve housing is typically between 77 and 90 degrees and create three orifices to allow the blood to flow through the valve, a central orifice and two lateral orifices. When the valve is closed, the leaflets' angle with respect to the plane of the valve is typically around 35 degrees and the two leaflets meet while leaving a narrow opening between the medial edges allowing for a small amount of blood leakage. This opening, along with the hinge gap, allows blood to regurgitate during ventricular diastole when the valve is implanted in the aortic position. All current BMHVs are manufactured from pyrolytic carbon, a material known to be

blood compatible with extremely high strength and wear resistance. This material has eliminated abrasive wear as a long term complication of heart valve replacements.

4.1.1 St. Jude Medical Bileaflet Mechanical Heart Valve Model

The valve used for this research is an acrylic model based on the design and dimensions of the St. Jude Medical (SJM) Standard bileaflet mechanical heart valve. The SJM Standard BMHV was first introduced for clinical use in the United States in the late 1970s and has become the gold standard for mechanical heart valve implantation and design parameters. The leaflet hinges for the SJM Standard BMHV are small semicircular protrusions from the leaflets (the ears) fit into a recess machined inside the annular housing of the valve. Relative to the plane of the orifice, the recess is bow-tie shaped and limits the opening and closing angle of the leaflets; 85 degrees open and 35 degrees closed.

4.2. Vortex Generator Equipped Leaflets

Improvements to the SJM Standard BMHV have been incremental and very conservative. The SJM Hemodynamics Plus and SJM Super Hemodynamics Plus simply increased the inner orifice diameter while keeping the annulus diameter equal for each specific valve size. All other design features were kept the same. In this research, leaflets were constructed with vortex generators added to the medial side of each leaflet.

The leaflet dimensions are based from micro-CT scans of the model SJM Standard BMHV with a resolution of 18 μm. As seen in Figure 9, the scans were then processed

with Mimics 16.0 (Materialise NV, Leuven, Belgium) to construct a 3D model that could be edited using commercial 3D modeling software.

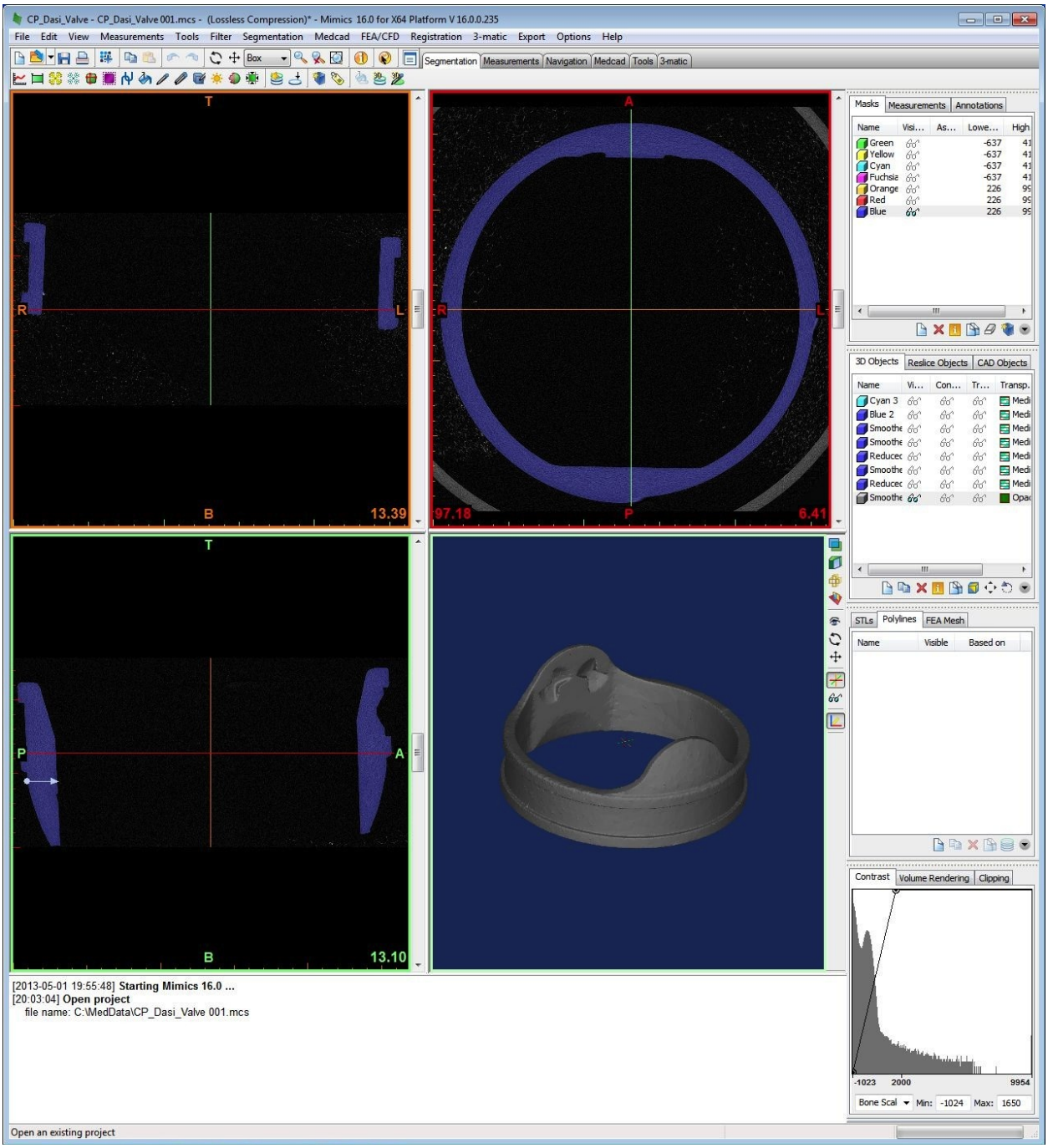

Figure 9: micro-CT scans of SJM BMHV being constructed into editable 3D model.

From this 3D model, the leaflets were used as the control and as the base for the leaflets with vortex generators. Two configurations of vortex generators were designed using SolidWorks 2013 (Dassault Systemes SolidWorks Corp., Velizy-Villacoublay, France); co-rotating vortex generators and counter-rotating vortex generators.

4.2.1 Co-Rotating Vortex Generators

Design parameters for the co-rotating VGs include height (*h*), thickness (*t*), spacing between features (λ), and angle of attack (β).

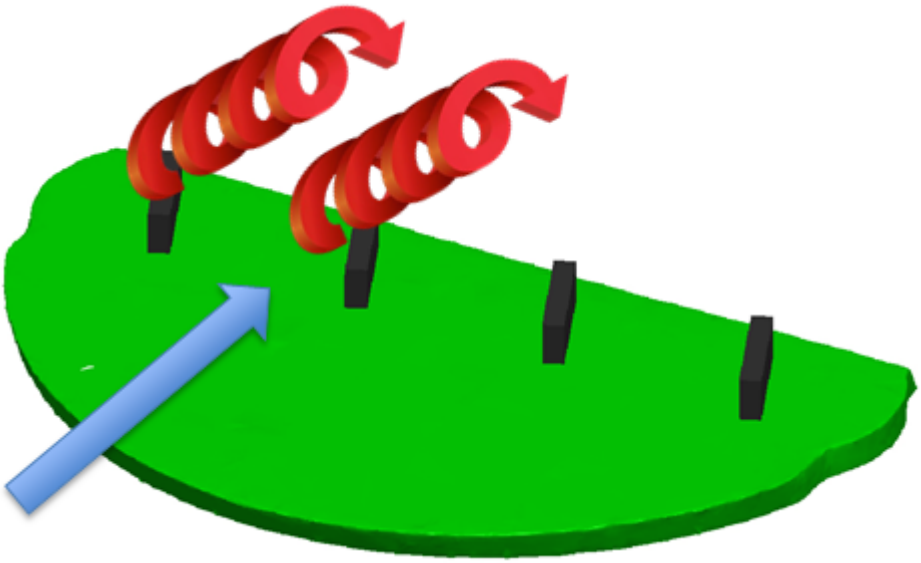

Figure 10: Co-Rotating Vortex Generator

4.2.2. Counter-Rotating Vortex Generators

Design parameters for the counter-rotating include all the parameters for the co-rotating VGs with the addition of spacing between feature pairs (s). Values for the parameters and configurations were chosen based on studies performed by Bradbury and Lin (Bradbury & Khadem, 2006; Lin, 2002).

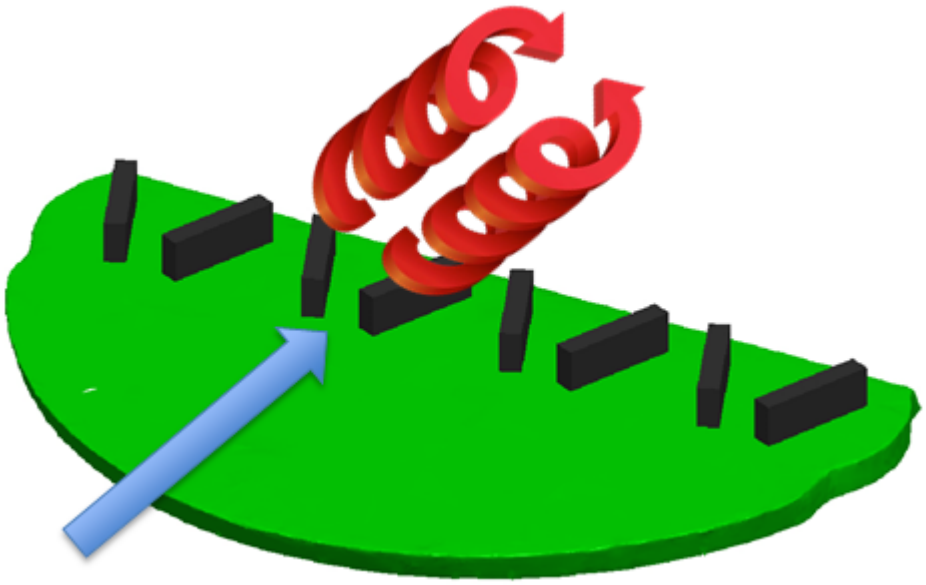

Figure 11: Counter-Rotating Vortex Generator

The leaflets (a control set without VGs and the leaflet sets with VGs) were 3D printed using the high resolution Stratasys Objet 30 Pro Desktop 3D Printer (Edina, Minnesota) using VeroClear rigid transparent material (Figure 12).

Figure 12: 3D printed control and VG equipped leaflets.

Figure 13 shows a schematic of the arrangement of the vortex generating features and Table 1 lists the design parameter values.

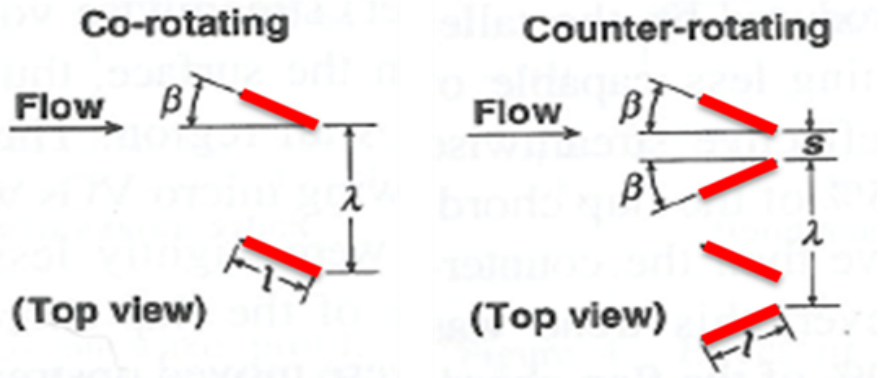

Figure 13: Arrangement of vortex generator features.

Table 1: Design parameter values for vortex generator features.

	Height (h) [mm]	Length (l) Height (h)	Spacing (s) Height (h)	Gap (λ) Height (h)	β [degrees]
Co-Rot VGs	**1**	**2.8**	**N/A**	**5**	**23**
Count-Rot VGs	**1**	**2.8**	**1**	**5**	**23**

4.3 Valve Mounting Chamber

The valve mounting chamber was designed to hold the SJM Standard BMHV model without creating any visual interference of the hinge and leaflets. This was achieved by sandwiching the valve within a main acrylic tube using two pieces of thin acrylic tubing whose outside diameter equals the inner diameter of the main acrylic tube. This setup thus created small steps which held the valve in place. Notches were cut on one of the thin acrylic tubes to hold the valve and keep it from rotating. See Figure 14 and 15 for a schematic and picture of the valve mounting chamber. The length of the main acrylic tube was 280mm long with an inner diameter of 25.4 mm; the same as the SJM Standard BMHV model. The valve was held in place at the middle of the valve mounting

chamber thus allowing for at least 5D (D corresponds to inner diameter of the tube) length of flow visualization. Pressure measurements taps were placed 1D upstream and 3D downstream of the valve location as specified by ISO 5840 guidelines for Prosthetic Heart Valves for measuring pressure drop and EOA.

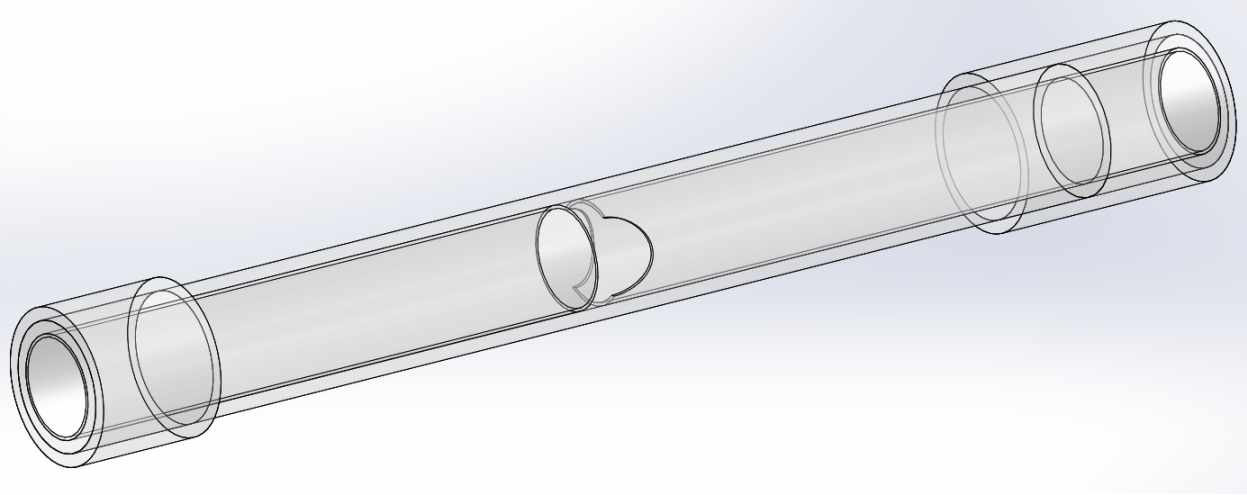

Figure 14: 3D model of valve mounting chamber.

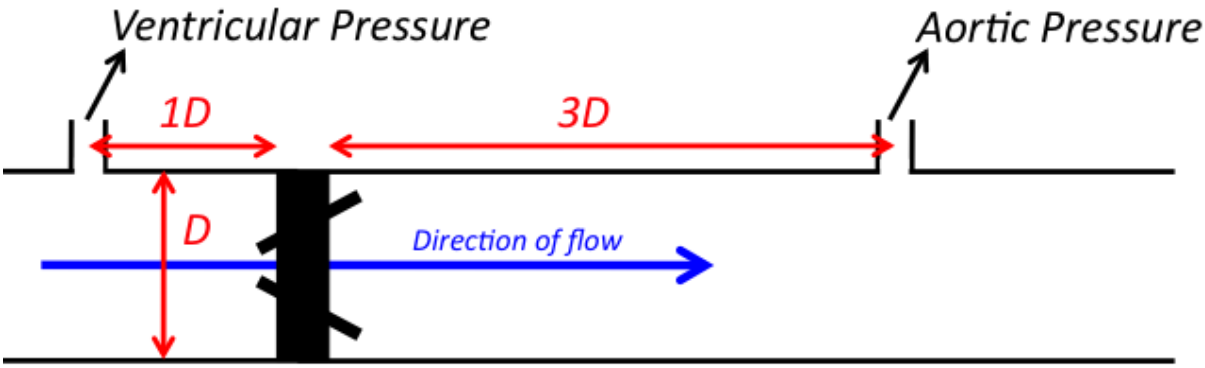

Figure 15: Pressure Locations

4.4 Steady Flow Loop

The steady flow loop was driven by a centrifugal style pump capable of producing flow rates up to 30L/min. Immediately downstream of the pump, a resistance valve allowed the flow rate to be controlled down to 5 L/min. The loop included a straight development length section immediately upstream of the valve mounting chamber to eliminate any swirl and avoid asymmetry in the flow reaching the BMHV, thus providing for a highly controlled inlet condition. The steady flow loop was used to measure pressure drop across the SJM Standard BMHV model with the control leaflets and VG equipped leaflets as specified by the ISO 5840 guidelines. Figure 16 shows a schematic of the steady flow loop setup.

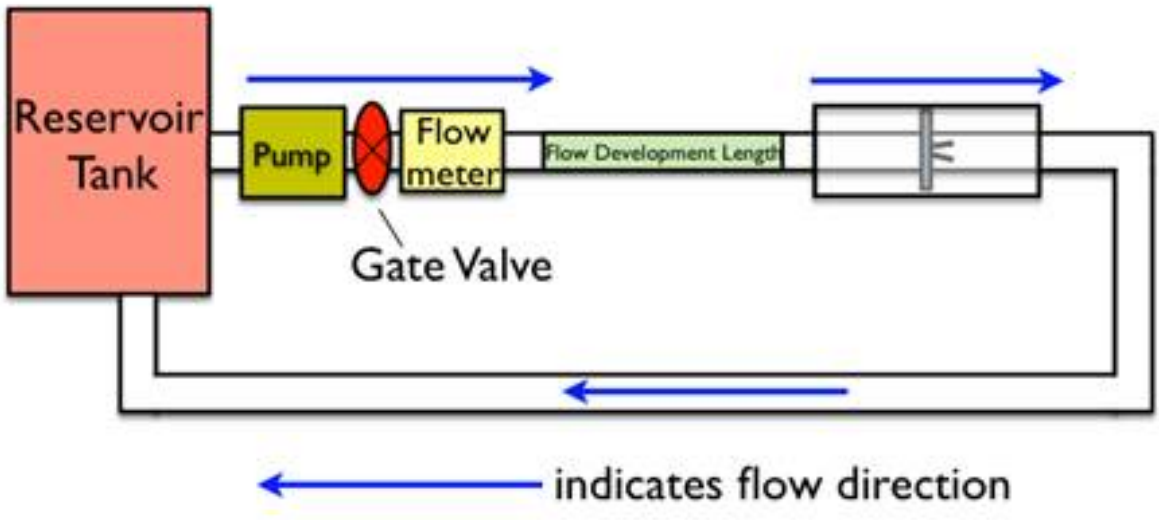

Figure 16: Schematic of Steady Flow Loop

4.5 Pulsatile Flow Loop

The pulsatile flow loop consists of a fluid reservoir, a bladder pump, a flow transducer, a straight development section, the valve mounting chamber, a compliance chamber, a

return line, and a resistance valve. The fluid reservoir acts as the left atrium and is separated from the bladder pump by a mitral valve. The bladder pump acts as the left ventricle and consisted of a flexible bulb sealed within an airtight acrylic cylinder which contains an inlet and outlet connection to compressed air and vacuum respectively. Figure 17 shows a schematic of the steady flow loop setup.

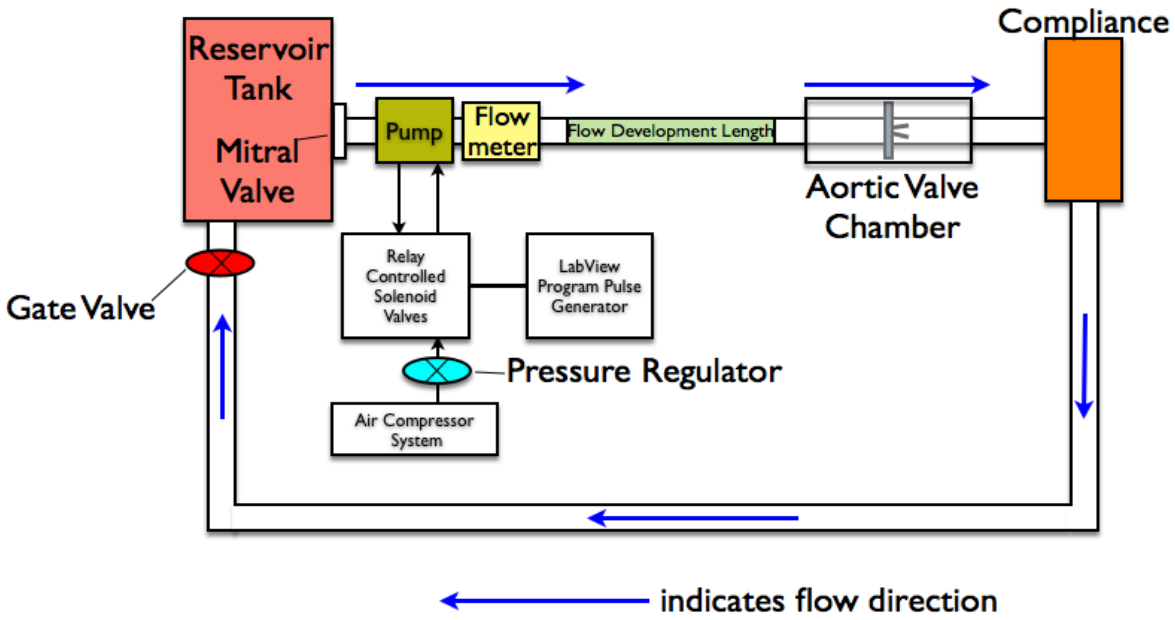

Figure 17: Schematic of Pulsatile Flow Loop

4.5.1 LabView/Flow Loop Interface

The inlet and outlet connections of the airtight acrylic cylinder were gated by two two-way normally closed (NC) solenoid valves which were controlled by a single Single Pole Double Throw (SPDT) relay. This relay allowed the solenoids valve to work in antiphase to each other (i.e. while one solenoid was “open”, the other solenoid was “closed”) by being controlled by a single 5V square wave generated by a LabView program. With the inlet solenoid valve “open” and the outlet solenoid “closed”, compressed air filled the

airtight acrylic cylinder, the flexible bulb was compressed thereby increasing the pressure of the fluid between the mitral valve upstream and the aortic valve (in the valve mounting chamber) downstream. The onset of flow caused the mitral valve to close and thus the fluid flowed through the aortic valve. When the relay “switched”, the inlet solenoid valve “closed” and the outlet solenoid valve “opened”, vacuum pulled air from the airtight acrylic cylinder and the flexible bulb relaxed. The decrease in pressure allows the mitral valve to reopen, fluid to refill the flexible bulb, and causes the aortic valve to close. The compliance chamber downstream of the valve mounting chamber allowed the pulse pressure (difference between systolic pressure and diastolic pressure) to be adjusted. By letting the chamber fill with more fluid, the pulse pressure increases as there is less compressible air in the chamber to dampen the pressure. Conversely, by filling the chamber with more compressible air, the pulse pressure decreases as there is more air to dampen the pressure. The resistance valve downstream of the compliance chamber allowed the mean aortic pressure (MAP) to be adjusted. By opening or closing the valve, the MAP decreased or increased respectively. Aortic and ventricular pressures were measure using pressure transducers (ValiDyne Engineering, Austin, TX) connected to the pressure measurements locations located on the valve mounting chamber; 1D upstream of the valve for ventricular pressure and 3D downstream of the valve for aortic pressure. Flow rate was measured directly downstream of the bladder pump using a 24mm in-line ultrasonic flow probe (Model, Transonic Inc., Ithaca, NY). The three transducers were connected to a National Instruments Data Acquisition box (National Instruments Corporation, Austin, TX) and recorded by a LabView program.

4.5.2 LabView Program and GUI

A custom LabView program was written to interface with the pulsatile flow loop to control heart rate (HR), diastolic fraction, and to monitor and record flow rate, ventricular pressure, and aortic pressure. The graphical user interface can be seen below in Figure 18.

Figure 18: LabView Program Graphical User Interface

The program generated a 5V square waveform to control the physical relay in the flow loop. The diastolic fraction and beats per minute were adjusted to create a physiological cardiac flow curve in the flow loop as seen in Figure 19.

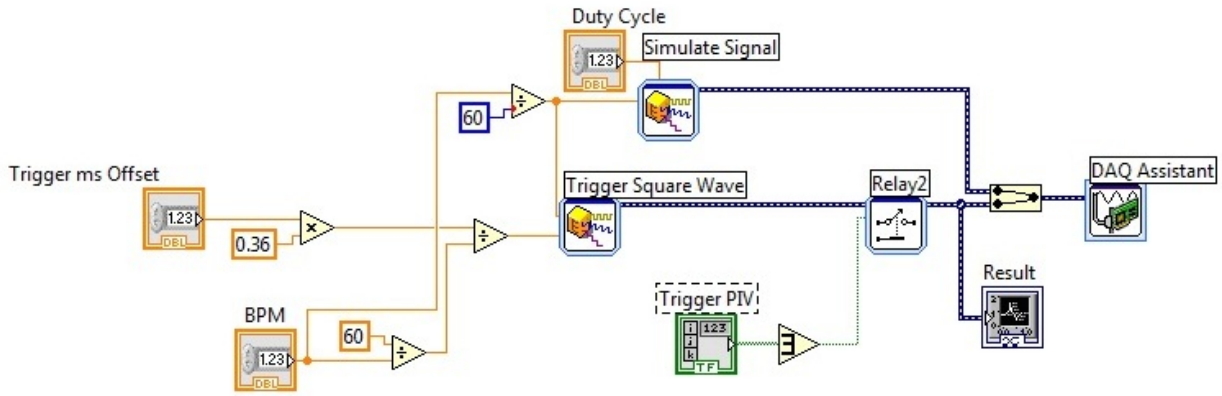

Figure 19: LabView code to control heart rate and duty cycle for pulsatile flow loop and to control PIV trigger.

The program also monitored and acquired the three transducers on the flow loop (ventricular pressure, aortic pressure, and flow rate) and recorded the values to a spreadsheet when triggered. For the aortic and the ventricular pressure, the program applied the calibration equation to the voltage signal to display the pressure values in mmHG. For the aortic pressure reading, the program displayed a “PASS” notification when the pressure values were within 10% of the desired systolic pressure (120mmHg) and diastolic pressure (80mmHg) to assist in monitoring the flow loop while in operation (Figures 20 and 21).

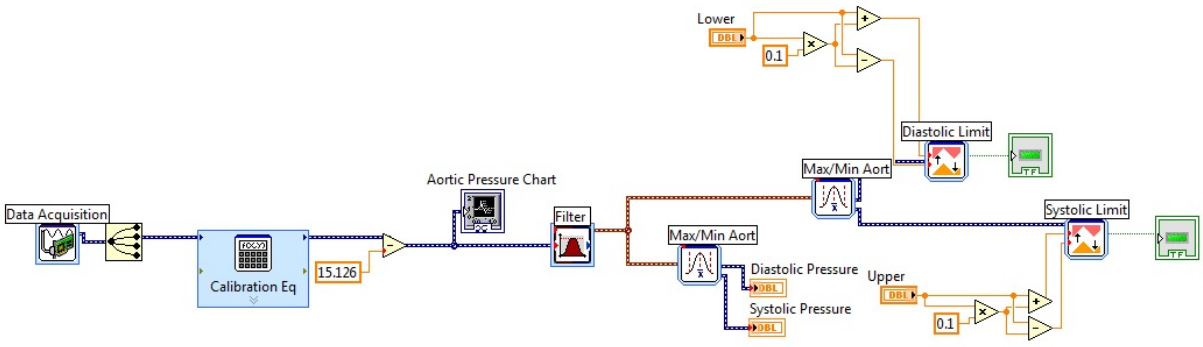

Figure 20: LabView code to acquire and monitor aortic pressure values.

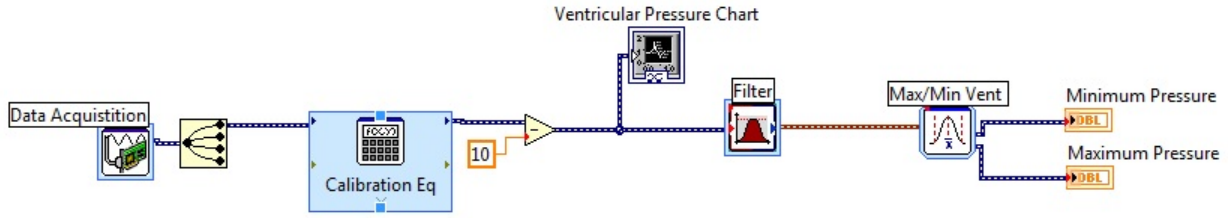

Figure 21: LabView code to acquire and monitor ventricular pressure values.

Similarly, for the flow rate, the program applied the calibration equation to the voltage signal to display the flow values in Liters. The program also displayed a “PASS” notification when the flow values were within 5% of the desired flow rate (5L/min) as seen in Figure 22.

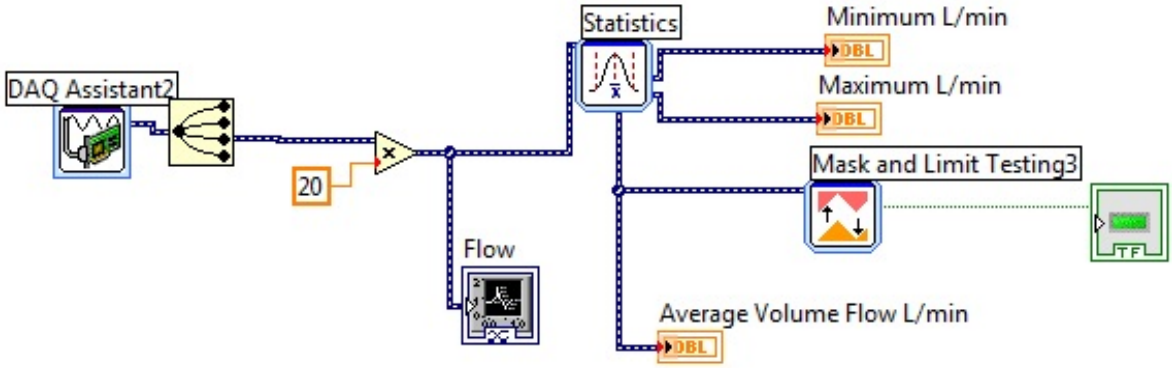

Figure 22: LabView code to acquire and monitor flow rate values.

4.5.3 Pulsatile Flow Loop Validation

As shown in Figure 23, the pulsatile flow loop is capable of loading aortic valves to physiological aortic flow and pressure waveforms equivalent to well established simulators in literature (L P Dasi, Ge, Simon, & Sotiropoulos, 2007; Hwa Liang Leo, Dasi, Carberry, Simon, & Yoganathan, 2006; Yap, Dasi, & Yoganathan, 2010).

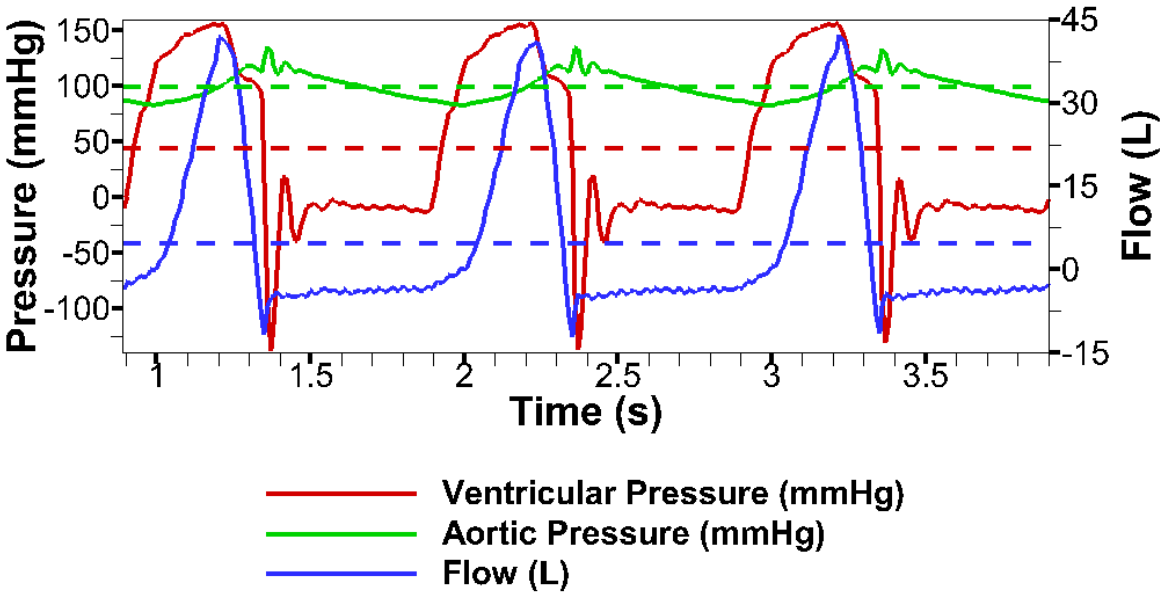

Figure 23: Ventricular pressure, aortic pressure, and flow rate waveforms during pulsatile flow experiments. Dashed lines correspond to average of curves.

In order to check if the valve mounting chamber and the acrylic model valve provide equivalent results to clinical quality SJM Standard BMHV, Figure 24 compares non-dimensionalized leaflet kinematics, and the downstream velocity profile a x/D = 0.33 during peak systole to published results for a clinical quality SJM Standard valve (L P Dasi et al., 2007). As seen in the figure, the two profiles show excellent match with the non-dimensionalized centerline velocity. However, the data here (as well as the published data) are ensemble averaged and therefore do not fully capture the instantaneous bounce that occurs just after closure. Small leaflet bounce (not shown in figure), did occur with variable temporal locations between the 10 closing events.

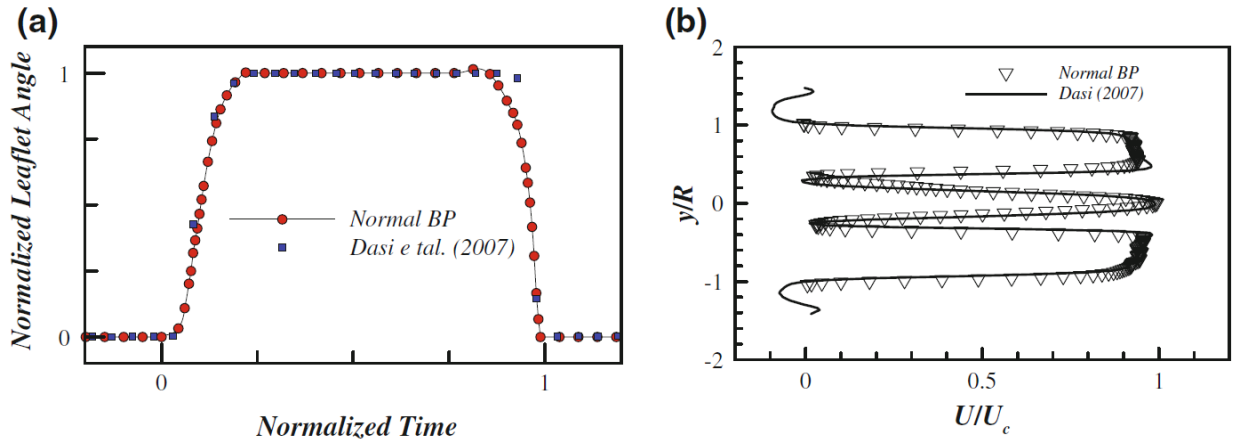

Figure 24: Comparison of leaflet kinematics (a) and downstream velocity profile (b) between model valve and clinical quality SJM valve results from Dasi et al. Normalized leaflet angle is defined such that 0 is closed and 1 is open. Time has been normalized by the duration of time the leaflet is not fully closed. All symbols have been down-sampled for clarity.

4.6 Blood Analogue Fluid and Particle Seedings

4.6.1 Glycerin/H20 Mixture

All experiments utilized a transparent Glycerin/Water mixture in a 40%/60% volumetric ratio as the blood analogue fluid to match the properties of blood and allow for visualization and PIV studies. The density of this mixture was about 1080 kg/m3 and the kinematic viscosity (*v*) was approximately 3.5 cP. The viscosity of the mixture was determined by using a glass viscometer.

4.6.2 Particle Seedings

The fluid was seeded with spherical fluorescent polymer particles (FPP) (Dantec Dynamics, Denmark) based on poly (methyl methacrylate) with fluorescent dye (Rhodamine B:) homogeneously distributed over the entire particle volume. The particles had an average size of 10 μm with a minimum and maximum particle size of 1 and 20 μm respectively. The fluorescent particles were used to eliminate any glare from

the laser, acrylic chamber surface, or the valve surface. The particles absorb the laser light at a wavelength of 550 nm and emit light at 590 nm.

4.7 Measurement Equipment and Calibration

4.7.1 Flow Rate Measurement

Flow rate was measured using a calibrated ultrasonic flow probe (Transonic Inc., Ithaca, NY). The probe output a voltage of 1V for a flow of 20L/min.

4.7.2 Pressure Measurement

Aortic and ventricular pressure were measured using pressure transducers (ValiDyne Engineering, Austin, TX) interfaces with a custom LabView program. The voltage signal from the pressure transducer was calibrated by connecting a water column at varying heights to the transducer and recording the voltage output. Water column height was plotted against the output voltage and a linear regression calculation was performed to determine the pressure for a given output voltage.

4.7.3 Velocity Measurements

Velocity field measurements and related flow characteristics were measured using Particle Image Velocimetry (PIV) techniques. The following section describes the working principles and components of the technique

4.7.3.1 Particle Image Velocimetry

The PIV system consisted of a diode-pump Q-switched nd:YAG laser (Dm40-527 Photonics Industries, Bohemia, NY). Laser optics (spherical lens, f = 1m) converted the output beam into an expended light laser sheet from an initial thickness of approximately 1mm down to a focused sheet less than 200 μm within the measurement region. A 1024×1024 CCD camera (Fastcam SA3, Photron, San Diego, CA) equipped

with a 50 mm Nikkor lens and 20mm extension tube (Nikon Corporation, Tokyo, Japan) with an Orange 21 filter (The Tiffen Company, Hauppauge, NY). A high speed controller (HSC) (LaVision, Ypsilanti, MI) synchronized the high speed camera image captures with the laser pulses. All these components were connected to a main computer which controlled the measurement parameters and analysis software (Davis 7.0, LaVision, Germany).

CHAPTER 5: EXPERIMENTAL PROCEDURE AND PROTOCOLS

The following sections in this chapter will describe the procedures which were performed to measure the velocity fields using PIV flow visualization, materials, and equipment described in the previous chapter. Also, protocols for calculation of TEP and EOA are described.

5.1 Pulsatile Flow Particle Image Velocimetry Experiments

Experiments for Specific Aims 1 and 2 utilized the pulsatile flow loop, PIV system, and valve mounting chamber to quantify the thromboembolic potential of each leaflet configuration in the downstream flow during ventricular systole and in the upstream b-datum regurgitant jet flow during ventricular diastole under physiological conditions. The next sections will detail the experimental procedure for Specific Aims 1 and 2, which are similar except for the type of leaflet configuration used.

The setup of the system required the laser to shine a laser sheet through the central plane of the valve mounting chamber along its long axis and the CCD camera to be placed perpendicular to the laser sheet. This was achieved by aiming the laser sheet at a mirror placed above the valve mounting chamber at a 45 degree angle and the camera pointing toward the valve mounting chamber and laser. Figure 25 illustrates this setup.

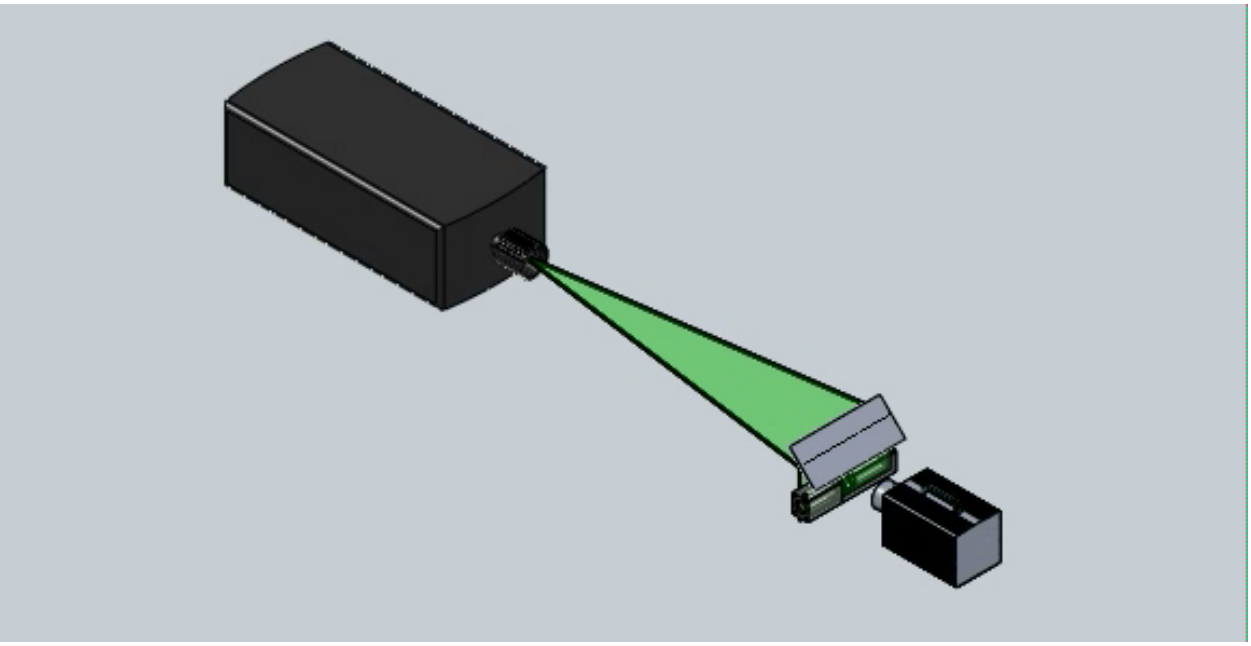

Figure 25: Simplified schematic of PIV experiment setup. Laser shines laser sheet onto mirror which aims laser sheet to the central plane of valve mounting chamber. The CCD camera is placed perpendicular to sheet and records flow as it passes through valve.

5.1.1 CCD Camera, Laser, and High Speed Controller Setup

The CCD camera was setup with the orange filter over the lens to record at 1Hz with the laser powered to 27 amps of power for all experiments. The camera and laser were connected and synchronized by the high speed controller to function in double frame mode with a laser pulse separation time of *dt* = 500 us. This ensured adequate particle displacements in the range of 10-15 pixels thus maximizing the accuracy of instantaneous velocity measurements to within 2% error. The high speed video camera synchronized to the laser system via the high speed controller captured focused images of the fluorescent polymer particles within the laser sheet in the measurement plane. For the forward flow experiments, the image area of interest was 1.5D wide and 1D tall with the valve body located on the left-hand edge of the image. Similarly, for the regurgitant flow experiments, the image area of interest was 1.5D wide and 1D tall with

the valve body located on the right-hand edge of the image. Image distortion due to curvature of the acrylic tube was compensated *in situ* with a calibration plate consisting markers placed in a regular square grid with 1 mm spacing. The DaVis calibration algorithm automatically tracks the markers and a map to evaluate the corrected image. Corrected image generated of the calibration plate verified successful calibration and distortion correction. The PIV setup achieved a raw data spatial resolution of 27 μm/pixel. Images were pre-conditioned by first subtracting the minimum image from every image acquired followed by a non-linear filter involving subtraction of sliding minimum through the image series with a corresponding bin width of five images. These pre-conditioning steps improve signal-to-noise of the raw data, which greatly reduces the likelihood of ‘‘dropped’’ vectors during vector calculations. Instantaneous two-dimensional velocity field was calculated from the raw particle images using cross-correlation processing with a multi-pass scheme. The initial interrogation window size for the multi-pass scheme was at 32 x 32 pixels, which progressively reduced to 8 x 8 pixels. Interrogation window overlap was fixed at 50%. Post-processing of the vector data included a median filter that rejected vectors outside 3 standard deviations of the neighbor vector. Gaussian smoothing was used to reduce noise in the vector data before calculating derived quantities such as vorticity and strain-rate.

5.2 Post-Processing

5.2.1 Lagrangian Tracking

To calculate the thromboembolic potential as a function of shear stress loading history, we first had to analyze the measured Eulerian velocity fields from PIV experiments using lagrangian tracking. Lagrangian tracking calculates the possible trajectory for a

massless particle released at a specific initial position and starting time through the recorded time-resolved flow field. Ten separate (n=10) full cardiac cycles were recorded using PIV for each leaflet configuration focusing on the downstream forward flow or the upstream regurgitant flow.

5.2.2 Systolic Phase Particle Initial Positions

Four areas of known high shear stresses were identified downstream of the opened leaflets. Figure 26 shows the four shear zones.

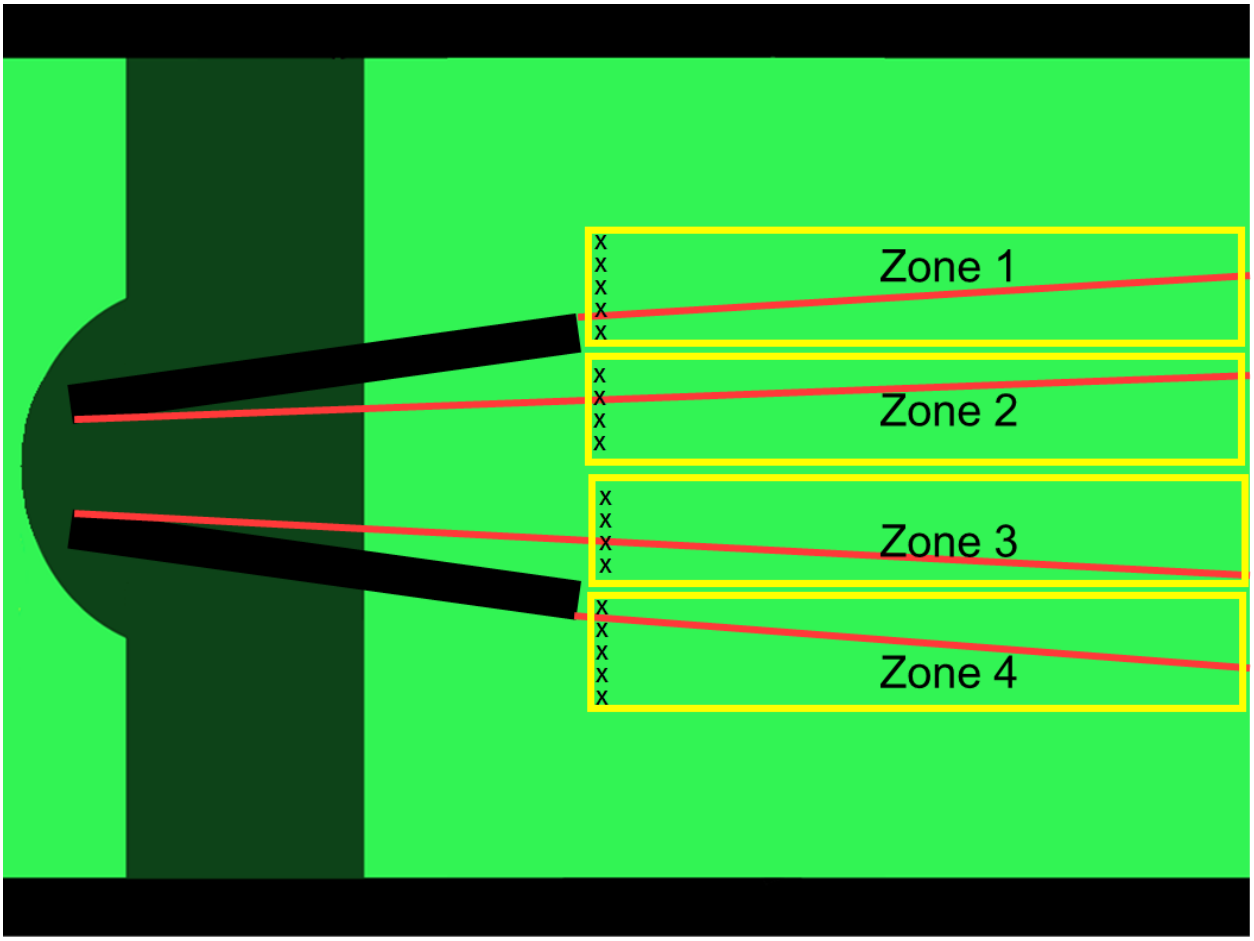

Figure 26: Schematic of the four shear stress zones selected (shown by yellow rectangles). Green velocity fields shows the lower velocity cause by the leaflets compared to rest of bulk flow in red.

For each zone, particle trajectories were initiated from a vertical rake of 100 particles uniformly distributed over the width of each of the four zones immediately downstream of the opened leaflet tips with initial position (x_o, y_o) and a starting time t_o. These linear particle rakes were released every 0.05 s starting with the beginning of valve opening and throughout systole (for a total of seven release events) and particle trajectories calculated for each particle (as seen in Figure 27).

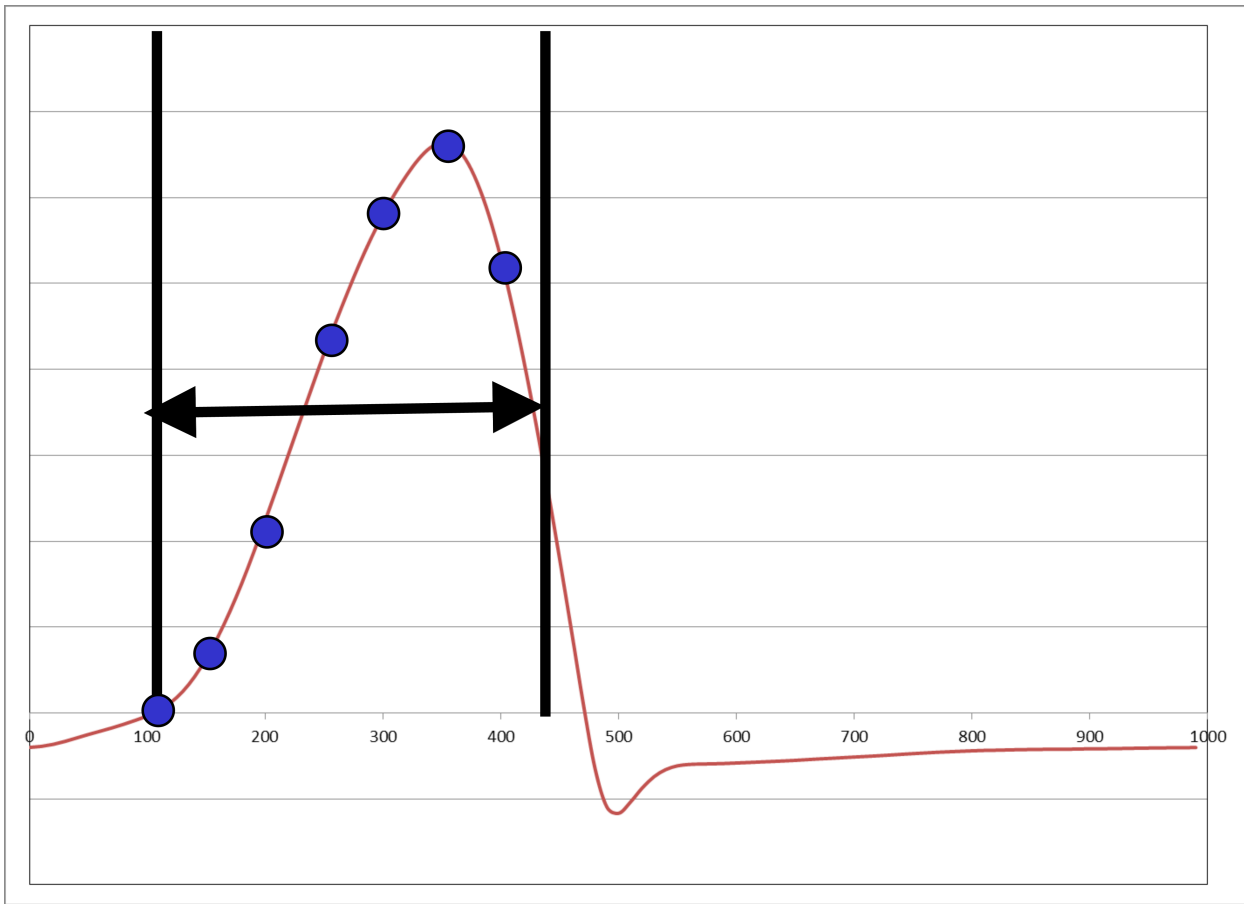

Figure 27: Location of particle release events through systole as shown in the cardiac flow curve.

5.2.3 Diastolic Phase Particle Initial Positions

Similarly, each particle trajectory was initiated from a vertical rake of 100 particles uniformly distributed immediately downstream and centered on the b-datum gap with

initial position (x_o, y_o) and starting time t_o. The 100 particles were divided into 3 groups, the middle group (Zone 2) consisted of 34 particles centered on b-datum jet centerline while the top and bottom group (Zone 1 and Zone 3) each consisted of 33 particles above and below the middle 34 particles as seen in Figure 28.

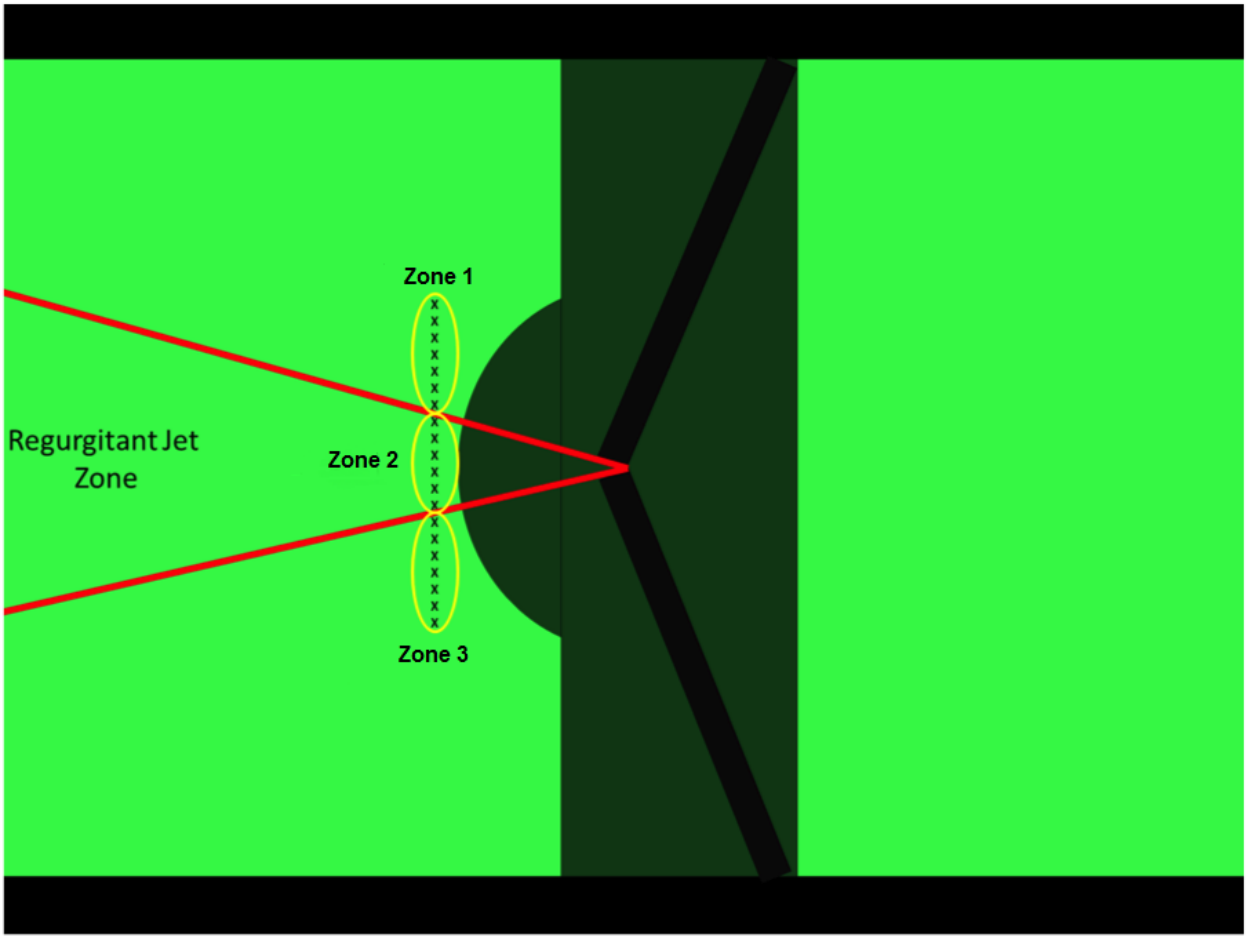

Figure 28: Schematic of initial position release locations showing the three particle zones.

These linear particle rakes were released every 0.1 s starting with the beginning of valve closure and throughout diastole (for a total of seven release events) and particle trajectories calculated for each particle (as seen in Figure 29).

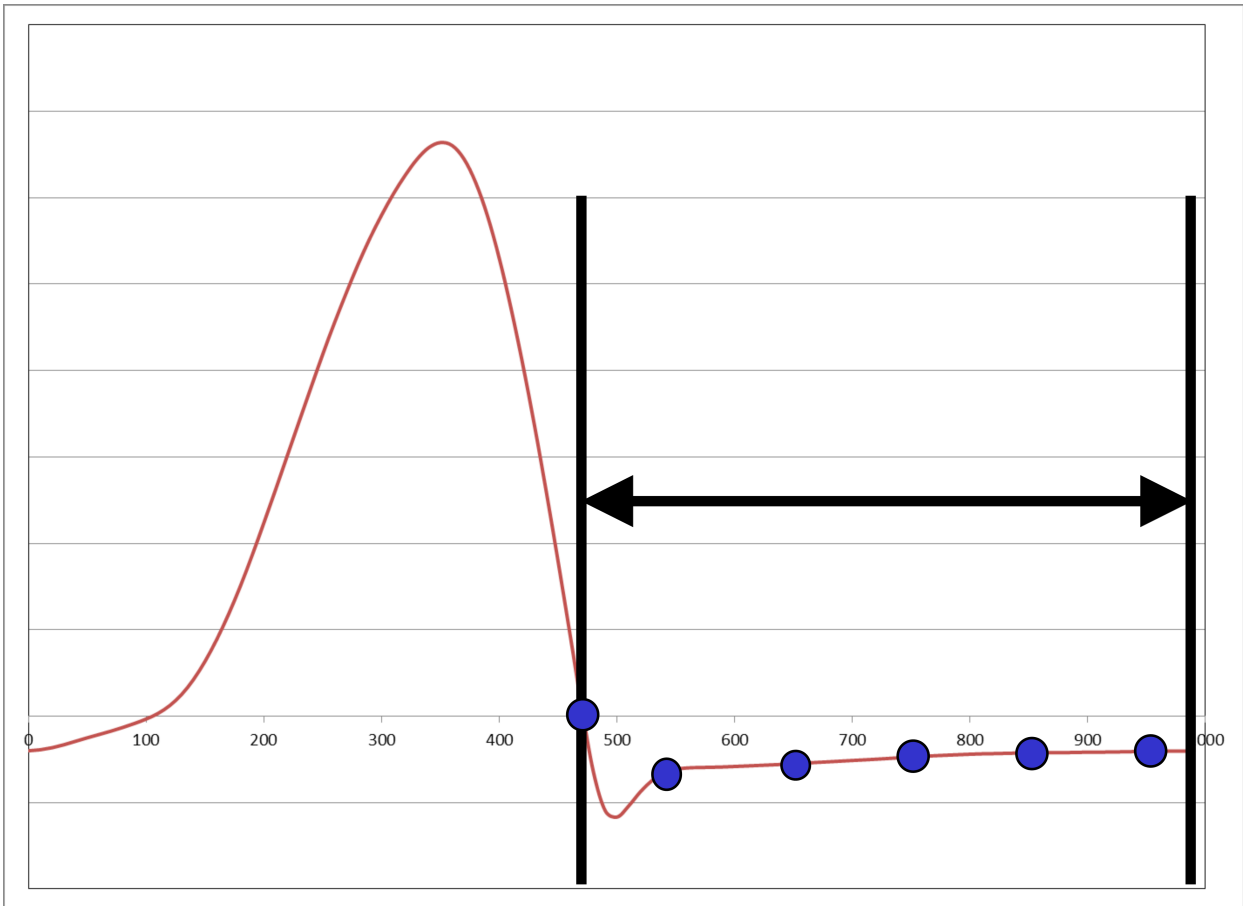

Figure 29: Location of particle release events through diastole as shown in the cardiac flow curve.

5.2.4 Particle Trajectories

The particle location (x_i, y_i), after i time steps, was evaluated based on the velocity components u_{i-1} and v_{i-1} integrated over the time step *dt* = 0.002 s to calculate (x_i, y_i), using a second-order Runge-Kutta scheme. Bi-linear interpolation of the discrete turbulence instantaneous velocity at the previous particle location provided u_{i-1}, v_{i-1}.

5.2.5 Thromboembolic Potential Numerical Calculations

To quantify the thromboembolic potential of particles, the shear stress acting upon the particles were evaluated along the calculated trajectories to quantify corresponding

shear stress loading history. Shear stress was estimated based on the measure strain rate as:

$$\tau = \mu\left(\frac{\partial u}{\partial y} + \frac{\partial v}{\partial x}\right) \tag{2}$$

The principal shear stress was calculated using the equation:

$$\tau_{max} = \frac{1}{2}\left|\sigma_{max} - \sigma_{min}\right| \tag{3}$$

where σ_{max} and σ_{min} are the principal normal stresses, based on the Eigen values of the 2D strain rate tensor.

The thromboembolic potential model utilized is based on the power law model that relates the differential damage accumulated to both the shear stress, τ and the exposure time t given by:

$$d(BDI) = C \cdot \tau^{b} \cdot dt^{a}, \tag{4}$$

The model used to implement the above was proposed by Grigioni et al. and is a function of the mechanical dose, D supplied to the particle. Here, each integration step considers the cumulative mechanical dose contributed to the i^{th} damage increment d(TEP). The total damage (TEP) is then calculated by summing all the discrete increments accumulated along a trajectory from t0 to ti, given by the equation:

$$\mathrm{BDI}(t_i) = \sum_{k=1}^{i} Ca\left[\sum_{j=1}^{k} \tau(t_j)^{b/a}\Delta t + D(t_0)\right]^{a-1} \times \tau(t_k)^{b/a}\Delta t \tag{5}$$

This model, termed TEP, evaluates the potential blood damage under the assumption of blood damage accumulation, respects the principle of causality, reproduces the original empirical model introduced by Giersiepen under constant shear stress, and accounts for the loading history previously sustained by the blood cell.

The model includes three empirically tuned parameters (*a, b,* and *C*). Two sets of coefficients were used which correspond to platelet activation and platelet lysis, respectively. Platelet lysis coefficients were proposed by Giersiepen and fit measurements of the lactate dehydrogenase (a marker of platelet lysis) released by platelets exposed to uniform shear stress in a Couette viscometer. The corresponding coefficients are given by:

$$(a_1, b_1, C_1) = \left(0.77,\ 3.075,\ 3.31 \times 10^{-6}\right) \tag{6}$$

Platelet activation coefficients used by Nobili et al. were tuned based on experimental measurements of thrombin generation from platelet activation under controlled dynamic shearing. The corresponding coefficients are given by:

$$(a_2, b_2, C_2) = \left(1.3198,\ 0.6256,\ 10^{-5}\right) \tag{7}$$

Figure 30 provides a flowchart that gives an overview of the entire post-processing and data -reduction performed beyond data acquisition.

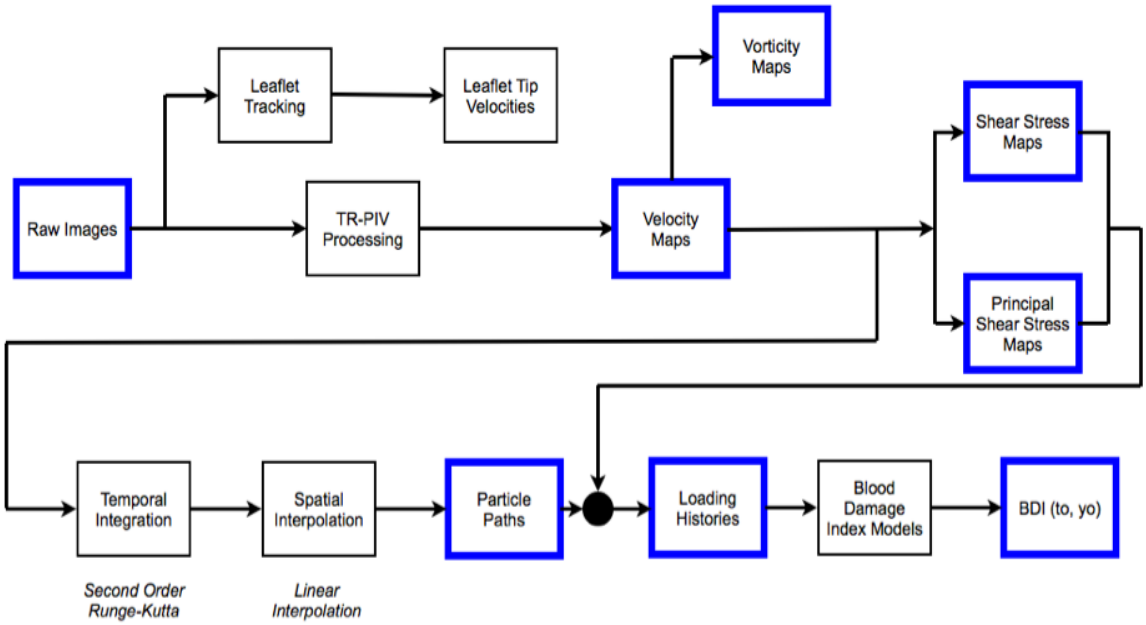

Figure 30: Flowchart of analysis performed in Specific Aims 1 and 2.

5.2.6 TEP Model Validation

The TEP model was validated by using a square waveform in which the stress alternates between 1 and 0 Pa at 1 Hz and a constant shear stress of 1 Pa for 1 s. The results were identical to predictions made by Giersiepen and Bellofiore and Quinlan thus validating the C++ code to calculate TEP.

5.3 Effective Orifice Area Experiments

Experiments for Specific Aim 3 utilized the valve mounting chamber, and the steady or pulsatile flow loop to quantify the hemodynamic performance of the BMHV with each leaflet configuration using EOA calculations.

5.3.1 Steady Flow Effective Orifice Area Experiments

Using the steady flow loop and the valve mounting chamber under steady flow conditions, experiments to calculate the effective orifice area of the control leaflets and

each VG equipped leaflets were performed by subjecting valve to flow rates ranging from 5 L/min to 30 L/min in 5 L/min increments as specified by the ISO 5840 Standard.

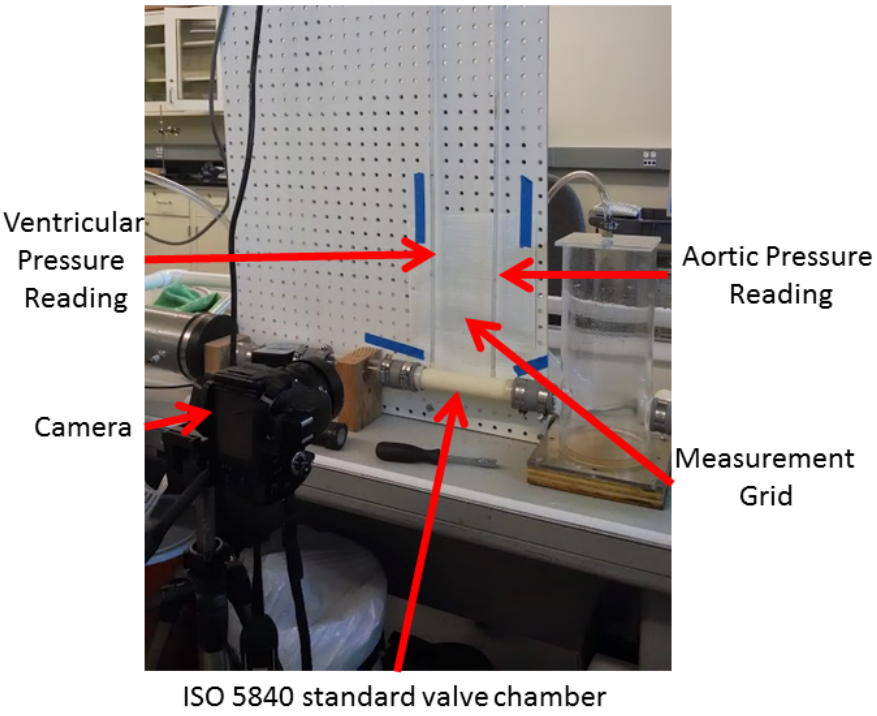

Figure 31: Experimental setup for steady flow pressure drop measurements.

The manometer heights at the pressure measurement locations were photographed 10 times at each flow rate value (5, 10, 15, 20, 25, and 30 L/min) and the difference between the two heights was measured. The pressure (in mmHg) was calculated using the equation for pressure of fluids at rest.

$$P = \rho g h \tag{8}$$

Next, the pressure difference between each pair of manometer pressure readings was calculated to obtain the pressure drop (ΔP) and the average and standard deviation

over of the 10 measurements calculated. Using the calculated pressure drop values and known flow rates, EOA was calculated using the Gorlin equation (1).

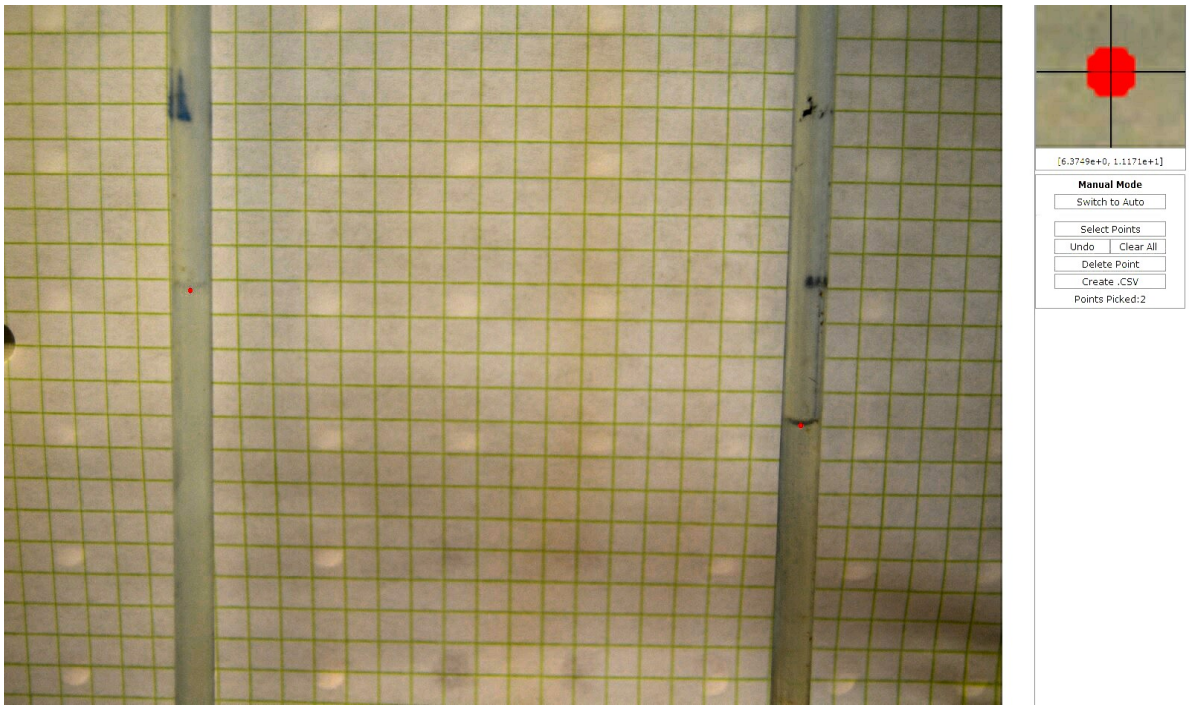

Figure 32: Manometer readings of pressure drop and markers of height difference.

5.3.2 Pulsatile Flow Effective Orifice Area Experiments

Using the pulsatile flow loop under physiological cardiac conditions, experiments to calculate the effective orifice area of the control leaflets and each VG equipped leaflets were performed by subjecting valve to a flow rate of 5 L/min, mean aortic pressure of 100mmHg, heart rate of 60 beats per minute, and systolic duration of 33%.

5.3.2.1 Flow and Pressure Waveforms

The pulsatile flow loop was tuned to reach the physiological cardiac conditions stated above and maintain them within 10% throughout the entire experiment. The loop was tuned by either opening/closing the resistance valve, increasing/decreasing bladder pump pressure, and increasing/decreasing compliance in the compliance chamber.

Figure 23 shows the typical pressure and flow curves achieved using the pulsatile flow loop under physiological cardiac conditions. For each leaflet pair, 50 cardiac cycles were recorded to subsequently calculate effective orifice area. Ventricular pressure, aortic pressure, and flow rate measurements over the 50 cycles were uploaded to a C++ program (code can be seen in Appendix C) to calculate the average pressure drop and EOA of the valve using the Gorlin equation (1).

CHAPTER 6: TEP OF BMHV - RESULTS AND DISCUSSION

The instantaneous velocity data from PIV experiments of the forward flow downstream of the valve and regurgitant flow upstream of the valve along with a numerical scheme using lagrangian tracking and TEP models allowed for the prediction of the thromboembolic potential. The next sections show and discuss the average exposure time, principle shear stress, platelet activation TEP, and platelet lysis TEP of 10 takes (either forward flow or regurgitant flow) each with 7 release events of 100 particles per zone (for forward flow) or 7 releases of 100 particles divided between 3 zones for the BMHV with the control leaflet configuration.

6.1 Forward Flow TEP

Figure 33 presents an image sequence of vorticity fields during valve opening. As the leaflet is opening, an area of low pressure is created in the medial surface of the leaflet, creating a vortex which pinches off as the leaflet comes to its full open position. Next, the unsteady separation of flow around the leaflet tip creates alternating vortices which shed periodically from both sides of the leaflets.

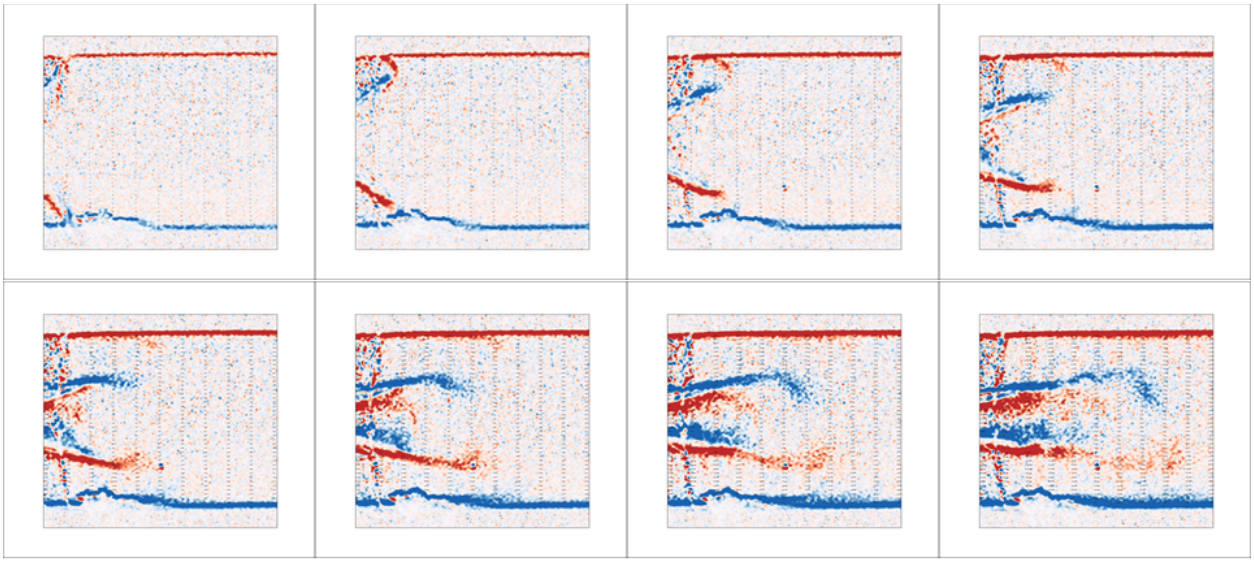

Figure 33: Image sequence of control leaflet opening showing opening vortex formation.

Animations A1 and A2 depict lagrangian particle trajectories for 100 particles released in the four shear zones identified earlier for each of the 10 independent repeated measurements simultaneously. The color of the particles represents the amount of platelet activation TEP and platelet lysis TEP accumulated by the particle. One hundred more particles per zone were released every 0.1s through ventricular systole for a total of 7 release events. As shown in the animation, trajectory calculations terminated once the particles left the measurement window. These trajectories represent blood element advection immediately downstream of the valve at the instant when the valve begins to open. Lagrangian tracking shows that most (if not all) particles regardless of initial position zone were quickly ejected from their shear stress zones as the bulk velocities immediately downstream of the valve are very uniform during ventricular systole. No recirculation areas or stagnation were observed, which is expected for forward flow.

Figure 34 and 35 shows the average exposure time and principal shear stress experienced by each particle at different release events by initial position zone. Overall, as the flow is accelerating between releases 1 and 6, exposure time decreases with each release event until Release 7 where exposure time increases when compared to Release 6. This behavior is expected as Release 7 occurs at the end of ventricular systole where the flow velocity has decreased and is becoming negative due to the aortic pressure being higher than the ventricular pressure. In all release events except Release 2, zones 2 and 3 (the two shear zones in the central orifice jet) experience shorter exposure times compared to zones 1 and 4 (the two zones in the lateral orifice jets). The particles in zones 2 and 3 experience higher magnitudes of vorticity, since they were released in the central jet, which caused some particles to exit the boundaries of their zones; thus exhibiting shorter exposure times in the TEP calculations.

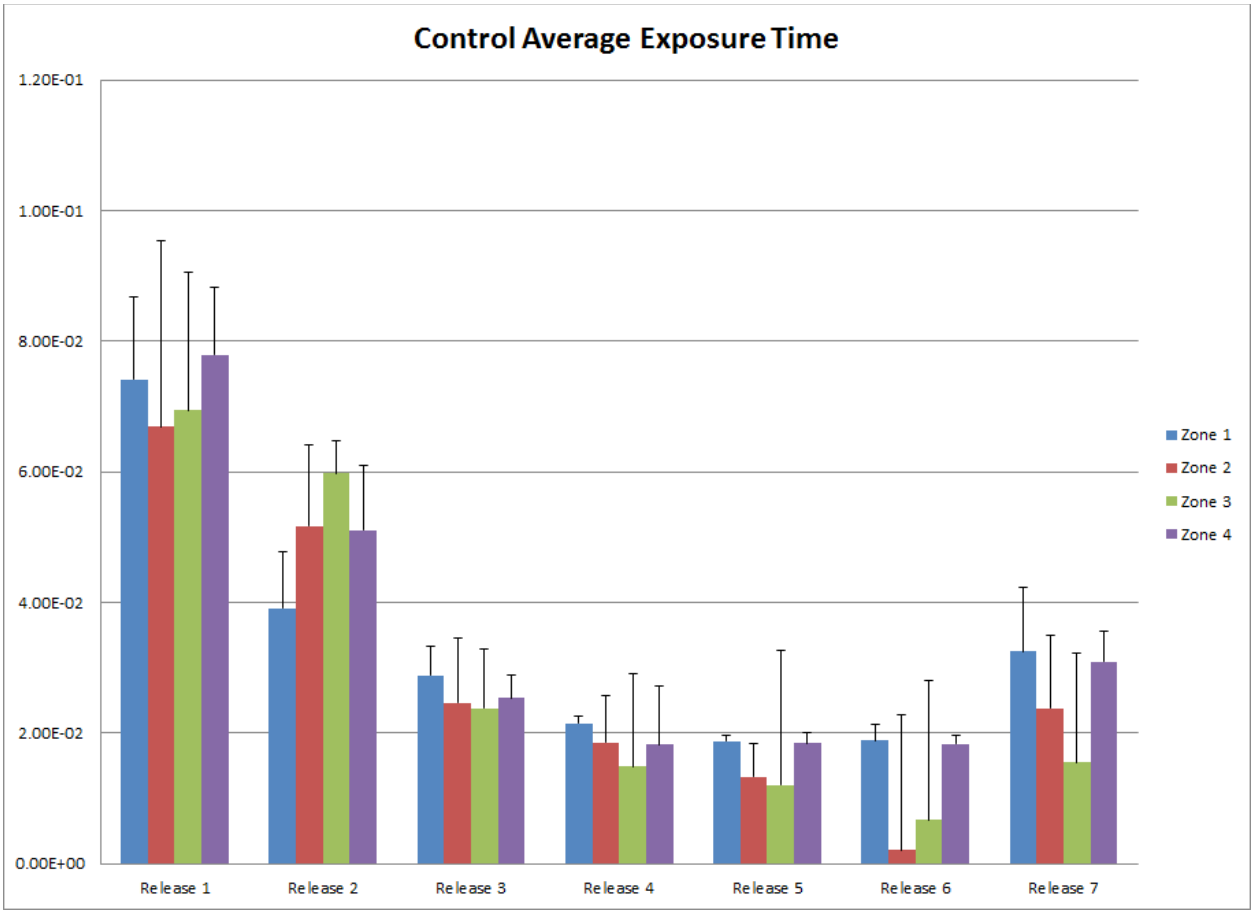

Figure 34: Average exposure time (s) for control leaflets during forward flow

Overall, principal shear stress increases with each release event until Release 7 where the principal shear stress decreases when compared to Release 6. This behavior is expected since, as mentioned earlier, the flow velocity has decreased and is becoming negative due to aortic pressure being higher than ventricular pressure. Principal shear stress is dependent on the velocity gradient of the fluid, therefore as velocity increases, principal shear stress also increases. From Release 3 forward, zones 2 and 3 (the two shear zones in the central orifice jet) experienced higher principal shear stress levels compared to zones 1 and 4 due. The particles in zones 2 and 3 experience unstable

wake turbulence (vorticity) from the flow separation caused by the leaflets which increases the velocity gradients and thus increases shear stress levels.

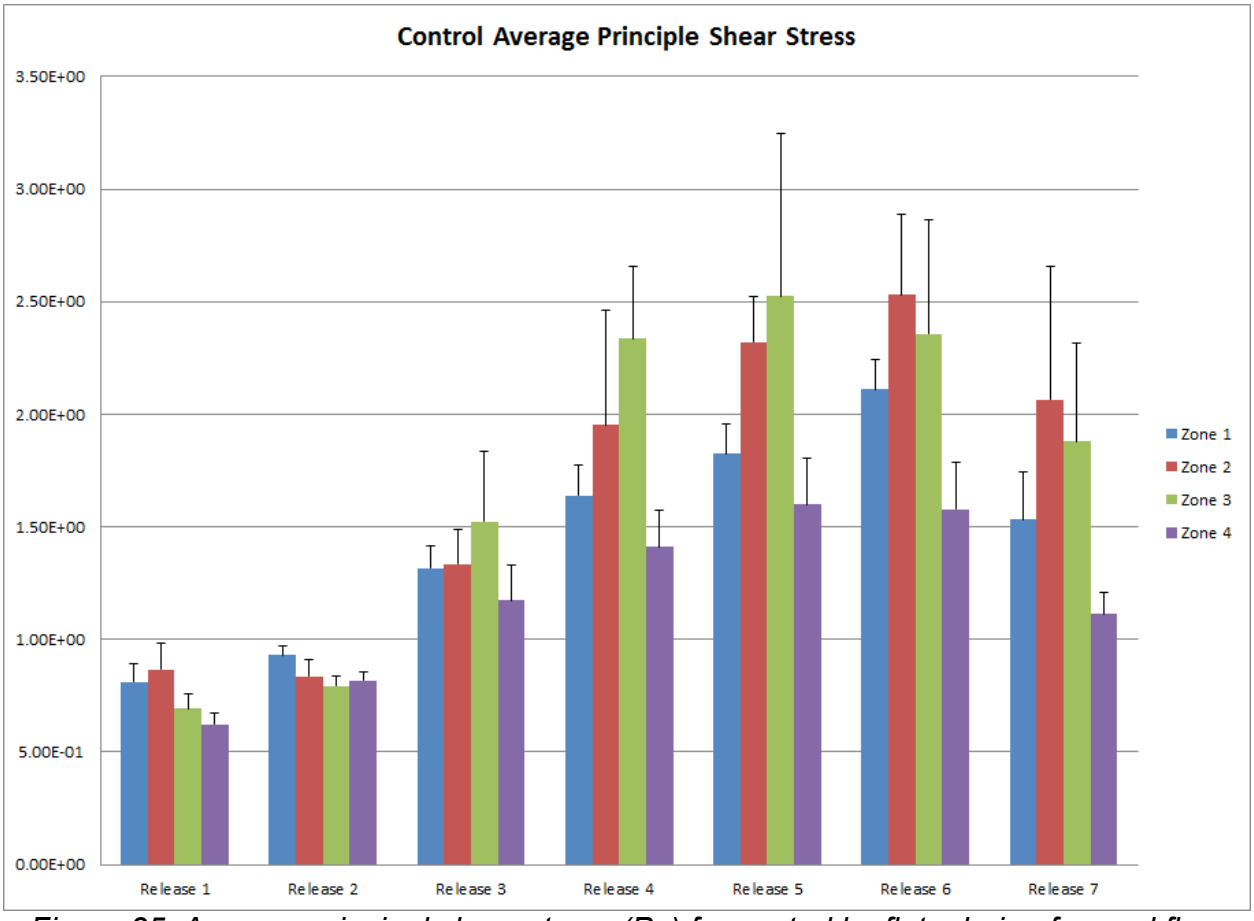

Figure 35: Average principal shear stress (Pa) for control leaflets during forward flow

Figure 36 and 37 shows the average platelet activation TEP and platelet lysis TEP experienced by each particle at different release events by initial position zone. Similarly to the average exposure time, platelet activation levels decrease with each release event until Release 7 where platelet activation increases when compared to Release 6. As the flow is accelerating through systole, the velocities of the particles released increased and they were quickly ejected from the high shear stress zones (lower exposure times). Since platelet activation TEP is strongly correlated to exposure times

in the TEP models, platelet activation TEP values decreased with decreasing exposure times.

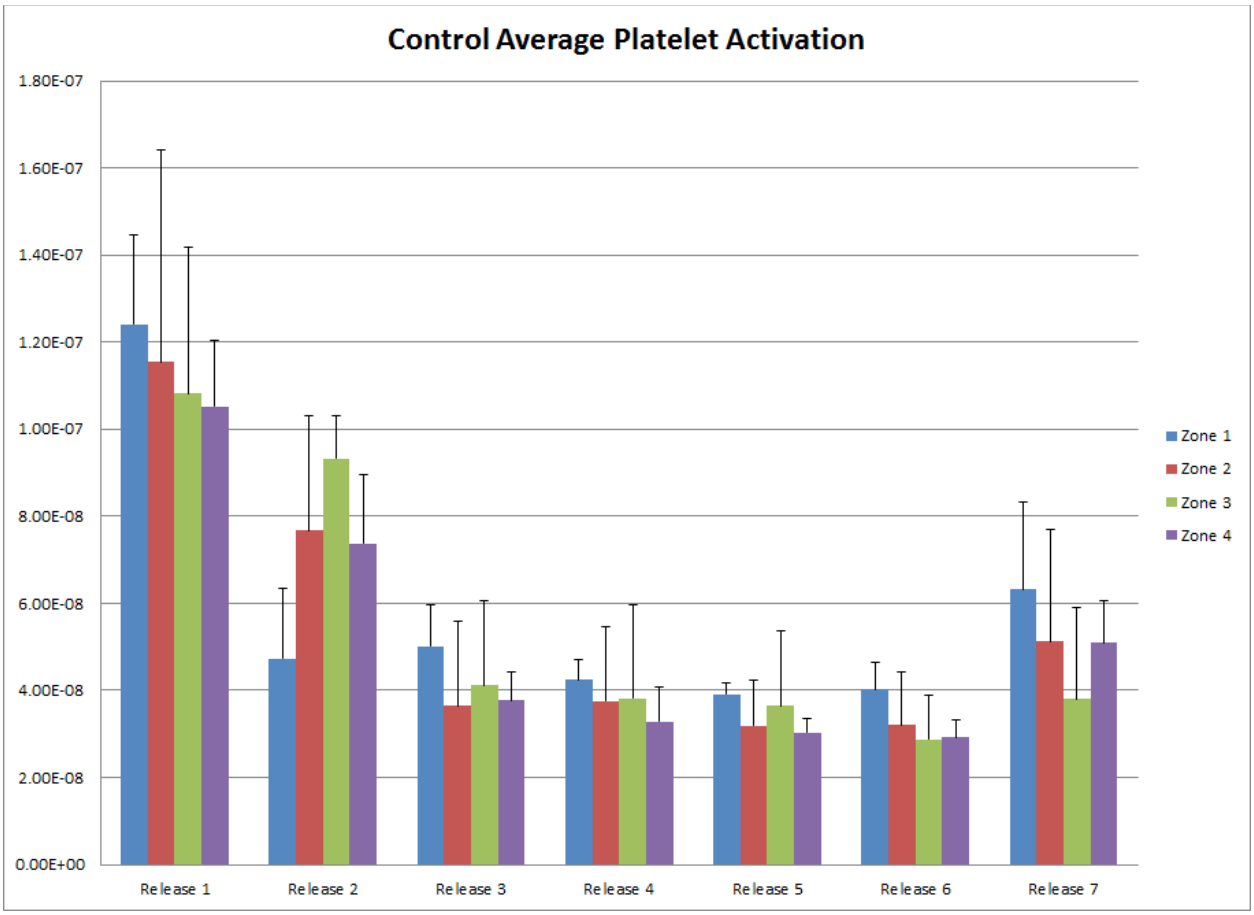

Figure 36: Average platelet activation TEP for control leaflets during forward flow

Similarly to the average principal shear stress, platelet lysis TEP levels increase with each release event until Release 7 where platelet lysis TEP levels decrease when compared to Release 6. As the flow is accelerating flow during systole, the principle shear stresses experienced by the particles also increased. Since platelet lysis TEP is strongly correlated to principal shear stress levels, in the TEP models, platelet lysis TEP values increased with increasing principle shear stresses. Beginning in Release 3 and through Release 6, zone 3 experiences a high amount of platelet lysis TEP. This zone

also experienced the highest average principal shear stress value and is located in the highly turbulent central orifice jet.

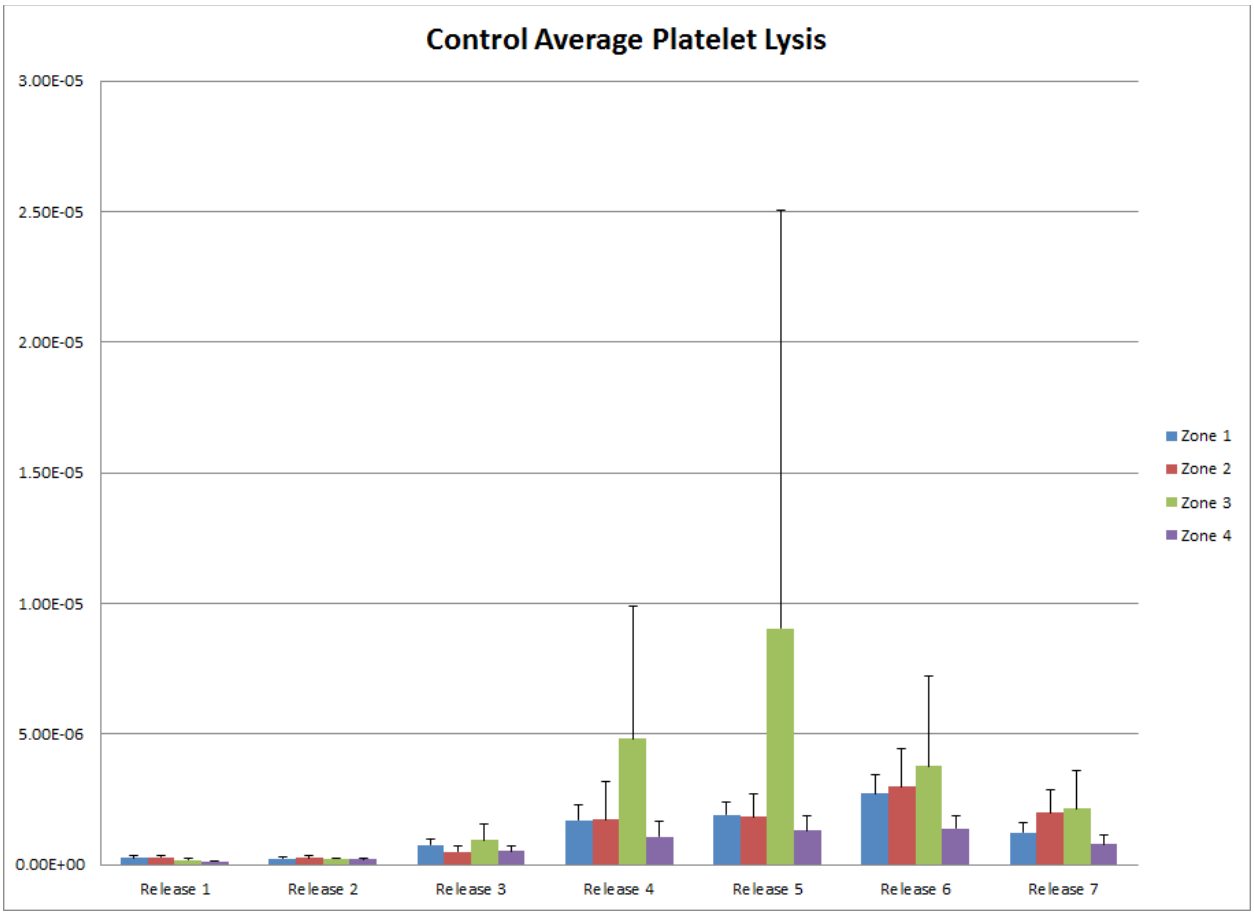

Figure 37: Average platelet lysis TEP for control leaflets during forward flow

Since the experiments are limited by the size of the measurement area, TEP for each particle is only calculated as long as they stay inside the measurement zone. By first normalizing both the platelet activation and platelet lysis TEP levels that each particle experienced by the corresponding exposure time raised to the power of their corresponding coefficients, a, from equations (7) and (8) before averaging the levels in each zone and release, the effect of shear stress on TEP can be seen per exposure time unit experienced by each particle. When the platelet activation TEP is normalized

by the exposure time, platelet activation TEP increases through the release events, meaning that the particles are experiencing higher platelet activation TEP per unit exposure time through the release events, particularly in the two middle zones corresponding to the central jet due to the wake instability from the flow separation caused by the leaflets. Figure 38 shows the platelet activation TEP normalized by exposure time.

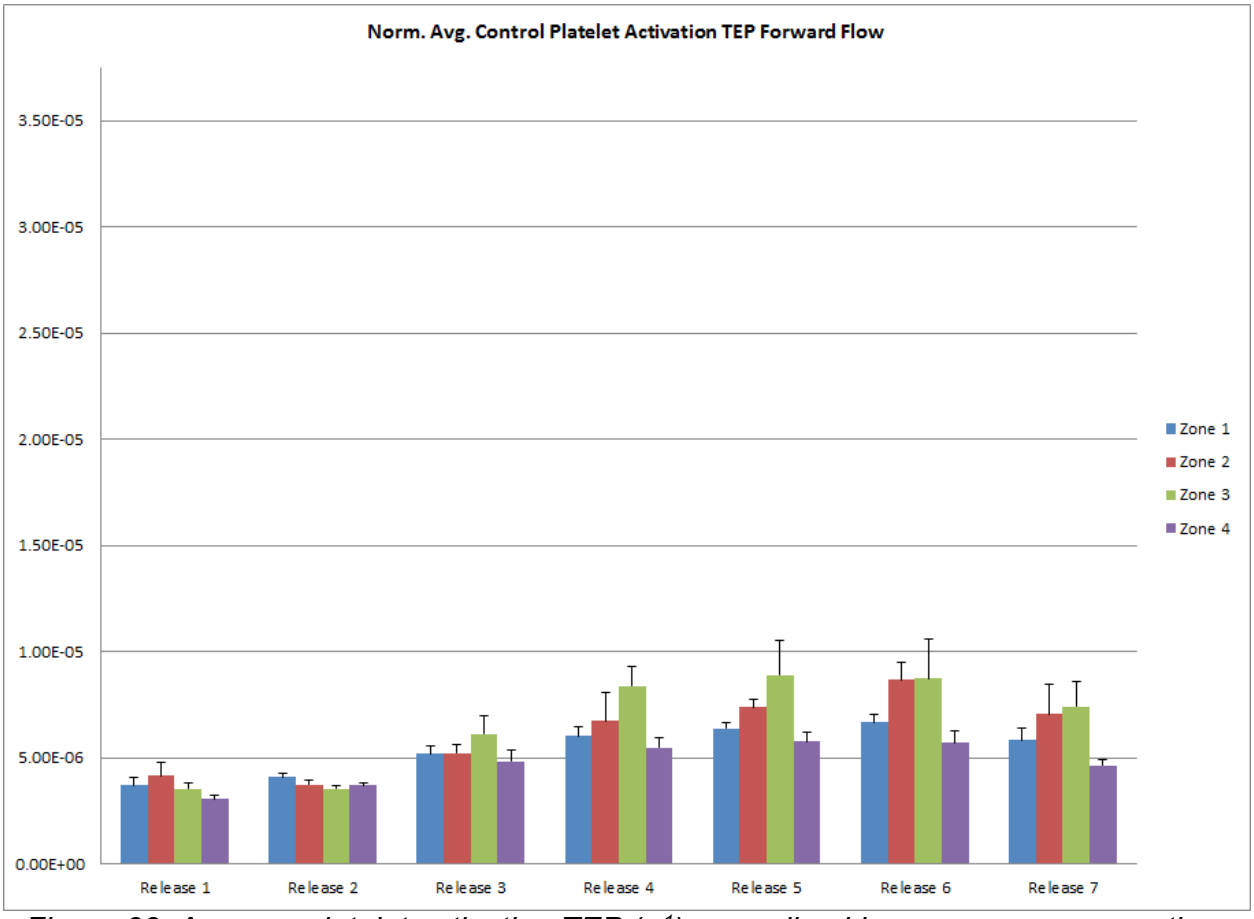

Figure 38: Average platelet activation TEP (s^{-1}) normalized by average exposure time for control leaflets during forward flow

When the platelet lysis TEP is normalized by the average exposure time, no significant change is seen in the overall trend, meaning that exposure time has little effect on

platelet lysis TEP and is heavily dependent on the shear stress loading histories. Figure 39 shows the platelet activation TEP normalized by exposure time.

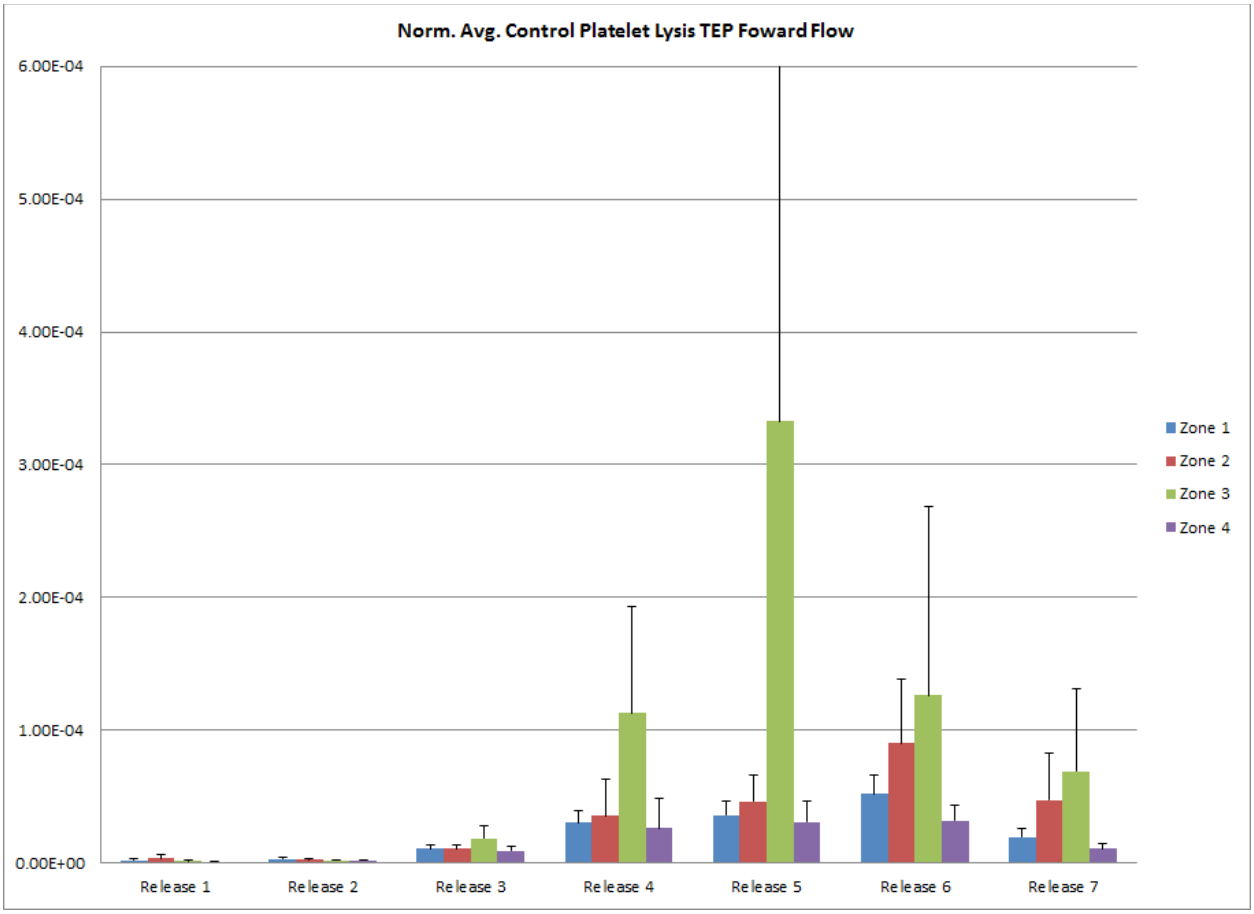

Figure 39: Average platelet lysis TEP (s^{-1}) normalized by average exposure time for control leaflets during forward flow

6.2 Regurgitant Flow TEP

Figure 40 presents an image sequence of vorticity fields during the valve closure phase and the diastolic phase. Immediately prior to leaflet closure, a closing vortex forms from the closing tips of the leaflets. This vortex is pinched off once the leaflet closes followed by the b-datum regurgitant jet.

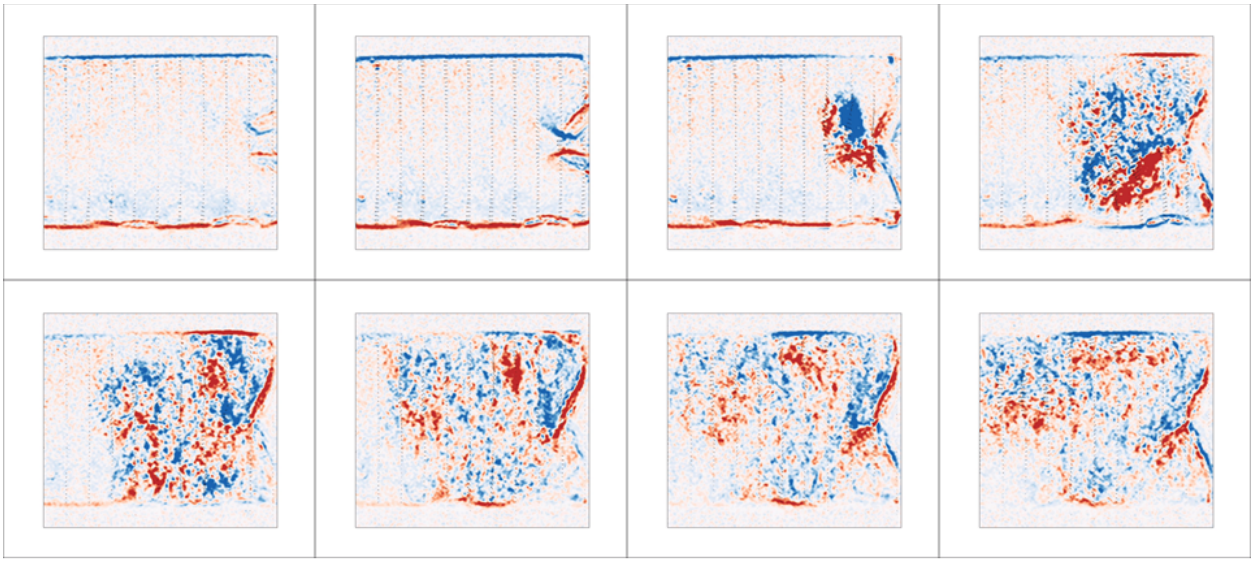

Figure 40: Image sequence of control leaflet closure showing closing vortex.

Animations A3 and A4 depict lagrangian particle trajectories calculated for 100 particles released on the line rake for each of the 10 independent repeated measurements simultaneously. The color of the particles represents the amount of platelet activation TEP and platelet lysis TEP accumulated by the particle. One hundred more particles were released every 0.1 s through ventricular diastole for a total of seven release events. For each release event, the particles were divided into three zones according to their initial position when released. The middle group (Zone 2) consisted of 34 particles centered on b-datum jet centerline while the top and bottom group (Zone 1 and Zone 3) each consisted of 33 particles above and below the middle 34 particles. As shown in the animation, trajectory calculations terminated once the particles left the measurement window. These trajectories represent blood element advection immediately upstream of the valve at the instant when the valve begins to close, an area where the closing vortex and the b-datum jet occur. Lagrangian tracking showed that particles originating outside of the b-datum regurgitant jet (zones 1 and 3) experienced high exposure times and low

principal shear stress levels in the zones of recirculation upstream of the closed leaflets outside of the regurgitant jet zone. As some particles recirculate in the zones upstream of the valve leaflets, they become entrapped in the high velocity regurgitant jet later during diastole. Particles with originated near the b-datum jet (zone 2) experienced less exposure time in the zones of high shear stress near and inside the regurgitant jet zone.

Figure 41 and 42 shows the average exposure time and principal shear stress experienced by each particle at different release events by initial position zone. Overall, exposure time remains nearly the same for the first five release events then decreases significantly at releases 6 and 7. The first five releases occur during the beginning and middle of ventricular diastole and the b-datum gap is creating a high-velocity regurgitant jet and two areas of recirculation above and below it. Releases 6 and 7 occur at the end of ventricular diastole where the ventricular pressure is increasing above aortic pressure and the b-datum regurgitant jet flow velocity is decreasing. Also, the experiment time window limits the length of the exposure time recording in Release 7. Zone 3 experiences higher exposure times when compared to zones 1 and 2 in the first four releases since it corresponds to an area of recirculation.

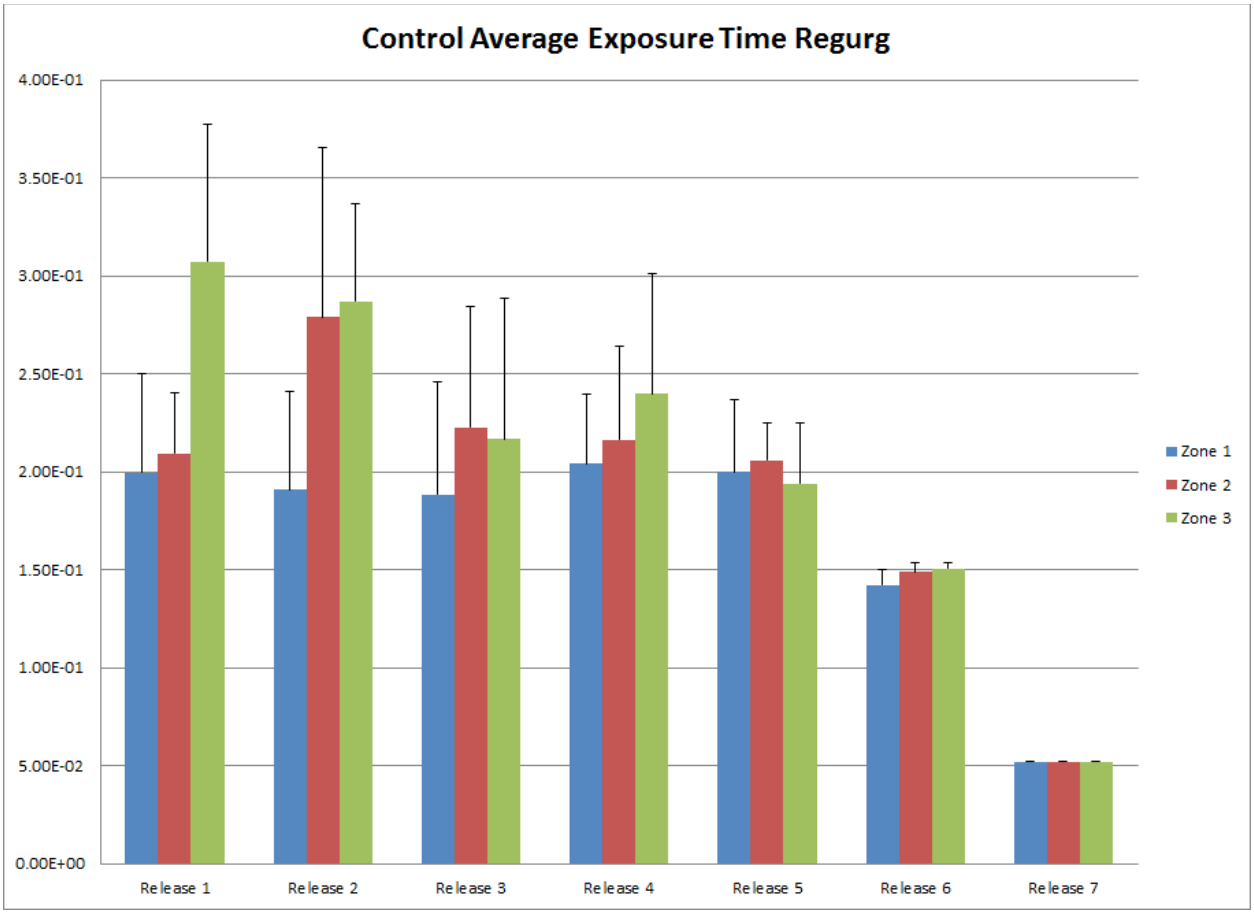

Figure 41: Average exposure time (s) for control leaflets in regurgitant flow

Overall, principal shear stress decreases slightly with each release event. This behavior is expected since the b-datum regurgitant jet flow velocity is slightly decreasing through ventricular diastole due to aortic pressure decreasing through ventricular diastole. Principal shear stress is dependent on the velocity gradient of the fluid, therefore as velocity decreases, principal shear stress also decreases.

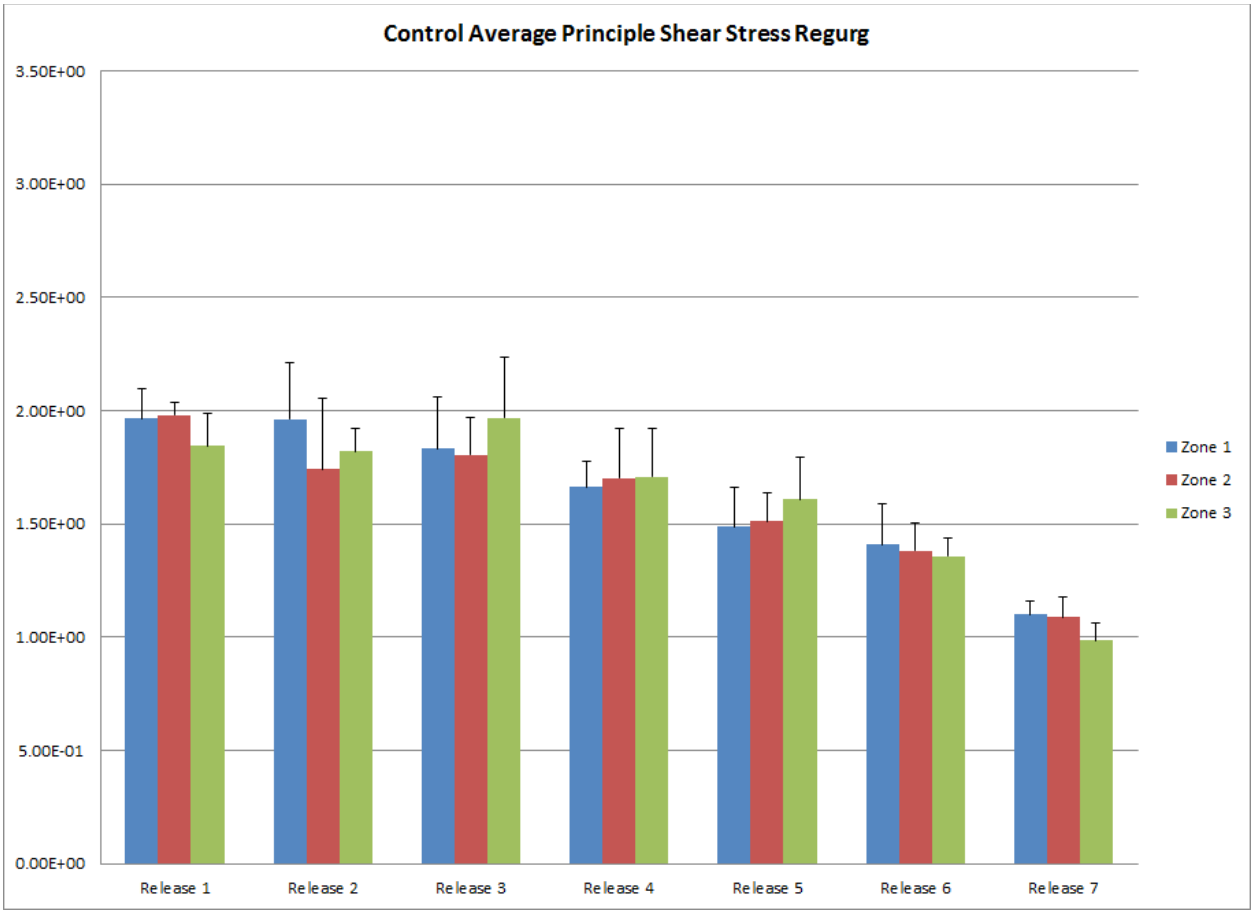

Figure 42: Average principal shear stress (Pa) for control leaflets in regurgitant flow

Figure 43 and 44 shows the average platelet activation TEP and platelet lysis TEP experienced by each particle at different release events by initial position zone. Similarly to the average exposure time, platelet activation decreases with each release event. Since platelet activation TEP is strongly correlated to exposure times in the TEP models, platelet activation TEP values decreased with decreasing exposure times. Zone 3 experiences higher platelet activation TEP when compared to zones 1 and 3 in the first four releases even though it experienced similar principal shear stress levels as zones 1 and 3.

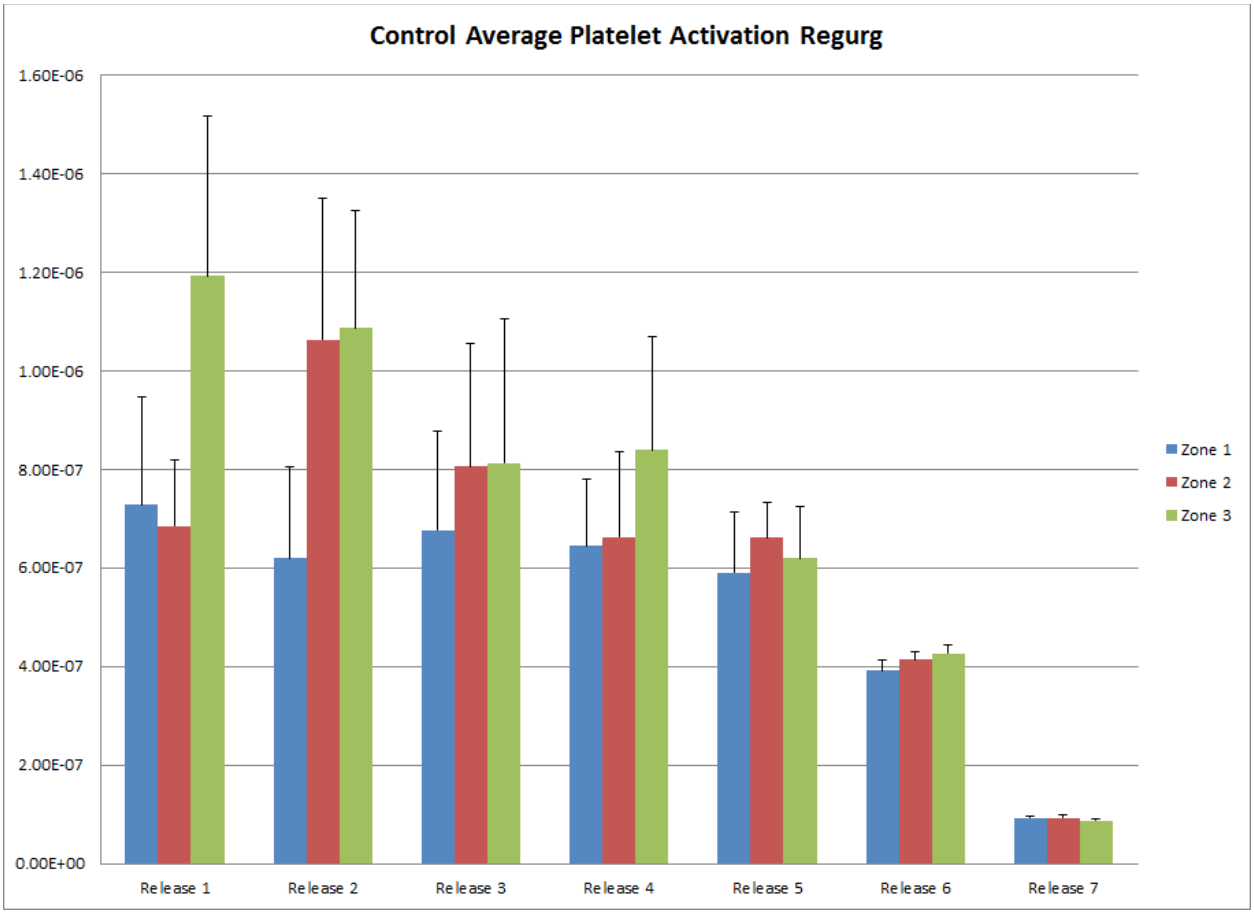

Figure 43: Average platelet activation TEP for control leaflets in regurgitant flow

Similarly to the average principal shear stress, platelet lysis TEP levels decreased with each release event. Since platelet lysis TEP is strongly correlated to principal shear stress in the TEP models, platelet lysis TEP values decreased with decreasing principle shear stresses. Zone 3 experiences higher platelet lysis TEP when compared to zones 1 and 3 in the first six releases even though it experienced similar principle shear stresses as zones 1 and 2. It is possible that the high exposure time was enough to raise the platelet lysis TEP levels above zones 1 and 2.

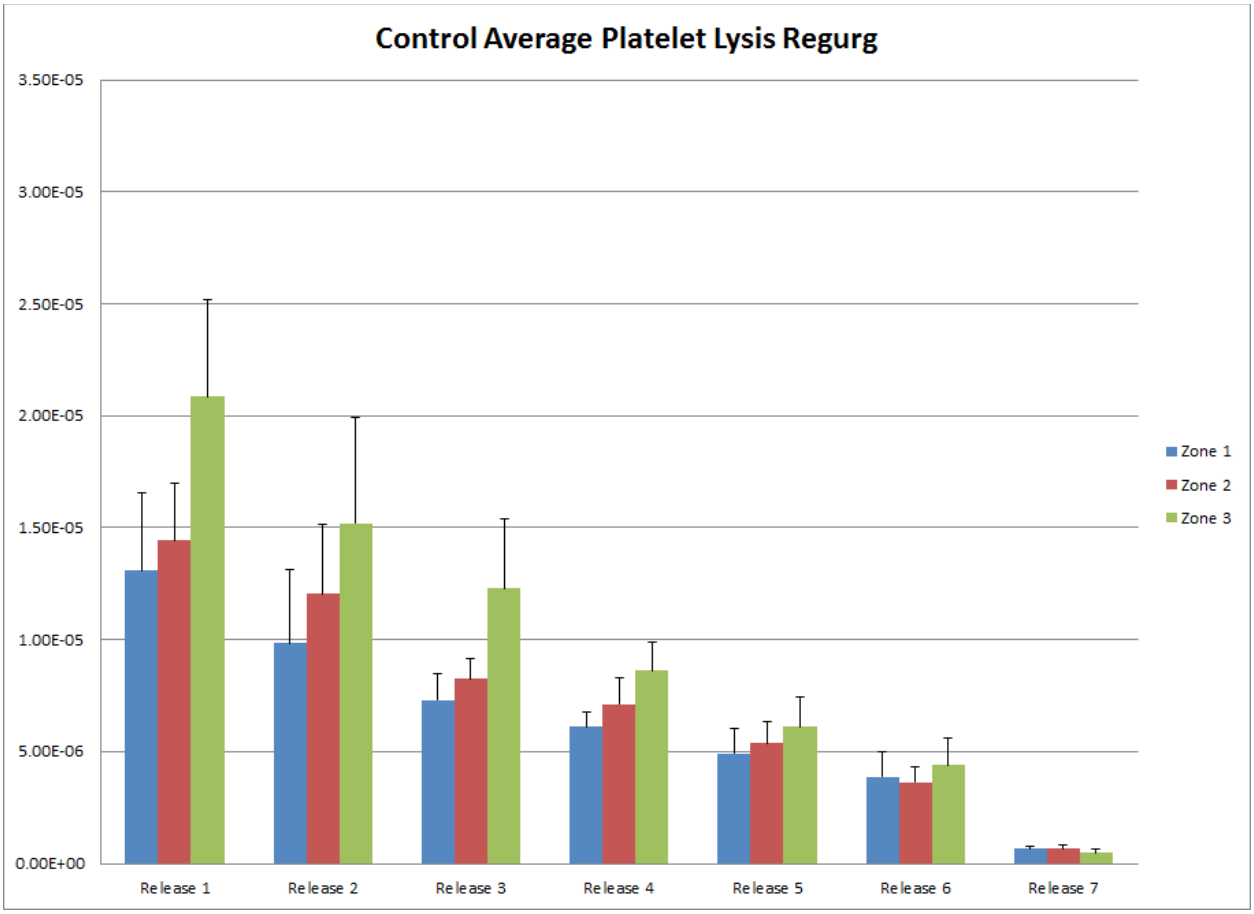

Figure 44: Average platelet lysis TEP for control leaflets in regurgitant flow

Again, since the experiments are limited by the size of the measurement area, TEP for each particle is only calculated as long as they stay inside the measurement zone. By first normalizing both the platelet activation and platelet lysis TEP levels that each particle experienced by the corresponding exposure time raised to the power of their corresponding coefficients, a, from equations (7) and (8) before averaging the levels in each zone and release, the effect of shear stress on TEP can be seen per exposure time unit experienced by each particle. When the platelet activation TEP is normalized by the exposure time, platelet activation TEP levels became fairly similar through the first 5 release events and zones and then significantly increased in the last 2 release

events. Since the last two releases occur at the end of diastole, the particles do not experience long exposure times but accumulate platelet activation very quickly. Figure 45 shows the platelet activation TEP normalized by exposure time.

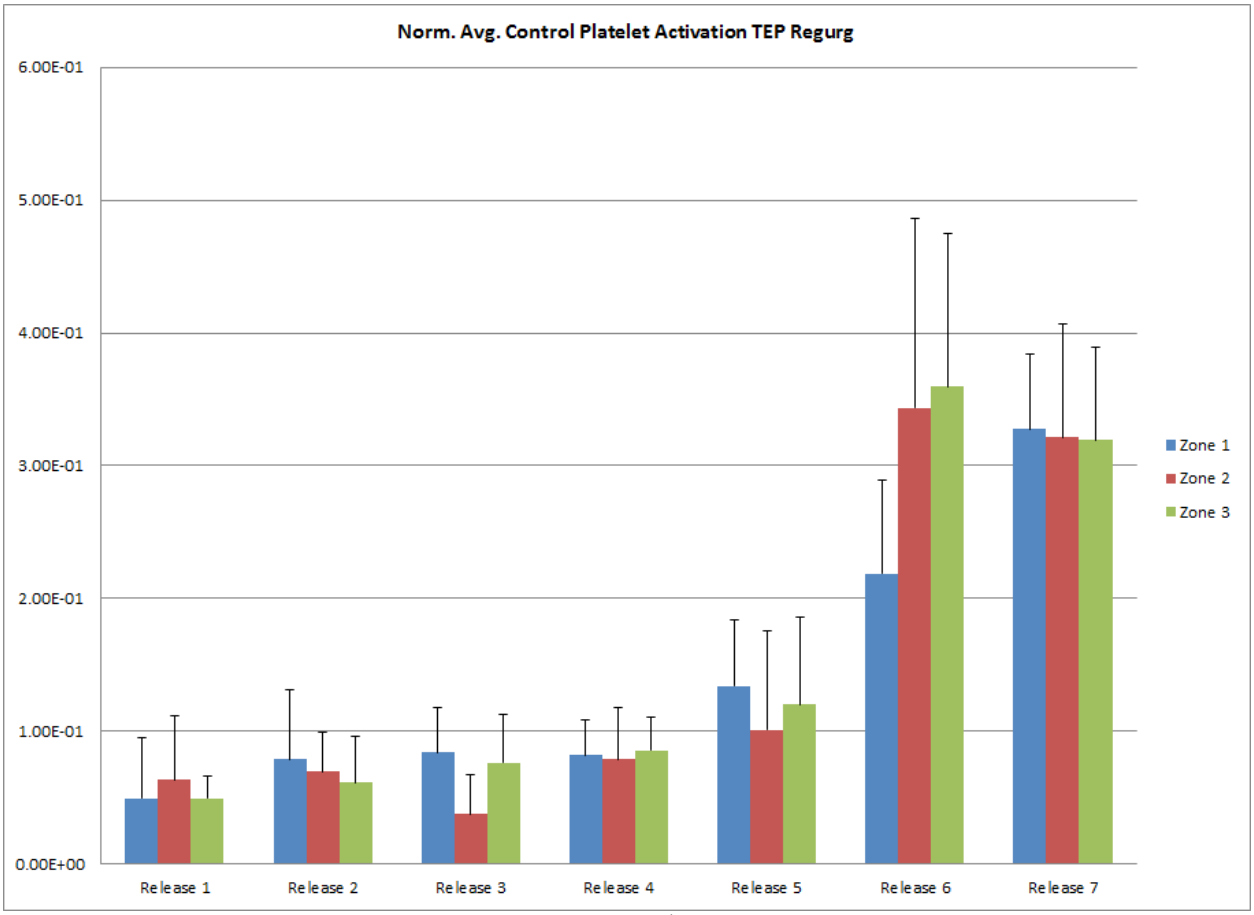

Figure 45: Average platelet activation TEP (s^{-1}) normalized by average exposure time for control leaflets in regurgitant flow.

When the platelet lysis TEP is normalized by the exposure time, the highest levels are seen in the zone corresponding to the b-datum regurgitant jet (Zone 2) during the Releases where the jet is at it's strongest. Also, zone 2 platelet lysis levels are high in Release 1 due to the strong closing vortex. The 2 zones corresponding to the recirculation areas experience similar levels of platelet lysis TEP levels per unit

exposure times since they experience similar low shear stresses. Figure 46 shows the platelet lysis TEP normalized by exposure time.

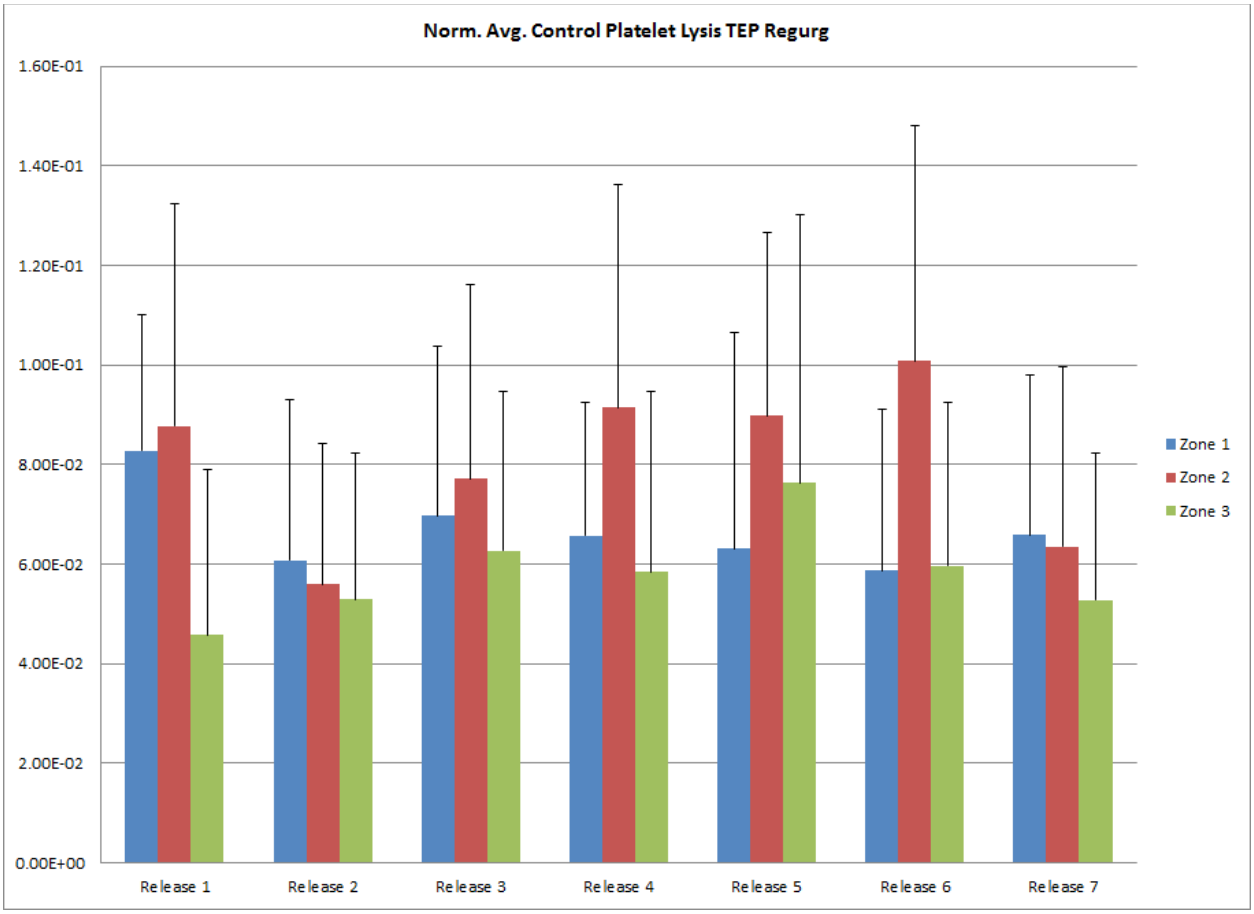

Figure 46: Average platelet lysis TEP (s^{-1}) normalized by average exposure time for control leaflets in regurgitant flow.

In summary, in systolic flow downstream of the valve, particles experienced higher platelet activation TEP levels in the beginning of systole. As the flow accelerated, platelet activation TEP levels decreased as they were exposed to the shear stress levels in the flow for shorter exposure times. However, as the flow accelerated, platelet lysis TEP levels increased through the release events as principle shear stresses increased. When both platelet activation and lysis TEP were normalized by their respective exposure time values, platelet activation TEP per unit exposure time

increased through the release events as the flow accelerated and platelet lysis TEP per unit exposure time also increased through the release events as the flow accelerated. In diastolic flow upstream of the valve, particles experienced higher platelet activation TEP levels in the beginning of diastole and in the zones corresponding to the recirculation areas above and below the regurgitant jet. As the release events occur, the ventricular pressure is increasing above the aortic pressure and the b-datum regurgitant jet flow velocity is decreasing, thus platelet activation TEP levels decrease slightly through the release events. Similarly, particles experienced higher platelet lysis TEP levels in the beginning of diastole as the regurgitant jet is stronger (higher velocity and higher principle shear stresses) when the transvalvular pressure is highest near the beginning of diastole. When both platelet activation and lysis TEP were normalized by their respective exposure time values, platelet activation TEP levels became fairly similar through the first 5 release events and zones and then significantly increased in the last 2 release events. and platelet lysis TEP per unit exposure time was highest in the b-datum regurgitant jet zone and in the initial closing vortex.

CHAPTER 7: EFFECT OF VGs ON TEP - RESULTS AND DISCUSSION

The next sections show and discuss the average exposure time, principal shear stress, platelet activation TEP, and platelet lysis TEP of 10 takes (either forward flow or regurgitant flow) each with 7 release events of 100 particles per zone (for forward flow) or 7 releases of 100 particles divided between 3 zones for the BMHV with the co-rotating VG of counter-rotating VG configurations.

7.1 Forward Flow with VG TEP

7.1.1 Co-Rotating VG

Figure 47 presents an image sequence of vorticity fields during valve opening. As the leaflet is opening, an area of low pressure is created in the medial surface of the leaflet, creating a vortex which pinches off as the leaflet comes to its full open position. Next, the unsteady separation of flow around the leaflet tip creates alternating vortices which shed periodically from both sides of the leaflets. In the figure, the bottom leaflet opens late (a common occurrence in BMHVs) and the opening vortex and shedding is delayed compared to the top leaflet.

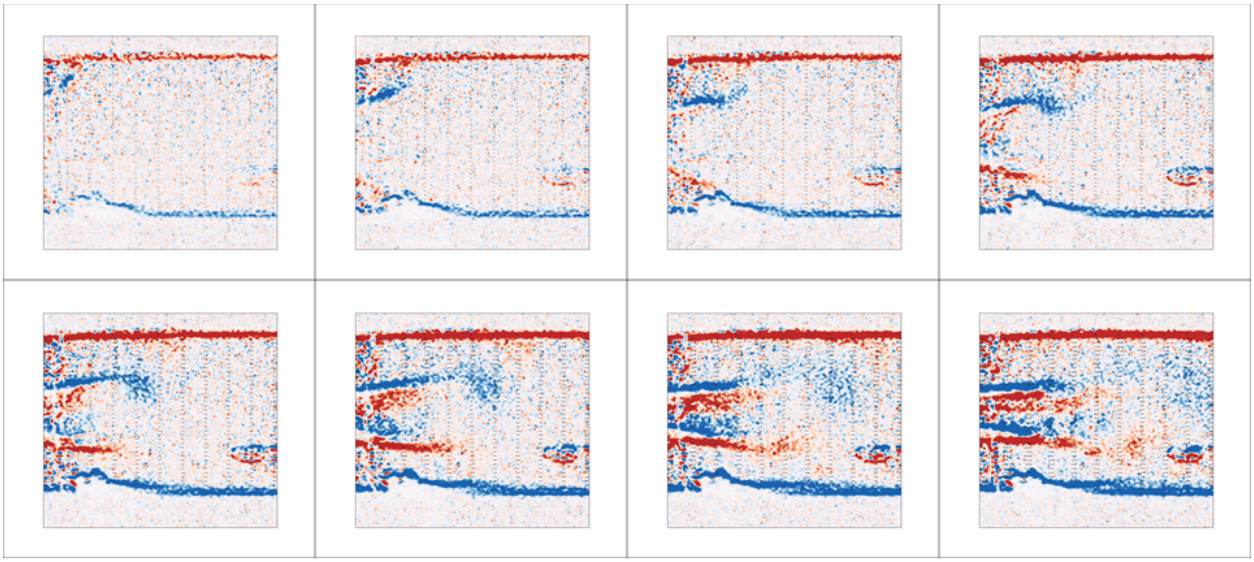

Figure 47: Image sequence of co-rotating VG leaflet opening showing opening vortex.

Animations A5 and A6 depict lagrangian particle trajectories for 100 particles released in the four shear zones identified earlier for each of the 10 independent repeated measurements simultaneously. The color of the particles represents the amount of platelet activation TEP and platelet lysis TEP accumulated by the particle. One hundred more particles per zone were released every 0.1s through ventricular systole for a total of 7 release events. As shown in the animation, trajectory calculations terminated once the particles left the measurement window. These trajectories represent blood element advection immediately downstream of the valve at the instant when the valve begins to open. Lagrangian tracking showed that most particles regardless of initial position zone were quickly ejected from their shear stress zones as the velocities immediately downstream of the valve are very uniform during ventricular systole. No recirculation areas or stagnation were observed, which is expected for forward flow.

Figure 48 and 49 shows the average exposure time and principal shear stress experienced by each particle at different release events by initial position zone. Overall, exposure time decreases with each release event until Release 7 where exposure time increases when compared to Release 6. As the velocities of the central jet and two lateral jets increased, the particles released are quickly ejected from the high shear stress zones (lower exposure times). This behavior is expected as Release 7 occurs at the end of ventricular systole where the flow velocity has decreased and becoming negative due to aortic pressure being higher than ventricular pressure. In releases 1 and 2, zones 3 and 4 experience higher exposure times compared to zones 1 and 2. This is attributed to the delayed opening of the bottom leaflet which delays the ejection of the particles from their initial position. During releases 3-6, all four zones experience similar exposure times, however, in Release 7, zones 2 and 3 experience lower exposure times compared to zones 1 and 4. The particles in zones 2 and 3 experience higher magnitudes of vorticity, since they were released in the central jet, which caused some particles to exit the boundaries of their zones; thus exhibiting shorter exposure times in the TEP calculations.

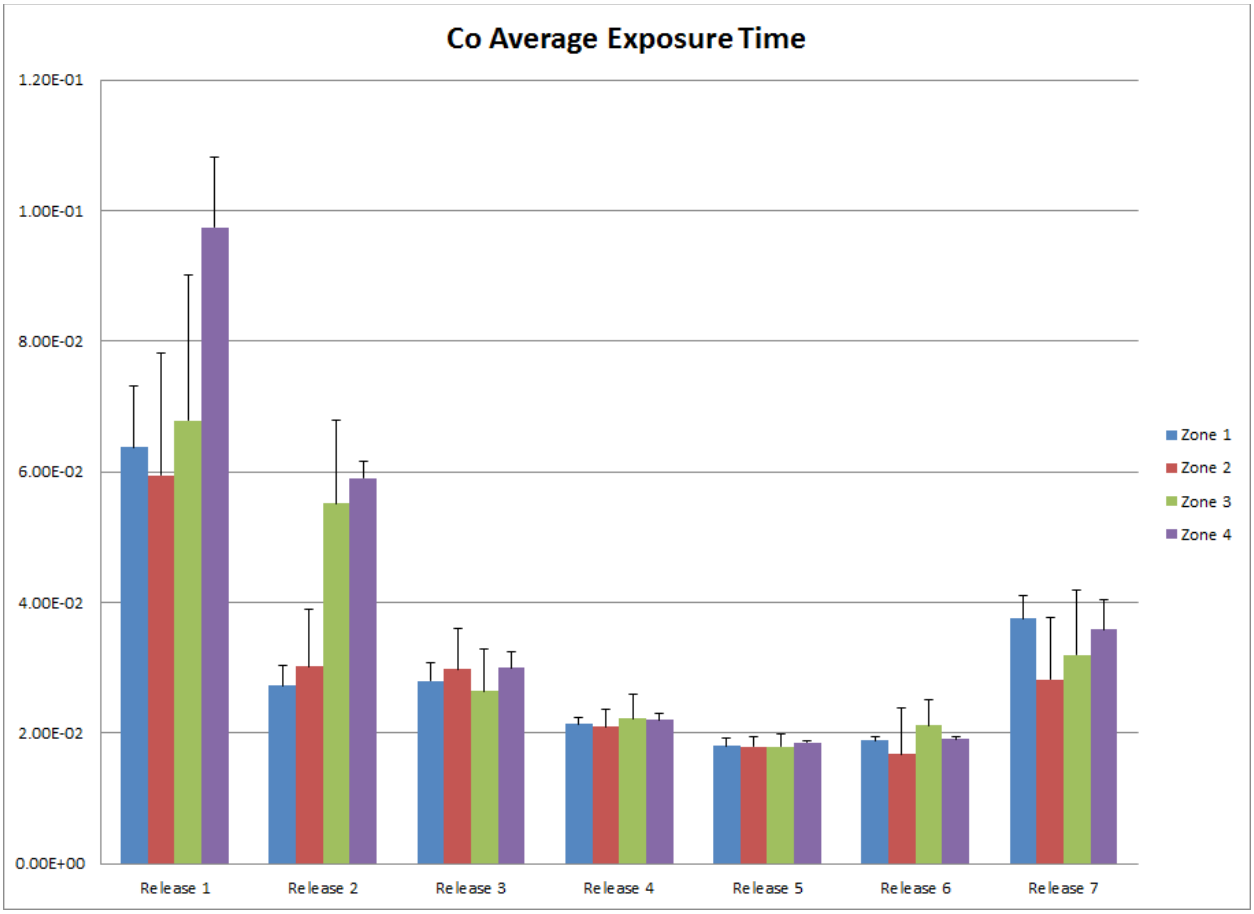

Figure 48: Average exposure time (s) for co-rotating VG leaflets during forward flow

Overall, principal shear stress increases with each release event until Release 7 where the principal shear stress decreases when compared to Release 6. This behavior is expected since, as mentioned earlier, the flow velocity has decreased and is becoming negative due to aortic pressure being higher than ventricular pressure. Principal shear stress is dependent on the velocity of the fluid, therefore as velocity increases, principal shear stress also increases. During releases 1 and 2, all four zones experience similar principal shear stress levels as the flow is in the beginning phase of systole and particle velocities are not very high, however, from Release 3 through Release 7, zones 2 and 3 (the two shear zones in the central orifice jet) experience higher principal shear stress

levels compared to zones 1 and 4. The particles in zones 2 and 3 experience wake turbulence from the vortices created by the vortex generators.

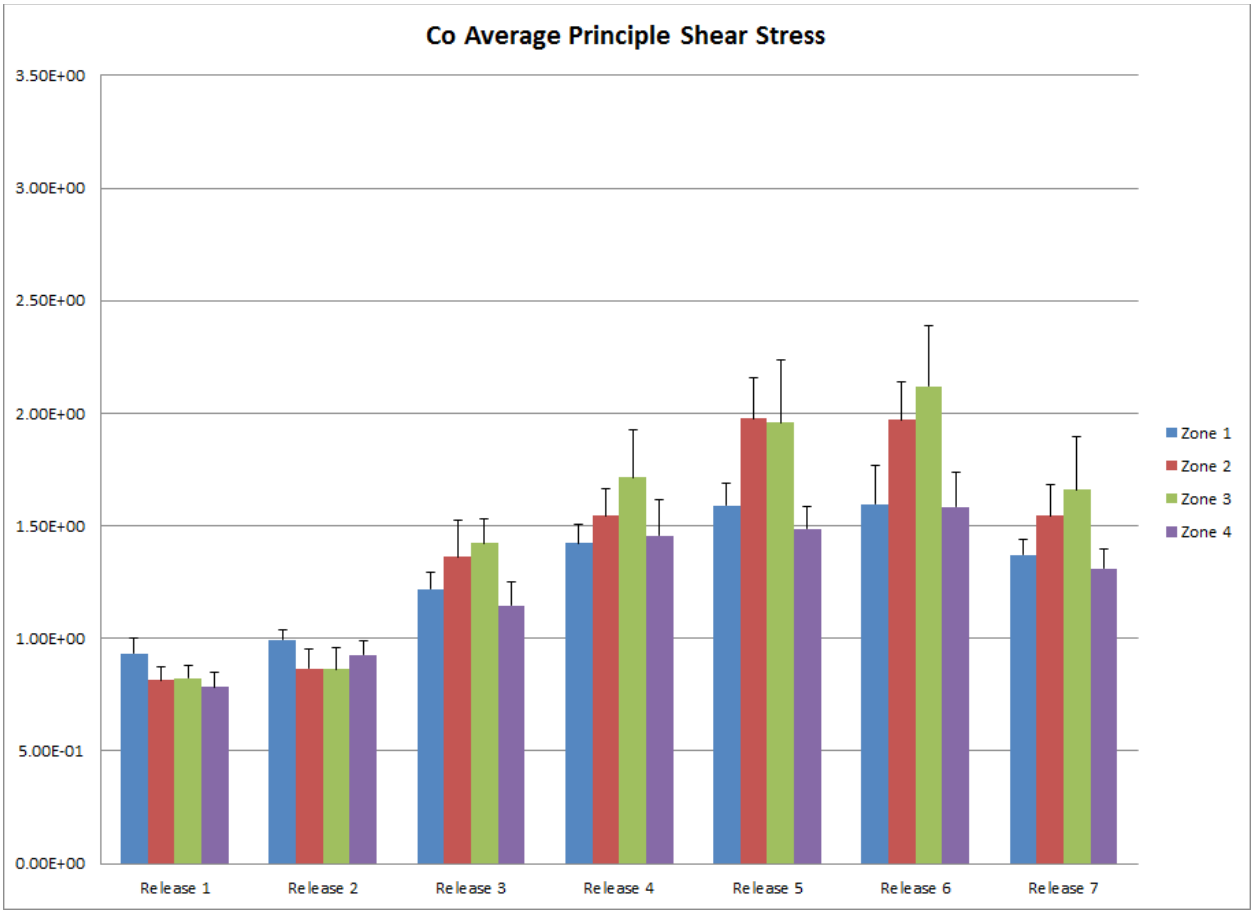

Figure 49: Average principal shear stress (Pa) for co-rotating VG leaflets during forward flow

Figure 50 and 51 shows the average platelet activation TEP and platelet lysis TEP experienced by each particle at different release events by initial position zone. Similarly to the average exposure time, platelet activation TEP levels decrease with each release event until Release 7 where platelet activation increases when compared to Release 6. As the flow is accelerating through systole, the velocities of the particles released increased and they were quickly ejected from the high shear stress zones (lower

exposure times). During releases 1 and 2, zone 4 has consistently higher platelet activation TEP compared to the other three zones. This is attributed to the higher exposure times caused by the delayed opening of the bottom leaflet. Since platelet activation TEP is strongly correlated to exposure time in the TEP models, platelet activation TEP levels decreased with decreasing exposure times. Through releases 3-7, platelet activation TEP remains similar for all four zones as they experienced similar exposure times.

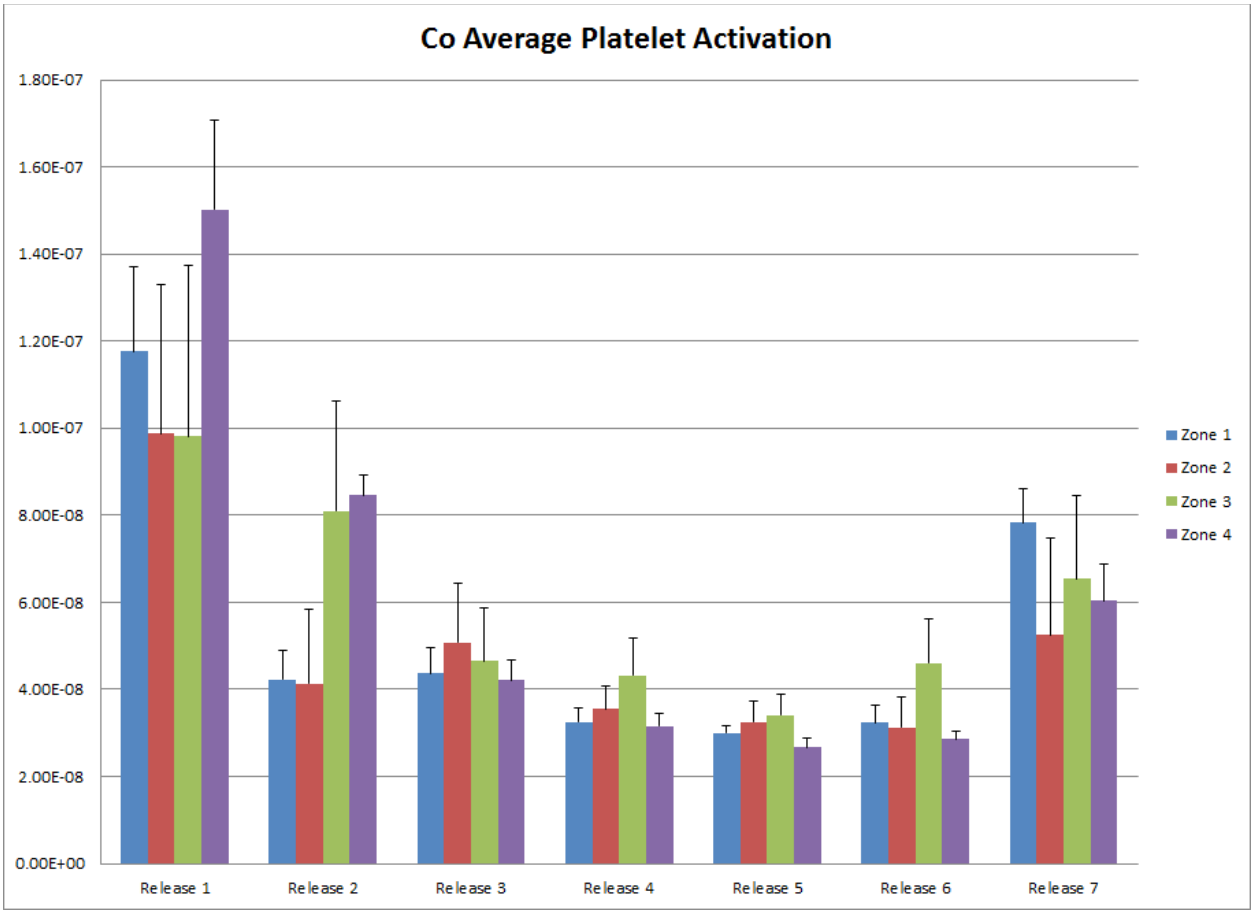

Figure 50: Average platelet activation TEP for co-rotating VG leaflets during forward flow

Similarly to the average principal shear stress, platelet lysis increases with each release event until Release 7 where platelet lysis decreases when compared to Release 6. As the flow is accelerating during systole, the principle shear stresses experienced by the particles also increased. Since platelet lysis TEP is strongly correlated to principal shear stress levels in the TEP models, platelet lysis TEP models increased with increasing principle shear stresses. During releases 1-3, all four zones show fairly equal platelet lysis TEP. However, in release 4, zone 4 shows a high level of platelet lysis TEP when compared to the other three zones. This is attributed to an air bubble that was caught in the valve mounting chamber and created a very small error zone in zone 4. 3At the following releases (5-7), zone 3 shows higher platelet lysis TEP compared to zone 4; which has lowered since Release 4. The zones that experienced the highest platelet lysis TEP levels are also the zones that experienced the highest principle shear stresses since they were located in the turbulent central orifice jet.

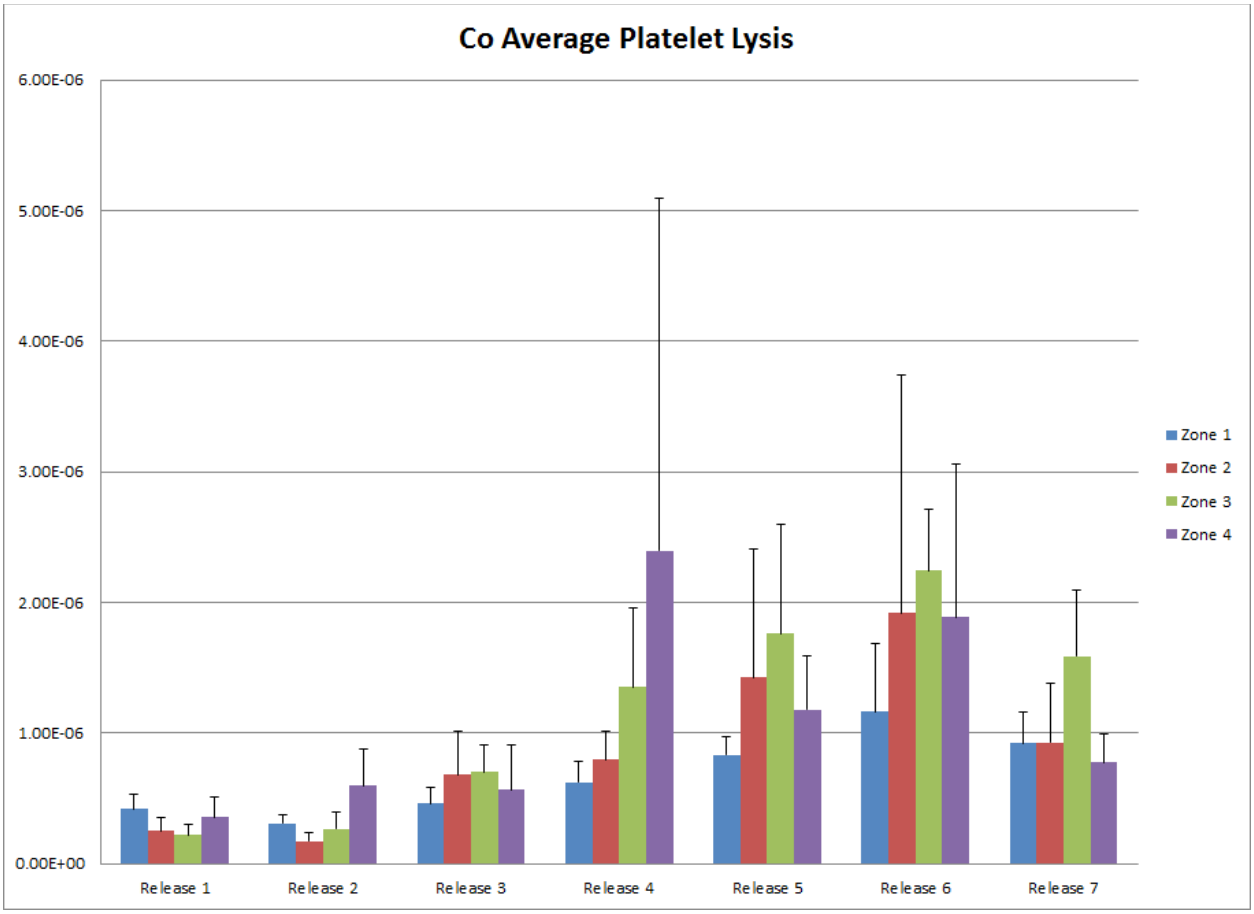

Figure 51: Average platelet lysis TEP for co-rotating VG leaflets during forward flow

Again, since the experiments are limited by the size of the measurement area, TEP for each particle is only calculated as long as they stay inside the measurement zone. By first normalizing both the platelet activation and platelet lysis TEP levels that each particle experienced by the corresponding exposure time raised to the power of their corresponding coefficients, a, from equations (7) and (8) before averaging the levels in each zone and release, the effect of shear stress on TEP can be seen per exposure time unit experienced by each particle. When the platelet activation TEP is normalized by the exposure time, platelet activation TEP levels became very similar through the release events and zones with a very slight increase in TEP levels through the first six

releases (corresponding to the increase in exposure times of each release) and zones 2 and 3 showing slightly higher levels than zones 1 and 4 (corresponding to the higher principle shear stresses experienced by the particles in the turbulent central orifice jet). Figure 52 shows the platelet activation TEP normalized by exposure time.

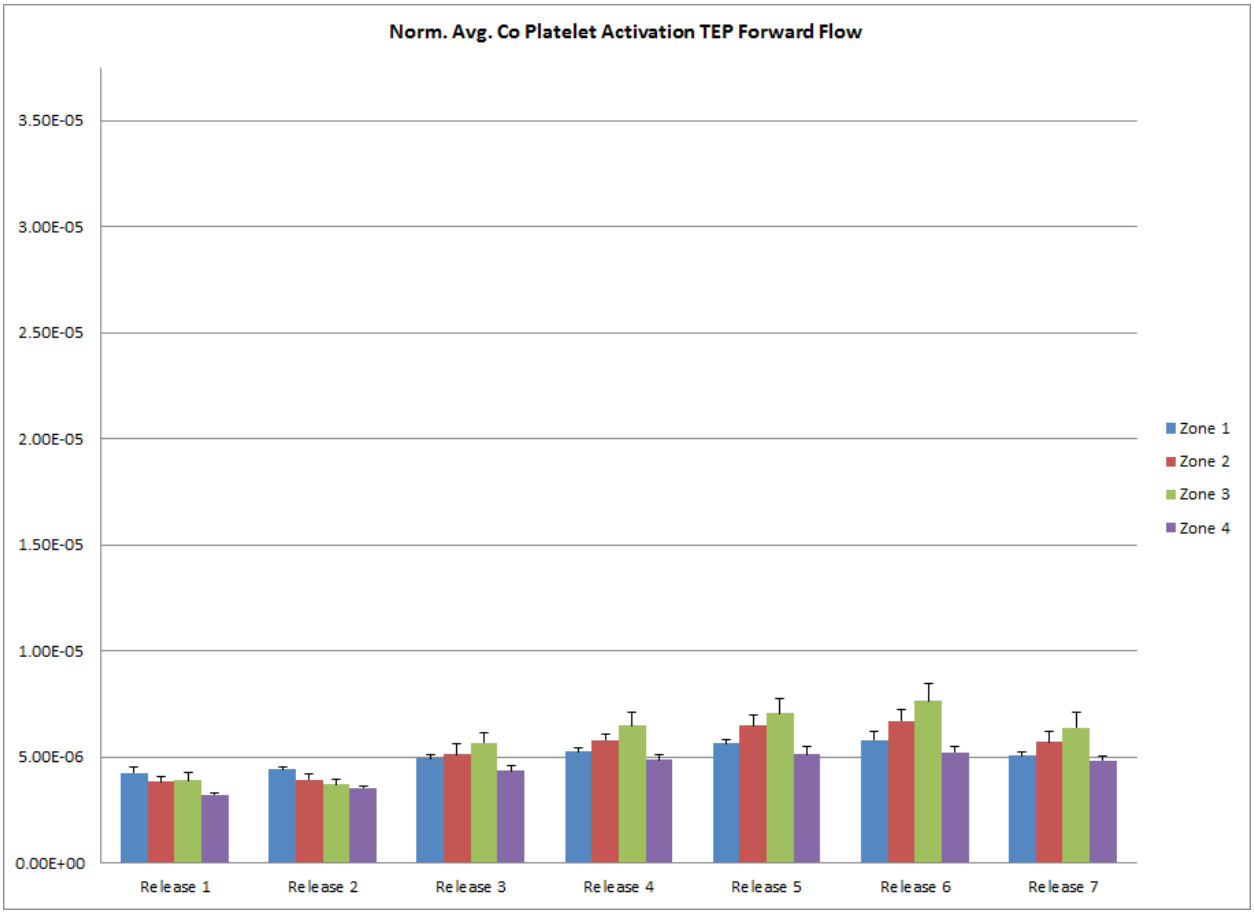

Figure 52: Average platelet activation TEP (s^{-1}) normalized by average exposure time for co-rotating VG leaflets during forward flow.

When the platelet lysis TEP is normalized by the average exposure time, no significant change is seen in the overall trend, but the TEP levels between each zone became similar to each other, meaning that exposure time has little effect on platelet lysis TEP and is heavily dependent on the shear stress loading histories. Figure 53 shows the platelet lysis TEP normalized by exposure time.

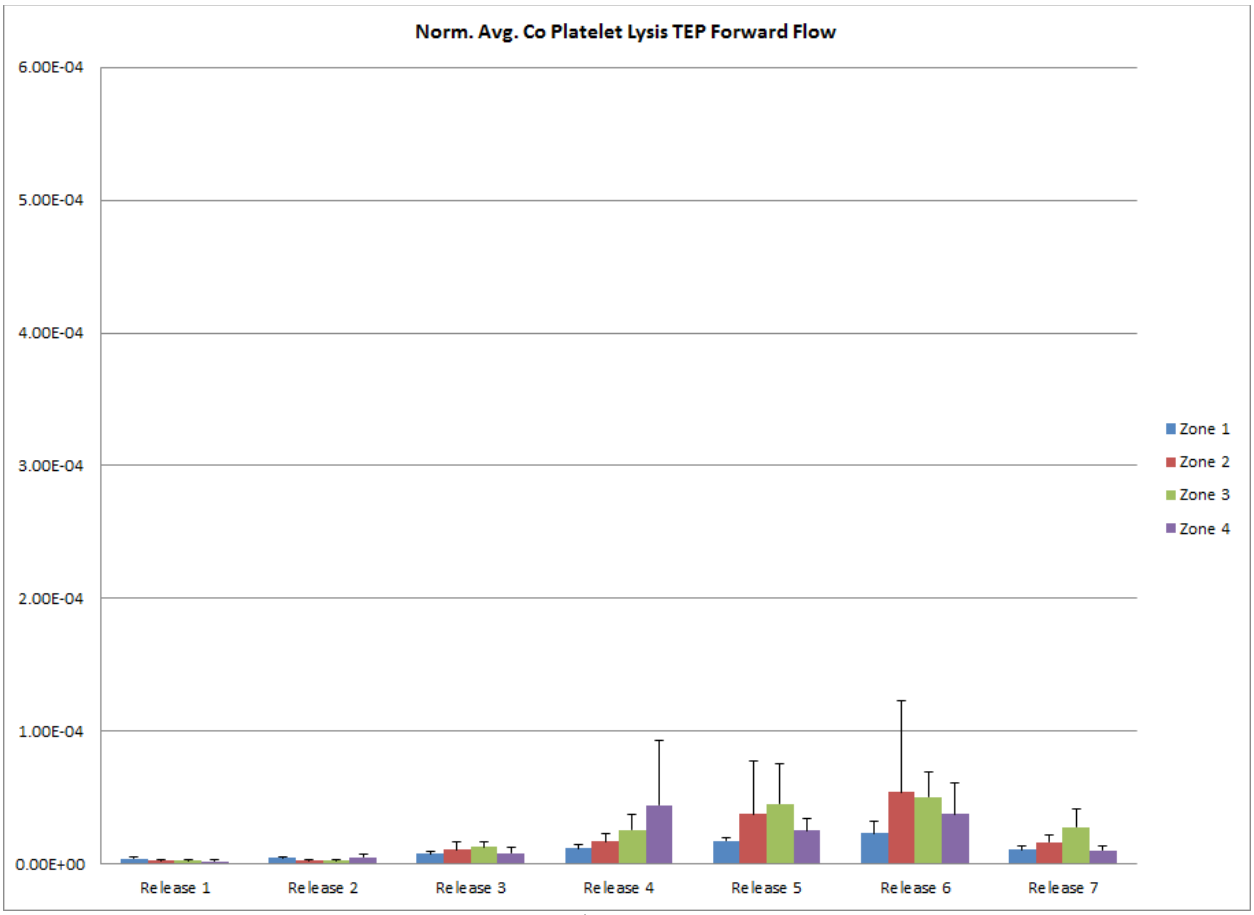

Figure 53: Average platelet lysis TEP (s^{-1}) normalized by average exposure time for co-rotating VG leaflets during forward flow.

7.1.2 Counter-Rotating VG

Figure 54 presents an image sequence of vorticity fields during valve opening. As the leaflets are opening, an area of low pressure is created in the medial surface of the leaflets, creating a vortex which pinches off as the leaflet comes to its full open position. Next, the unsteady separation of flow around the leaflet tip creates alternating vortices which shed periodically from both sides of the leaflets..

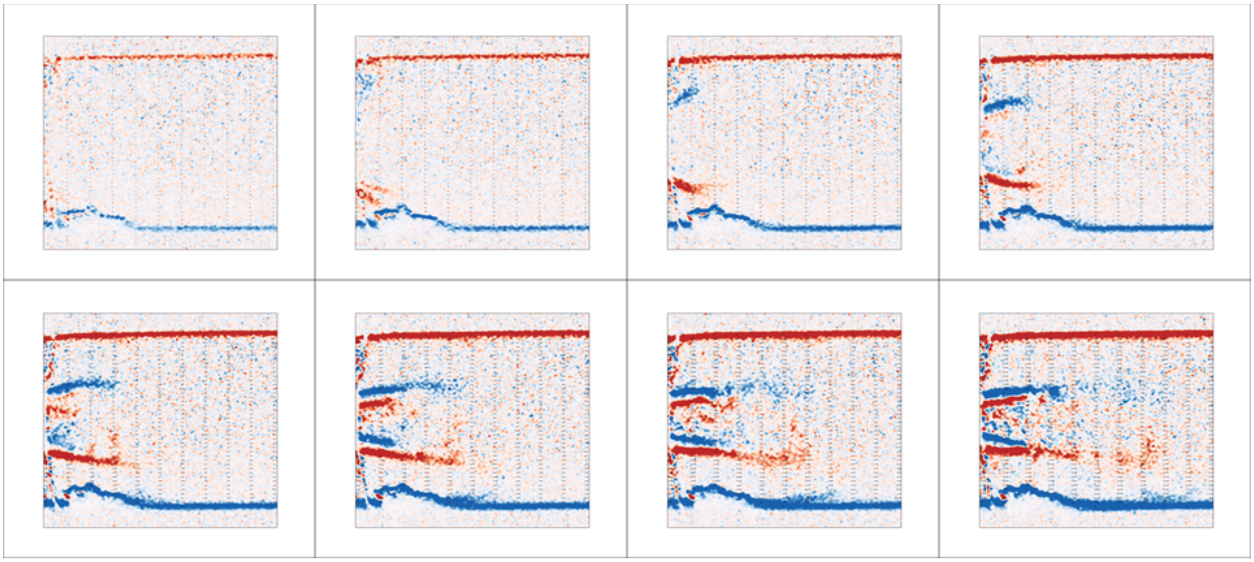

Figure 54: Image sequence of counter-rotating VGI leaflet opening showing opening vortex.

Animations A7 and A8 depict lagrangian particle trajectories for 100 particles released in the four shear zones identified earlier for each of the 10 independent repeated measurements simultaneously for platelet activation TEP and platelet lysis TEP respectively. The color of the particles represents the amount of platelet activation TEP and platelet lysis TEP accumulated by the particle. These trajectories represent blood element advection immediately downstream of the valve at the instant when the valve begins to open. One hundred more particles per zone were released every 0.1s through ventricular systole for a total of 7 release events. As shown in the animation, trajectory calculations terminated once the particles left the measurement window. These trajectories represent blood element advection immediately downstream of the valve at the instant when the valve begins to open. Lagrangian tracking showed that most particles, regardless of initial position zone, were quickly ejected from their shear stress zones as the velocities immediately downstream of the valve are very uniform during

ventricular systole. No recirculation areas or stagnation were observed, which is expected for forward flow.

Figure 55 and 56 shows the average exposure time and principal shear stress experienced by each particle at different release events by initial position zone. Overall, as the flow is accelerating between releases 1 and 6, exposure time decreases with each release event until Release 7 where exposure time increases when compared to Release 6. This behavior is expected as Release 7 occurs at the end of ventricular systole where the flow velocity has decreased and becoming negative due to aortic pressure being higher than ventricular pressure. Throughout all releases, all four zones experience similar exposure times compared to each other with zones 2 and 3 showing slightly shorter exposure times from Release 3 to Release 7. The particles in zones 2 and 3 experience higher magnitudes of vorticity, since they were released in the central jet, which caused some particles to exit the boundaries of their zones; thus exhibiting shorter exposure times in the TEP calculations.

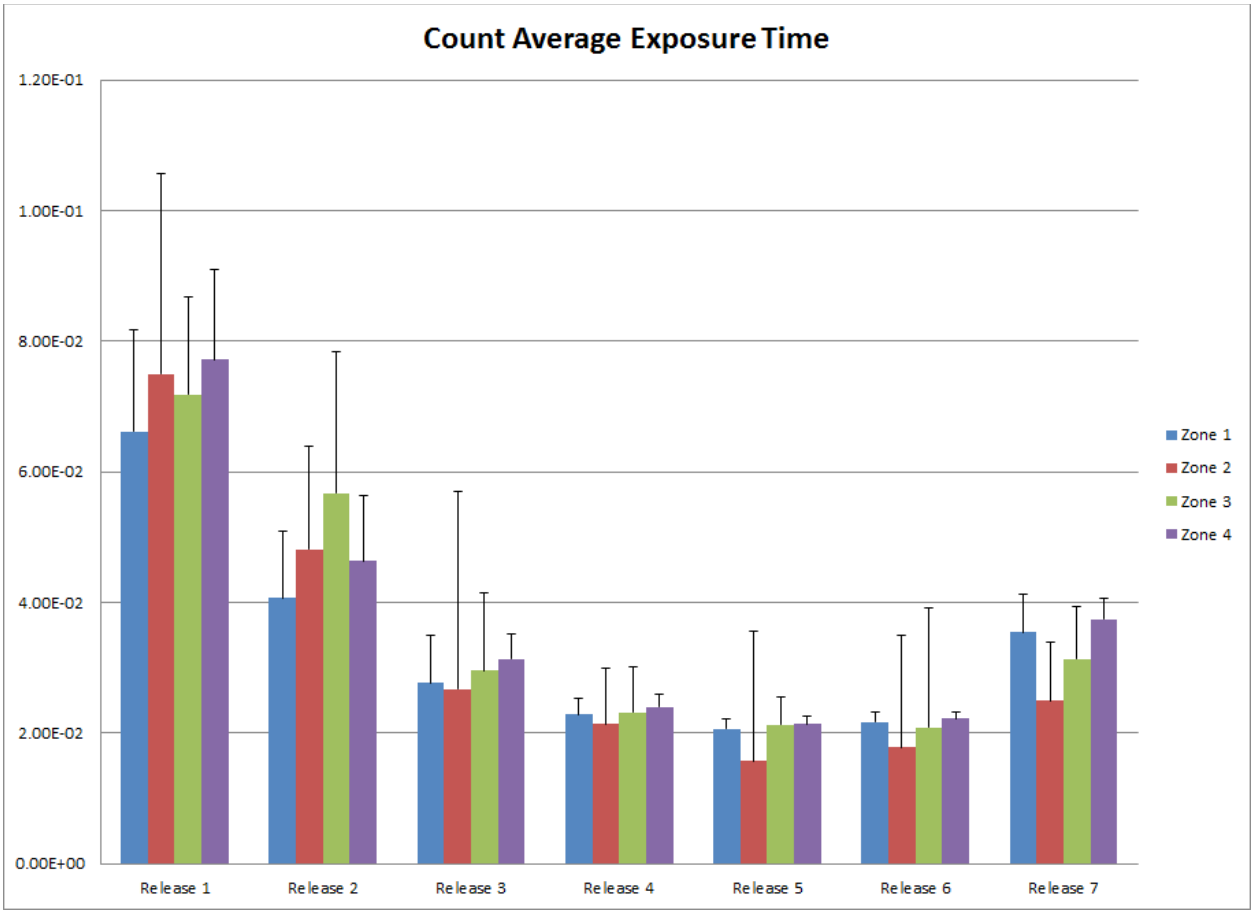

Figure 55: Average exposure time (s) for counter-rotating VG leaflets during forward flow

Overall, principal shear stress increases with each release event until Release 6 where the principal shear stress decreases when compared to Release 5 and continues decreasing through Release 7. This behavior is expected since, as mentioned earlier, the flow velocity has decreased and is becoming negative due to aortic pressure being higher than ventricular pressure. Principal shear stress is dependent on the velocity of the fluid, therefore as velocity decreases, principal shear stress also decreases. From Release 3 to Release 7, zones 2 and 3 (the two shear zones in the central orifice jet) experience higher principal shear stress levels compared to zones 1 and 4. The

particles in zones 2 and 3 experience wake turbulence from the vortices created by the vortex generators.

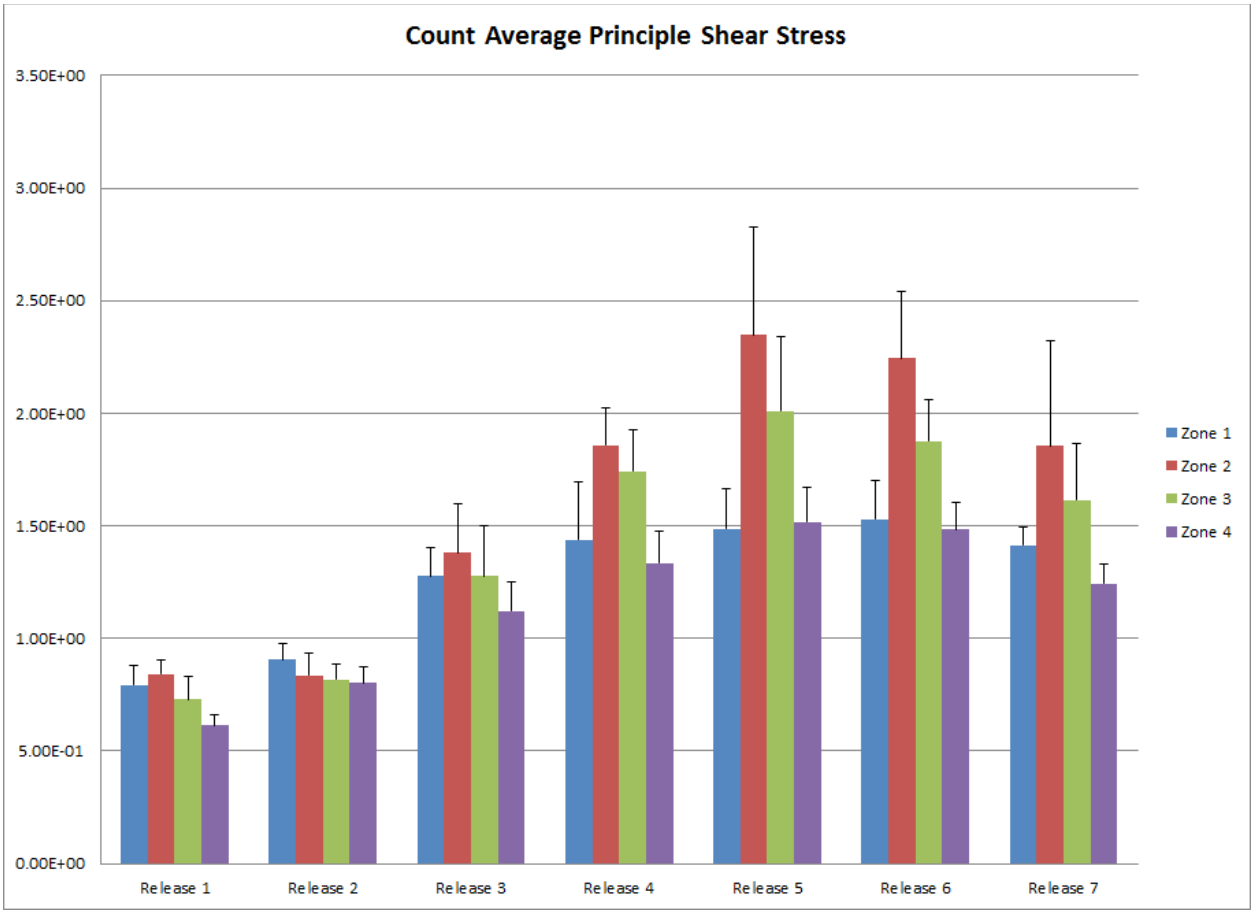

Figure 56: Average principal shear stress (Pa) for counter-rotating VG leaflets during forward flow

Figure 57 and 58 shows the average platelet activation TEP and platelet lysis TEP experienced by each particle at different release events by initial position zone. Similarly to average exposure time, platelet activation TEP levels decrease with each release event until Release 6 where platelet activation levels increases when compared to Release 5 and continues increasing through Release 7. As the flow is accelerating through systole, the velocities of the particles released increased and they were quickly

ejected from the high shear stress zones (lower exposure times). However, through the first six release events, zones 2 and 3 (the two shear zones in the central orifice jet) show higher levels of platelet activation TEP than zones 1 and 4 even though the two zones did not experience higher exposure times than zones 1 and 4. It is possible that the high average principle shear stresses experience by zones 2 and 3 contributed to the higher activation levels even with low exposure times

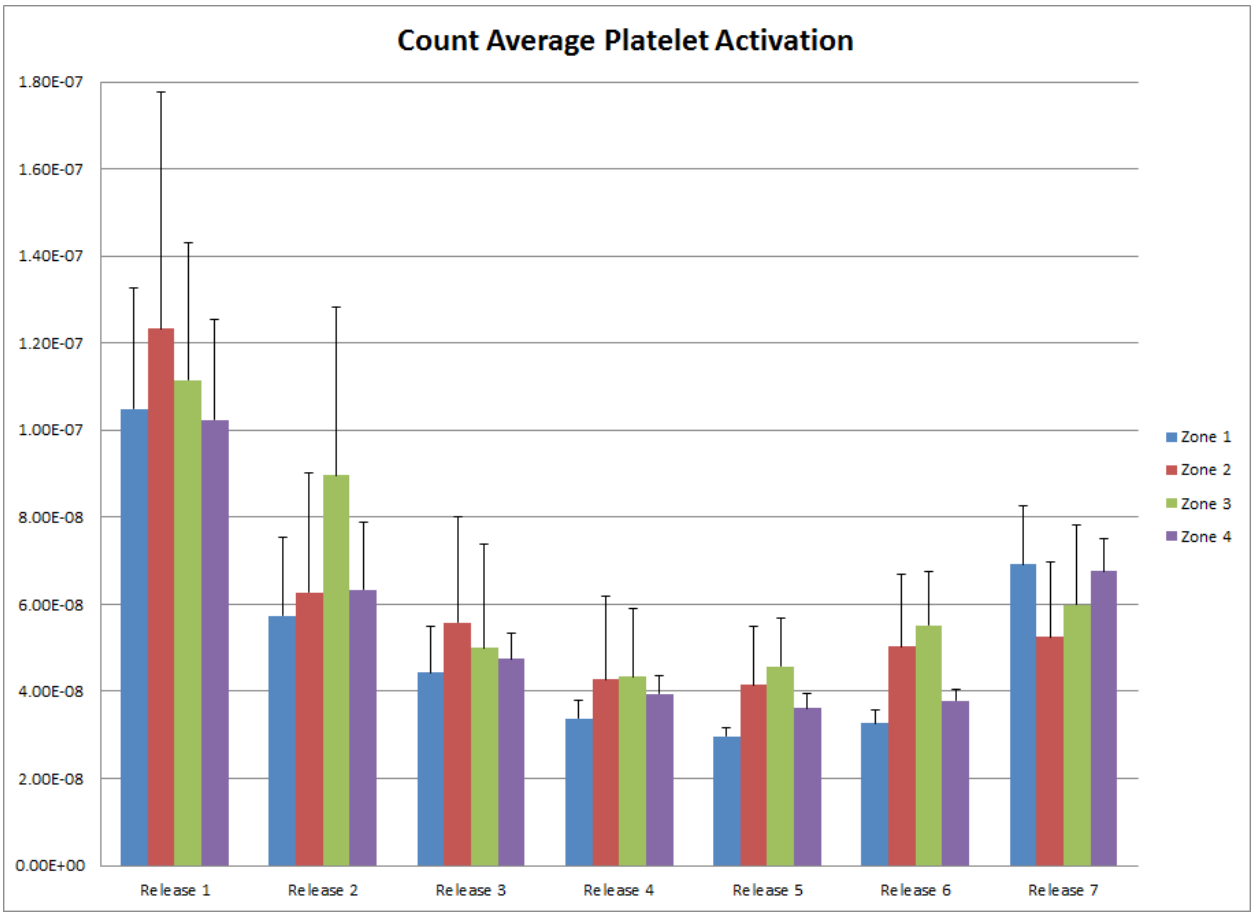

Figure 57: Average platelet activation TEP for counter-rotating VG leaflets during forward flow

Similarly to the average principal shear stress, platelet lysis TEP levels increase with each release event until Release 6 where platelet lysis decreases when compared to

Release 5 and continues decreasing through Release 7. As the flow is accelerating during systole, the principle shear stresses experienced by the particles also increased. Since platelet lysis TEP is strongly correlated to principal shear stress leaves in the TEP models, platelet lysis TEP levels increased with increasing principle shear stresses. Beginning at Release 3, zones 2 and 3 show higher levels of platelet lysis TEP compared to zones 1 and 4. These zones experienced the highest average principal shear stress levels and are located in the highly turbulent central orifice jet.

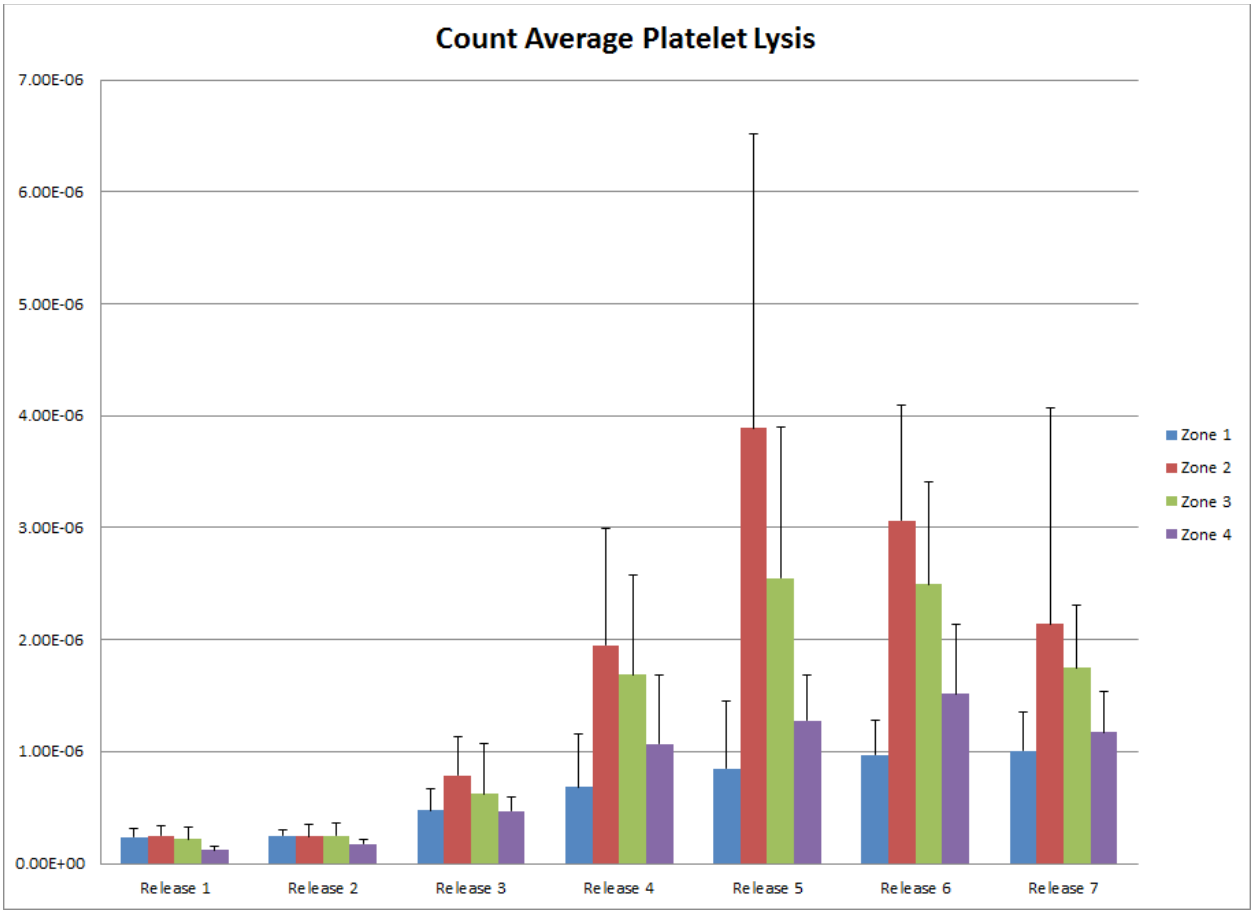

Figure 58: Average platelet lysis TEP for counter-rotating VG leaflets during forward flow

Again, since the experiments are limited by the size of the measurement area, TEP for each particle is only calculated as long as they stay inside the measurement zone. By first normalizing both the platelet activation and platelet lysis TEP levels that each particle experienced by the corresponding exposure time raised to the power of their corresponding coefficients, a, from equations (7) and (8) before averaging the levels in each zone and release, the effect of shear stress on TEP can be seen per exposure time unit experienced by each particle. When the activation TEP is normalized by the exposure time, platelet activation TEP levels per unit exposure time became very similar through the release events and zones with a slight increase in TEP levels through the first six releases (corresponding to the increase in exposure times of each release) and zones 2 and 3 showing slightly higher levels than zones 1 and 4 in releases 3 to 7 (corresponding to the higher principle shear stresses experienced by the particles in the turbulent central orifice jet). Figure 59 shows the platelet activation TEP normalized by exposure time.

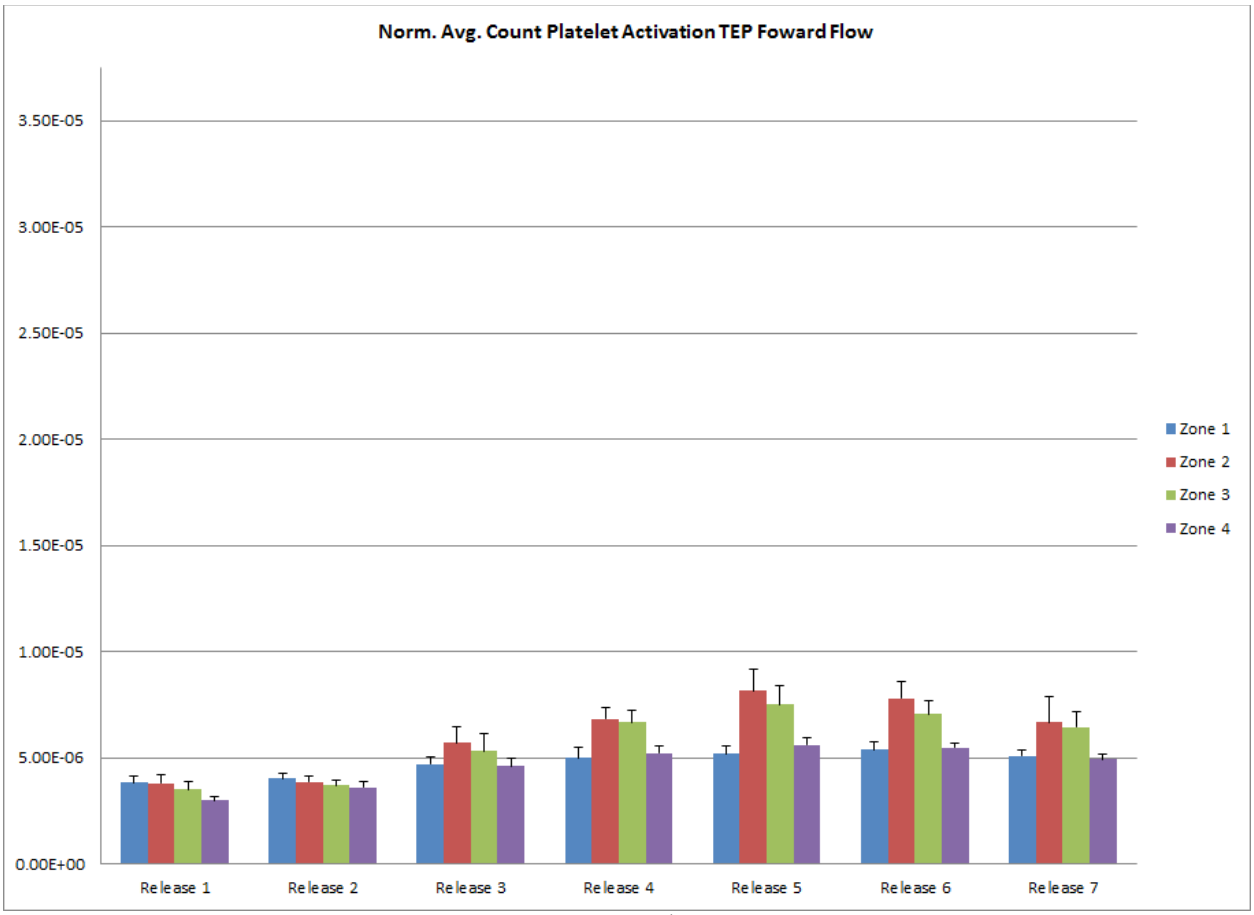

Figure 59: Average platelet activation TEP (s^{-1}) normalized by average exposure time for counter-rotating VG leaflets during forward flow.

When the platelet lysis TEP is normalized by the exposure time, no significant change is seen in the overall trend, meaning that exposure time has little effect on platelet lysis TEP and is heavily dependent on the shear stress loading histories. Figure 60 shows the platelet lysis TEP normalized by exposure time.

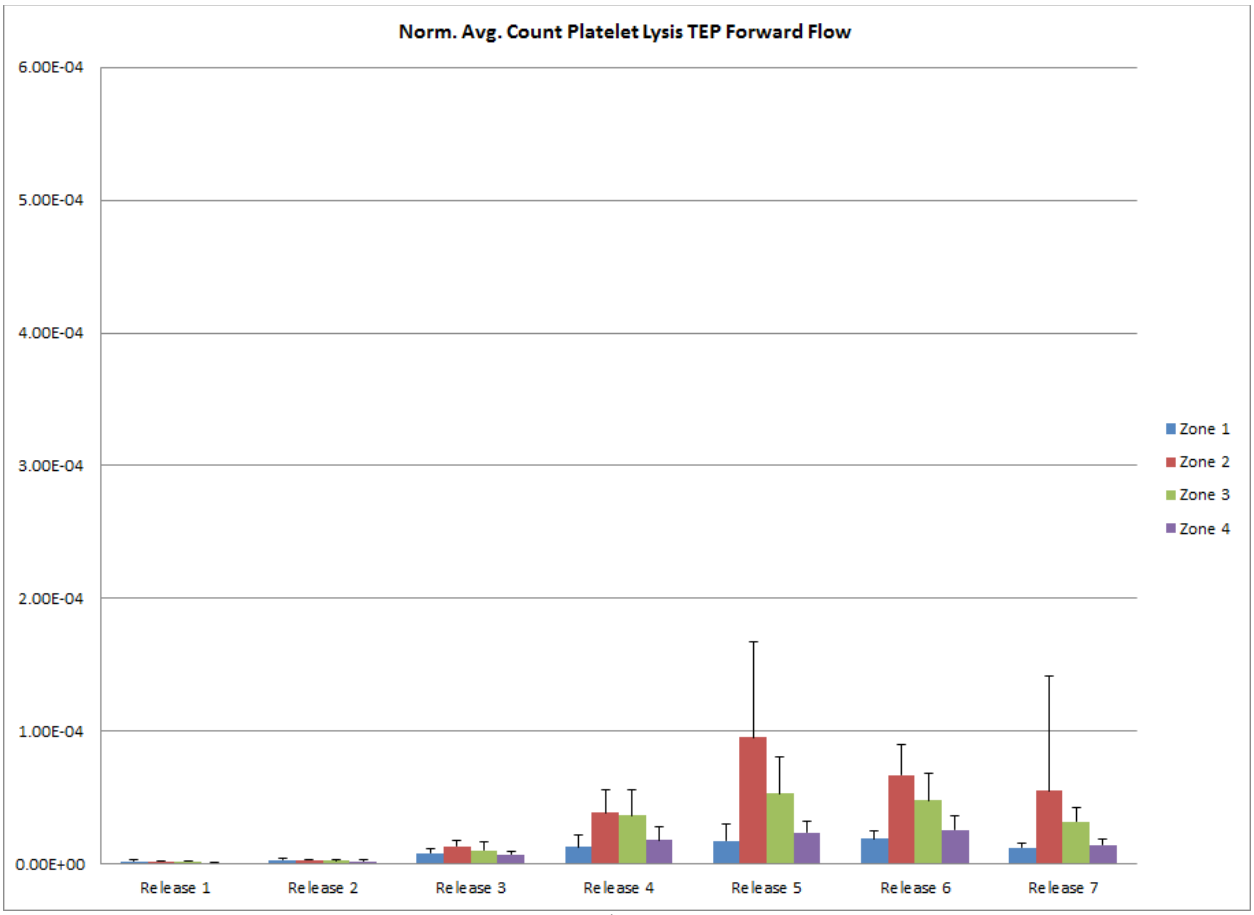

Figure 60: Average platelet lysis TEP (s^{-1}) normalized by average exposure time for counter-rotating VG leaflets during forward flow.

In summary, for both VG configurations (co-rotating and counter-rotating) in systolic flow downstream of the valve, particles experienced higher platelet activation TEP levels in the beginning of systole. For the co-rotating VG configuration, as the flow accelerated, platelet activation TEP levels decreased as they were exposed to the shear stress levels in the flow for shorter exposure times. However, for the counter-rotating VG configuration, as the flow accelerated and the particles were exposed to the shear stress levels in the flow for shorter exposure times, platelet activation TEP levels for the two zones (2 and 3) in the central orifice jet increased compared to the two outside zones (1 and 4). For both VG configurations, as the flow accelerated, platelet lysis TEP

levels increased through the release events as principle shear stresses increased. When both platelet activation and lysis TEP were normalized by their respective exposure time values, platelet activation TEP per unit exposure time increased through the release events as the flow accelerated and platelet lysis TEP per unit exposure time also increased through the release events as the flow accelerated.

7.2 Regurgitant Flow with VG TEP

7.2.1 Co-Rotating VG

Figure 61 presents an image sequence of vorticity fields during valve closure and the diastolic phase. Immediately prior to leaflet closure, a closing vortex forms from the closing tips of the leaflets. This vortex is pinched off once the leaflet closes followed by the b-datum regurgitant jet which points down towards the bottom wall of the test chamber.

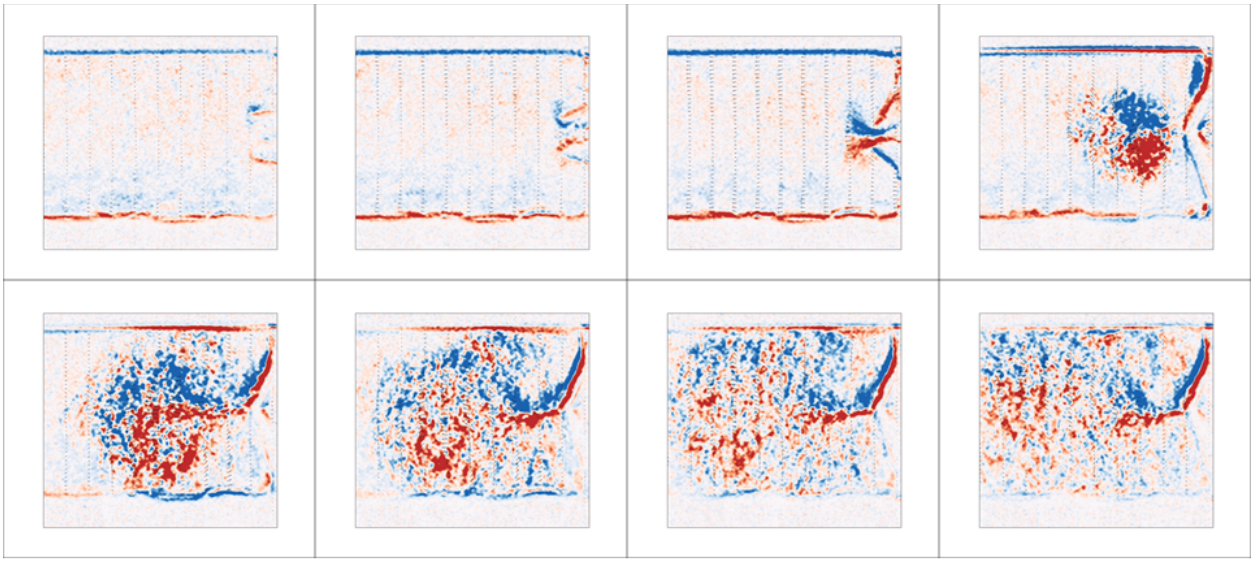

Figure 61: Image sequence of co-rotating VG leaflet closure showing closing vortex.

Animations A9 and A10 depict lagrangian particle trajectories for 100 particles released on the line rake for each of the 10 independent repeated measurements simultaneously

for platelet activation TEP and platelet lysis TEP respectively. The color of the particles represents the amount of platelet activation TEP and platelet lysis TEP accumulated by the particle. One hundred more particles per zone were released every 0.1s through ventricular diastole for a total of 7 release events. The middle group (Zone 2) consisted of 34 particles centered on the b-datum jet centerline while the top and bottom group (Zones 1 and 3) each consisted of 33 particles above and below the middle 34 particles. As shown in the animation, trajectory calculations terminated once the particles left the measurement window. These trajectories represent blood element advection immediately upstream of the valve at the instant when the valve begins to close, an area where the closing vortex and the b-datum jet occur. Lagrangian tracking showed that particles originating outside of the b-datum regurgitant jet (zones 1 and 3) experienced high exposure times and low principal shear stress levels in the zones of recirculation upstream of the closed leaflets outside of the regurgitant jet zone. As some particles recirculate in the zones upstream of the valve leaflets, they become entrapped in the regurgitant jet later during diastole. Lagrangian tracking showed that particles with originated near the b-datum jet (zone 2) experienced less exposure time in the zones of high shear stress near and inside the regurgitant jet zone.

Figure 62 and 63 shows the average exposure time and principal shear stress experienced by each particle at different release events by initial position zone. Overall, exposure time decreases in the first six releases then decreases significantly at Release 7. The first releases occur during the beginning and middle of ventricular diastole and the b-datum gap is creating a high-velocity regurgitant jet and two areas of recirculation

above and below it. However, after Release 2, exposure time increases at Release 3. Release 1 occurs when the closing vortex is formed which causes the particles to recirculate back near the closed leaflets. Release 2 occurs when the regurgitant jet has formed and is at its strongest which causes the particles to be quickly ejected from the measurement area. Releases 6 and 7 occur at the end of ventricular diastole where the ventricular pressure is increasing above the aortic pressure and the b-datum regurgitant jet flow velocity is decreasing. Also, the experiment time window limits the length of the exposure time recording in Release 7. For most of the release events, zone 2 experiences shorter exposure times compared to zones 1 and 3. Zones 1 and 3 experience higher exposure times when compared to zone 2 in the first five releases since they correspond to the area of recirculation above and below the regurgitant jet.

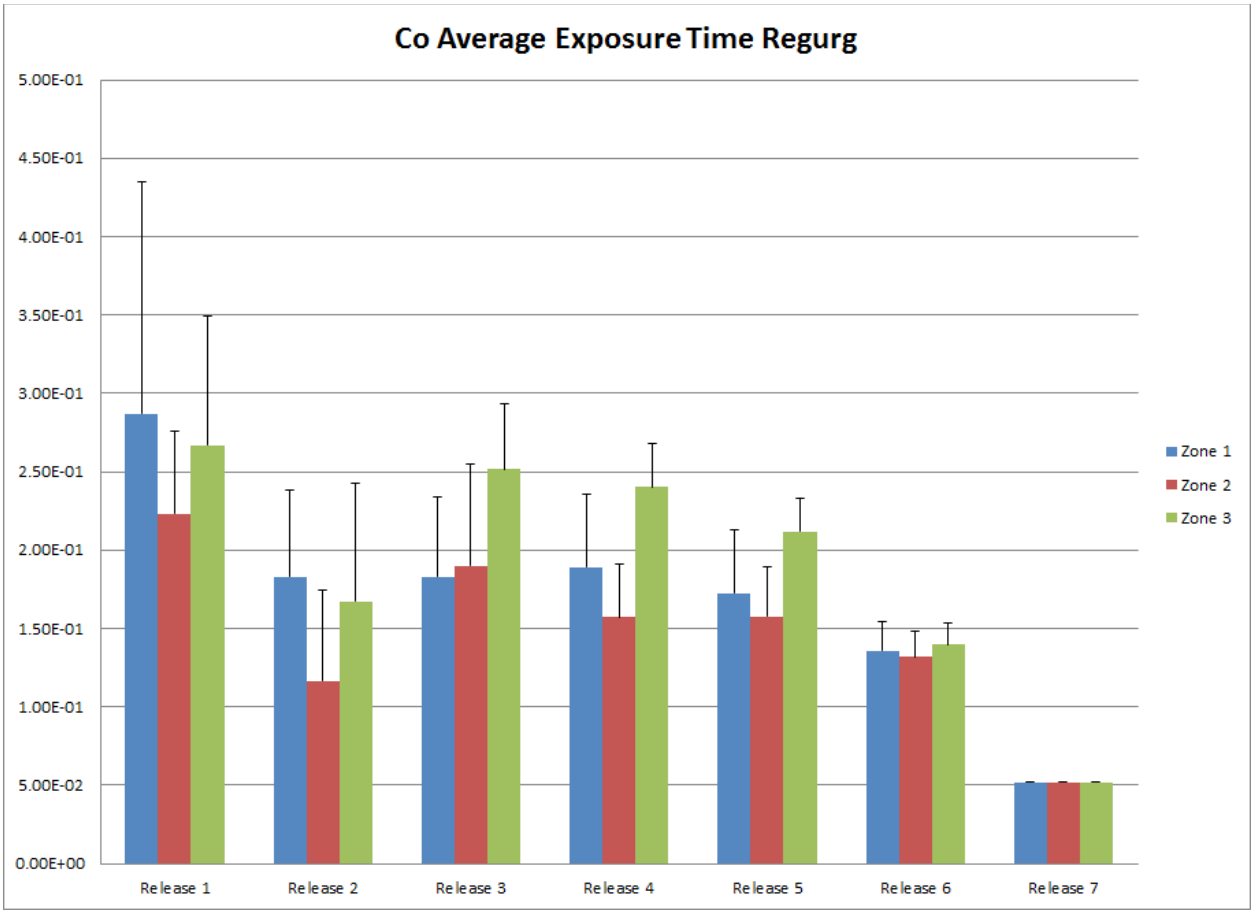

Figure 62: Average exposure time (s) for co-rotating VG leaflets in regurgitant flow

Overall, principal shear stress decreases slightly with each release event except at Release 1 where shear stress increases between Release 1 and 2. Again, Release 1 occurs when the closing vortex is formed which causes the particles to recirculate back near the closed leaflets and experience low shear stresses. Release 2 occurs when the regurgitant jet has formed and is at its strongest which creates high principle shear stresses. The slight decrease through Releases 2 and 7 is expected since the b-datum regurgitant jet flow velocity is slightly decreasing through ventricular diastole due to aortic pressure decreasing through ventricular diastole. Principal shear stress is dependent on the velocity of the fluid, therefore as velocity decreases, principal shear

stress also decreases. For all release events, zone 2 experiences higher principal shear stress levels compared to zones 1 and 3 as it corresponds to the area of the high-velocity regurgitant jet.

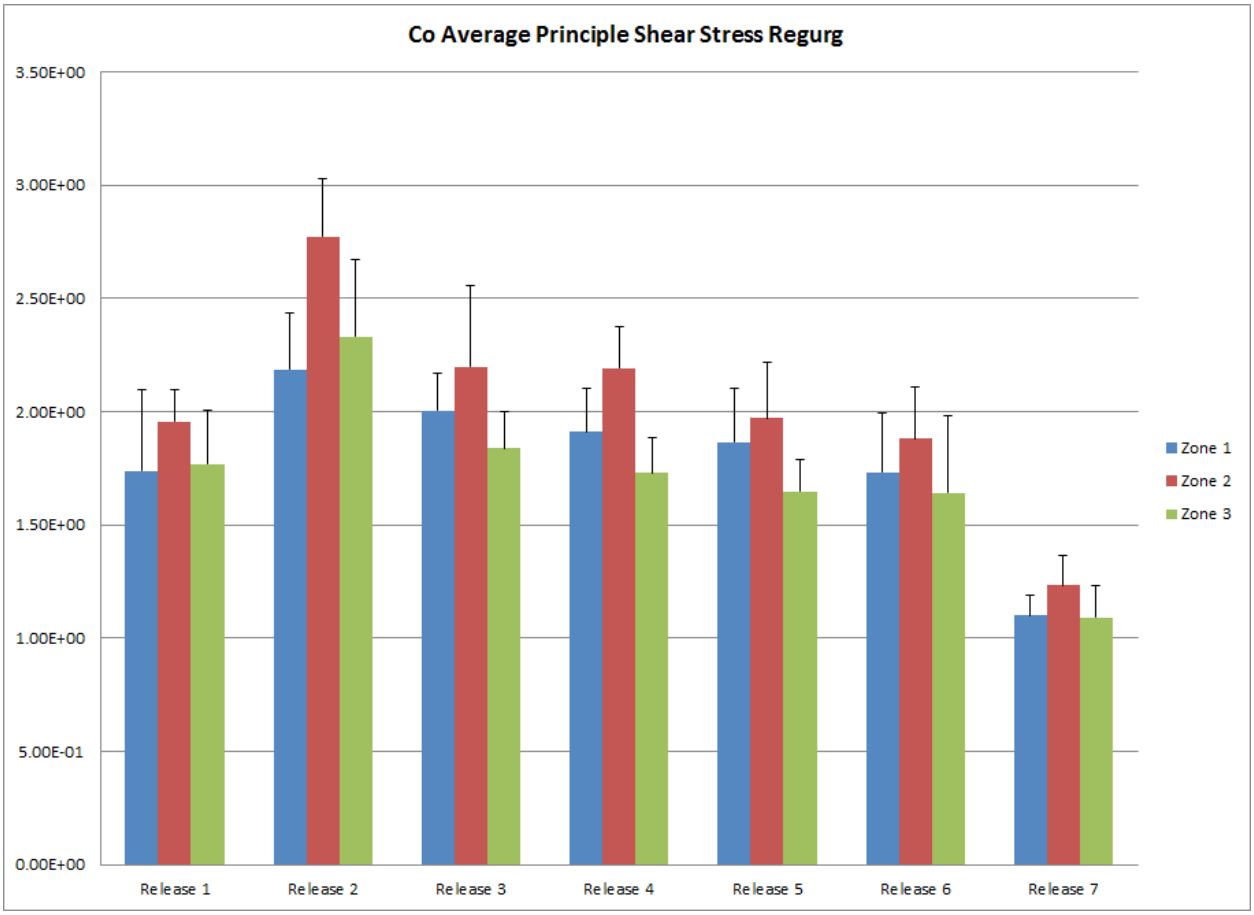

Figure 63: Average principal shear stress (Pa) for co-rotating VG leaflets in regurgitant flow

Figure 64 and 65 shows the average platelet activation TEP and platelet lysis TEP experienced by each particle at different release events by initial position zone. Similarly to the average exposure time, platelet activation TEP decreases in the first five releases then decreases significantly at Release 6 and 7, except for at Release 2 which decreases after Release 1 but then increases at Release 3. During releases 1-5, zone 2

shows lower platelet activation TEP compared to zones 1 and 3. Since platelet activation TEP is strongly correlated to exposure times in the TEP models, platelet activation TEP values will increase or decrease depending on exposure times of the particles. Zone 2 experiences the lowest levels of platelet activation TEP as it corresponds to particles that were release in or near the regurgitant jet. These particles were quickly ejected (lower exposure times) from the measurement area by the high-velocity jet.

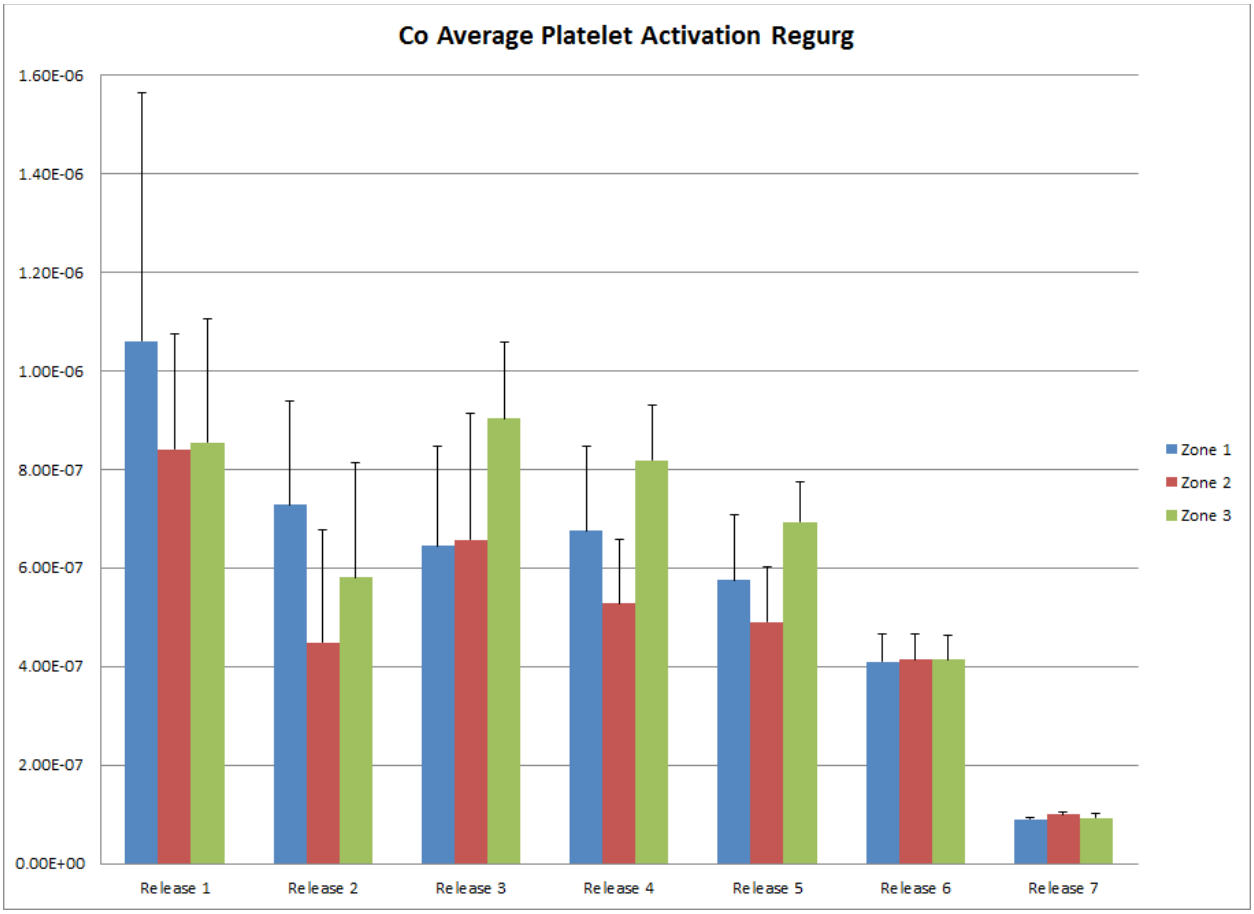

Figure 64: Average platelet activation TEP for co-rotating VG leaflets in regurgitant flow

Similarly to the average principal shear stress, platelet lysis decreases slightly with each release event except at Release 1 and 2 where platelet lysis increases before

decreasing at Release 3 and through Release 7. Since platelet lysis TEP is strongly correlated to principal shear stress in the TEP models, platelet lysis TEP values increase or decrease depending on the principle shear stresses experienced by the particles. During all releases, zone 2 shows higher platelet lysis TEP compared to zones 1 and just slightly higher than zone 3. Zone 2 corresponds to particles that were released in or near the r b-datum gap and experienced higher levels of principal shear stress due to the high-velocity regurgitant jet. Zone 3 also experiences high platelet lysis TEP values as the regurgitant jet does not point evenly in the mountain chamber but “points down” into the area where particles assigned to zone 3 are.

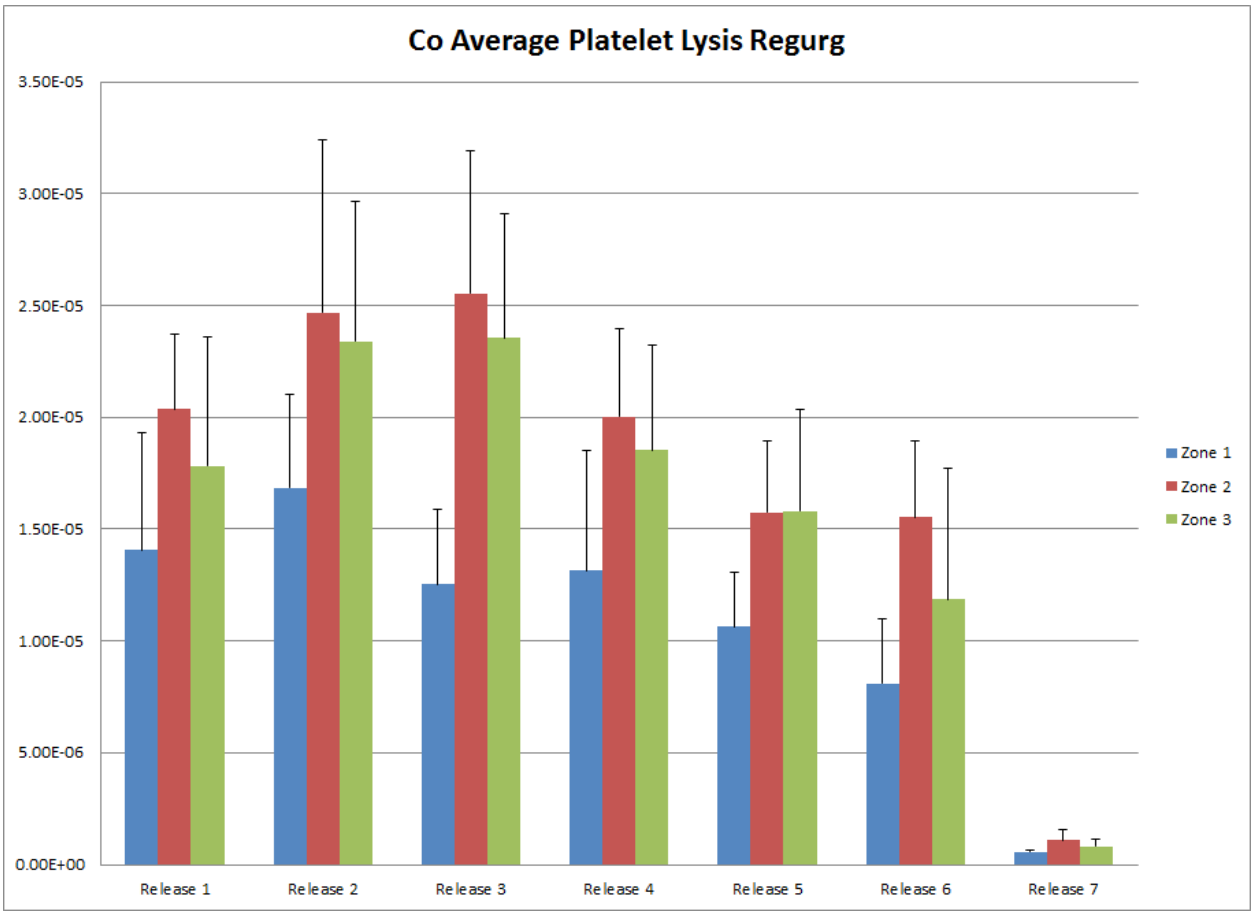

Figure 65: Average platelet lysis TEP for co-rotating VG leaflets in regurgitant flow

Again, since the experiments are limited by the size of the measurement area, TEP for each particle is only calculated as long as they stay inside the measurement zone. By first normalizing both the platelet activation and platelet lysis TEP levels that each particle experienced by the corresponding exposure time raised to the power of their corresponding coefficients, a, from equations (7) and (8) before averaging the levels in each zone and release, the effect of shear stress on TEP can be seen per exposure time unit experienced by each particle. When the platelet activation TEP is normalized by the exposure time, platelet activation TEP levels became fairly similar through the first 5 release events and zones and then significantly increased in the last 2 release events. Figure 66 shows the platelet activation TEP normalized by exposure time.

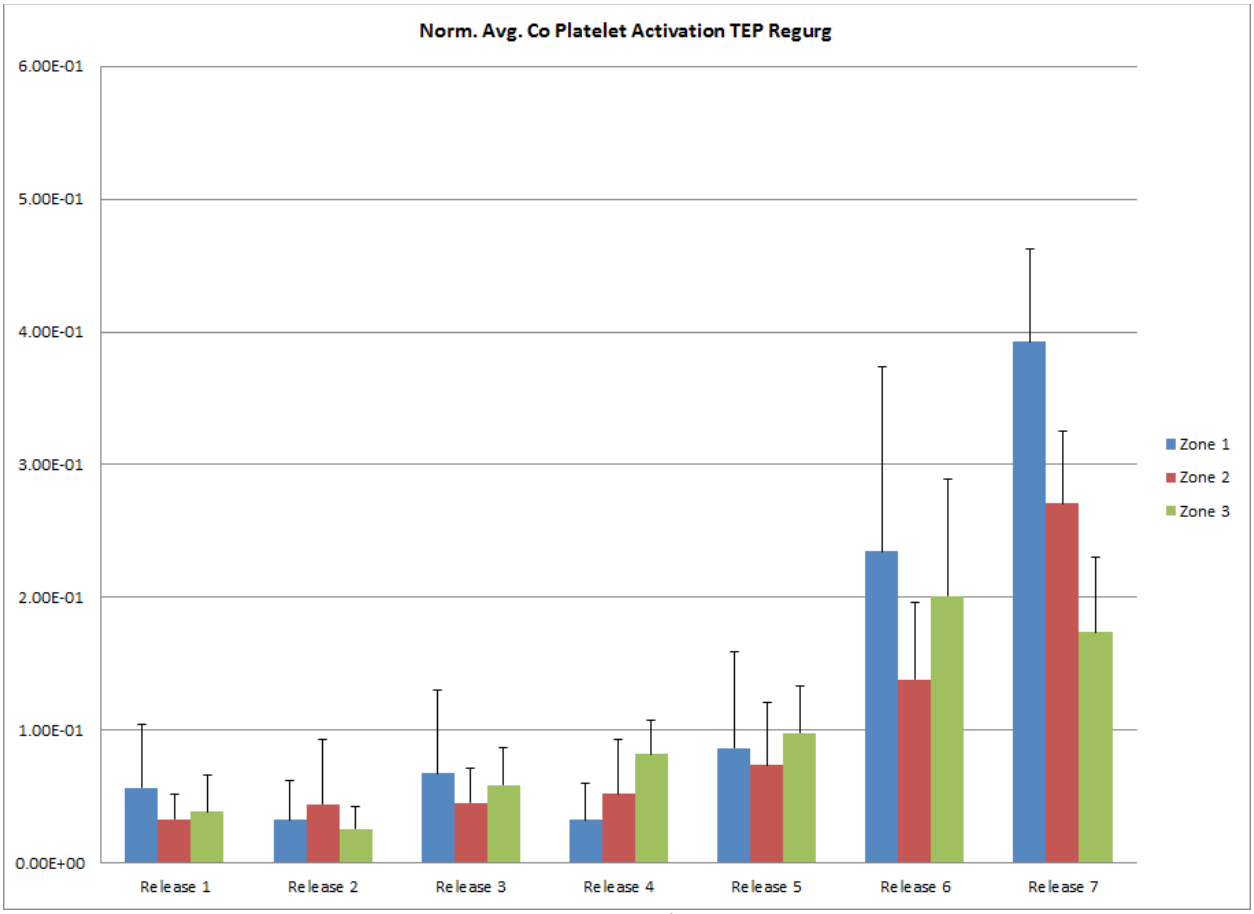

Figure 66: Average platelet activation TEP (s^{-1}) normalized by average exposure time for co-rotating VG leaflets in regurgitant flow.

When the average platelet lysis TEP is normalized by the average exposure time, the highest levels are seen in the zone corresponding to the b-datum regurgitant jet (Zone 2) and the zone above the regurgitant jet (Zone 1). Overall between releases, the TEP levels became very similar. Figure 67 shows the platelet lysis TEP normalized by exposure time.

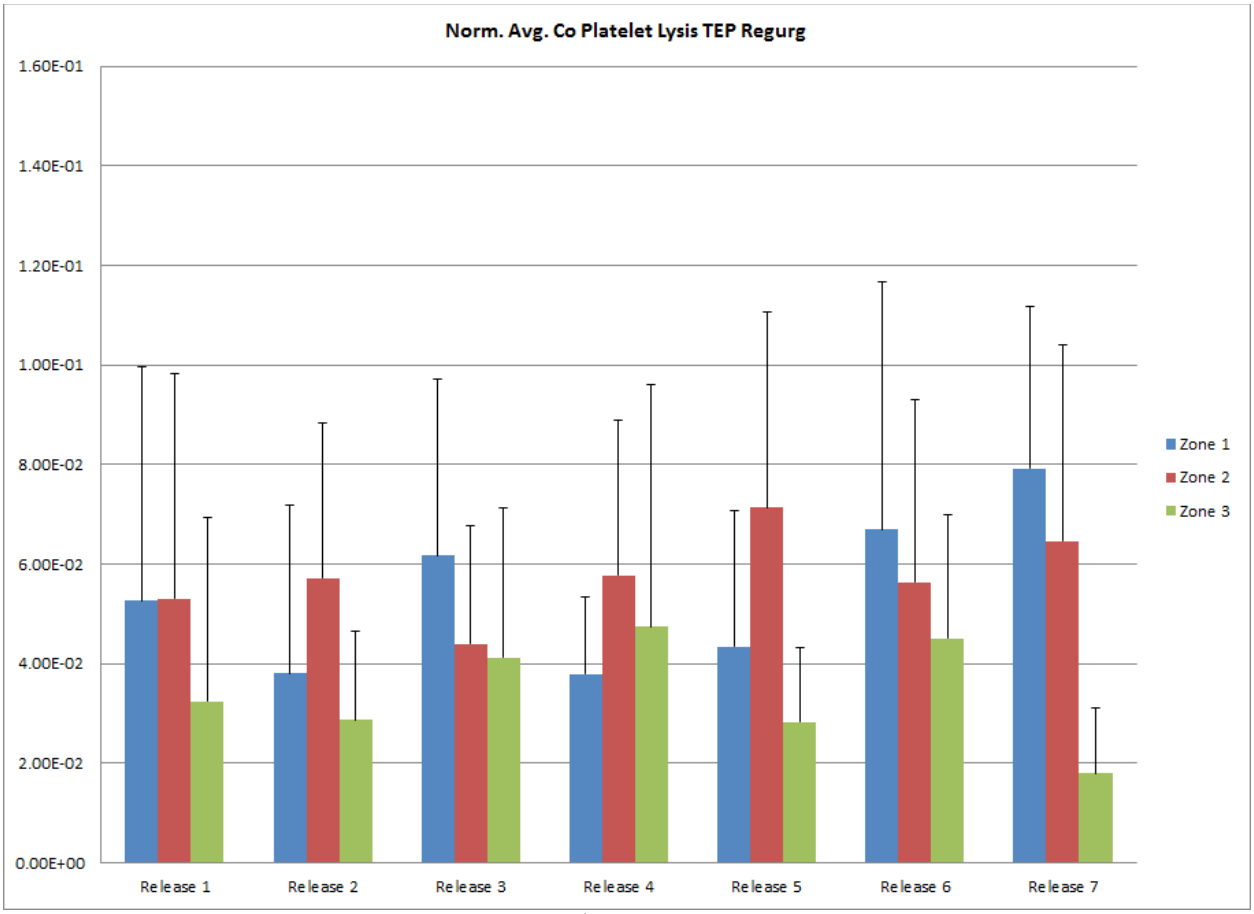

Figure 67: Average platelet lysis TEP (s^{-1}) normalized by average exposure time for co-rotating VG leaflets in regurgitant flow.

7.2.2 Counter-Rotating VG

Figure 68 presents an image sequence of vorticity fields during valve closure and the diastolic phase. Immediately prior to leaflet closure, a closing vortex forms from the

closing tips of the leaflets. This vortex is pinched off once the leaflet closes followed by the b-datum regurgitant jet which points up towards the top wall of the test chamber.

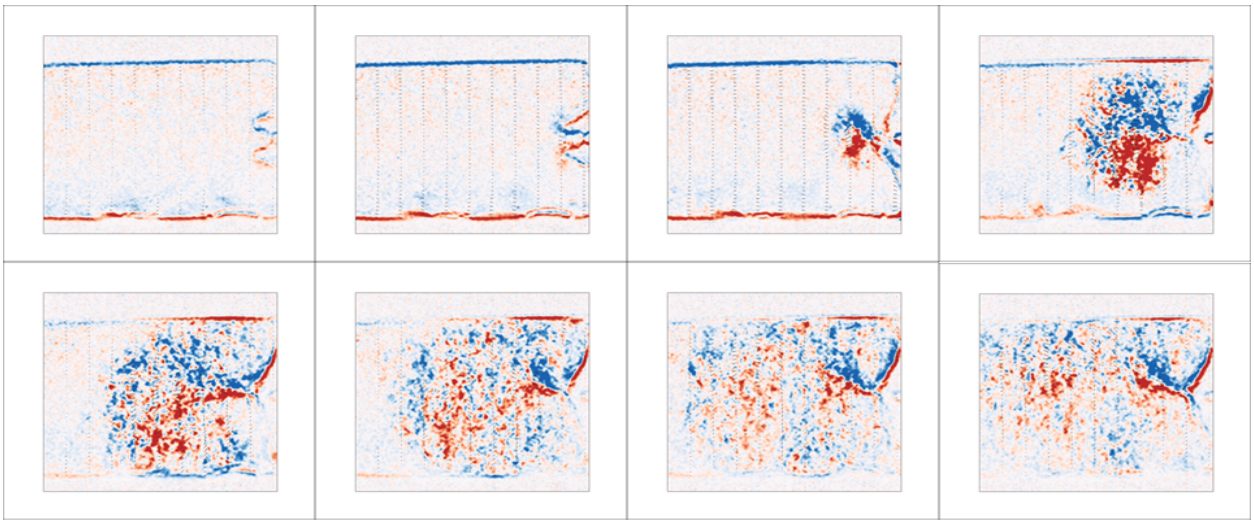

Figure 68: Image sequence of counter-rotating VG leaflet closure showing closing vortex.

Animations A11 and A12 depict lagrangian particle trajectories for 100 particles released on the line rake for each of the 10 independent repeated measurements simultaneously for platelet activation TEP and platelet lysis TEP respectively. The color of the particles represents the amount of platelet activation TEP and platelet lysis TEP accumulated by the particle. One hundred more particles per zone were released every 0.1s through ventricular diastole for a total of 7 release events. The middle group (Zone 2) consisted of 34 particles centered on the b-datum jet centerline while the top and bottom group (Zones 1 and 3) each consisted of 33 particles above and below the middle 34 particles. As shown in the animation, trajectory calculations terminated once the particles left the measurement window. These trajectories represent blood element advection immediately upstream of the valve at the instant when the valve begins to close, an area where the closing vortex and the b-datum jet occur. Lagrangian tracking showed

that particles originating outside of the b-datum regurgitant jet (zones 1 and 3) experienced high exposure times and low principal shear stress levels in the zones of recirculation upstream of the closed leaflets outside of the regurgitant jet zone. as some particles recirculate in the zones upstream of the valve leaflets, they become entrapped in the regurgitant jet later during diastole. Lagrangian tracking showed that particles with originated near the b-datum jet (zone 2) experienced less exposure time in the zones of high shear stress near and inside the regurgitant jet zone.

Figure 69 and 70 shows the average exposure time and principal shear stress experienced by each particle at different release events by initial position zone. Overall, exposure time decreases with each release event, except for at zone 2 at Release 2 which decreases after Release 1 but then increases at Release 3. Release 2 occurs then the regurgitant jet has formed and is at its strongest which causes the particles to be quickly ejected from the measurement area. For all release events, zone 2 experiences shorter exposure times compared to zones 1 and 3 since it corresponds to particles near the regurgitant gap which experience the high-velocity regurgitant jet and are quickly ejected form the measurement area. Zones 1 and 3 experience higher exposure times when compared to zone 3 since they correspond to the area of recirculation above and below the regurgitant jet. Also, the experiment time window limits the length of the exposure time recording in Release 7.

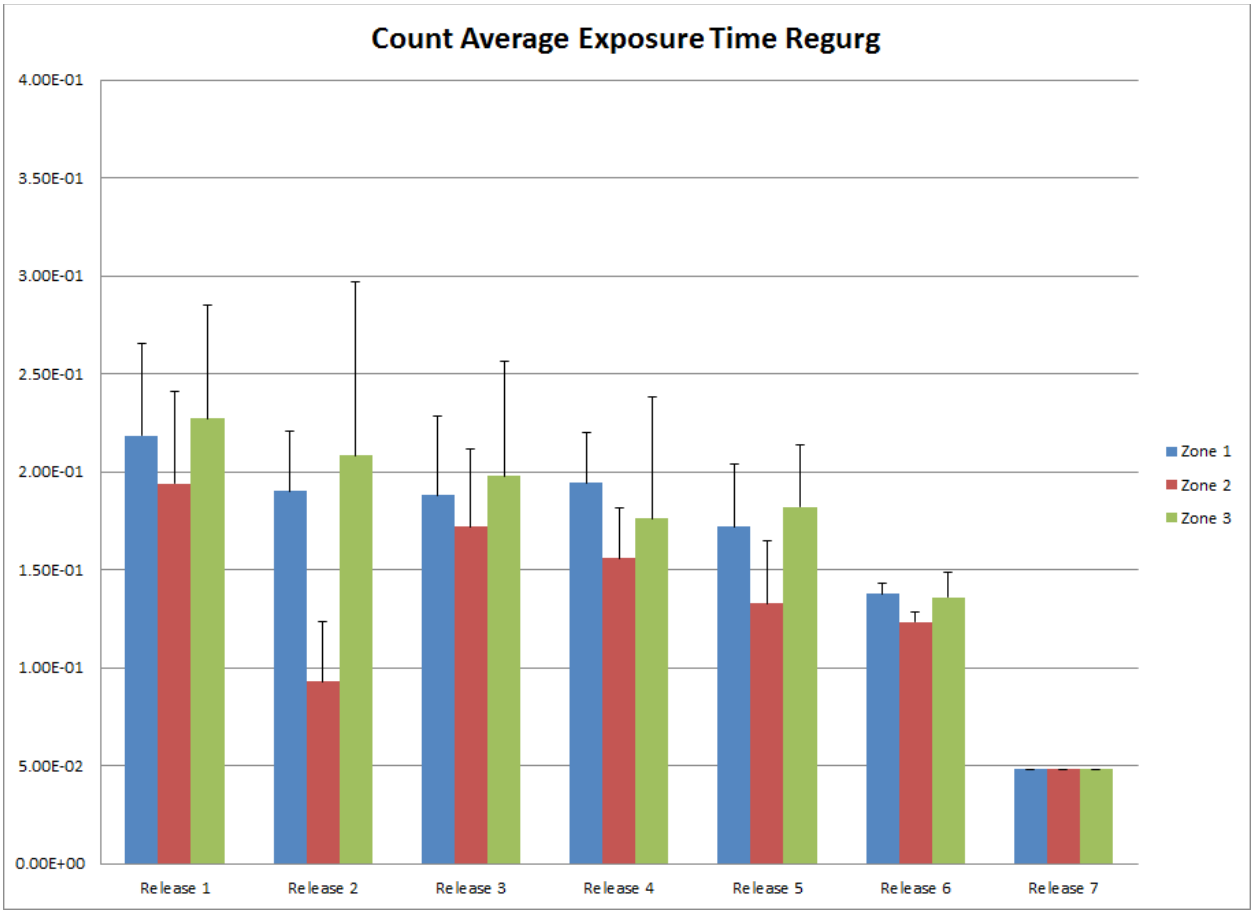

Figure 69: Average exposure time (s) for counter-rotating VG leaflets in regurgitant flow

Overall, principal shear stress decreases slightly with each release event except at Release 1 where shear stress increases between Release 1 and 2. Again, Release 1 occurs when the closing vortex is formed which causes the particles to recirculate back near the closed leaflets and experience low shear stresses. Release 2 occurs when the regurgitant jet has formed and is at its strongest which creates high principle shear stresses. The slight decrease through Releases 2 and 7 is expected since the b-datum regurgitant jet flow velocity is slightly decreasing through ventricular diastole due to aortic pressure decreasing through ventricular diastole. Principal shear stress is dependent on the velocity of the fluid, therefore as velocity decreases, principal shear

stress also decreases. For the first six release events, zone 2 experiences high principal shear stress levels compared to zones 1 and 3 as it corresponds to the area of the high-velocity regurgitant jet.

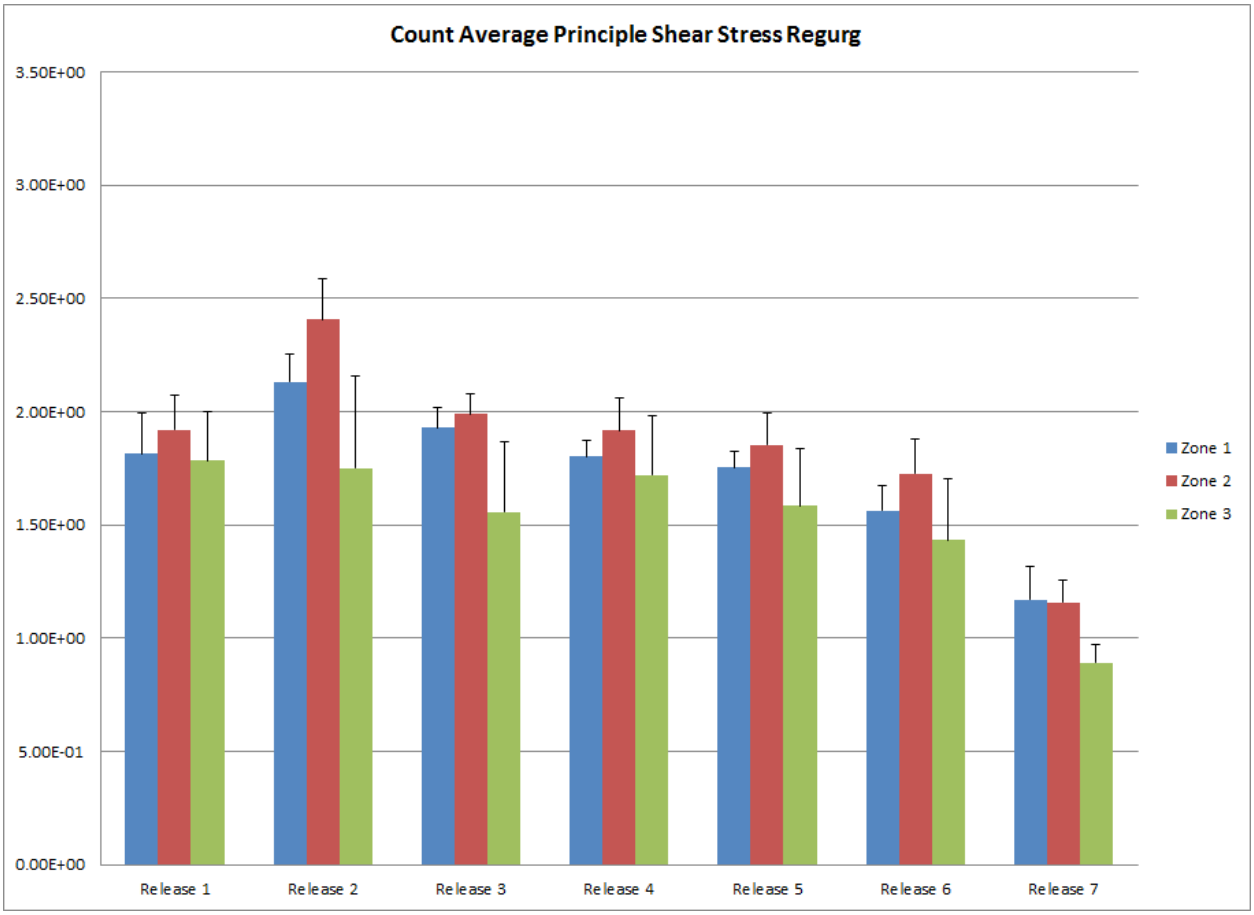

Figure 70: Average principal shear stress (Pa) for counter-rotating VG leaflets in regurgitant flow

Figure 71 and 72 shows the average platelet activation TEP and platelet lysis TEP experienced by each particle at different release events by initial position zone. Similarly to the average exposure time, platelet activation TEP decreases with each release event, except for at zone 2 in Release 2 which decreases after Release 1 but then increases at Release 3. During releases 2-5 and 7, zone 2 shows lower platelet

activation TEP compared to zones 1 and 3. Since platelet activation TEP is strongly correlated to exposure times in the TEP models, platelet activation TEP values will increase or decrease depending on exposure times of the particles. Zone 2 experiences the lowest levels of platelet activation TEP as it corresponds to the particles that were released in or near the regurgitant jet. These particles were quickly ejected (lower exposure times) from the measurement area by the high-velocity jet.

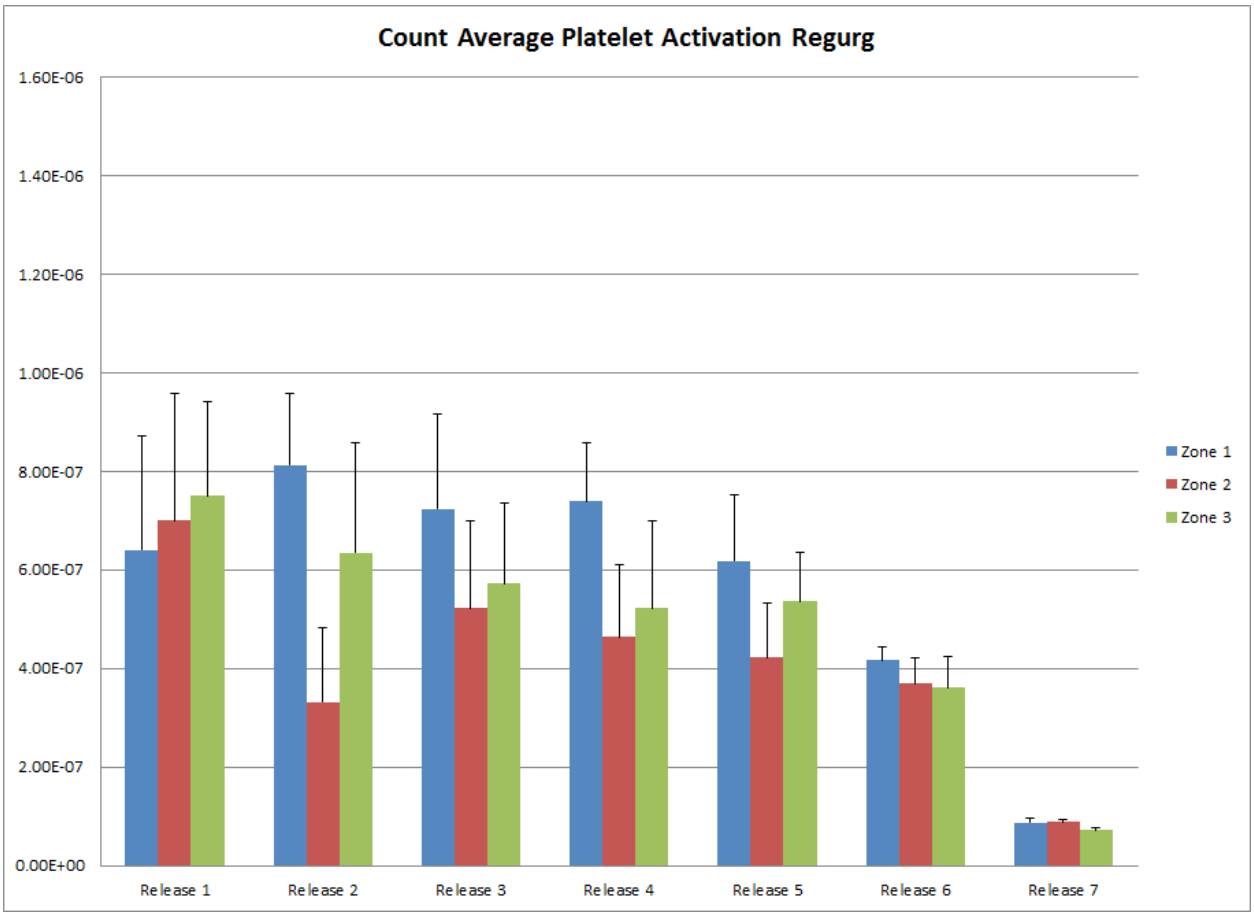

Figure 71: Average platelet activation TEP for counter-rotating VG leaflets in regurgitant flow

Similarly to the average principal shear stress, platelet lysis TEP decreases slightly with each release event except at Release 1 and 2 where platelet lysis increases before

decreasing at Release 3 and through Release 7. During most of the releases, zone 2 shows the highest platelet lysis TEP levels. This zone corresponds to the particles that were released in or near the b-datum gap and experienced higher levels of principal shear stress due to the high-velocity regurgitant jet.

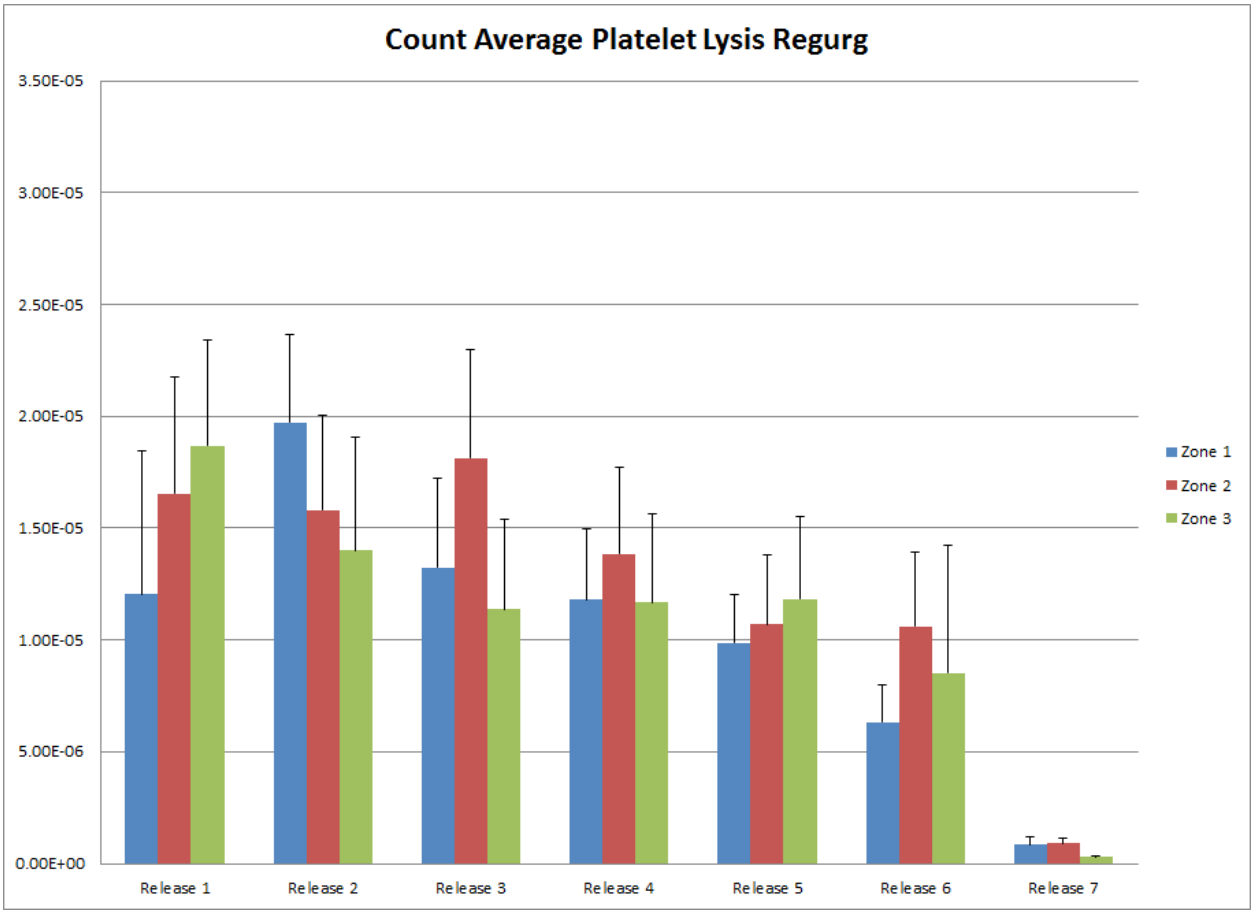

Figure 72: Average platelet lysis TEP for counter-rotating VG leaflets in regurgitant flow

Again, since the experiments are limited by the size of the measurement area, TEP for each particle is only calculated as long as they stay inside the measurement zone. By first normalizing both the platelet activation and platelet lysis TEP levels that each particle experienced by the corresponding exposure time raised to the power of their corresponding coefficients, a, from equations (7) and (8) before averaging the levels in

each zone and release, the effect of shear stress on TEP can be seen per exposure time unit experienced by each particle. When the platelet activation TEP is normalized by the exposure time, platelet activation TEP levels became fairly similar through the first 5 release events and zones and then significantly increased in the last 2 release events. Figure 73 shows the platelet activation TEP normalized by exposure time.

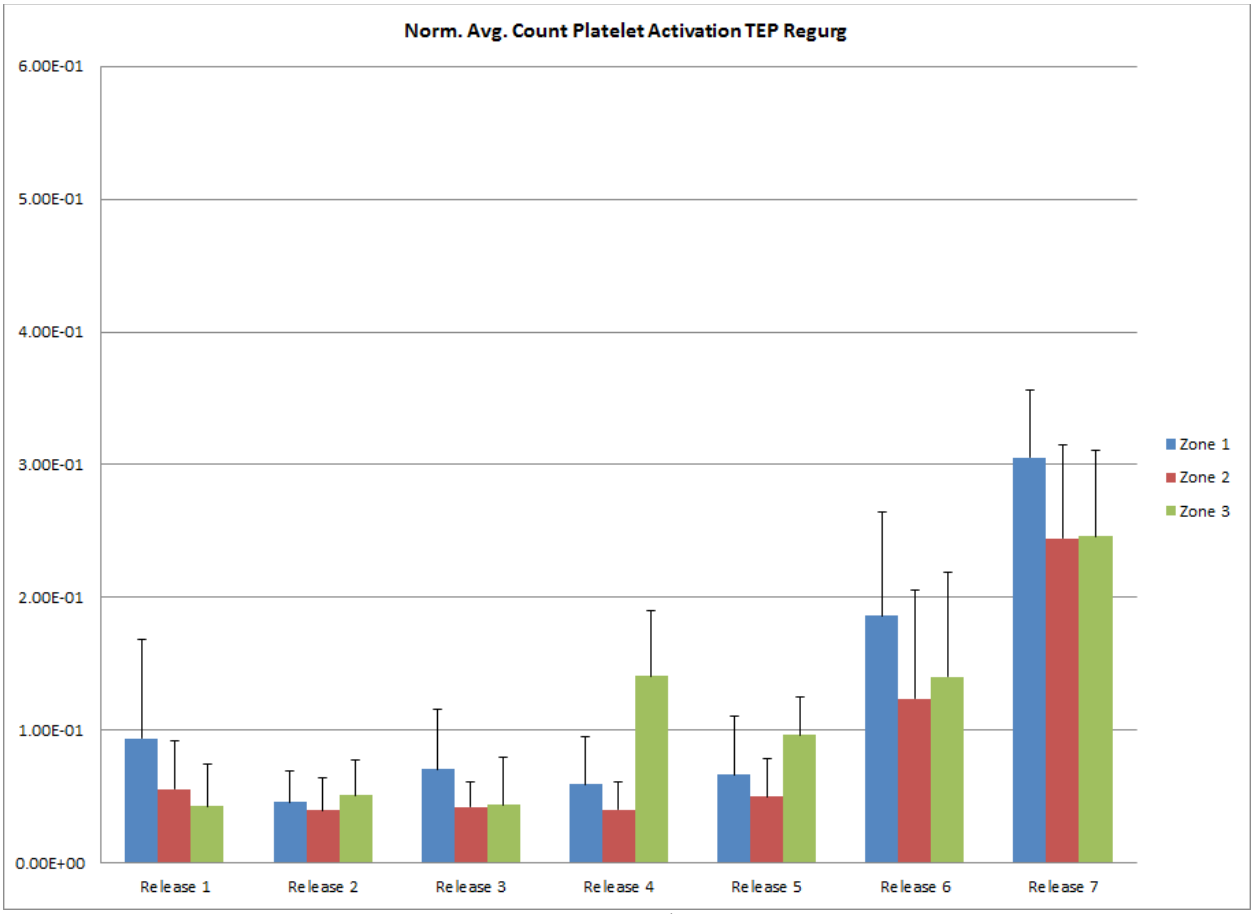

Figure 73: Average platelet activation TEP (s^{-1}) normalized by average exposure time for counter-rotating VG leaflets in regurgitant flow.

When the average platelet lysis TEP is normalized by the average exposure time, the highest levels are seen in the zone corresponding to the b-datum regurgitant jet (Zone 2) and the zone above the regurgitant jet (Zone 1). Overall between releases, the TEP

levels became very similar. Figure 74 shows the platelet lysis TEP normalized by exposure time.

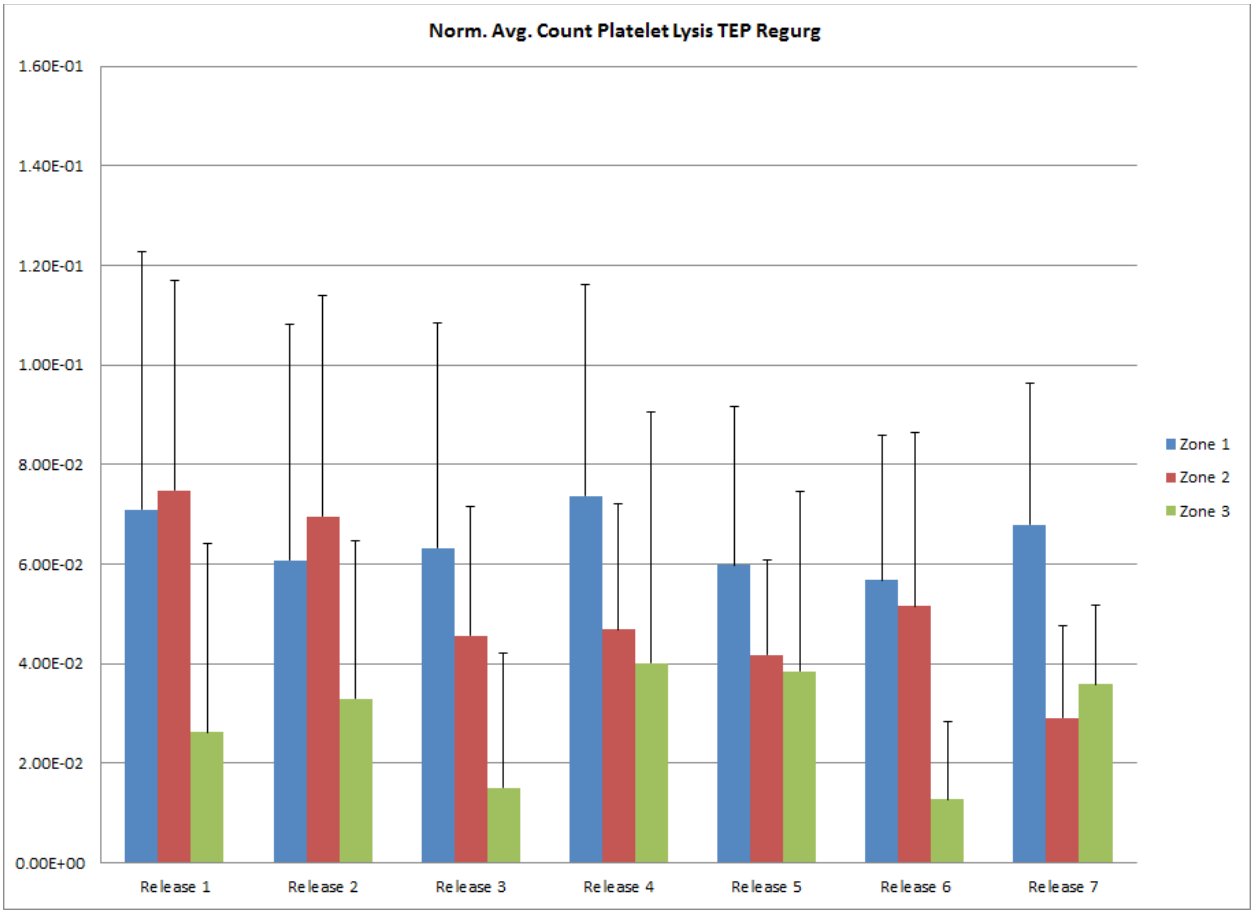

Figure 74: Average platelet lysis TEP (s^{-1}) normalized by average exposure time for counter-rotating VG leaflets in regurgitant flow.

In summary, for both VG configurations (co-rotating and counter-rotating) in diastolic flow upstream of the valve, particles experienced higher platelet activation TEP levels in the beginning of diastole and in the zones corresponding to the recirculation areas above and below the regurgitant jet. As the release events occur, the ventricular pressure is increasing above the aortic pressure and the b-datum regurgitant jet flow velocity is decreasing, thus platelet activation TEP levels decrease slightly through the release events. When platelet activation was normalized by its respective exposure time

values, platelet activation TEP levels became fairly similar through the first 5 release events and zones and then significantly increased in the last 2 release events. Similarly, particles experienced higher platelet lysis TEP levels in the beginning of diastole as the regurgitant jet is stronger (higher velocity and higher principle shear stresses) when the transvalvular pressure is highest near the beginning of diastole. When platelet lysis TEP was normalized by the exposure time, platelet lysis TEP per unit exposure time was highest in the b-datum regurgitant jet zone (Zone 2) and the zone above the regurgitant jet (Zone 1). The complex and asymmetrical structure of the b-datum regurgitant jet caused particles which were released above or below it to become entrained in the jet and experience high platelet lysis TEP levels.

7.3 Control Leaflet vs. Vortex Generator Leaflets

7.3.1 Forward Flow

Vortex generators have been used to mitigate shear stress and control flow separation. Figure 75 shows the average principal shear stress values for each of the four identified zones of high shear stress for all leaflet configurations. In comparison with the control leaflets, in zones 1 and 4 (the two outer zones outside of the central jet), the average principal shear stress decreased with the co-rotating VG configuration but increased with the counter-rotating VG configuration. On the other hand, in zones 2 and 3 (the two inner zones inside the central jet), the average principal shear stress decreased with the counter-rotating VG configuration and the co-rotating VG configuration showed a slight decrease in principal shear stress. Since the VG features are located in the medial surface of the leaflets, the center jet is most affected by the VGs while the lateral jets experience little change. The VGs are dissipating the energy of the center jet into

vortices and turbulent flow, the two outside shear layers experience a higher velocity gradient and therefore higher principle shear stresses.

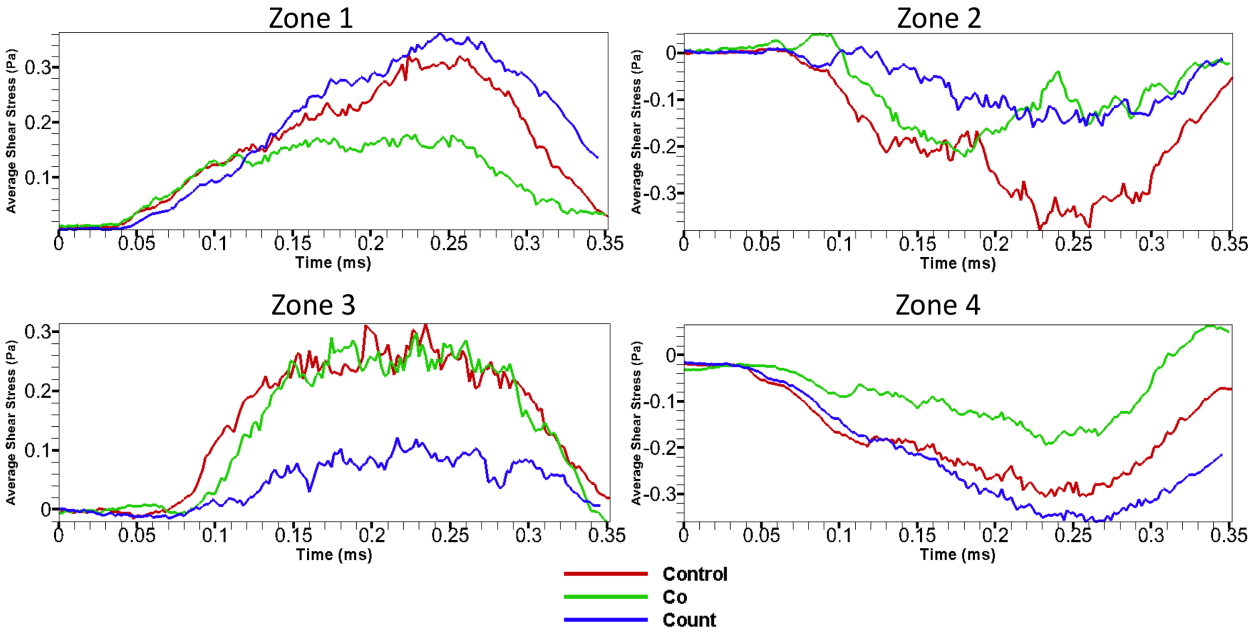

Figure 75: Average principal shear stress values for each zone during systole.

Both VG configurations slightly increased the exposure times experience by the particles released downstream of the open valve during ventricular systole. The particles in or near the central jet (zones 2 and 3) experienced lower exposure times than the particles near the lateral jets (zones 1 and 4). Since the exposure times were increased, it was expected to see that platelet activation TEP levels also slightly increased in the VG leaflet configurations compared to the control leaflet. However, the normalized average platelet activation TEP levels significantly decreased for many zones in the VGs cases, especially in the co-rotating VGs case and near peak systole (later releases). Table 2 and 3 show the statistical difference between the control leaflet vs. co-rotating and counter-rotating VG configurations respectively.

Table 2: Statistical difference between Control Leaflets vs. Co-rotating VGs for platelet activation TEP (p-value =.05) in forward flow. L=Lower, H=Higher.

	Release 1	**Release 2**	**Release 3**	**Release 4**	**Release 5**	**Release 6**	**Release 7**
Zone 1	SIG. H	SIG. H	NOT SIG.	SIG. L	SIG. L	SIG. L	SIG. L
Zone 2	NOT SIG.	NOT SIG.	NOT SIG.	SIG. L	SIG. L	SIG. L	SIG. L
Zone 3	SIG. H	NOT SIG.	NOT SIG.	SIG. L	SIG. L	NOT SIG.	NOT SIG.
Zone 4	SIG. H	NOT SIG.	SIG. L	SIG. L	SIG. L	NOT SIG.	NOT SIG.

Table 3: Statistical difference between Control Leaflets vs. Counter-rotating VGs for platelet activation TEP (p-value =.05) in forward flow. L=Lower, H=Higher.

	Release 1	**Release 2**	**Release 3**	**Release 4**	**Release 5**	**Release 6**	**Release 7**
Zone 1	NOT SIG.	NOT SIG.	SIG. L	SIG. L	SIG. L	SIG. L	SIG. L
Zone 2	NOT SIG.	NOT SIG.	NOT SIG.	NOT SIG.	SIG. H	SIG. L	NOT SIG.
Zone 3	NOT SIG.	SIG. H	NOT SIG.	SIG. L	NOT SIG.	SIG. L	NOT SIG.
Zone 4	NOT SIG.	NOT SIG.	NOT SIG.	NOT SIG.	NOT SIG.	NOT SIG.	SIG. H

Similarly, for both VG configurations, the principal shear stress experienced by the particles decreased from Release 3 to Release 7 compared to the control leaflet. Since the principal shear stress experience by the particles decreased, it was expected to see that platelet lysis TEP levels also decrease in the VG leaflet configurations compared to the control leaflet. The normalized average platelet lysis TEP levels significantly increased for some zones in the early releases and significantly decreases for some zones in later releases in the co-rotating VGs case. For the counter-rotating VGs case, no significant changes were seen in the early releases and levels significantly decreased for some zones in later releases. Table 4 and 5 show the statistical difference between the control leaflet vs. co-rotating and counter-rotating VG configurations respectively.

Table 4: Statistical difference between Control Leaflets vs. Co-rotating VGs for platelet lysis TEP (p-value =.05) in forward flow. L=Lower, H=Higher.

	Release 1	**Release 2**	**Release 3**	**Release 4**	**Release 5**	**Release 6**	**Release 7**
Zone 1	SIG. H	SIG. H	SIG. L	SIG. L	SIG. L	SIG. L	SIG. L
Zone 2	NOT SIG.	NOT SIG.	NOT SIG.	SIG. L	NOT SIG.	NOT SIG.	SIG. L
Zone 3	SIG. H	NOT SIG.	NOT SIG.	SIG. L	NOT SIG.	NOT SIG.	NOT SIG.
Zone 4	SIG. H	SIG. H	NOT SIG.	NOT SIG.	NOT SIG.	NOT SIG.	NOT SIG.

Table 5: Statistical difference between Control Leaflets vs. Counter-rotating VGs for platelet lysis TEP (p-value =.05) in forward flow. L=Lower, H=Higher.

	Release 1	**Release 2**	**Release 3**	**Release 4**	**Release 5**	**Release 6**	**Release 7**
Zone 1	NOT SIG.	NOT SIG.	SIG. L	SIG. L	SIG. L	SIG. L	SIG. L
Zone 2	NOT SIG.	NOT SIG.	SIG. H	NOT SIG.	SIG. H	NOT SIG.	NOT SIG.
Zone 3	NOT SIG.	NOT SIG.	NOT SIG.	SIG. L	NOT SIG.	NOT SIG.	NOT SIG.
Zone 4	NOT SIG.	NOT SIG.	NOT SIG.	NOT SIG.	NOT SIG.	NOT SIG.	NOT SIG.

In forward flow during ventricular systole, the vortex generators alter the flow of the central jet, creating streamwise vortices which effectively adds spanwise velocity (in the Y direction) to the flow and lowers the streamwise velocity of the flow (in the X direction). This effect lowers the velocity gradient of the flow in the central jet and effectively lowers the shear stress in the flow but increases the exposure time experienced by the particles.

7.3.2 Regurgitant Flow

Both VG configurations lowered the exposure times experienced by the particles released upstream of the closed valve during ventricular diastole both in the b-datum regurgitant jet and in the recirculation zones above and below the b-datum line. With the decrease in exposure time caused by the leaflets with VGs, it would be expected to see platelet activation TEP levels to decrease. The normalized average platelet activation

TEP levels significantly decreased for some releases and zones (mostly near mid and late diastole) in both VGs configurations. Table 6 and 7 show the statistical difference between the control leaflet vs. co-rotating and counter-rotating VG configurations respectively.

Table 6: Statistical difference between Control Leaflets vs. Co-rotating VGs for platelet activation TEP (p-value =.05) in regurgitant flow. L=Lower, H=Higher.

	Release 1	**Release 2**	**Release 3**	**Release 4**	**Release 5**	**Release 6**	**Release 7**
Zone 1	NOT SIG.	NOT SIG.	NOT SIG.	SIG.L	NOT SIG.	NOT SIG.	NOT SIG.
Zone 2	NOT SIG.	NOT SIG.	NOT SIG.	NOT SIG.	NOT SIG.	SIG. L	NOT SIG.
Zone 3	NOT SIG.	SIG. L	NOT SIG.	NOT SIG.	NOT SIG.	SIG. L	SIG. L

Table 7: Statistical difference between Control Leaflets vs. Counter-rotating VGs for platelet activation TEP (p-value =.05) in regurgitant flow. L=Lower, H=Higher.

	Release 1	**Release 2**	**Release 3**	**Release 4**	**Release 5**	**Release 6**	**Release 7**
Zone 1	NOT SIG.	NOT SIG.	NOT SIG.	NOT SIG.	SIG. L	NOT SIG.	NOT SIG.
Zone 2	NOT SIG.	NOT SIG.	NOT SIG.	NOT SIG.	NOT SIG.	SIG. L	NOT SIG.
Zone 3	NOT SIG.	NOT SIG.	NOT SIG.	SIG. H	NOT SIG.	SIG. L	NOT SIG.

For both VG configurations, the principal shear stress levels experienced by the particles increased for most of the release events and zones. However, the normalized platelet lysis TEP levels decreased for some releases and zones (mostly near mid and late diastole) in both VGs configurations. Table 8 and 9 show the statistical difference between the control leaflet vs. co-rotating and counter-rotating VG configurations respectively.

Table 8: Statistical difference between Control Leaflets vs. Co-rotating VGs for platelet lysis TEP (p-value =.05) in regurgitant flow. L=Lower, H=Higher.

	Release 1	**Release 2**	**Release 3**	**Release 4**	**Release 5**	**Release 6**	**Release 7**
Zone 1	NOT SIG.	NOT SIG.	NOT SIG.	SIG. L	NOT SIG.	NOT SIG.	NOT SIG.
Zone 2	NOT SIG.	NOT SIG.	NOT SIG.	NOT SIG.	NOT SIG.	SIG. L	NOT SIG.
Zone 3	NOT SIG.	NOT SIG.	NOT SIG.	NOT SIG.	SIG. L	NOT SIG.	SIG. L

Table 9: Statistical difference between Control Leaflets vs. Counter-rotating VGs for platelet lysis TEP (p-value =.05) in regurgitant flow. L=Lower, H=Higher.

	Release 1	**Release 2**	**Release 3**	**Release 4**	**Release 5**	**Release 6**	**Release 7**
Zone 1	NOT SIG.	NOT SIG.	NOT SIG.	NOT SIG.	NOT SIG.	NOT SIG.	NOT SIG.
Zone 2	NOT SIG.	NOT SIG.	NOT SIG.	SIG. L	SIG. L	NOT SIG.	SIG. L
Zone 3	NOT SIG.	NOT SIG.	SIG. L	NOT SIG.	NOT SIG.	SIG. L	NOT SIG.

CHAPTER 8: EFFECT OF VGs ON HEMODYNAMIC PERFORMANCE – RESULTS AND DISCUSSION

The sections in this chapter will show and discuss the effect of the vortex generators on the hemodynamic performance of the valve. Performance will be quantified using geometric orifice area (GOA) and effective orifice area (EOA); two indexes for valve area that are commonly used by researchers and clinicians to characterize valve performance. Also, PIV and computational fluid dynamics (CFD) visualization and qualitative analysis will be discussed to describe the effect of the VGs on flow.

8.1 Steady Flow EOA

To calculate the steady flow EOA of the BMHV with control leaflets and with each VG configuration, the pressure drop was first measured using manometer readings for each case at 10 separate instances under flow rates ranging from 5 L/min to 30 L/min. Figure 76 shows the average pressure drop in mmHg for each leaflet configuration at six different flow rates.

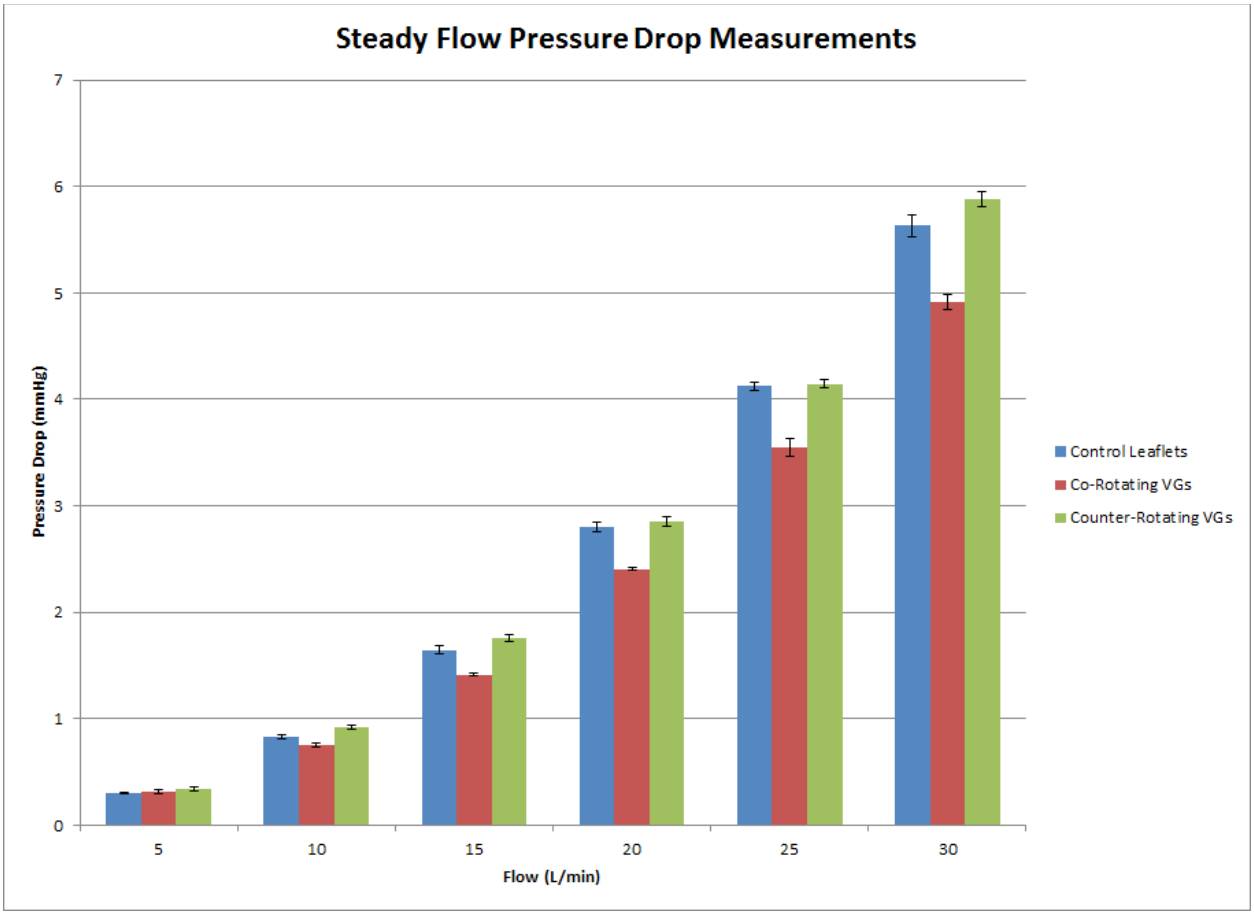

Figure 76: Steady Flow Pressure Drop

For all cases, as flow rate increases, the pressure crop caused by the valve also increases exponentially. This is expected as pressure drop is proportional to V2 (velocity) according to Bernoulli's Principle. Compared to the control leaflets, the co-rotating VG configuration showed the most improvement (least pressure drop) at all flow rates while the counter-rotating VG configuration performed slightly worse (more pressure drop).

By plotting the square root of the pressure drop (in $mmHg^{.5}$) versus flow rate (in cm^3/sec) and performing a linear regression analysis, the slope of the line can be used to calculate EOA for each leaflet configuration (shown in Table 10).

Table 10: Steady Flow Effective Orifice Area

	Steady Flow EOA (cm^2)
Control	3.96
Co-Rotating VG	4.21
Counter-Rotating VG	3.88

The co-rotating VG configuration improved the EOA of the model BMHV by 6.3% while the counter-rotating VG configuration worsened the EOA of the model BMHV by 2%. Steady flow experiments showed that both VG configurations (co-rotating and counter-rotating VGs) significantly improved the EOA of the model BMHV (4.83 cm^2 and 4.41 cm2 respectively) compared to the control leaflet (4.40 cm^2). The co-rotating VG configuration showed greater EOA improvement than the counter-rotating VG configuration. A possible explanation for the counter-rotating VG configuration not improving the EOA of the valve as much as the co-rotating VG configuration is the decreased geometric orifice area caused by the greater number of rectangular features (16 in the counter-rotating VG configuration compared to eight in the co-rotating VG configuration). There may be a threshold point where the decrease in GOA caused by adding vortex generator features may be too much for any improvement caused by the vortex generators to be seen.

8.2. Pulsatile Flow EOA

To calculate the pulsatile flow EOA of the BMHV with control leaflets and with each VG configuration, the flow rate and aortic and ventricular pressures were recorded over 50 consecutive cycles for each leaflet configuration (Figure 77).

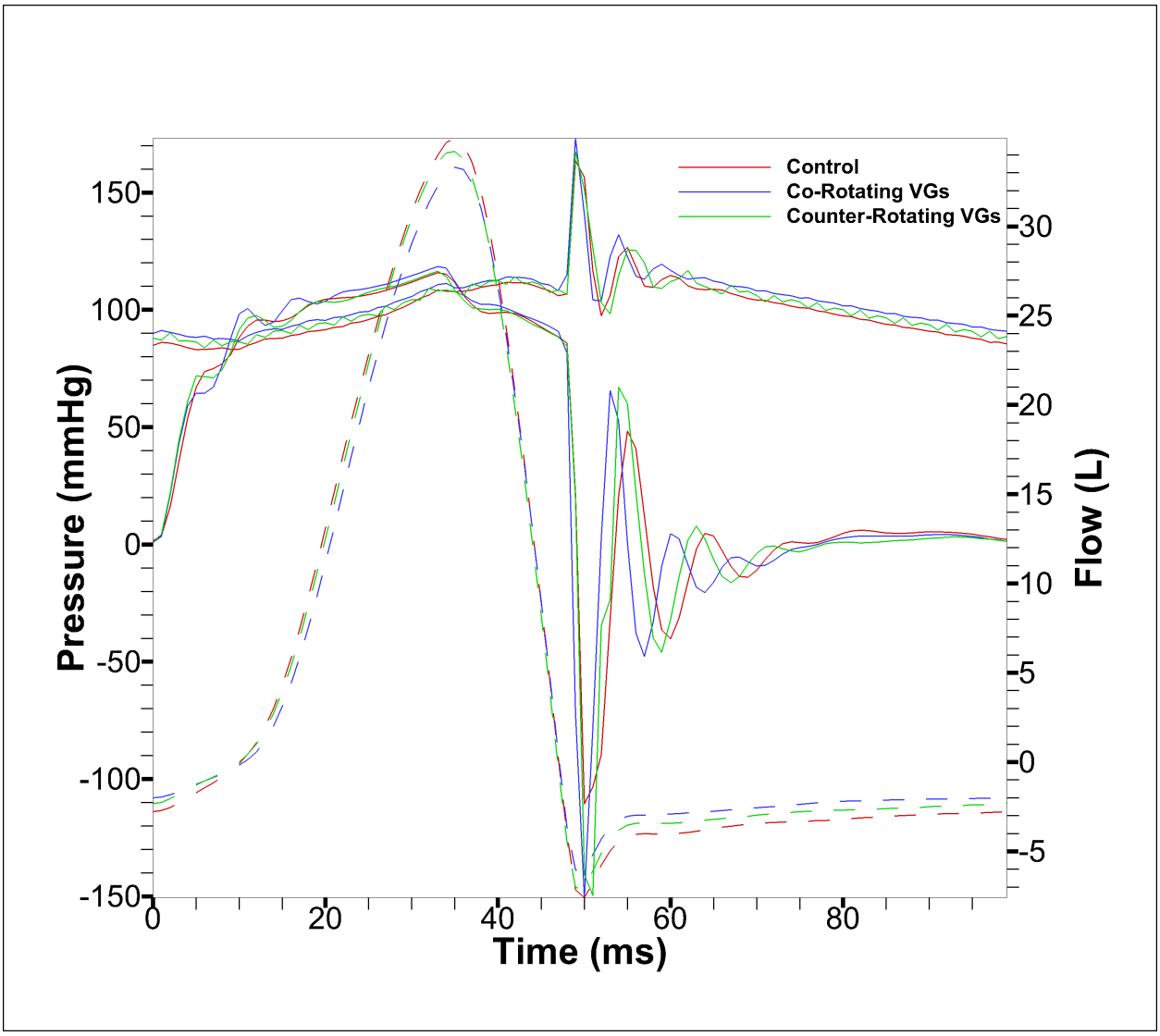

Figure 77: Pulsatile flow pressure and flow rate readings.

Using the flow and pressure data, the EOA was then calculated using a C++ program (code can be seen in Appendix D) and is shown in Figure 78 and Table 11.

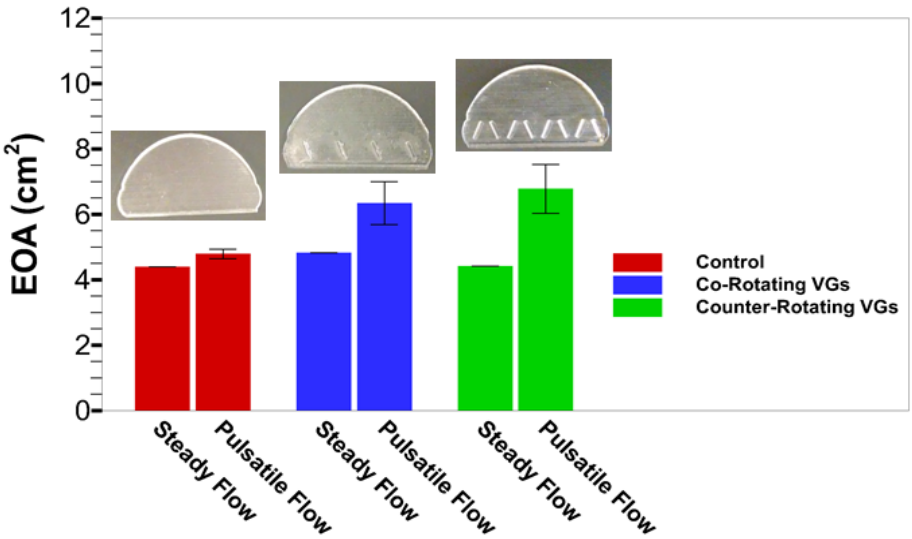

Figure 78: Steady and Pulsatile Effective Orifice Area.

Table 11: Pulsatile Flow Effective Orifice Area

	Pulsatile Flow EOA (cm^2)
Control	4.79
Co-Rotating VG	6.34
Counter-Rotating VG	6.78

The counter-rotating VG configuration improved the EOA of the model BMHV by 41.5% and the co-rotating VG configuration improved the EOA of the model BMHV by 32.3%. Both are significantly larger than the control leaflet. Yoganathan et. al. summarized in-vitro hemodynamic data for common valve prostheses including the St. Jude Medical Standard BMHV (the basis for the model used in this research) of various sizes — 23,

25, and 27mm — and reported the EOAs to be 2.24, 3.23, and 4.09 cm2 respectively (A. P. Yoganathan, He, & Casey Jones, 2004).

Compared to the EOA for the valve size used in this research (25mm), the model BMHV equipped with the control leaflets was calculated to have a higher EOA which may be attributed to different protocols for measuring pressure drops *in-vitro.* However, when the model BMHV was equipped with VG leaflets, the EOA calculated is significantly higher than the EOAs reported by Yoganathan et. al.

The contraction coefficient of each leaflet configuration BMHV was calculated using the ratio of pulsatile EOA to the GOA and is shown in Table 13. First, the GOA of the leaflet configurations in the BMHV model were measured using planimetry (shown in Table 12).

Table 12: Geometric Orifice Areas.

	Geometric Orifice Area (cm^2)
Control	3.10
Co-Rotating VG	2.99
Counter-Rotating VG	2.87

As more vortex generator features are added to the leaflet surface, GOA decreases. The co-rotating VG configuration had eight VG features (four on each leaflet) and decreased the GOA by 3.7%. The counter-rotating VG configuration had 16 VG features (eight on each leaflet) and decreased the GOA by 8%.

Table 13: Contraction coefficients of each leaflet configuration using pulsatile EOA.

	Contraction Coefficient
Control	1.54
Co-Rotating VG	2.12
Counter-Rotating VG	2.36

The counter-rotating VG configuration improved the contraction coefficient of the model BMHV by 53.2% and the co-rotating VG configuration improved the contraction coefficient of the model BMHV by 37.7%.

The performance index (PI) of each leaflet configuration BMHV was calculated using the ratio of the pulsatile EOA to the orifice area of the model BMHV housing (4.91 cm^2) and is shown in Table 14.

Table 14: Performance Index of each leaflet configuration using pulsatile EOA.

	Performance Index (PI)
Control	.97
Co-Rotating VG	1.29
Counter-Rotating VG	1.38

The counter-rotating VG configuration improved the performance index of the model BMHV by 42.3% and the co-rotating VG configuration improved the performance index of the model BMHV by 33%.

By calculating the EOA using transvalvular pressure, the pulsatile flow experiments showed that both VG configurations significantly improved the EOA of the model BMHV (6.3 cm^2 for co-rotating VG and 6.78 cm^2 for counter-rotating VG) compared to the control leaflet (4.79 cm^2). Unlike the steady flow results, the counter-rotating configuration showed greater EOA improvement than the co-rotating VG configuration.

Figure 79 shows the transvalvular pressure during the systolic portion of the cardiac cycle of the control leaflet and VG configurations. During the acceleration phase of systole, the transvalvular pressure values for the VGs configuration leaflets have periodic fluctuations compared to the control leaflet. This fluctuation causes the overall mean pressure to be greater in the VG configurations, thus increasing the EOA. During peal flow and deceleration, the transvalvular pressure for the control leaflet and the VG configurations follow the same trends, however, with the counter-rotating VG configuration having lower values.

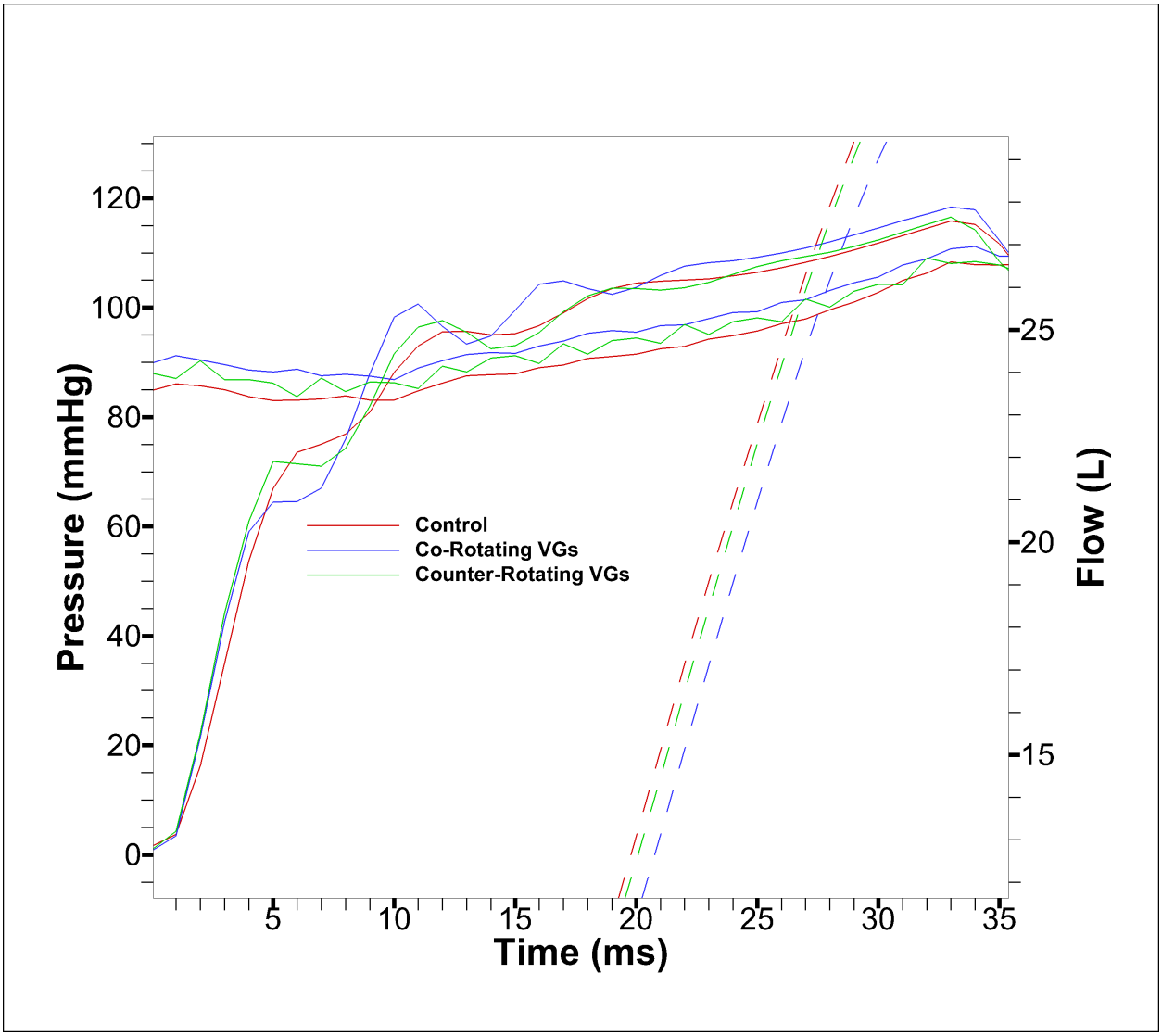

Figure 79: Detailed pulsatile pressure and flow measurements.

The function of VGs is to delay flow separation at the surface of the leaflet by increasing the near-wall momentum through momentum transfer from the outer flow to the wall region. Figure 80 compares the boundary layer and flow separation effect of the VGs compared to the control leaflet. The thickness of the boundary layer is smaller in the two cases of the VGs. Also, in the counter-rotating VG case, the area immediately

downstream of the leaflet tip does not show an area of low velocity which indicates that momentum is indeed transferring from the outer flow to the wall region.

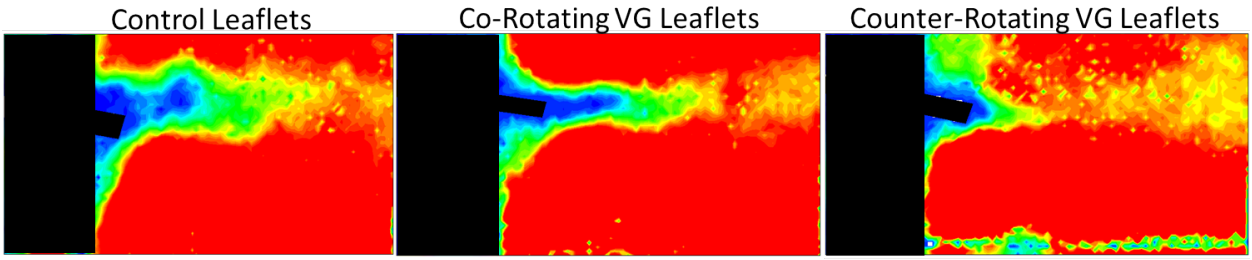

Figure 80: Detailed view of bottom leaflet showing differences in flow separation cause by VGs.

Figure 81 shows the effect of the vortex generators on the velocity in the x direction of the fluid at maximum velocity during ventricular systole. The central jet is affected by the vortex generators significantly. The velocity of the central jet in the BMHV with VG leaflets is decreased when compared to the BMHV with the control leaflets.

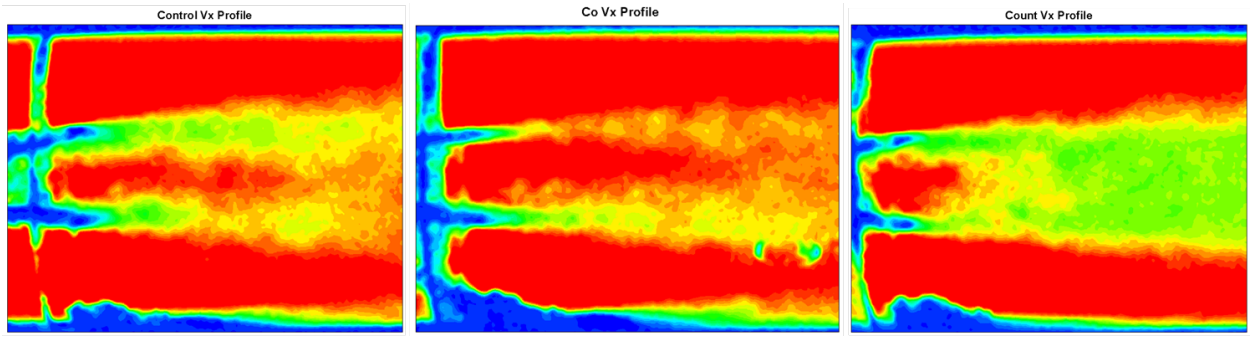

Figure 81: Velocity profiles of control leaflet and VG configurations at max velocity during systole.

Figure 82 presents the average central jet velocity in the y direction of the control leaflets and VG leaflets over the systolic phase. In the acceleration phase (first 0.15 seconds), there is a significant difference in behavior between the leaflets. The co-rotating and counter-rotating VG configurations both show a large fluctuation in

velocities in the y direction when compared to the control leaflet which can be attributed to the vortex formation by the VG elements as they add velocity fluctuations in the y direction.

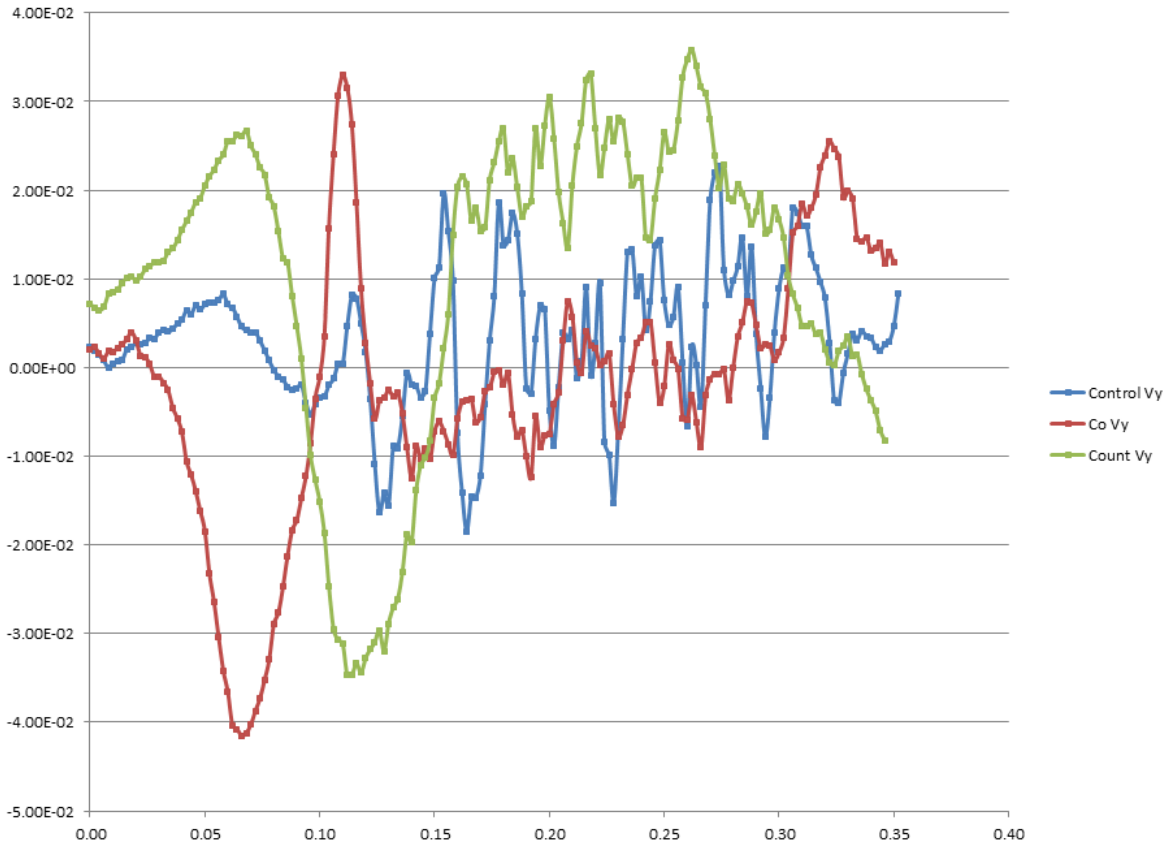

Figure 82: Average central jet velocity (m/s) in the y direction.

Since pressure drop and effective orifice area are measures of flow potential energy losses that happen when blood flows through the heart valve, it is important to quantify and compare the energy losses of the model BMHV with control leaflets and VG leaflets. The product of pressure drop and flow rate provides the energy loss across the valve. Figure 83 shows the energy loss in Watts of the control leaflets and VG configurations.

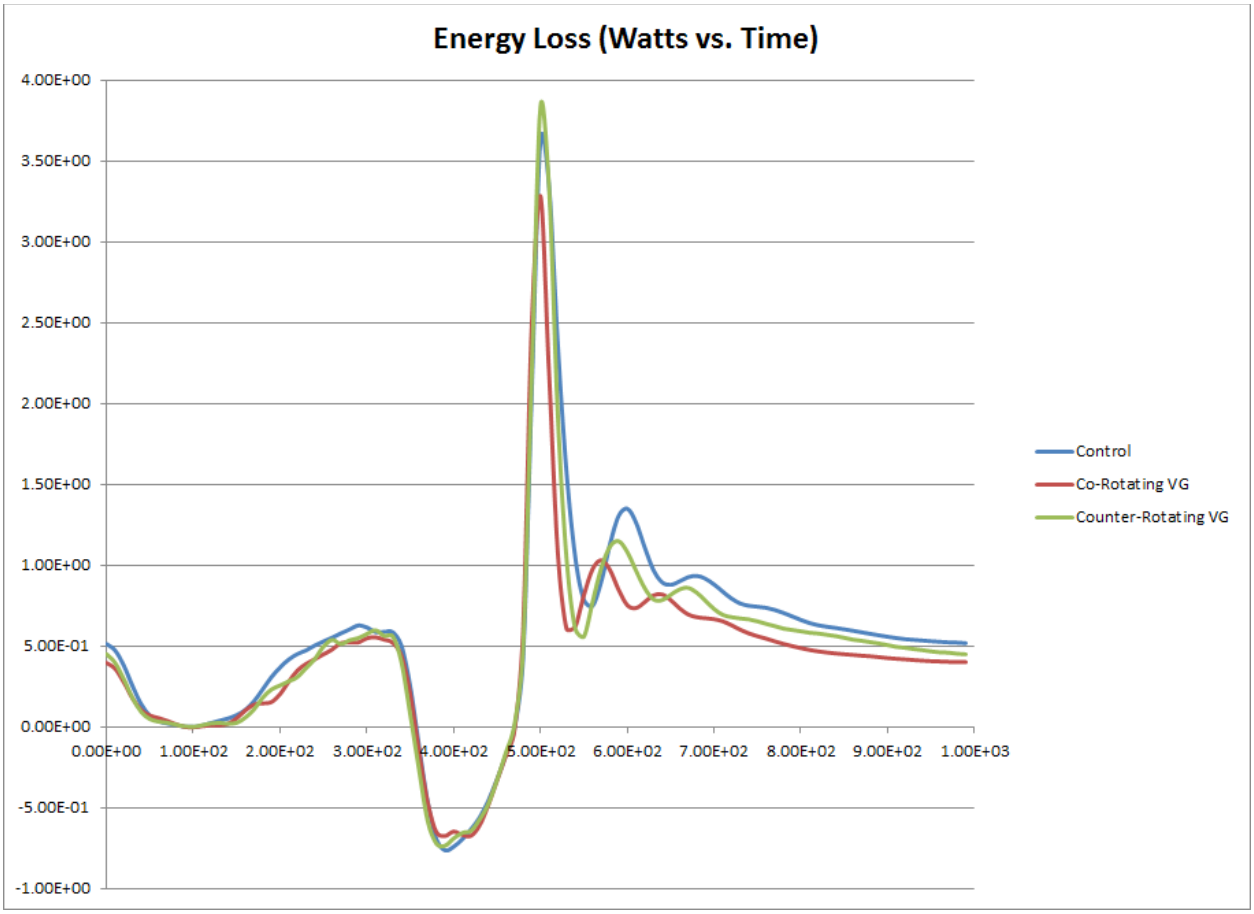

Figure 83: Comparison of energy loss of the BMHV with control leaflets and VGs.

Compared to the control leaflets, both VG configurations decreased the energy loss caused by the BMHV valve in both systole (seen between time steps 1.00e+02 and 3.50e+02 ms) and diastole (seen between time steps 6.00e+02 and 1.00e+03 ms). During systole, both VG configurations decreased the energy loss of the BMHV by around 25%. During diastole, the co-rotating and counter-rotating VG configurations decreased the energy loss of the BMHV by around 25% and 12% respectively.

For comparison, computation fluid dynamics simulations were performed to see the effect of the vortex generators under ideal flow conditions. Figure 84 shows the effect of

the vortex generators on the velocity in the x direction of the fluid at maximum velocity during ventricular systole. The velocity of the central jet in the BMHV with VG leaflets is decreased when compared to the BMHV with the control leaflets. These simulations match up qualitatively to the PIV visualization experiments described in this chapter (Figure 81).

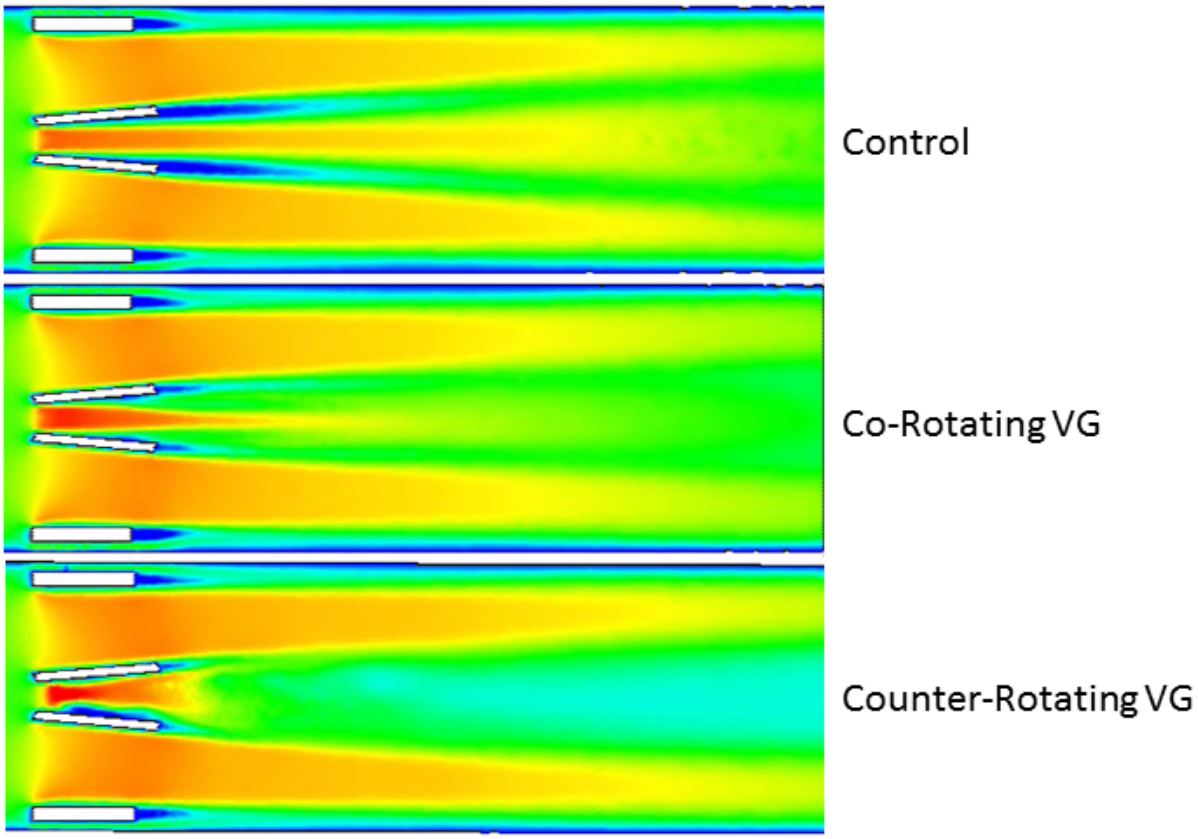

Figure 84: CFD simulations of control leaflet and VG configurations showing velocity in the x direction.

Figure 85 shows the effect of the vortex generators on the velocity in the y direction of the fluid at maximum velocity during ventricular systole. As can be seen, the counter-rotating VG configuration added velocity in the spanwise direction (Y direction).

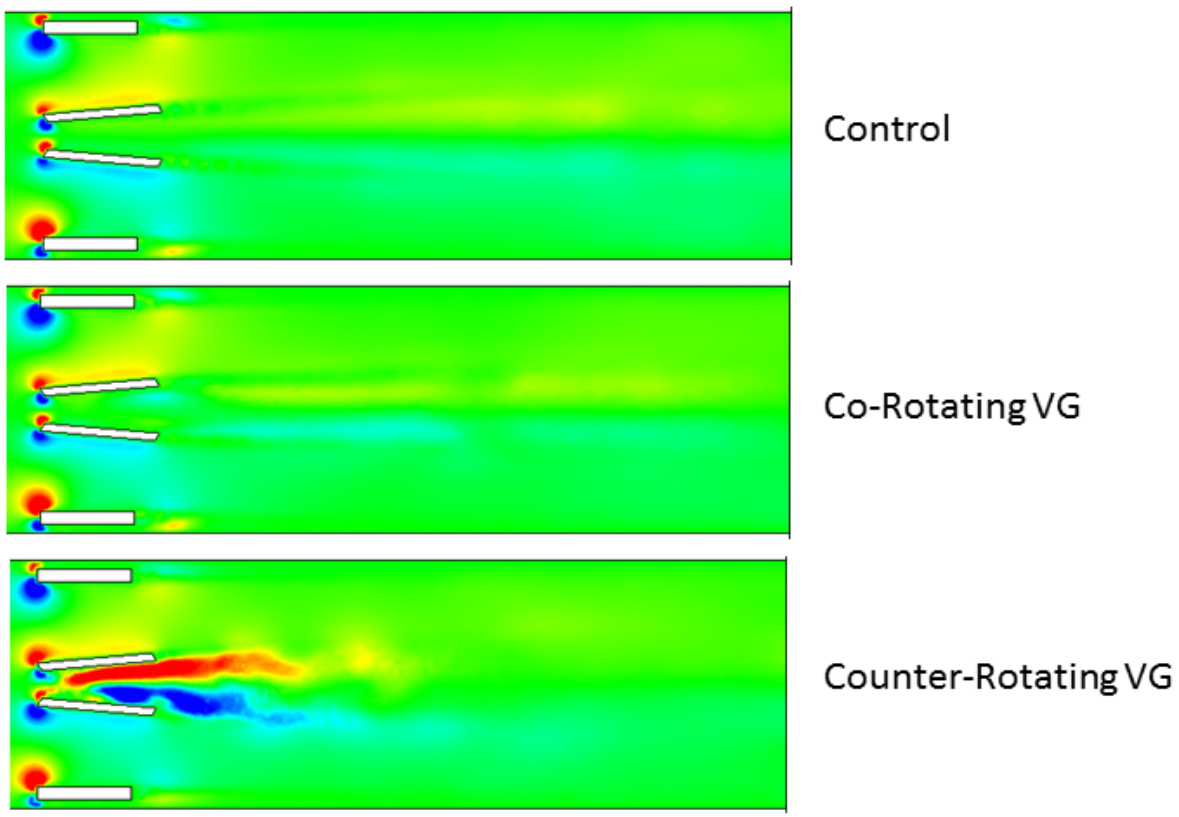

Figure 85: CFD simulations of control leaflet and VG configurations showing velocity in the y direction.

By extracting a slice normal to the flow near the leaflet tips for the model valve with the control leaflets and the VG equipped leaflets and plotting vorticity, we can compare the effect of the vortex generators. Figure 86 shows the evolution of the vorticity structures created by the control leaflets through systole at a fixed slice normal to the flow immediately downstream of the valve. The only vorticity structures seen are four (two per leaflets) opposing vortices created by the edge of the leaflets near the valve housing walls.

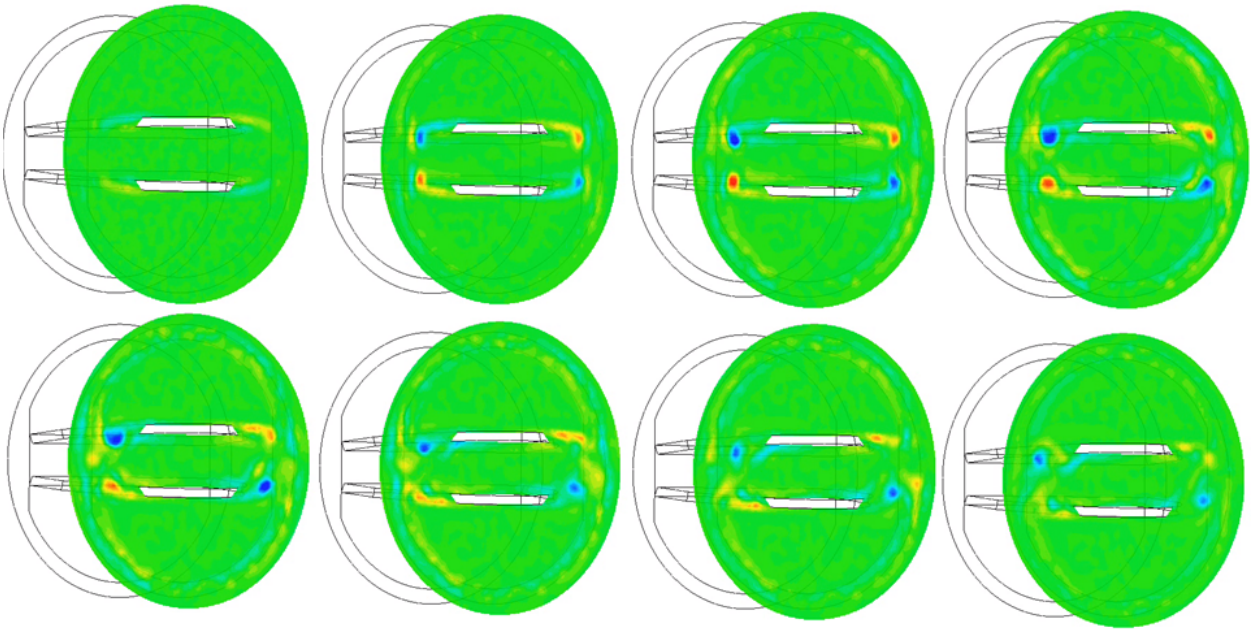

Figure 86: Evolution of the vorticity structure created by the control leaflets during systole at a fixed slice normal to the flow immediately downstream of the valve.

Figure 87 shows the evolution of the vorticity structures created by the co-rotating VG leaflets through systole at a fixed slice normal to the flow immediately downstream of the valve. As predicted, the co-rotating VGs create co-rotating vortices (shown in blue) in the central orifice of the valve. The vorticity structures created by the edge of the leaflets near the valve housing walls seen in the control leaflets also appear in the co-rotating VG configuration.

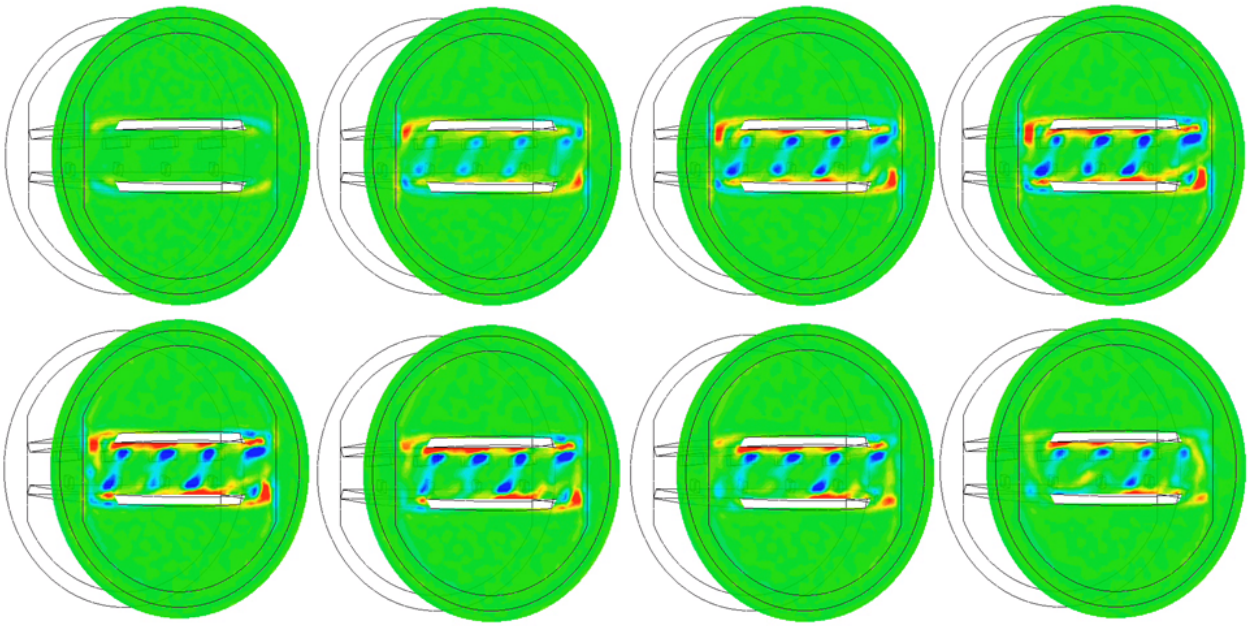

Figure 87: Evolution of the vorticity structure created by the co-rotating VG leaflets during systole at a fixed slice normal to the flow immediately downstream of the valve.

Figure 88 shows the evolution of the vorticity structure created by the counter-rotating VG leaflets through systole at a fixed slice normal to the flow immediately downstream of the valve. As predicted, the counter-rotating VGs create alternating counter-rotating vortices (shown in blue and red) in the central orifice of the valve. The vorticity structures created by the edge of the leaflets near the valve housing walls seen in the control leaflets also appear in the co-rotating VG configuration.

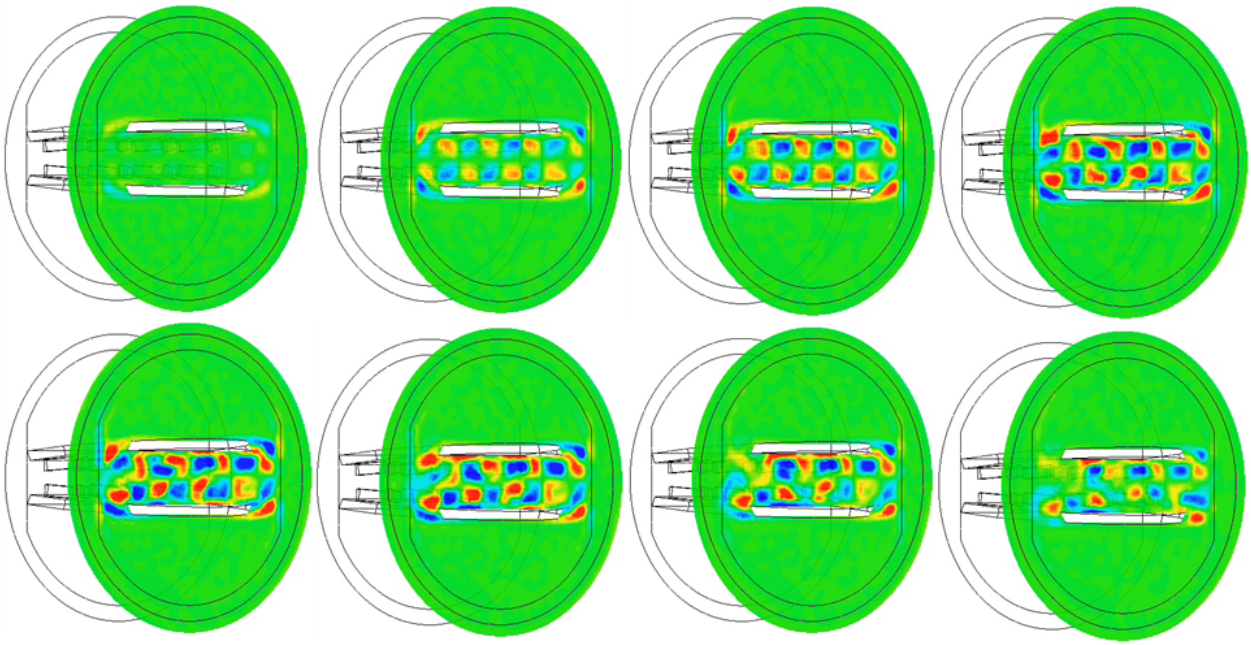

Figure 88: Evolution of the vorticity structure created by the counter-rotating VG leaflets during systole at a fixed slice normal to the flow immediately downstream of the valve.

Figure 89 shows evolution of the vorticity structure created by the control leaflets at various slices downstream of the valve during peak flow in systole. Again, the only vorticity structures seen are four (two per leaflets) opposing vortices created by the edge of the leaflets near the valve housing walls. The structures are strongest immediately downstream of the leaflet tips and dissipates in form and intensity as they get further downstream from the valve.

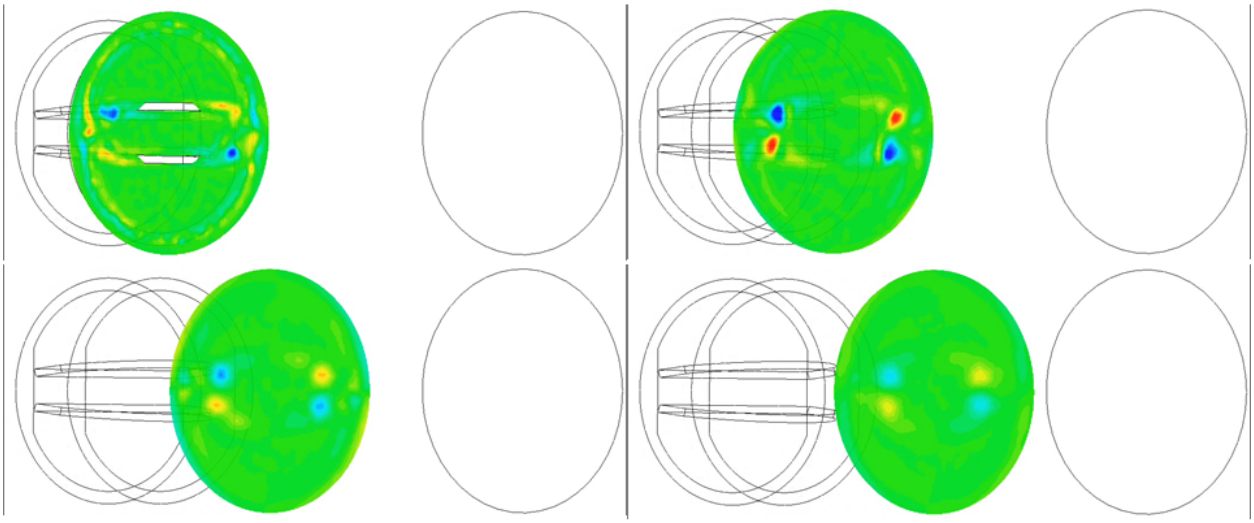

Figure 89: Evolution of the vorticity structure created by the control leaflets at various slices downstream of the valve during peak flow in systole.

Figure 90 shows evolution of the vorticity structure created by the co-rotating VG leaflets at various slices downstream of the valve during peak flow in systole. Again, the co-rotating VGs create co-rotating vortices (shown in blue) in the central orifice of the valve. The structures are strongest immediately downstream of the leaflet tips However, the structures quickly dissipate in form and intensity as they get further downstream from the valve. By the third slice, the structures look very similar to the control leaflets case.

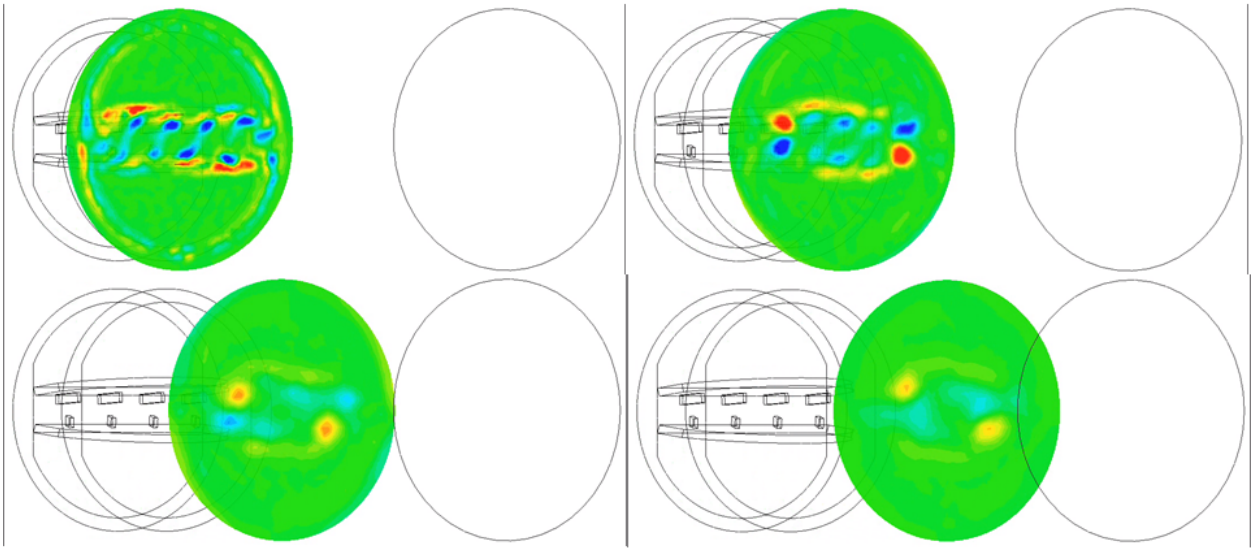

Figure 90: Evolution of the vorticity structure created by the co-rotating VG leaflets at various slices downstream of the valve during peak flow in systole.

Figure 91 shows evolution of the vorticity structure created by the counter-rotating VG leaflets at various slices downstream of the valve during peak flow in systole. Again, the counter-rotating VGs create alternating counter-rotating vortices (shown in blue and red) in the central orifice of the valve. Likewise to the co-rotating VG configuration, The structures are strongest immediately downstream of the leaflet tips However, the structures quickly dissipate in form and intensity as they get further downstream from the valve. By the third slice, the structures look very similar to the control leaflets case.

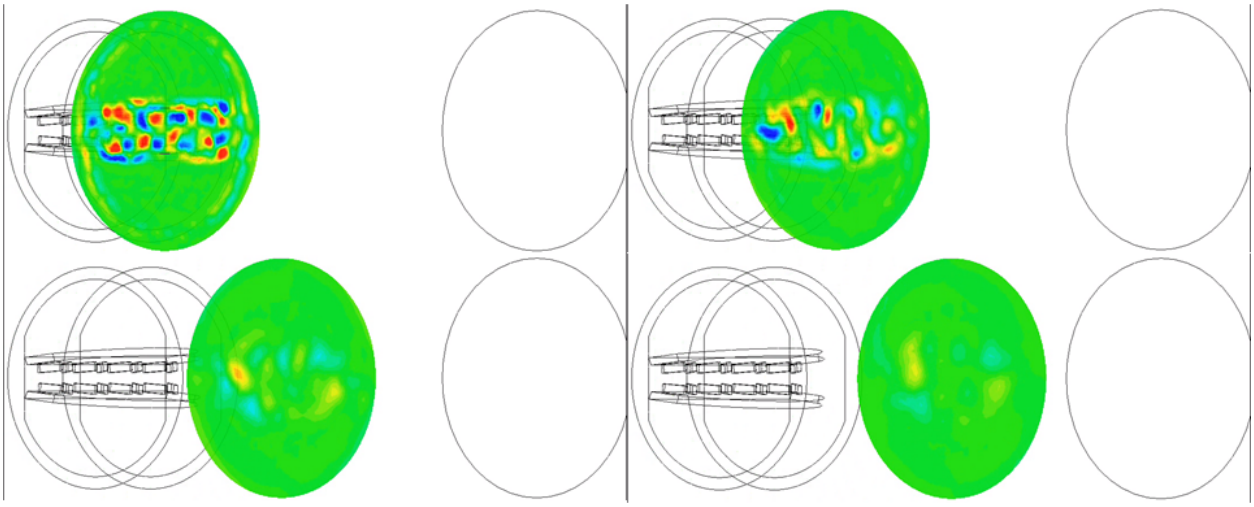

Figure 91: Evolution of the vorticity structure created by the counter-rotating VG leaflets at various slices downstream of the valve during peak flow in systole.

CHAPTER 9: CONCLUSIONS

This research sought to relate the propensity of blood element damage to the flow structures of the bileaflet heart valves and to better understand the fluid mechanics of VGs in BMHVs as a possible improvement to decrease the thromboembolic potential by mitigating shear stress. The specific aims (1) developed a methodology to evaluate thromboembolic potential (TEP) of BMHVs using *in-vitro* particle image velocimetry technique, (2) quantified the efficacy of rectangular VGs distributed on BMHV leaflets to reduce TEP, and (3) quantified the hemodynamic performance impact of rectangular VGs.

The methodology presented in specific aim 1 accurately quantified the thromboembolic potential of the control BMHV during both systolic flow downstream of the valve and diastolic flow upstream of the valve. Downstream of the valve during systolic flow, the results agreed with Bellofiore et. al. who reported that the highest platelet lysis TEP levels occurred during the acceleration phase of the flow. Bellofiore also reported that the highest platelet activation TEP levels occur after the systolic peak during the deceleration phase. Even though the research presented here did not focus on the deceleration phase (recordings stopped right after systolic peak), the results from Release 7 (where platelet activation increases compared to Release 6) are consistent with his results since release 7 occurs at the beginning of the deceleration phase. However, Bellofiore focused only on the area immediately downstream of the leaflets and did not characterize the flow structures or relate them to blood damage. This study

looked at the entire flow field downstream of the valve, characterized the flow structures, and related them to blood damage. Particles were quickly ejected from the measurement area due to the high velocity bulk flow and experienced higher platelet activation and platelet lysis TEP levels per unit exposure time in the central jet due to the presence of strong shear stress layers formed by flow separation due to the leaflets' open angle. Upstream of the valve during diastolic flow, particles released near the b-datum regurgitant jet were quickly ejected from the measurement area and experienced lower platelet activation TEP and higher platelet lysis TEP than particles that were released above and below the regurgitant gap. Particles released above and below the regurgitant gap became trapped in recirculation areas near the closed valve and valve chamber walls and experienced higher platelet activation TEP and lower platelet lysis TEP than particles that were released near the regurgitant gap. No previous studies have quantified the thromboembolic potential of the b-datum regurgitant jet and surrounding areas during diastole. Bellofiore also only studied a simplified non-continuous forward flow condition with the BMHV leaflets fixed at their open position. On the other hand, the study shown here was a dynamic continuous pulsatile study under realistic physiological conditions. The methodology presented in Specific Aim 1 can be expanded to study the TEP of BMHVs to other conditions such abnormal MAP (hypertension), increased/decreased aortic impedance, or other non-physiological conditions.

Specific aim 2 showed that there is room for improvement in BMHV design using passive flow control elements such as vortex generators. Downstream of the valve

during systolic flow, the vortex generators used in this study (co-rotating and counter-rotating VGs) altered the flow in the central orifice jet of the model BMHV by controlling the flow separation, decreasing the principle shear stresses, and decreasing the platelet activation TEP levels. Upstream of the valve during diastolic flow, the vortex generators altered the structure of the regurgitant jet as seen in the animations. The regurgitant jet in the model BMHV with control leaflets pointed slightly up, while the jet in the model BMHV with VG leaflets pointed down (co-rotating) or up (counter-rotating). The VG leaflets decreased the platelet activation TEP levels compared to the control leaflets which agrees with the findings of Murphy et. al., who performed in-vitro blood experiments to measure the effect of VGs on platelet activation in the regurgitant jet utilizing thrombin-antithrombin (TAT) assays. Also, platelet lysis TEP levels decreased in the b-datum regurgitation jet with the VGs configurations even though its structure during diastole is very complex and the interactions between it and the recirculation zones can be very complicated.

The calculations of TEP in both Specifics Aim 1 and 2 were limited by the experimental setup utilized, specifically, the 2 dimensional measurement plane and measurement window size which are both limited due the 1 camera and 1 laser PIV system. The 2D measurement plane limits the TEP calculations to the central plane of the valve only. While the central plane is representative of the bulk flow in forward flow, it does not capture the complex 3 dimensional flow structures in regurgitant flow. It is also possible that since the leaflets in this study were not constructed from clinical quality pyrolytic carbon, but instead more compliant ABS plastic, the closing dynamics of the valve may

have been affected as the leaflets can absorb more of the closing energy and thus decrease the energy transferred to the fluid.

Specific aim 3 showed the major and significant improvement that the vortex generators had on the hemodynamic performance of the BMHV. Leaflets equipped with both the co-rotating and counter-rotating VGs increased the effective orifice area of the BMHV by at least 37% and decreased the energy losses in both systolic and diastolic flow by at least 25% and 12% respectively. This significant improvement in BMHV performance has the possibility to decrease the occurrence of prosthesis-patient mismatch (PPM) which is present when the effective orifice area of the prosthesis being implanted is less than that of the normal human valve (Rahimtoola, 1978). According to Rahimtoola, all prostheses have an in-vitro EOA that is smaller than that of normal human valve and tissue ingrowth and endothelialization further reduces the in-vivo EOA. Therefore, all valve replacements can be considered to be “stenotic”. The problem is made worse when the size of the prosthesis is physically limited by the size of the patient's annulus and cavity in which the prosthesis must lie. PPM has been shown to be a strong and independent predictor of short-term mortality in patients undergoing aortic valve replacement. By utilizing vortex generators in BMHVs, it is possible to improve the EOA of the valve to a level which removes the patient from having severe PPM (Blais et al., 2003).There is even a possibility of improving the hemodynamic performance even more since the vortex generators used in this study were based on parameters and configurations previously optimized by Bradbury and Lin, however, they were not optimized for use in blood contacting surfaces or for prosthetic heart valve use. With

optimization of passive flow control configuration and design, it is possible to further decrease the TEP of BMHVs while increasing their hemodynamic performance; thus creating a safer, more efficient BMHV.

REFERENCES

Ahuja, K. K., & Brown, W. H. (1989). Shear flow control by mechanical tabs. *AIAA, 2nd Shear Flow Conference*, *-1*. Retrieved from http://adsabs.harvard.edu/abs/1989shfl.confQ....A

Ashikhmina, E. A., Schaff, H. V, Dearani, J. A., Sundt, T. M., Suri, R. M., Park, S. J., … Daly, R. C. (2011). Aortic valve replacement in the elderly: determinants of late outcome. *Circulation*, *124*, 1070–1078. doi:10.1161/CIRCULATIONAHA.110.987560

Bakker, C. J. G., Kouwenhoven, M., Hartkamp, M. J., Hoogeveen, R. M., & Mali, W. P. T. M. (1995). Accuracy and precision of time-averaged flow as measured by nontriggered 2D phase-contrast MR angiography, a phantom evaluation. *Magnetic Resonance Imaging*, *13*(7), 959–965. Retrieved from http://linkinghub.elsevier.com/retrieve/pii/0730725X9502005E

Bellofiore, A. (2011). High-Resolution Measurement of the Unsteady Velocity Field to Evaluate Blood Damage Induced by a Mechanical Heart Valve. *Annals of Biomedical Engineering*. Retrieved from http://www.springerlink.com/index/3J56J54181212215.pdf

Bellofiore, A., Donohue, E. M., & Quinlan, N. J. (2011). Scale-up of an unsteady flow field for enhanced spatial and temporal resolution of PIV measurements: application to leaflet wake flow in a mechanical heart valve. *Experiments in Fluids*, *51*(1), 161–176. Retrieved from http://gateway.webofknowledge.com/gateway/Gateway.cgi?GWVersion=2&SrcAuth=mekentosj&SrcApp=Papers&DestLinkType=FullRecord&DestApp=WOS&KeyUT=000291889300012

Bernstein, E. F., Marzec, U., & Johnston, G. G. (1977). Structural correlates of platelet functional damage by physical forces. *Transactions - American Society for Artificial Internal Organs*, *23*, 617–625. doi:10.1097/00002480-197700230-00167

Black, M. M., & Drury, P. J. (1994). Mechanical and other problems of artificial valves. *Current Topics in Pathology Ergebnisse Der …*. Retrieved from http://www.ncbi.nlm.nih.gov/pubmed/8162709

Blackshear, P. L. (1972). Mechanical Hemolysis of Flowing Blood. In Y. C. Fung, N. Perrone, & Anliker (Eds.), *Biomechanics*. Prentice Hall.

Blais, C., Dumesnil, J. G., Baillot, R., Simard, S., Doyle, D., & Pibarot, P. (2003). Impact of valve prosthesis-patient mismatch on short-term mortality after aortic valve replacement. *Circulation*, *108*, 983–988. doi:10.1161/01.CIR.0000085167.67105.32

Bluestein, D., Li, Y. M., & Krukenkamp, I. B. (2002). Free emboli formation in the wake of bi-leaflet mechanical heart valves and the effects of implantation techniques. *Journal of Biomechanics*, *35*(12), 1533–1540. Retrieved from http://www.sciencedirect.com/science/article/pii/S0021929002000933

Bluestein, D., Niu, L., Schoephoerster, R. T., & Dewanjee, M. K. (1996). Steady Flow in an Aneurysm Model: Correlation Between Fluid Dynamics and Blood Platelet Deposition. *Journal of Biomechanical Engineering*, *118*(3), 280–286. Retrieved from http://biomechanical.asmedigitalcollection.asme.org/article.aspx?articleid=1400451

Bluestein, D., Rambod, E., & Gharib, M. (2000). Vortex shedding as a mechanism for free emboli formation in mechanical heart valves. *Journal of Biomechanical Engineering*, *122*, 125–134. doi:10.1115/1.429634

BR, T., UM, M., JT, E., P, D., T, M., SR, H., … AP, Y. (2001). The sensitivity of indicators of thrombosis initiation to a bileaflet prosthesis leakage stimulus. *The Journal of Heart Valve Disease*, *10*(2), 228–238. Retrieved from http://europepmc.org/abstract/MED/11297211

Bradbury, L. J. S., & Khadem, A. H. (2006). The distortion of a jet by tabs. *Journal of Fluid Mechanics*, *70*(04), 801–813. Retrieved from http://www.journals.cambridge.org/abstract_S0022112075002352

Bushnell, D. M., & McGinley, C. B. (1989). Turbulence control in wall flows. *Annual Review of Fluid Mechanics*. Retrieved from http://www.annualreviews.org/doi/pdf/10.1146/annurev.fl.21.010189.000245

Cannegieter, S. C., Rosendaal, F. R., & Briet, E. (1994). Thromboembolic and bleeding complications in patients with mechanical heart valve prostheses. *Circulation*, *89*(2), 635–641. Retrieved from http://circ.ahajournals.org/content/89/2/635.short

Cebi, N., & Bozkurt, E. (2004). Mid-term results of mitral valve repair for complicated active bacterial endocarditis in high-risk patients. *Heart and Vessels*, *19*, 179–182. doi:10.1007/s00380-004-0767-7

CHANDRAN, K. B., & Aluri, S. (1997). Mechanical valve closing dynamics: Relationship between velocity of closing, pressure transients, and cavitation initiation. *Annals of Biomedical Engineering*, *25*(6), 926–938. Retrieved from http://gateway.webofknowledge.com/gateway/Gateway.cgi?GWVersion=2&SrcAuth=mekentosj&SrcApp=Papers&DestLinkType=FullRecord&DestApp=WOS&KeyUT=A1997YG99300002

Chien, S. (1977). Red Cell Membrane and Hemolysis, in Cardiovascular Flow Dynamics and Measurements. Baltimore: University Park Press.

Danziger, J. (2008). Vitamin K-dependent proteins, warfarin, and vascular calcification. *Clinical Journal of the American Society of Nephrology : CJASN*, *3*, 1504–1510. doi:10.2215/CJN.00770208

Dasi, L. P., Ge, L., Simon, H. A., & Sotiropoulos, F. (2007). Vorticity dynamics of a bileaflet mechanical heart valve in an axisymmetric aorta. *Physics of Fluids*. Retrieved from http://link.aip.org/link/?PHFLE6/19/067105/1

Dasi, L. P., Murphy, D. W., & Glezer, A. (2008). Passive flow control of bileaflet mechanical heart valve leakage flow. *Journal of Biomechanics*. Retrieved from http://www.sciencedirect.com/science/article/pii/S0021929008000432

Dasi, L. P., Simon, H. A., Sucosky, P., & Yoganathan, A. P. (2009). Fluid mechanics of artificial heart valves. *Clinical and Experimental Pharmacology & Physiology*, *36*(2), 225–237. Retrieved from http://eutils.ncbi.nlm.nih.gov/entrez/eutils/elink.fcgi?dbfrom=pubmed&id=19220329&retmode=ref&cmd=prlinks

De la Fuente Galán, L., San Román Calvar, J. A., Muñoz San José, J. C., Vega Barbado, J. L., del Pozo Crespo, F., Martín, J. A., … Fernández-Avilés, F. (1996). *Influence of the degree of aortic valve calcification on the estimate of valvular area using planimetry with transesophageal echocardiography*. *Revista espanola de cardiologia* (Vol. 49, pp. 663–668).

Ellis, J. T., Wick, T. M., & Yoganathan, A. P. (1998). Prosthesis-induced hemolysis: Mechanisms and quantification of shear stress. *JOURNAL OF HEART VALVE DISEASE*, *{7}*({4}), {376–386}. Retrieved from http://www.google.com/search?client=safari&rls=10_7_4&q=Prosthesis+induced+hemolysis+Mechanisms+and+quantification+of+shear+stress&ie=UTF-8&oe=UTF-8

Emery, R. W., Emery, A. M., Raikar, G. V, & Shake, J. G. (2008). Anticoagulation for mechanical heart valves: a role for patient based therapy. *Journal of Thrombosis and Thrombolysis*, *25*, 18–25. doi:10.1007/s11239-007-0105-x

Fallon, A. M. (2006). The Development of a Novel in vitro Flow System to Evaluate Platelet Activation and Procoagulant Potential Induced by Bileaflet Mechanical Heart Valve Leakage Jets, 1–339. Retrieved from papers3://publication/uuid/A27493A9-D5F4-4283-A58D-0E5B635DFDA3

Fallon, A. M., Shah, N., Marzec, U. M., Warnock, J. N., Yoganathan, A. P., & Hanson, S. R. (2006). Flow and Thrombosis at Orifices Simulating Mechanical Heart Valve Leakage Regions. *Journal of Biomechanical Engineering*, *128*(1), 30. Retrieved from http://link.aip.org/link/JBENDY/v128/i1/p30/s1&Agg=doi

Garcia, D., & Kadem, L. (2006). What do you mean by aortic valve area: geometric orifice area, effective orifice area, or gorlin area? *The Journal of Heart Valve Disease*, *15*, 601–608.

Giersiepen, M., Wurzinger, L. J., Opitz, R., & Reul, H. (1990). Estimation of shear stress-related blood damage in heart valve prostheses--in vitro comparison of 25 aortic valves. *The International Journal of Artificial Organs*, *13*(5), 300. Retrieved from http://ukpmc.ac.uk/abstract/MED/2365485

GILLJEONG, C., & CHANDRAN, K. B. (1995). Dynamics of a Mechanical Monoleaflet Heart-Valve Prosthesis in the Closing Phase - Effect of Squeeze Film. *Annals of Biomedical Engineering*, *23*(2), 189–197. Retrieved from http://www.springerlink.com/index/7G71K486667U5416.pdf

Gilon, D., Cape, E. G., Handschumacher, M. D., Song, J. K., Solheim, J., VanAuker, M., … Levine, R. A. (2002). Effect of three-dimensional valve shape on the hemodynamics of aortic stenosis: Three-dimensional echocardiographic stereolithography and patient studies. *Journal of the American College of Cardiology*, *40*, 1479–1486. doi:10.1016/S0735-1097(02)02269-6

Goodman, W. L. (1985). Emmons spot forcing for turbulent drag reduction. *AIAA Journal*, *23*(1), 155–157. Retrieved from http://arc.aiaa.org/doi/abs/10.2514/3.8886

Govindarajan, V., Udaykumar, H. S., Herbertson, L. H., Deutsch, S., Manning, K. B., & Chandran, K. B. (2010). Two-Dimensional FSI Simulation of Closing Dynamics of a Tilting Disk Mechanical Heart Valve. *Journal of Medical Devices-Transactions of the Asme*, *4*(1). Retrieved from http://gateway.webofknowledge.com/gateway/Gateway.cgi?GWVersion=2&SrcAuth=mekentosj&SrcApp=Papers&DestLinkType=FullRecord&DestApp=WOS&KeyUT=000283764000001

Grigioni, M., Daniele, C., Morbiducci, U., D'Avenio, G., Di Benedetto, G., & Barbaro, V. (2004). The Power-law Mathematical Model for Blood Damage Prediction: Analytical Developments and Physical Inconsistencies. *Artificial Organs*, *28*(5), 467–475. Retrieved from http://doi.wiley.com/10.1111/j.1525-1594.2004.00015.x

Grigioni, M., Morbiducci, U., D'Avenio, G., Benedetto, G. Di, & Gaudio, C. Del. (2005). A novel formulation for blood trauma prediction by a modified power-law mathematical model. *Biomechanics and Modeling in Mechanobiology*, *4*(4), 249–260. Retrieved from http://www.springerlink.com/index/10.1007/s10237-005-0005-y

Grunkemeier, G. L., & Anderson, W. N. (1998). Clinical evaluation and analysis of heart valve substitutes. *The Journal of Heart Valve Disease*, *7*, 163–169.

Guezennec, Y. G., & Nagib, H. M. (1990). Mechanisms leading to net drag reduction in manipulated turbulent boundary layers. *AIAA Journal*. Retrieved from http://arc.aiaa.org/doi/pdf/10.2514/3.10381

Hellums, J. D. (1994). 1993 Whitaker lecture: Biorheology in thrombosis research. *Annals of Biomedical Engineering*. doi:10.1007/BF02367081

Hellums, J. D., & Brown, C. H. (1977). Blood cell damage by mechanical forces. *Cardiovascular Flow Dynamics and Measurements*, 799–823.

Herbertson, L. H., Deutsch, S., & Manning, K. B. (2011). Near Valve Flows and Potential Blood Damage During Closure of a Bileaflet Mechanical Heart Valve. *Journal of Biomechanical Engineering*. Doi:10.1115/1.4005167

Hyde, J. A., Chinn, J. A., & Phillips, R. E. (1999). Polymer heart valves. *The Journal of Heart Valve Disease*, *8*, 331–339.

Jamieson, W. R. E., Burr, L. H., Anderson, W. N., Chambers, J. B., Gams, J. P., & Dowd, C. M. (2002). Prosthesis-related complications: first-year annual rates. *The Journal of Heart Valve Disease*, *11*, 758–763.

Kawahito, K., Adachi, H., & Ino, T. (2000). Platelet Activation in the Gyro C1E3 Centrifugal Pump: Comparison with the Terumo Capiox and the Nikkiso HPM-15. *Artificial Organs*, *24*(11), 889–892. Retrieved from http://doi.wiley.com/10.1046/j.1525-1594.2000.06639.x

Korossis, S. A., Fisher, J., & Ingham, E. (2000). Cardiac valve replacement: a bioengineering approach. *Bio-Medical Materials and Engineering*, *10*, 83–124.

LAMSON, T. C., ROSENBERG, G., GESELOWITZ, D. B., Deutsch, S., STINEBRING, D. R., FRANGOS, J. A., & TARBELL, J. M. (1993). Relative Blood Damage in the Three Phases of a Prosthetic Heart Valve Flow Cycle. *Asaio Journal*, *39*(3), M634. Retrieved from http://journals.lww.com/asaiojournal/Fulltext/1993/07000/Relative_Blood_Damage_in_the_Three_Phases_of_a.98.aspx

Leo, H. L. (2005). An in vitro investigation of the flow fields through bileaflet and polymeric prosthetic heart valves. Retrieved from http://smartech.gatech.edu/handle/1853/11644

Leo, H. L., Dasi, L. P., Carberry, J., Simon, H. A., & Yoganathan, A. P. (2006). Fluid dynamic assessment of three polymeric heart valves using particle image velocimetry. *Annals of Biomedical Engineering*, *34*, 936–952. doi:10.1007/s10439-006-9117-5

Leverett, L. B., Hellums, J. D., Alfrey, C. P., & Lynch, E. C. (1972). Red blood cell damage by shear stress. *Biophysical Journal*, *12*, 257–273. doi:10.1016/S0006-3495(72)86085-5

Lin, J. C. (2002). Review of research on low-profile vortex generators to control boundary-layer separation. *Progress in Aerospace Sciences*, *38*(4-5), 389–420. Retrieved from http://linkinghub.elsevier.com/retrieve/pii/S0376042102000106

Linde, T., Hamilton, K. F., Navalon, E. C., Schmitz-Rode, T., & Steinseifer, U. (2012). Aortic root compliance influences hemolysis in mechanical heart valve prostheses: an in-vitro study. *The International Journal of Artificial Organs*. doi:10.5301/ijao.5000108

Lu, P. C., Lai, H. C., & Liu, J. S. (2001). A reevaluation and discussion on the threshold limit for hemolysis in a turbulent shear flow. *Journal of Biomechanics*, *34*(10), 1361–1364. Retrieved from http://linkinghub.elsevier.com/retrieve/pii/S0021929001000847

Manning, K. B., Herbertson, L. H., Fontaine, A. A., & Deutsch, S. (2008). A detailed fluid mechanics study of tilting disk mechanical heart valve closure and the implications to blood damage. *Journal of Biomechanical Engineering*, *130*(4), 41001. Retrieved from http://eutils.ncbi.nlm.nih.gov/entrez/eutils/elink.fcgi?dbfrom=pubmed&id=18601443&retmode=ref&cmd=prlinks

Manning, K. B., Kini, V., Fontaine, A. A., Deutsch, S., & Tarbell, J. M. (2003). Regurgitant flow field characteristics of the St. Jude bileaflet mechanical heart valve under physiologic pulsatile flow using particle image velocimetry. *Artificial Organs*, *27*(9), 840–846. Retrieved from http://gateway.webofknowledge.com/gateway/Gateway.cgi?GWVersion=2&SrcAuth=mekentosj&SrcApp=Papers&DestLinkType=FullRecord&DestApp=WOS&KeyUT=000185112700015

Maugeri, N., Santarelli, M. T., & Lazzari, M. A. (2000). Circulating platelet/polymorphonuclear leukocyte mixed-cell aggregates in patients with mechanical heart valve replacement. *American Journal of Hematology*, *65*(2), 93–98. Retrieved from http://doi.wiley.com/10.1002/1096-8652(200010)65:2<93::AID-AJH1>3.0.CO;2-4

Mecozzi, G., Milano, A. D., De Carlo, M., & Sorrentino, F. (2002). Intravascular hemolysis in patients with new-generation prosthetic heart valves: a prospective study. *Vortex Shedding as a Mechanism for Free Emboli Formation in Mechanical Heart Valves*. Retrieved from http://www.sciencedirect.com/science/article/pii/S0022522302315435

Murphy, D. W., Dasi, L. P., Vukasinovic, J., Glezer, A., & Yoganathan, A. P. (2010). Reduction of Procoagulant Potential of b-Datum Leakage Jet Flow in Bileaflet Mechanical Heart Valves via Application of Vortex Generator Arrays. *Journal of Biomechanical Engineering*, *132*(7), 71011. Retrieved from http://biomechanical.asmedigitalcollection.asme.org/article.aspx?articleid=1429242

Nevaril, C. G., Lynch, E. C., & Alfrey, C. P. (1968). Erythrocyte Damage and Destruction Induced by Shearing Stresses. *Journal of Laboratory and Clinical Medicine*, (71), 784.

Pibarot, P., & Dumesnil, J. G. (2007). New concepts in valvular hemodynamics: implications for diagnosis and treatment of aortic stenosis. *The Canadian Journal of Cardiology*, *23 Suppl B*, 40B–47B.

Rahimtoola, S. H. (1978). The problem of valve prosthesis-patient mismatch. *Circulation*, *58*, 20–24. doi:10.1161/01.CIR.58.1.20

Rieck, Å. E., Cramariuc, D., Boman, K., Gohlke-Bärwolf, C., Staal, E. M., Lønnebakken, M. T., … Gerdts, E. (2012). Hypertension in aortic stenosis: implications for left ventricular structure and cardiovascular events. *Hypertension*, *60*(1), 90–97. Retrieved from http://eutils.ncbi.nlm.nih.gov/entrez/eutils/elink.fcgi?dbfrom=pubmed&id=22647889&retmode=ref&cmd=prlinks

Rodriguez-Aumente, P., Ruiz-Rivas, U., & Lecuona, A. (2001). Near field vortex dynamics in axially forced, laminar, co-flowing jets: A descriptive study of the flow configurations. *European Journal of Mechanics, B/Fluids*, *20*(5), 673–698.

Spanier, T., Oz, M., Levin, H., & Weinberg, A. (1996). Activation of coagulation and fibrinolytic pathways in patients with left ventricular assist devices. *Vortex Shedding as a Mechanism for Free Emboli Formation in Mechanical Heart Valves*. Retrieved from http://www.sciencedirect.com/science/article/pii/S0022522396701113

Travis, B. R., Marzec, U. M., Leo, H. L., Momin, T., Sanders, C., Hanson, S. R., & Yoganathan, A. P. (2001). Bileaflet Aortic Valve Prosthesis Pivot Geometry Influences Platelet Secretion and Anionic Phospholipid Exposure. *Annals of Biomedical Engineering*, *29*(8), 657–664. Retrieved from http://link.springer.com/10.1114/1.1385808

Turitto, V. T., & Hall, C. L. (1998). Mechanical factors affecting hemostasis and thrombosis. In *Thrombosis Research* (Vol. 92). doi:10.1016/S0049-3848(98)00157-1

Vongpatanasin, W., Hillis, L. D., & Lange, R. A. (1996). Prosthetic heart valves. *The New England Journal of Medicine*, *335*(6), 407–416. Retrieved from http://eutils.ncbi.nlm.nih.gov/entrez/eutils/elink.fcgi?dbfrom=pubmed&id=8676934&retmode=ref&cmd=prlinks

Walker, P. G., & Yoganathan, A. P. (1992). In vitro pulsatile flow hemodynamics of five mechanical aortic heart valve prostheses. *European Journal of Cardio-Thoracic Surgery : Official Journal of the European Association for Cardio-Thoracic Surgery*, *6 Suppl 1*, S113–S123. doi:10.1016/1010-7940(92)90034-U

Yap, C.-H., Dasi, L. P., & Yoganathan, A. P. (2010). Dynamic hemodynamic energy loss in normal and stenosed aortic valves. *Journal of Biomechanical Engineering*, *132*, 021005. doi:10.1115/1.4000874

Yoganathan, A. (1997). Heart valve dynamics. *Annals of Biomedical Engineering*, *25*(1), S–19. Retrieved from http://link.springer.com/10.1007/BF02647355

Yoganathan, A. P., He, Z., & Casey Jones, S. (2004). Fluid mechanics of heart valves. *Annual Review of Biomedical Engineering*, *6*, 331–362. doi:10.1146/annurev.bioeng.6.040803.140111

Yun, B. M., Wu, J., Simon, H. A., Arjunon, S., Sotiropoulos, F., Aidun, C. K., & Yoganathan, A. P. (2012). A numerical investigation of blood damage in the hinge area of aortic bileaflet mechanical heart valves during the leakage phase. *Annals of Biomedical Engineering*, *40*, 1468–1485. doi:10.1007/s10439-011-0502-3

Zaman, K. B. M. Q., & Foss, J. K. (1997). The effect of vortex generators on a jet in a cross-flow. *Physics of Fluids*, *9*(1), 106–114. Retrieved from http://link.aip.org/link/PHFLE6/v9/i1/p106/s1&Agg=doi

Zaman, K., Reeder, M. F., & Samimy, M. (1994). Control of an axisymmetric jet using vortex generators. *Physics of Fluids*. Retrieved from http://link.aip.org/link/?PHFLE6/6/778/1

APPENDIX A: EFFECT OF HYPERTENSION ON THE CLOSING DYNAMICS AND LAGRANGIAN BLOOD DAMAGE INDEX MEASURE OF THE B-DATUM REGURGITANT JET IN A BILEAFLET MECHANICAL HEART VALVE

A.1. Background

It is important to understand how MAP regulates blood damage and platelet activation potential of the b-datum jet. If increased MAP significantly changes thromboembolic characteristics, such information is critical to develop realistic ‘‘worst case’’ scenarios for evaluating thromboembolic potential of all mechanical valves, or revisiting anti-coagulation regimen in BMHV patients with hypertension (HT). From an engineering standpoint, if hypertensive conditions indeed turn out to be the worst-case scenario, then it should govern the next generation valve designs to further reduce thromboembolism risk in future BMHVs. Further, it may also warrant the inclusion of hypertensive conditions during regulatory and/or pre-clinical testing. In this study, we examine the effect of MAP on the closing dynamics of BMHV leaflets including the strength of the closing vortex and the subsequent b-datum regurgitant jet, and quantify blood damage index using the framework of Bellofiore and Quinlan (A Bellofiore, 2011). In addition to the relevance from an engineering perspective in the context of future valve designs, this study further demonstrates at least some physical mechanisms behind hypertension being a well-established risk factor for thromboembolic events in prosthetic heart valves (Ashikhmina et al., 2011; Emery, Emery, Raikar, & Shake, 2008; Linde, Hamilton, Navalon, Schmitz-Rode, & Steinseifer, 2012). Further, hypertension is highly prevalent in patients needing heart valve replacement (Rieck et al., 2012).

Therefore, the study of blood damage caused by BMHVs as a function of mean aortic pressure is important to fully appreciate the true thromboembolic potential of BMHVs in realistic clinical conditions.

A.2. Equipment, Materials, and Methods

The experiments for the effect of hypertension on closing dynamics and blood damage index utilized the same materials and equipment described in Chapter 4 and similar experimental procedures described in Chapter 5. In summary, we utilized the *in-vitro* pulsatile flow loop capable of imposing physiological aortic flow conditions on a test BMHV to perform particle image velocimetry (PIV) experiments under normal blood pressure (NBP) conditions and hypertension (HT) conditions. NBP conditions were 100 +/- 5 mmHG mean aortic pressure (MAP), 5 +/- 0.2 L/min cardiac output, 60 beats/min heart beat, and 33% systolic fraction. HT conditions were 140 +/- 5 mmHG mean aortic pressure (MAP), 5 +/- 0.2 L/min cardiac output, 60 beats/min heart beat, and 33% systolic fraction. Lagrangian tracking and blood damage index was calculated using the mathematical models described in Chapter 5.

A.3. Results

The peak leaflet closing speed for the model BMHV was 0.75 m/s for both NPB and HT cases. The time to closure at NBP was 40 ms while the time to closure at HT was around 30ms (Figure 92a).

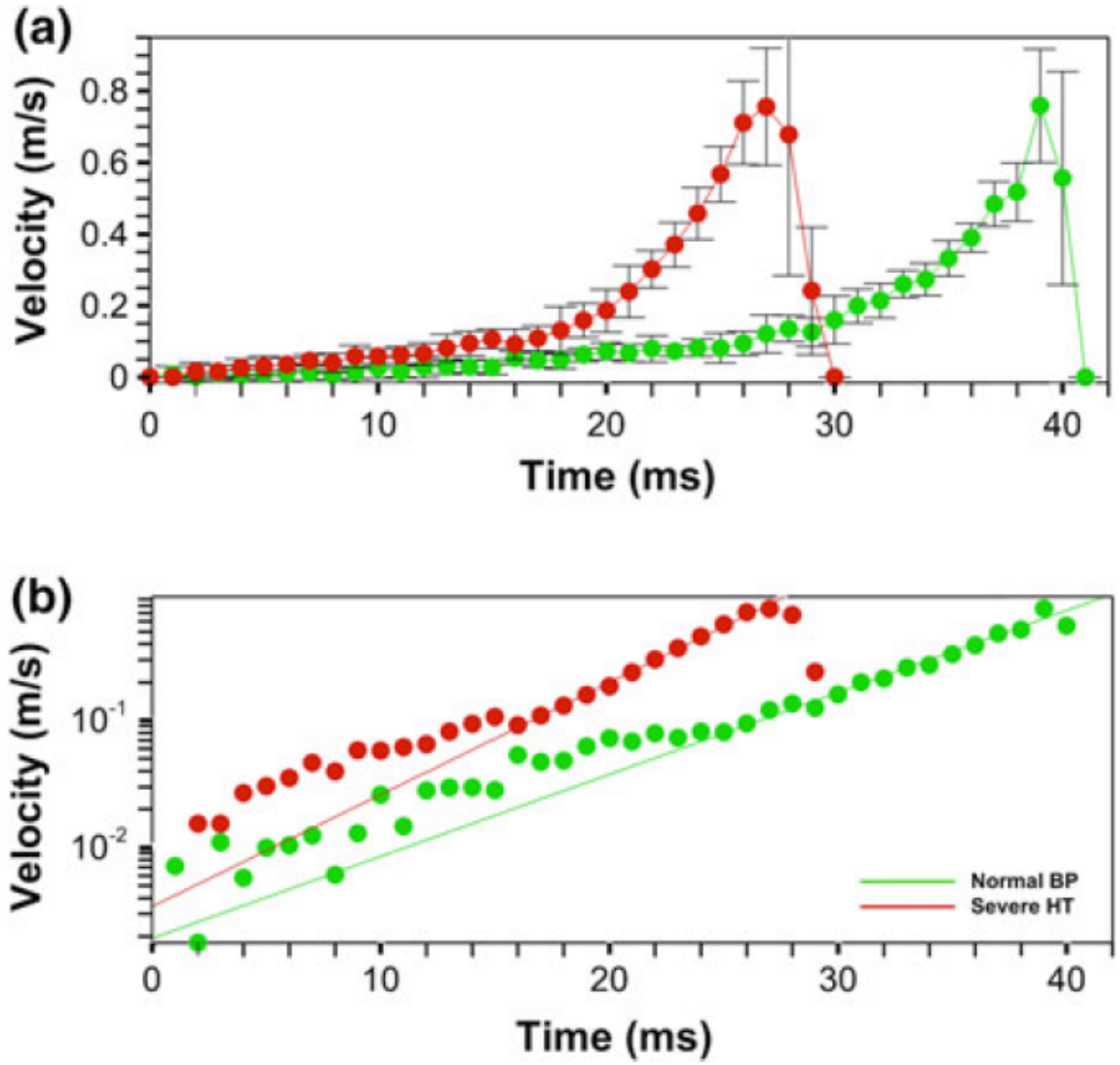

Figure 92: Leaflet tip speed shown on a linear (a) and logarithmic scale (b) for the normal and hypertensive cases. Time origin is defined as the moment leaflet begins closing motion.

The standard deviation of approximately 0.4 m/s indicated that cycle-to-cycle variation is highest during the last few milliseconds before impact. We note a consistent exponential increase in velocity as a function of time for roughly 15ms prior to attaining peak velocity (Figure 92b).

Figure 93 presents the ensemble averages vorticity fields during the valve closure and the diastolic phase for both NBP and HT cases. The maximum mean vorticity magnitude under NBP was about 625 s^{-1} (Figure 93a and 93b). This magnitude increased significantly to 927 s^{-1} for the HT case (Figure 93c and 93d). The maximum principal shear stress magnitude under NBP was calculated to be around 7 Pa, which occurred along the high-shear edges of the regurgitant jet. For the HT case, the maximum principal shear stress magnitude was calculated to be around 9 Pa, which also occurred in the high-shear edges of the regurgitant jet.

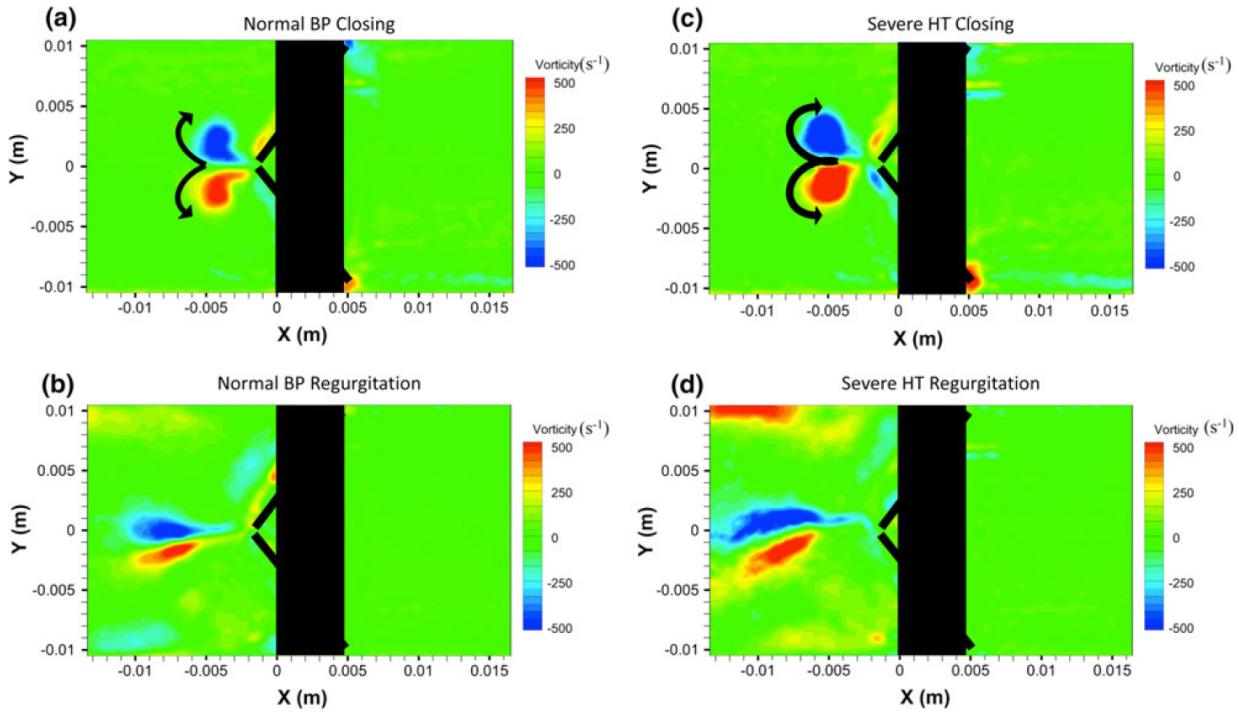

Figure 93: Vorticity map during closing (top row) and regurgitant phase (bottom row) for the normal blood pressure (left column) and hypertensive (right column) cases.

The two sets of parameters defined for platelet activation and platelet lysis showed significantly different BDI magnitudes by a factor of three during the closing and regurgitant phases. For platelet activation, particles attain higher BDI platelet activation

values with exposure time in the region corresponding to the b-datum jet. For platelet lysis, the particles attain higher BDI platelet lysis magnitudes as soon as they experience high shear stress in vicinity of the regurgitant jet. Figure 94a compares the BDI experienced by the particles at different release events sorted by group, and between NBP and HT cases using platelet activation parameters. Error bars represent standard deviation and the symbols on the error bar indicates statistical significance at **p<** 0.05. For the NBP case, the chart shows significantly higher platelet activation at the first release event compared to the other release events. It immediately decreases after the first release event and remains relatively low through the rest of ventricular diastole. For HT, the chart shows platelet activation is relatively low throughout all release events. Comparing between blood pressure cases, NBP produced higher platelet activation values than HT. Similarly, Figure 94b compares the BDI experienced by the particles at different release events by position group and between NBP and HT cases using platelet lysis parameters. Error bars represent standard deviation and the symbols on the error bar indicates statistical significance at **p<** 0.05. For NBP, platelet lysis values remained at about the same values through the first six release events and then significantly decreased at the last release event. For HT case however, platelet lysis BDI values increased through the first two release events, dipped at the third release event, increased at the fourth release event, and then steadily decreased through the remaining three release events. Comparing Figures 94a and 94b we see that platelet lysis parameters predicted higher BDIs values than platelet activation parameters regardless of blood pressure.

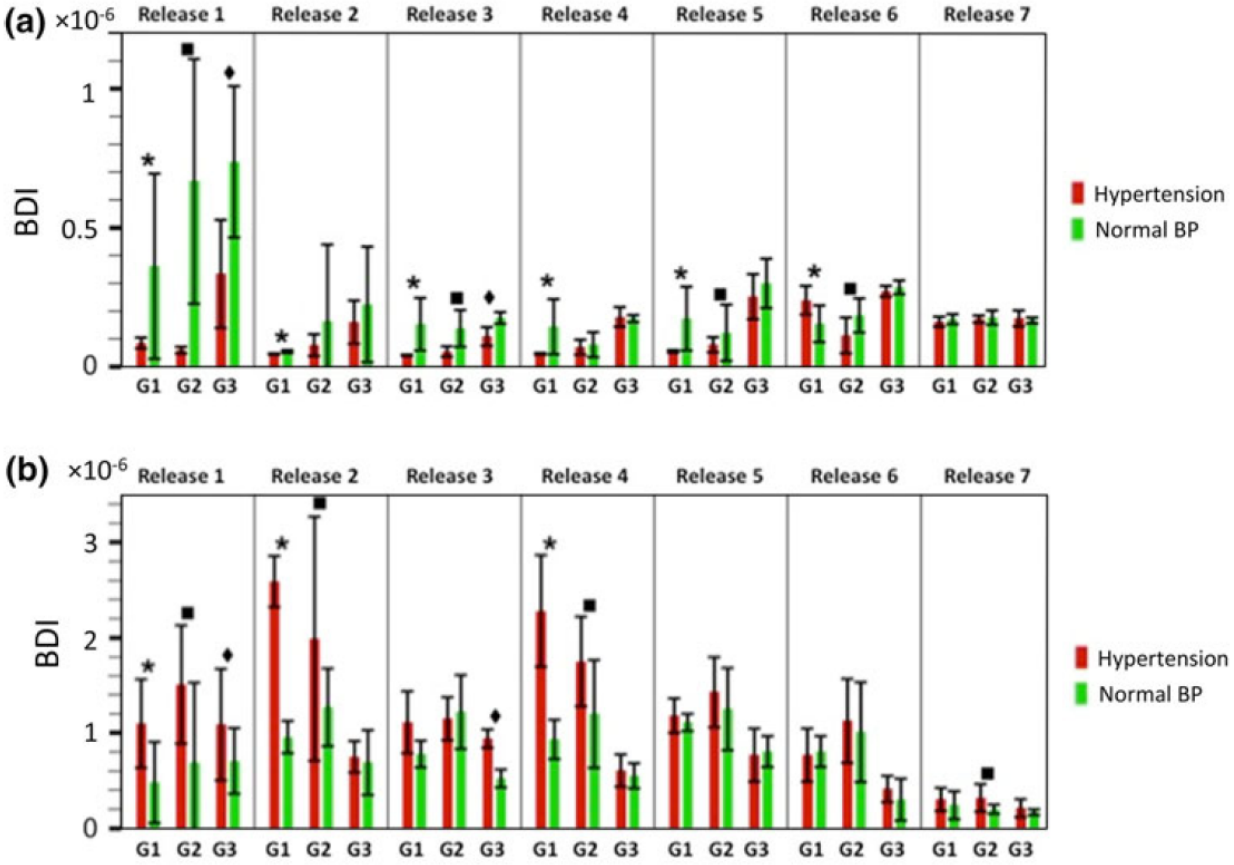

Figure 94: Platelet activation (a) and platelet lysis (b) blood damage indices calculated by position group and for the normal and hypertensive cases.

A.4. Discussion

The peak leaflet closing speed for the model SJM BMHV at both NBP (MAP of 100 mmHg) and HT (MAP of 140 mmHg) remained around 0.75 m/s. However, the time-to-closure at NBP was around about 10 ms longer than that for HT case. The shorted closing times for HT cases is physically expected due to the larger reverse pressure gradient. Given that for both cases the peak speed is around roughly the same, it is clear that indeed the leaflets accelerate more presumably from the larger net closing moment generated from the stronger back-pressure in the HT case. The linear response of the leaflet tip velocities in a lognormal plot (Figure 92) demonstrates that the closing

leaflet develops a positive feedback mechanism, as the back pressure moment increases with the increasing projected area. This explains the exponential behavior. We note here that the slope was directly proportional to MAP for the two cases. The high standard deviation in leaflet tip speed just prior to impact illustrates the high cycle-to-cycle variation during this time point. This high variability can be attributed to turbulent flow structures advecting past the valve.

As shown in Figure 93, immediately prior to full leaflet closure, a closing vortex forms at the b-datum line generated from the closing tips of the leaflets. This vortex is pinched off once the leaflet closes followed by the b-datum jet. Note the stronger closing vortex and the subsequent jet for the HT case. This can be attributed to the larger pressure gradient across the valve leaflets, creating a stronger closing vortex and regurgitant jet. For shear stress, the maximum magnitude was calculated at 5 Pa and occurred in the regurgitant jet area of the flow field within the b-datum jet field. For the case of principal shear stress, the maximum magnitude was calculated at 7 Pa. The higher magnitude of stresses may be attributed to the stronger flow, which in turn is due to the stronger back-pressure for the HT case.

At NBP, Lagrangian tracking showed that particles originating outside of the b-datum line (Groups 1 and 3) experienced a high exposure time and low shear stress in the zones of recirculation upstream of the closed leaflets outside of the regurgitant jet zone. However, as some particles recirculate in the zones upstream of the valve leaflets, they became entrapped in the regurgitant jet later during diastole. Lagrangian tracking showed that particles, which originated near the b-datum line (Group 2), experienced less exposure in the zones of high shear stress near and inside the regurgitant jet zone.

At HT, particles originating outside of the b-datum line (Groups 1 and 3) experienced lower exposure times in the zones of recirculation upstream of the closed leaflets because the regurgitant jet quickly entrained them when they came close. Particles from Group 2, which originated inside the regurgitant jet zone in the b-datum line, experienced the highest values of shear stress. However, the higher jet speed transports the particles into lower shear stress zones much quicker leading to lower exposure times.

Furthermore, HT causes higher magnitudes of averaged principal shear stress over trajectories when compared to NBP case as shown in Figure 95. This is clearly due a direct consequence of the stronger back-pressure that leads to a stronger jet as evidenced in Figure 93.

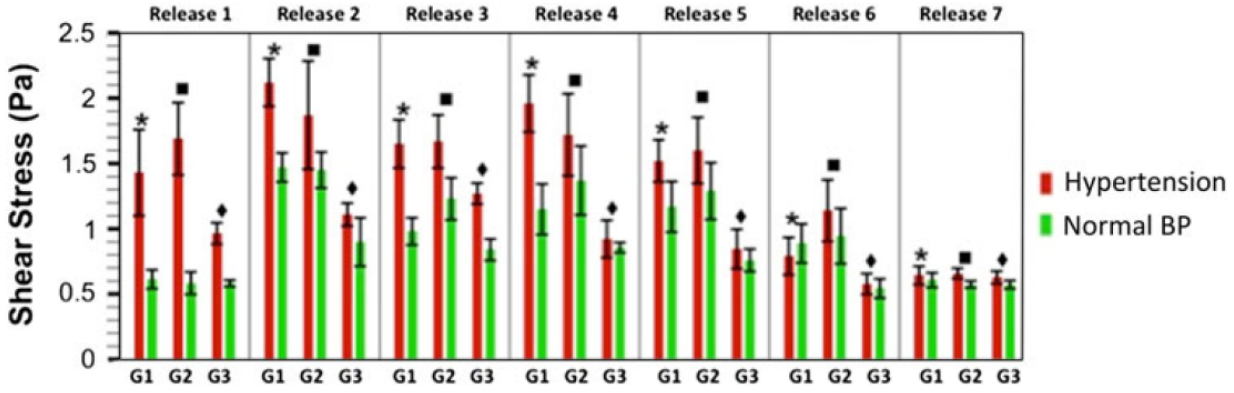

Figure 95: Comparison of average principal shear stress experience by the particles at different release events by position group shown for normal and hypertensive cases.

Under NBP using platelet activation parameters, the models estimated higher BDI for cells experiencing long exposure time in the two zones of recirculation zones immediately upstream of the closed leaflets where shear stress values are low to moderate. Using platelet lysis parameters, the models estimated higher blood damage

in the same recirculation zones. Platelet lysis parameters also estimated high blood damage where particles are exposed to large shear stresses in the regurgitant jet zone. These trends are consistent with the observations made by Bellofiore using BDI platelet lysis and activation parameters during forward flow (ventricular systole).

Under HT using platelet activation parameters, the models estimated lower values when compared to the NBP case. This can be attributed to the further decrease in exposure time as the particles were more quickly transported to lower shear stress zones due to the increased velocity of the regurgitant jet. However, using platelet lysis parameters, the models estimated higher values for the HT case when compared to the NBP case. This can be attributed to the significant increase in shear stresses experienced by the particles under HT. The parameters for lysis clearly place a higher weightage on the shear stress

APPENDIX B: C++ CODE TO CALCULATE THROMBOEMBOLIC POTENTIAL

The thromboembolic potential was calculated using a custom C++ code using the mathematical models for blood damage index described in Chapter 5. The program required values for X position, Y position, U velocity, V velocity, Vorticity, dX/dU, dX/dV, dY/dU, and dY/dV for each particle location from particle paths calculated from lagrangian tracking. The code outputted Shear Stress, Principle Shear Stress, Dosing, Dosing calculated from principal shear stress, Blood Damage Index using first mathematical model, Blood Damage Index using second mathematical model, Blood Damage Index using first mathematical model with principal shear stress, and Blood Damage Index using second mathematical model with principal shear stress,

```
#include <stdio.h>
#include <conio.h>
#include <stdlib.h>
#include <math.h>
#include <string.h>
#include "TecIO.h"

typedef struct  {
double   *t,   *X,*Y,*Vx,*Vy,*Vort,*ddx_Vx,*ddx_Vy,*ddy_Vx,*ddy_Vy,*s,   *D,   *D_p,*SS,
*P_SS, *bdi1, *bdi2, *bdi1_p, *bdi2_p;
int num_pts;
} Particle_Path;

void load_particle_path(char *filename, Particle_Path *pp);
Particle_Path *  load_multi_particle_path(char *filename);

INTEGER4 Debug=0,I,III,DIsDouble=1,VIsDouble=1,KMax=1;  // tecplot variables..
double bdi_a1 = 1.3198;
double bdi_b1 = 0.6256;
double bdi_C1 = 0.00001;
//double bdi_a1 = 0.77;
//double bdi_b1 = 3.075;
//double bdi_C1 = 3.31E-6;
```

```
double visc = 3.5E-6*1060.0;
double pi = 3.14159265358979323846264338327 95;
double DIA = 25E-3;
double TSTEP = 0.002;
int NTSTEPS;
double SKIP_STEPS;
int NUM_PATHS, max_t_steps;
double offset;
char out[1500],out2[1500];

void BDI(Particle_Path *pp);
void WriteTecplotFile(char *zone,char *filename, Particle_Path *pp);
double principle_SS(double dudx, double dudy, double dvdx, double dvdy);
void eigen_values(double *lamda1, double *lamda2, double a, double b, double c);

void main( int argc, char *argv[] )
{

        int i,j,k,startframe,endframe;
        double bdi;

        Particle_Path  A;
        Particle_Path  *PP;

        if(argc < 5) {printf("Usage: %s filename offset startframe endframe\n",argv[0]);
exit(0);}

        sprintf(out,"%s",argv[1]);
        sprintf(out2,"%s",argv[1]);
        k = strlen(out);
        sprintf(&(out[k-4]),"_Activation_out.dat");
        sprintf(&(out2[k-4]),"_Activation_out2.dat");
        //sprintf(&(out[k-4]),"_Lysis_out.dat");
        //sprintf(&(out2[k-4]),"_Lysis_out2.dat");
        sscanf(argv[2],"%lf",&offset);
        sscanf(argv[3],"%d",&startframe);
        sscanf(argv[4],"%d",&endframe);
        printf("Output Filename: %s\n",out);
        printf("Offset: %lf\n",offset);
        printf("startframe: %d\n",startframe);
        printf("endframe: %d\n",endframe);

        NTSTEPS = endframe-startframe+1;
        SKIP_STEPS = offset/1000/TSTEP;
        printf("Total Frames: %d\n",NTSTEPS);
        printf("Skipped_Steps: %lf\n",SKIP_STEPS);
```

```
	PP = load_multi_particle_path(argv[1]);
	for(i=0;i<NUM_PATHS;i++) {
		BDI(&(PP[i]));
	}
	WriteTecplotFile("test",out,PP);
}
Particle_Path * load_multi_particle_path(char *filename) {
	int i,k,count,p_count,t_count,num_pts;
	char dumb[100];
	FILE *fp;
	double t, X,Y,Vx,Vy,Vort,ddx_Vx,ddx_Vy,ddy_Vx,ddy_Vy;
	static Particle_Path *pp;
	fp = fopen(filename,"r");
	count =0;
	printf("Counting number of particle paths...");
	while(!feof(fp)) {
		fscanf(fp,"%s",dumb);
		if(0 == strcmp(dumb,"ZONE")) count++;
	}
	printf("done; number of particle paths =%d\n",count);
	NUM_PATHS = count;
	fclose(fp);

	pp = (Particle_Path *) malloc(NUM_PATHS*sizeof(Particle_Path));
	p_count =0;
	t_count =0;
	fp = fopen(filename,"r");

	while (!feof(fp)) {
		k = fscanf(fp,"%lf%lf%lf%lf%lf%lf%lf%lf%lf",
&X,&Y,&Vx,&Vy,&Vort,&ddx_Vx,&ddx_Vy,&ddy_Vx,&ddy_Vy);
		if (k!=9) {
			fscanf(fp,"%s",dumb); /*printf("%s\n",dumb);*/
			if(0 == strcmp(dumb,"ZONE")) {
				num_pts = t_count;
				if(p_count > 0 ) {
					pp[p_count - 1].num_pts = num_pts;
				}
				p_count++;
				t_count = 0;
			}
		}
		else {
			if(0==1) printf("%lf\t%lf\t%lf\t%lf\t%lf\t%lf\t%lf\t%lf\t%lf\t%lf\t
%lf\n",t,X,Y,Vx,Vy,Vort,ddx_Vx,ddx_Vy,ddy_Vx,ddy_Vy);
```

```
                t_count++;
            }
        }
        pp[NUM_PATHS-1].num_pts = t_count;
        fclose(fp);
        max_t_steps = 0;
        for(i=0;i<NUM_PATHS;i++) if(max_t_steps < pp[i].num_pts) max_t_steps =
pp[i].num_pts;

        for(i=0;i<NUM_PATHS;i++) {
            pp[i].t = (double *) malloc(pp[i].num_pts*sizeof(double));
            pp[i].X = (double *) malloc(pp[i].num_pts*sizeof(double));
            pp[i].Y = (double *) malloc(pp[i].num_pts*sizeof(double));
            pp[i].Vx = (double *) malloc(pp[i].num_pts*sizeof(double));
            pp[i].Vy = (double *) malloc(pp[i].num_pts*sizeof(double));
            pp[i].Vort = (double *) malloc(pp[i].num_pts*sizeof(double));
            pp[i].ddx_Vx = (double *) malloc(pp[i].num_pts*sizeof(double));
            pp[i].ddx_Vy = (double *) malloc(pp[i].num_pts*sizeof(double));
            pp[i].ddy_Vx = (double *) malloc(pp[i].num_pts*sizeof(double));
            pp[i].ddy_Vy = (double *) malloc(pp[i].num_pts*sizeof(double));
            pp[i].s = (double *) malloc(pp[i].num_pts*sizeof(double));
            pp[i].D = (double *) malloc(pp[i].num_pts*sizeof(double));
            pp[i].D_p = (double *) malloc(pp[i].num_pts*sizeof(double));
            pp[i].SS = (double *) malloc(pp[i].num_pts*sizeof(double));
            pp[i].P_SS = (double *) malloc(pp[i].num_pts*sizeof(double));
            pp[i].bdi1 = (double *) malloc(pp[i].num_pts*sizeof(double));
            pp[i].bdi2 = (double *) malloc(pp[i].num_pts*sizeof(double));
            pp[i].bdi1_p = (double *) malloc(pp[i].num_pts*sizeof(double));
            pp[i].bdi2_p = (double *) malloc(pp[i].num_pts*sizeof(double));
            }
        fp = fopen(filename,"r");
        p_count =-1;
        t_count =0;
        while (!feof(fp)) {
            k                =                fscanf(fp,"%lf%lf%lf%lf%lf%lf%lf%lf%lf",
&(pp[p_count].X[t_count]),&(pp[p_count].Y[t_count]),&(pp[p_count].Vx[t_count]),&(pp[p_
count].Vy[t_count]),&(pp[p_count].Vort[t_count]),&(pp[p_count].ddx_Vx[t_count]),&(pp[p
_count].ddx_Vy[t_count]),&(pp[p_count].ddy_Vx[t_count]),&(pp[p_count].ddy_Vy[t_count
]));
            if (k!=9) {
                fscanf(fp,"%s",dumb); /*printf("%s\n",dumb);*/
                if(0 == strcmp(dumb,"ZONE")) {
                    p_count++;
                    t_count = 0;
                }
            }
```

```
                else {
                        if(1==0)                printf("%lf\t%lf\t%lf\t%lf\t%lf\t%lf\t%lf\t%lf\t%lf\t%lf\n",
(pp[p_count].X[t_count]),(pp[p_count].Y[t_count]),(pp[p_count].Vx[t_count]),
(pp[p_count].Vy[t_count]),(pp[p_count].Vort[t_count]),(pp[p_count].ddx_Vx[t_count]),
(pp[p_count].ddx_Vy[t_count]),(pp[p_count].ddy_Vx[t_count]),
(pp[p_count].ddy_Vy[t_count]));
                        t_count++;
                }
        }
        fclose(fp);

        for(i=0;i<NUM_PATHS;i++)
                for(k=0;k<pp[i].num_pts;k++) {
                        pp[i].t[k] = offset/1000+k*TSTEP;
                }

        return pp;
}


void load_particle_path(char *filename, Particle_Path *pp) {
        int k,count;
        char dumb[100];
        FILE *fp;
        double t, X,Y,Vx,Vy,Vort,ddx_Vx,ddx_Vy,ddy_Vx,ddy_Vy;
        fp = fopen(filename,"r");
        count =0;
        while (!feof(fp)) {
                k               =               fscanf(fp,"%lf%lf%lf%lf%lf%lf%lf%lf%lf%lf",&t,
&X,&Y,&Vx,&Vy,&Vort,&ddx_Vx,&ddx_Vy,&ddy_Vx,&ddy_Vy);
                if (k!=10) fscanf(fp,"%s",dumb);
                else {
                        if(1==0)                printf("%lf\t%lf\t%lf\t%lf\t%lf\t%lf\t%lf\t%lf\t%lf\t%lf\t
%lf\n",t,X,Y,Vx,Vy,Vort,ddx_Vx,ddx_Vy,ddy_Vx,ddy_Vy);
                        count++;
                }
        }
        fclose(fp);
        pp->num_pts = count;

        pp->t = (double *) malloc(count*sizeof(double));
        pp->X = (double *) malloc(count*sizeof(double));
        pp->Y = (double *) malloc(count*sizeof(double));
        pp->Vx = (double *) malloc(count*sizeof(double));
        pp->Vy = (double *) malloc(count*sizeof(double));
        pp->Vort = (double *) malloc(count*sizeof(double));
```

```
	pp->ddx_Vx = (double *) malloc(count*sizeof(double));
	pp->ddx_Vy = (double *) malloc(count*sizeof(double));
	pp->ddy_Vx = (double *) malloc(count*sizeof(double));
	pp->ddy_Vy = (double *) malloc(count*sizeof(double));
	pp->s = (double *) malloc(count*sizeof(double));
	pp->D = (double *) malloc(count*sizeof(double));
	pp->SS = (double *) malloc(count*sizeof(double));
	pp->P_SS = (double *) malloc(count*sizeof(double));
	pp->bdi1 = (double *) malloc(count*sizeof(double));
	pp->bdi2 = (double *) malloc(count*sizeof(double));

	fp = fopen(filename,"r");
	count =0;
	pp->s[0] = 0.0;
	while (!feof(fp)) {
		k		=		fscanf(fp,"%lf%lf%lf%lf%lf%lf%lf%lf%lf%lf",&t,
&X,&Y,&Vx,&Vy,&Vort,&ddx_Vx,&ddx_Vy,&ddy_Vx,&ddy_Vy);
		if (k!=10) fscanf(fp,"%s",dumb);
		else {
			if(1==0)		printf("%lf\t%lf\t%lf\t%lf\t%lf\t%lf\t%lf\t%lf\t%lf\t%lf\t
%lf\n",t,X,Y,Vx,Vy,Vort,ddx_Vx,ddx_Vy,ddy_Vx,ddy_Vy);
			pp->t[count] = t;
			pp->X[count] = X;
			pp->Y[count] = Y;
			pp->Vx[count] = Vx;
			pp->Vy[count] = Vy;
			pp->Vort[count] = Vort;
			pp->ddx_Vx[count] = ddx_Vx;
			pp->ddx_Vy[count] = ddx_Vy;
			pp->ddy_Vx[count] = ddy_Vx;
			pp->ddy_Vy[count] = ddy_Vy;
			if(count>0) pp->s[count] = pp->s[count-1] + sqrt(pow((pp->X[count]-
pp->X[count-1]),2)+pow((pp->Y[count]-pp->Y[count-1]),2));
			count++;
		}
	}
	fclose(fp);
}

void BDI(Particle_Path *pp) {

	int i;
//calculate stress
	for(i=0;i<pp->num_pts;i++) {
		pp->SS[i] = visc*fabs((pp->ddy_Vx[i]+pp->ddx_Vy[i]));
```

```
		pp->P_SS[i] = principle_SS(pp->ddx_Vx[i],pp->ddy_Vx[i],pp->ddx_Vy[i],pp->ddy_Vy[i]);
	//	printf("%e\n",pp->ddy_Vx[i]);
	}

//calculate stress
// VALIDATION CODE WITH SINE WAVE STRESS
/*	for(i=0;i<pp->num_pts;i++) {
		pp->SS[i] = 10.0 + 10.0*sin(((double)i)/pp->num_pts*pi*4.0);
		pp->t[i] = 2000.0*i/pp->num_pts;

	}
*/
//calculate dosing
	pp->D[0] = 0.0;
	pp->D_p[0] = 0.0;
	for(i=1;i<pp->num_pts;i++) {
		pp->D[i] = pp->D[i-1] + (pp->t[i]-pp->t[i-1])*pow(pp->SS[i],bdi_b1/bdi_a1);
		pp->D_p[i] = pp->D_p[i-1] + (pp->t[i]-pp->t[i-1])*pow(pp->P_SS[i],bdi_b1/bdi_a1);
	}

//calculate bdi 1
	pp->bdi1[0] = 0.0;
	pp->bdi1_p[0] = 0.0;
	for(i=1;i<pp->num_pts;i++) {
		pp->bdi1[i] = pp->bdi1[i-1] + bdi_C1*bdi_a1*pow(pp->D[i],bdi_a1-1.0)*(pp->t[i]-pp->t[i-1])*pow(pp->SS[i],bdi_b1/bdi_a1);
		pp->bdi1_p[i] = pp->bdi1_p[i-1] + bdi_C1*bdi_a1*pow(pp->D_p[i],bdi_a1-1.0)*(pp->t[i]-pp->t[i-1])*pow(pp->P_SS[i],bdi_b1/bdi_a1);
	}

//calculate bdi 2
	pp->bdi2[0] = 0.0;
	pp->bdi2_p[0] = 0.0;
	for(i=1;i<pp->num_pts;i++) {
		pp->bdi2[i] = bdi_C1*pow(((pp->t[i]-pp->t[i-1])+pow(((pp->bdi2[i-1])/(bdi_C1*pow(pp->SS[i],bdi_b1))),1.0/bdi_a1)),bdi_a1)*pow(pp->SS[i],bdi_b1);
		pp->bdi2_p[i] = bdi_C1*pow(((pp->t[i]-pp->t[i-1])+pow(((pp->bdi2_p[i-1])/(bdi_C1*pow(pp->P_SS[i],bdi_b1))),1.0/bdi_a1)),bdi_a1)*pow(pp->P_SS[i],bdi_b1);
	}
}

double principle_SS(double dudx, double dudy, double dvdx, double dvdy) {

	double a,b,c,lamda1,lamda2;
```

```
	double P_SS;
	a = dudx;
	b = 0.5*(dudy+dvdx);
	c = dvdy;
	eigen_values(&lamda1,&lamda2,a,b,c);
	P_SS = visc*fabs(lamda1-lamda2);
	return P_SS;
}

void eigen_values(double *lamda1, double *lamda2, double a, double b, double c) {

	double Trace, double Determinant;
	Trace = a+c;
	Determinant = a*c - b*b;
	*lamda1 = 0.5*(Trace + sqrt(Trace*Trace-4.0*Determinant));
	*lamda2 = 0.5*(Trace - sqrt(Trace*Trace-4.0*Determinant));
}

void WriteTecplotFile(char *zone,char *filename, Particle_Path *pp)
{
	FILE *fp;
	int Imax,Jmax,i,j,k;
	printf("\nSaving following results in %s\n",filename);

	Imax = NTSTEPS - (int) SKIP_STEPS;
	Jmax = NUM_PATHS;

	fp = fopen(filename,"w");
	fprintf(fp,"VARIABLES = t, Yo, Xo, Y, X, D, D_p, SS, SS_p, BDI1, BDI2, BDI1_p,
BDI2_p\n");
	fprintf(fp,"ZONE I=%d J=%d F=POINT\n",Jmax,Imax);

	fprintf(fp,"\n");

	for(i=0;i<Imax;i++)
		for(j=0;j<Jmax;j++) {
			if(i >= pp[j].num_pts) k = pp[j].num_pts - 1; else k = i;
			fprintf(fp,"%e\t%e\t%e\t%e\t%e\t%e\t%e\t%e\t%e\t%e\t%e\t%e\t%e\t
%e\n",pp[j].t[k],pp[j].Y[0],pp[j].X[0],pp[j].Y[k],pp[j].X[k],pp[j].D[k],pp[j].D_p[k],pp[j].SS[k],pp
[j].P_SS[k],pp[j].bdi1[k],pp[j].bdi2[k],pp[j].bdi1_p[k],pp[j].bdi2_p[k]);
		}
	fclose(fp);

	fp = fopen(out2,"w");
```

```
	fprintf(fp,"VARIABLES = t, Yo, Xo, Y, X, D, D_p, SS, SS_p, BDI1, BDI2, BDI1_p,
BDI2_p\n");

	fprintf(fp,"\n");

	for(i=0;i<Imax;i++) {
		fprintf(fp,"ZONE I=%d J=%d F=POINT\n",Jmax,1);
		for(j=0;j<Jmax;j++) {
			if(i >= pp[j].num_pts) k = pp[j].num_pts - 1; else k = i;
			fprintf(fp,"%e\t%e\t%e\t%e\t%e\t%e\t%e\t%e\t%e\t%e\t%e\t%e\t%e\t
%e\n",pp[j].t[k],pp[j].Y[0],pp[j].X[0],pp[j].Y[k],pp[j].X[k],pp[j].D[k],pp[j].D_p[k],pp[j].SS[k],pp
[j].P_SS[k],pp[j].bdi1[k],pp[j].bdi2[k],pp[j].bdi1_p[k],pp[j].bdi2_p[k]);
		}
	}
	fclose(fp);
}
```

APPENDIX C: C++ CODE TO CALCULATE EFFECTIVE ORIFICE AREA (EOA)

The effective orifice area was calculated using a custom C++ code the Gorlin equation.

$$EOA\ (cm^2) = \frac{Q_{rms}}{51.6\sqrt{\Delta P}} \quad (1)$$

where

EOA	is the effective orifice area
Q_{rms}	is the root mean square flow rate in mL/s
ΔP	is the mean pressure drop in mmHg

The program required values for time step (s), flow rate (L/min), aortic pressure (mmHg), and ventricular pressure (mmHg). The code outputted the average and standard deviation of the Closing Volume, Regurgitant Volume, Forward Flow Volume, Regurgitant Fraction, Pressure Gradient, root mean square Flow Rate, and Effective Orifice Area (EOA).

```
#include <stdio.h>
#include <conio.h>
#include <math.h>
#include <stdlib.h>
#include <string.h>

double time_step = 0.01;
void beat_stat(double *quantity,int num_beats,double *avg,double *stdev);

void main( int argc, char *argv[] ) {
FILE *fp;
double P_ao[10000], P_lv[10000], Q[10000], t[10000];
int cycle[10000];
double temp_P_ao, temp_P_lv, temp_Q, temp_t;
```

```
int
k,i=0,num_data,c_regurg[1000],c_cv[1000],c_rv[1000],c_fv[1000],c_dp[1000],c_Qrms[1
000];
int i_start,check=1,beat=0,num_beats;

double
regurg[1000],cv[1000],rv[1000],fv[1000],rf[1000],dp[1000],Qrms[1000],EOA[1000];
double mean,stdev;

if(argc < 2) {printf("Usage: %s filename\n",argv[0]); exit(0);}

sprintf(out,"%s",argv[1]);
k = strlen(out);
sprintf(&(out[k-4]),"_out.txt");
printf("Output Filename: %s\n",out);

fp = fopen(argv[1],"r");
if (fp == NULL) {
      printf("Failed to open file\n");exit(0);
   }

//reading data and tagging beat numbers
while(!feof(fp)) {

        k=fscanf(fp,"%lf%lf%lf%lf",&temp_t,&temp_P_lv,&temp_P_ao,&temp_Q);
        if(k==4) {
                t[i] = temp_t;
                P_lv[i] = temp_P_lv;
                P_ao[i] = temp_P_ao;
                Q[i] = temp_Q;
                if( Q[i] > 5.0  && Q[i-1] < 5.0) beat++;
                cycle[i] = beat;
                i++;
        }
}
fclose(fp);
num_data = i;
num_beats = beat;
printf("Number of time points = %d\n",num_data);
printf("Number of heart beats = %d\n",num_beats);

//beatwise closing volume threshold calculation
for(beat = 1;beat<=num_beats;beat++) {
regurg[beat] = 0;
c_regurg[beat] = 0;
        for(i=0;i<num_data;i++) {
```

```
                if(Q[i] < 0.0 && cycle[i] == beat) {
                        regurg[beat] +=Q[i]; c_regurg[beat]++;
                }
}
        regurg[beat] /= c_regurg[beat];
        printf("beat %d %lf\n",beat,regurg[beat]);
}

//beatwise closing volume calculation

for(beat = 1;beat<=num_beats;beat++) {
        cv[beat]=0.0;
        c_cv[beat]=0;
        for(i=0;i<num_data;i++) {
                if(Q[i] < regurg[beat] && cycle[i] == beat) { cv[beat] +=Q[i]; c_cv[beat]++;}
        }
        cv[beat] = cv[beat]/c_cv[beat]/60.0*1000.0*c_cv[beat]*time_step;
        printf("beat =%d %lf\n",beat,cv[beat]);
}

//beatwise regurgitant volume calculation
for(beat = 1;beat<=num_beats;beat++) {
        rv[beat]=0.0;
        c_rv[beat]=0;
        for(i=0;i<num_data;i++) {
                if(Q[i] < 0.0 && cycle[i] == beat) { rv[beat] +=Q[i]; c_rv[beat]++;}
        }
        rv[beat] = rv[beat]/c_rv[beat]/60.0*1000.0*c_rv[beat]*time_step;
        rv[beat] -= cv[beat];
        printf("beat =%d %lf\n",beat,rv[beat]);
}

//beatwise forward flow volume calculation
i_start = 0;
for(beat = 1;beat<=num_beats;beat++) {
        fv[beat]=0.0;
        c_fv[beat]=0;
        for(i=i_start;i<num_data;i++) {
                if(Q[i]>0) {
                        fv[beat] += Q[i];
                        c_fv[beat]++;
                        c_dp[beat]++;
                }
                if(Q[i] < 0.0 && Q[i-1]>0 && cycle[i] == beat) {
                        i_start = i;
                        break;
```

```
                }

        }
        fv[beat] = fv[beat]/c_fv[beat]/60.0*1000.0*c_fv[beat]*time_step;
        printf("beat =%d %lf\n",beat,fv[beat]);
}

//beatwise regurgitant fraction calculation
for(beat = 1;beat<=num_beats;beat++) {
        rf[beat]=-1*rv[beat]/fv[beat]*100;
        printf("beat =%d %lf\n",beat,rf[beat]);
}

//beatwise mean pressure difference (gradient) delta P
i_start = 0;
for(beat = 1;beat<=num_beats;beat++) {
        dp[beat]=0.0;
        c_dp[beat]=0;

        for(i=1;i<num_data;i++) if(Q[i] < 0.0 && Q[i-1] > 0.0 && cycle[i] == beat) break;
        k = i-1;
        for(i=k;i>=1;i--) if(P_lv[i] - P_ao[i] < 0.0 && cycle[i] == beat-1) break;
        i_start = i;

        for(i=i_start;i<=k;i++) {
                dp[beat] += P_lv[i] - P_ao[i];
                c_dp[beat] ++;
        }

        dp[beat] = dp[beat]/c_dp[beat];
        printf("beat =%d %lf\n",beat,dp[beat]);
}

//beatwise Qrms
for(beat = 1;beat<=num_beats;beat++) {
        Qrms[beat]=0.0;
        c_Qrms[beat]=0;

        for(i=1;i<num_data;i++) if(Q[i] < 0.0 && Q[i-1] > 0.0 && cycle[i] == beat) break;
        k = i-1;
        for(i=k;i>=0;i--) if(Q[i] < 0.0 && cycle[i] == beat-1) break;
        i_start = i+1;

        for(i=i_start;i<=k;i++) {
                Qrms[beat] += (Q[i]*Q[i])*1000/60*1000/60;
                c_Qrms[beat] ++;
```

```
        }

        Qrms[beat] = sqrt(Qrms[beat]/c_Qrms[beat]);
        printf("beat =%d %lf\t EOA =
%lf\n",beat,Qrms[beat],EOA[beat]=Qrms[beat]/51.6/sqrt(dp[beat]));
}

fp = fopen(out,"w");
mean = 0; stdev = 0;
beat_stat(cv,num_beats,&mean,&stdev);
fprintf(fp,"cv %lf %lf\n",mean,stdev);
beat_stat(rv,num_beats,&mean,&stdev);
fprintf(fp,"rv %lf %lf\n",mean,stdev);
beat_stat(fv,num_beats,&mean,&stdev);
fprintf(fp,"fv %lf %lf\n",mean,stdev);
beat_stat(rf,num_beats,&mean,&stdev);
fprintf(fp,"rf %lf %lf\n",mean,stdev);
beat_stat(dp,num_beats,&mean,&stdev);
fprintf(fp,"dp %lf %lf\n",mean,stdev);
beat_stat(Qrms,num_beats,&mean,&stdev);
fprintf(fp,"Qrms %lf %lf\n",mean,stdev);
beat_stat(EOA,num_beats,&mean,&stdev);
fprintf(fp,"EOA %lf %lf\n",mean,stdev);
fclose(fp);
}

void beat_stat(double *quantity,int num_beats,double *avg,double *stdev)
{
        double average,sd;
        int i;
        average = 0.0;
        sd = 0.0;

        for(i=1;i<=num_beats;i++) {
                average += quantity[i];
                sd += quantity[i]*quantity[i];
        }

        average /= num_beats;
        sd /= num_beats;

        sd = sd - average*average;

        *avg = average;
        *stdev = sqrt(sd);
}
```